BUILDING THE TRINITY RIVER DELTA HYDRODYNAMIC MODEL

TECHNICAL REPORT
CENTER FOR WATER AND THE ENVIRONMENT
UNIVERSITY OF TEXAS AT AUSTIN
SUBMITTED TO TWDB UNDER CONTRACT NO. 1800012195
DOI: 10.18738/T8/BWOOPM

Zi Li, Ph.D.

Ben R. Hodges, Ph.D.

Paola Passalcqua, Ph.D.

June 19, 2020

ABSTRACT

The Trinity River Delta Hydrodynamic Model (TDHM) has been constructed under a contract with the Texas Water Development Board based on prior work with the Nueces Delta Hydrodynamic Model (NDHM) and a new Fine Resolution Environmental Hydrodynamics Model written in C (*FrehdC*). The model has been designed to run at practical grid scales from 10×10 m to 50×50 m using new approaches to handling the subgrid features that are known at the 1×1 m lidar scale but cannot be directly represented in the governing flow equations. Details of the *FrehdC* model are presented in §2. Numerical discretization for the new approach to handling subgrid data (contract Task 2) is presented in §3. The operational sensitivity of the TDHM model results to perturbation of the boundary conditions (contract Task 1) is discussed in §4. The sensitivity analyses are used to recommend sensor locations for a future field study for model validation. Methods for a coupled surface-groundwater version of TDHM (contract Task 3) are presented in §5. Appendices provide further details in the form of pre-publication copies of peer-reviewed journal papers written in the course of this study.

Contents

List of Figures

List of Tables

Acknowledgements

This work was supported by the Texas Water Development Board under contract 1800012195 to the University of Texas at Austin. Appendix B was completed under the prior contract 1600011928, but is provided herein so that the combined project has a single reference source. The study was conducted by Zhi Li as part of his Ph.D. work, culminating in the dissertation Z. Li (2019), supervised by Dr. Ben R. Hodges and with the guidance of dissertation committee member and co-investigator Dr. Paola Passalacqua. Appendix C provides the pre-publication text and figures of an article developed under this research project that has been published in *Environmental Fluid Mechanics* as Z. Li and Hodges (2019b) Appendix D is the text and figures of a second article that has been published in *Advances in Water Resources* as Z. Li and Hodges (2019a). Appendix E is the text and figures of a third article that has been published in *Advances in Water Resources* as Z. Li and Hodges (2020).

1 Introduction

The mismatch of river discharge between United States Geological Survey (USGS) Romayor gage (08066500) and Wallisville gage (08067252) on the downstream reaches Trinity River is an indicator that we do not fully understand the fate, timing and spatial distribution of river water moving across the Trinity River Delta and into Galveston Bay. To better understand these behaviors, the Texas Water Development Board (TWDB) commissioned the Center for Water and the Environment at the University of Texas at Austin to develop a Trinity River Delta Hydrodynamic Model (TDHM). This report provides an overview of the modeling and the status of the project development.

The first stage of this effort – under a prior contract, see Z. Li, Passalacqua, and Hodges (2017) and Appendix B, herein – developed and tested the two-dimensional (2D) TDHM. The model is built on the *FrehdC* code, which was originally developed for the Nueces Delta Hydrodynamic Model (Z. Li & Hodges, 2019a). The prior TDHM development project was focused on processing high-resolution lidar data to generate model bathymetry at practical grid scales that accurately reflects the surface water connectivity through the marsh. The TDHM was been successfully run as part of the prior project.

The present study advances the TDHM by completing three tasks that were identified as critical issues along the path of developing and validating the model:

1. Implementing subgrid-scale algorithms.
2. Sensitivity testing of the TDHM.
3. Adapting TDHM for coupled surface/groundwater flows.

The subgrid-scale algorithms, described in §3) are used to represent the effects of topographic features that cannot be directly represented at the grid scales used for the TDHM. Model sensitivities to tide, wind and river stage boundary conditions are investigated herein by varying one boundary condition at a time and evaluate the differences in predicted salinity (see §4). The results can be used to provide guidance on how a potential field campaign might be arranged for collecting field data that validates the model. In §5, a new groundwater model was developed and coupled to the TDHM to enable simulation of surface-subsurface exchange, which is thought to play a significant role in the fate of river water moving through the delta. The summary and conclusions for this study are presented in §6. Note that a new lidar dataset become available before this project was completed. Although processing this new data set for an improved TDHM is beyond the scope of the present project, we provide a preliminary investigation and discussion in Appendix A.

2 FrehdC model description

2.1 Overview of FrehdC

The Trinity River Delta Hydrodynamic Model (TDHM) is built on the Fine Resolution Environmental Hydrodynamics Model written in the C programming language (*FrehdC*) during the prior phase of this project (see Appendix B for prior project report). The model descriptions in the following section are extracted from papers published as Z. Li and Hodges (2019a, 2019b, 2020) that are included for completeness as Appendices C, D, and E. Because available data is relatively sparse for the Trinity River Delta and there exists a detailed data set for the Nueces River Delta, the testing and validation of the *FrehdC* code in the appendices uses a model setup and data for the Nueces Delta Hydrodynamic Model (NDHM).

Numerical scheme: The *FrehdC* code solves the 2D depth-integrated hydrostatic Navier-Stokes equations on a Cartesian (square) grid. The nonhydrostatic pressure and density gradients neglected in the governing equations. The solution algorithm is a hybrid finite-difference/finite-volume semi-implicit scheme that follows the methods originally designed by Casulli (Casulli & Cattani, 1994; Casulli & Cheng, 1992) with updates for turbulence modeling, accuracy, and stability (Hodges, 2015; Hodges, Imberger, Saggio, & Winters, 2000; Hodges & Rueda, 2008; Rueda, Sanmiguel-Rojas, & Hodges, 2007; Wadzuk & Hodges, 2009). The model is fundamentally mass conservative and allows the advective Courant-Friedrichs-Lewy (CFL) number to be slightly greater than unity in limited time/space areas without causing catastrophic instabilities. Furthermore, the barotropic CFL

(associated with surface waves) can be significantly larger than unity across the entire domain while retaining a stable solution. When running in parallel mode, the computational domain is divided into equal subdomains based on the number of computational threads available. The subdomains communicate with each other by sharing the variables along their common boundaries. Ideally, linearly-increased speedup can be obtained with an increasing number of threads, but in practice the speedup is limited by overhead costs associated with a large number of threads. When executing with four threads, the *FrehdC* code is approximately 10 times faster than the original Frehd (see Appendix B for discussion). This speed-up is due to both the parallelization and the computational efficiency of a compiled C code compared to MATLAB. The *FrehdC* was compiled on Mac Pro OSX El Capitan system (version 10.11.6) with Intel Xeon processor (64 GB memory). Further details on the *FrehdC* numerical approach are provided §2.2.

Wetting & drying: *FrehdC* models wetting and drying processes directly through the free surface solution, which follows the semi-implicit algorithm designed by Casulli and Cheng (1992). This approach allows dry cells to transition into wet cells based where the depth goes from zero to a positive value in the free-surface solution. To avoid both instabilities and the small time steps required for extremely small depths, a minimum depth threshold ($h_{\min} = 10^{-3}$ m) is used. Where the local depth is below the threshold, a formerly wet cell is designated as a dry cell and the water surface elevation is set equal to the bottom bathymetry elevation. Dry cells remain in the computational domain but do not incur computational costs until they become wet. To ensure scalar transport (e.g., salinity) remains conservative, *FrehdC* limits the propagation of the wetting front in a single time step so that a newly-wet cell must be adjacent to an existing wet cell. As is typical of wetting/drying algorithms, the need to truncate very small depths and limit the wet front propagation speed leads to minor non-conservation of mass. This mass loss is tracked during the solution so that the user can be sure the solution is not degraded. Further details on wetting and drying are provided in §2.4.

Stability: In general, the semi-implicit numerical method is unconditionally linearly stable for any barotropic (wave speed) Courant-Friedrich-Lewy number (i.e., CFL_B), and is conditionally stable for an advection (i.e., CFL_A) for $\text{CFL}_A < 1$ (Casulli & Cattani, 1994). The discrete scalar advection in *FrehdC* is an explicit finite-volume advance that strictly requires $\text{CFL}_A < 1$ everywhere for both mass conservation and stability. In general, the semi-implicit approach for momentum is robust to an occasional high-CFL_A transient as the implicit free surface solution serves to damp and re-distribute effects of localized instabilities. Practical experience has shown that momentum stability is retained for $\text{CFL}_A > 1$ in limited space-time locations as long as the the majority of the domain is at $\text{CFL}_A < \sqrt{2}/2$ and care is taken with the nonlinear terms. Similarly, smaller perturbations of scalar concentrations caused by localized hydrodynamic instabilities can be neglected if they do not grow and scalar distributions remain within physical ranges. Unfortunately, the combination of thin layers, wind-driven flows, and wetting/drying across a marsh can lead to high velocities (both real and unreal) in a simulation that can develop into catastrophic instability. In our experience, trying to reduce the global time step to maintain stability in a high-resolution marsh simulation results in absurdly small time steps that are simply impractical for the seasonal-to-annual time frames that are of interest. We have investigated approaches to using local subtime-stepping in lakes (Hodges, 2014) and broader estuaries (Hajduk, Hodges, Aizinger, & Reuter, 2018) but to date have not been able to efficiently implement these approaches in the coastal marsh simulations. In the present work we focus on measures to identify and address the causes of instabilities rather than refining the time step to resolve the flow. Our philosophical argument for this approach is that resolving the flow associated with instabilities in a marsh is of little importance given their localized time/space locations – especially in consideration of the uncertainty and approximations of the system geometry at practical model grid scales. Thus, we seek methods to prevent instabilities by constraining the solution with physically plausible bounds. We have identified three key sources of instability and developed measure to address each: (i) instability caused by flow reversal, §2.3, (ii) instability due to wetting/drying §2.4, and (iii) instability due to wind-driven thin layers §2.5. These measures are necessary, but not entirely sufficient to ensure stable solutions, so we have added an *ad hoc* approach to truncating nonlinear terms (§2.6) to prevent a locally-high CFL from being propagated forward in time. Further details on methods for handling sources of instabilities due to flow reversals and thin layers are provided in §2.3 and 2.5, respectively.

Connectivity in a marsh: Simulating system connectivity in a channelized marsh is an interesting challenge as we often have finer-resolution digital elevation models (e.g., lidar) than we can practically

represent in a simulation. The relative coarseness of the mesh has implications for the advective discretization, which can be readily solved as discussed in §2.7. More difficult is ensuring that a (relatively) coarse model mesh has a reasonable representation of the channel connectivity, flow areas, and blockages – i.e., a question of upscaling to maintain hydrodynamics and transport. In §2.8 we apply a concept of positive and negative objects that can be identified and modeled with automated processes. This approach provides some success, as discussed in Appendix C.4 with application to the Nueces River Delta. There remains a number of outstanding issues (see Appendix C.5).

Outline for §2: The remainder of this section covers: the governing equations and methods for *FrehdC* (§2.2), numerical treatment for stability and flow reversals (§2.3), wetting and drying algorithms (§2.4), effects of thin layers and drag (§2.5), numerical treatment for instabilities in the nonlinear advection term (§2.6), issues associated with the advection discretization and the scales of small channels (2.7), and bathymetry edge processing for connectivity (2.8).

2.2 Governing equations and methods

The TDHM as implemented using *FrehdC* is a semi-implicit, volume-conservative implementation of the depth-integrated, hydrostatic Navier-Stokes (shallow water) equations on a rectilinear (structured) Cartesian grid. The governing equation for momentum is:

$$\frac{\partial u_j}{\partial t} + u_k \frac{\partial u_j}{\partial x_k} = -g \frac{\partial \eta}{\partial x_j} + \frac{\partial}{\partial x_k}\left(\nu \frac{\partial u_j}{\partial x_k}\right) + \frac{\tau_{wj} - \tau_{bj}}{\rho h} \quad : \quad j,k \in \{1,2\} \tag{1}$$

where η is the free surface elevation, u_j are depth-averaged velocities, x_j are the corresponding Cartesian axes, h is the depth, ρ is the local density, ν is an eddy viscosity, and τ_{wj}, τ_{bj} are the wind and bottom stress boundary conditions in the x_j direction. Note that the discretization of the boundary stresses has effects on model stability, as discussed in §2.3, below.

For Eq. (1), the depth at a grid cell center is defined as $h = \eta - b$, where b is the local bottom elevation above a baseline (herein NAVD88). The momentum equations are closed by the depth-integration of the kinematic boundary condition applied to continuity (Casulli, 1999), resulting in

$$\frac{\partial \eta}{\partial t} + \frac{\partial h u_k}{\partial x_k} = 0 \tag{2}$$

Salinity transport is modeled with a standard advection-diffusion equation for incompressible flow:

$$\frac{\partial C}{\partial t} + u_k \frac{\partial C}{\partial x_k} = \frac{\partial}{\partial x_k}\left(\kappa \frac{\partial C}{\partial x_k}\right) \tag{3}$$

where C is the salt concentration (kg/m^3) and κ is the turbulent diffusivity. For simplicity the TDHM uses a uniform, constant, small value of $\nu = 10^{-4}$ m^2/s. This simplification is reasonable where numerical diffusion associated with a low-order advection scheme (see §2.7) provides significant horizontal mixing (Gross, Koseff, & Monismith, 1999; Wang, Fringer, Giddings, & Fong, 2009). Furthermore, for shallow estuaries, fluxes could be controlled by bottom stress and topographical restrictions rather than horizontal shear in the velocity field. In keeping with this simple approach, for the salinity we use $\kappa = \nu$, which is equivalent to setting the turbulent Schmidt number to unity.

Model mesh: *FrehdC* follows the approach of Casulli (1990) in using uniform Cartesian grid cells with an Arakawa-C stencil where the governing equations are solved for velocities on cell faces whereas surface elevations and scalar concentrations are solved on cell centers. The bathymetry is represented as a standard "z-level" system where the bottom elevation at the cell center is considered a uniform value across the entire cell. A finite-volume formulation is used in continuity, Eq. (2), and scalar transport, Eq. (3), so that volume and scalar mass are conserved to numerical precision (the latter as long as $\mathrm{CFL}_A < 1$).

Classification of method: The advection terms on cell faces are finite-difference discretizations, so with the semi-implicit integration of continuity over each grid cell the overall method can be considered a hybrid finite difference/volume approach. The details of the *FrehdC* discretization are similar to the semi-implicit approach described in Casulli (1990) and Casulli and Cattani (1994), except where otherwise noted herein. The choice of discretization for nonlinear terms in advection, Eq. (1), and scalar transport, Eq. (3), is inherently tied to the bathymetric resolution, and is discussed in §2.7, below. The diffusion terms for momentum and scalar diffusivity are discretized with central difference stencils.

Time-marching scheme: For time-marching, *FrehdC* uses the standard semi-implicit "theta method" (Casulli & Cattani, 1994) that is almost (but not quite) 2nd-order accurate (Hodges, 2004). In keeping with the use 1st-order upwind scheme for advection (see §2.7), herein we use a simple 1st-order $\theta = 1$ method, which is a 3-step method consisting of (i) a non-conservative, explicit-Euler approximation of the velocity time advance, (ii) an implicit solution of the free surface elevation (continuity) time advance, and (iii) a finite-volume correction of the velocity field to ensure flux conservation, stability, and consistency with continuity (Gross, Bonaventura, & Rosatti, 2002).

2.3 Stability and flow reversals

Bottom and surface drag terms: As is common in shallow-water models, we model the bottom stresses with a standard drag relationship such that the stress in the x_j direction is

$$\tau_{bj} = \frac{1}{2} C_D \, \rho u_j \sqrt{u_1^2 + u_2^2} \quad : \quad j \in \{1, 2\} \tag{4}$$

where C_D is a drag coefficient. The wind stress in the direction of the wind is modeled as

$$\tau_w = C_{D(w10)} \, \rho_a \left(\vec{U}_{w10} - \vec{U}_\eta \cos\beta \right)^2 \tag{5}$$

where $\vec{U}_{w10}$ is the wind speed measured at 10 m above the surface, $\vec{U}_\eta$ is the water speed at the surface, β is the angle between the wind direction and the water direction, $C_{D(w10)}$ is a drag coefficient based on the 10 m wind measurement height, and ρ_a is the air density. The wind drag in the x_1 and x_2 directions is found from

$$\tau_{w1} \quad = \tau_w \cos\omega \qquad \tau_{w2} \quad = \tau_w \sin\omega \tag{6}$$

where ω is the angle from the x_1 axis to the wind direction.

Preventing destabilization in flow reversals: One of the issues that does not seem to be addressed in the literature is the destabilizing effect that boundary stresses can have in a reversing flow for a semi-implicit solution. In the semi-implicit momentum solution of Casulli (1990) the boundary stresses are defined in terms of the time n values, which implies that the drag between time n and $n + 1$ steps in the implicit solution must oppose the time n flow direction. However, when the flow reverses direction during a time step the explicit drag is effectively an input of momentum, which is destabilizing (i.e., it does not oppose the time $n + 1$ flow direction and is hence anti-dissipative). Although this problem is unlikely to lead to catastrophic instability in simulations of a large-scale estuarine flow where reversals have a long time-scale, it can be a vexing issue in a shallow, wind-driven marsh where reversals are small in spatial-scale and short in time-scale. To fix this problem, the bottom drag term is time-linearized and solved implicitly as part of the free-surface solution. Specifically, the bottom drag term in Eq. (1) is represented as

$$\frac{\tau_{bj}}{\rho h} = \frac{C_D \, u_j^{n+1} \left([u_1^n]^2 + [u_2^n]^2 \right)^{1/2}}{2h^n} \quad : \quad j \in \{1, 2\} \tag{7}$$

where n superscripts indicate data at the known time level and $n + 1$ superscripts are the unknown solution time level. This approach is similar to time-linearization ideas developed by Patankar (Burchard, Deleersnijder, & Meister, 2003; Patankar, 1980). Time-linearization ensures that the bottom drag is always in opposition to the velocity direction at time $n + 1$ by moving the drag term from the $\mathbf{b}$ side of $\mathbf{Ax} = \mathbf{b}$ to the $\mathbf{A}$ side in the matrix inversion step of the semi-implicit method. The details of the semi-implicit matrix can be found in Casulli (1990); Casulli and Cattani (1994). The time-linearization approach guarantees the net effect of drag term is *always* in opposition to the time $n + 1$ velocity and thus is always dissipative. Note that simply discretizing drag as an implicit term without this time-linearization is possible, but it creates a nonlinear term of $(u^{n+1})^2$ that destroys the simple linear solution technique at the heart of the semi-implicit method (Casulli, 1990). Failure to use implicit drag discretization can destabilize the solution during flow reversals, which is a particular problem for wind-driven flows in a marsh.

2.4 Wetting and drying

Challenges and mass conservation: Wetting and drying of tidal flats is always a challenge for numerical modeling and has a wide literature (e.g., Candy, 2017; Martins, Leandro, & Djordjevic,

2018; Medeiros & Hagen, 2013; Teng et al., 2017). Wetting/drying methods are typically somewhat *ad hoc* and related to the underlying numerical discretization techniques. In the semi-implicit approach, dry cells do not cause instability as they simply imply $\eta^{n+1} = \eta^n = b$ if there are no fluxes into a cell (R. T. Cheng, Casulli, & Gartner, 1993). However, a wetting/drying challenge for the semi-implicit theta-method is that the theory (Casulli & Cattani, 1994) does not constrain the implicit solution of η relative to the bottom elevation b, so it is entirely possible to have a time step where a wet grid cell starting with $\eta^n > b$ will end with $\eta^{n+1} < b$. This unphysical condition is typically remedied with an *ad hoc* clamping of $\eta^{n+1} = b$ to create a dry cell. Unfortunately, as the original solution of $\eta^{n+1} < b$ is volume conservative, such clamping inherently causes non-conservation of volume, which cascades to non-conservation of scalars.

Thin layer effects, rapid drying: A related problem is that real-world wetting/drying involves thin layers where the flow is strongly affected by the local bottom slope; however, the z-level grid system only represents the dynamic effects of the larger-scale bottom slope between grid cells and does not directly consider the volume effects of the slope within a grid cell itself. Thus, during the model drying process a rapid drawdown can create the conditions shown in Fig. 1 where water on the upstream tidal flats has a dramatically different free surface elevation. If the free surface gradient between the two cells is used as the momentum source for the flow (as in the standard solution algorithm), then extreme unrealistic velocities are produced. The result is typically $\eta^{n+1} < b$ in the next time step and a large loss of conservation. We solve this problem through an *ad hoc* approach that treats the flow from the upland as though it is similar to flow over weir (Tracy, 1957) where the velocity is given by

$$u_f = C_f \sqrt{2gh_f} \tag{8}$$

where u_f is the velocity across the cell face, C_f is an empirical coefficient (herein 0.7) and h_f is the water depth at the face. The u_f computed from time n data can be used directly in the discretization of the free surface evolution (removing the dependency on the free surface pressure gradient across the face), which ensures that the velocity remains limited to physically reasonable values and the drying step to $\eta < b$, if it occurs, will be small.

Rapid wetting: Rapid wetting can cause a problem similar to rapid drying. For efficient computation of scalar transport, wetting should ideally occur with a wet/dry front that moves less than Δx in a time step (i.e., wetting only dry cells that are adjacent to wet cells), otherwise, the scalar computation must be subtime-stepped to ensure stability. However, the semi-implicit method is stable for $\text{CFL}_B > 1$, which implies that water can appear in a dry cell that is *not* adjacent to the wet/dry front. These non-adjacent wetting cells typically have very thin layers containing little volume or scalar mass, so the simplest *ad hoc* approach is to maintain these cells as dry until the wet/dry front moves adjacent, which is accomplished with a $\text{CFL}_A < 1$ limiter for movement of the wet/dry front. This approach necessarily is non-conservative (similar to other aspects of wet/dry algorithms), but the volumes lost in the tested simulations are negligible.

Minimum practical depth: Finally, to prevent wetting and drying from becoming a computational burden as $h \to 0$, we set a minimum depth such that $h < h_{\min}$ results in $\eta = b$ and a small loss of volume. The present work uses $h_{\min} = 10^{-3}$ m.

2.5 Thin layers and drag

Nonlinearity of drag in thin layers: As water layers get thinner, i.e., $h \to 0$, the bottom drag of Eq. (41) requires an increasing value of C_D to represent the nonlinearly-increasing drag as the flow evolves toward laminar. That is, a Reynolds number defined as $uh\nu^{-1}$ is expected to decrease as the layer thins and result in an increasing C_D (Bricker, Inagaki, & Monismith, 2005; Chao, Jia, Shields, Wang, & Cooper, 2008; Spitz & Klinck, 1998). We use a simple buffer layer approach for this problem, similar to Chou et al. (2015); Ip, Lynch, and Friedrichs (1998); Wang et al. (2009); Zheng, Chen, and Liu (2003). For our implementation, a drag buffer layer thickness (h_{bd}) is defined such that $h < h_{bd}$ provides a linearly-increasing drag from the standard value to a maximum value as $C_{D(b)} = (C_{Dmax} - C_D)\,(h_{bd} - h)\,h_{bd}^{-1}$. Herein the $C_{Dmax} = 1.0$ and $h_{bd} = 0.1$ m.

Wind effects on thin layers: The wind acting on thin-layer flows creates further challenges. The empirical wind stress relationship of Eqs. (4) and (5) are based upon data where the wind and

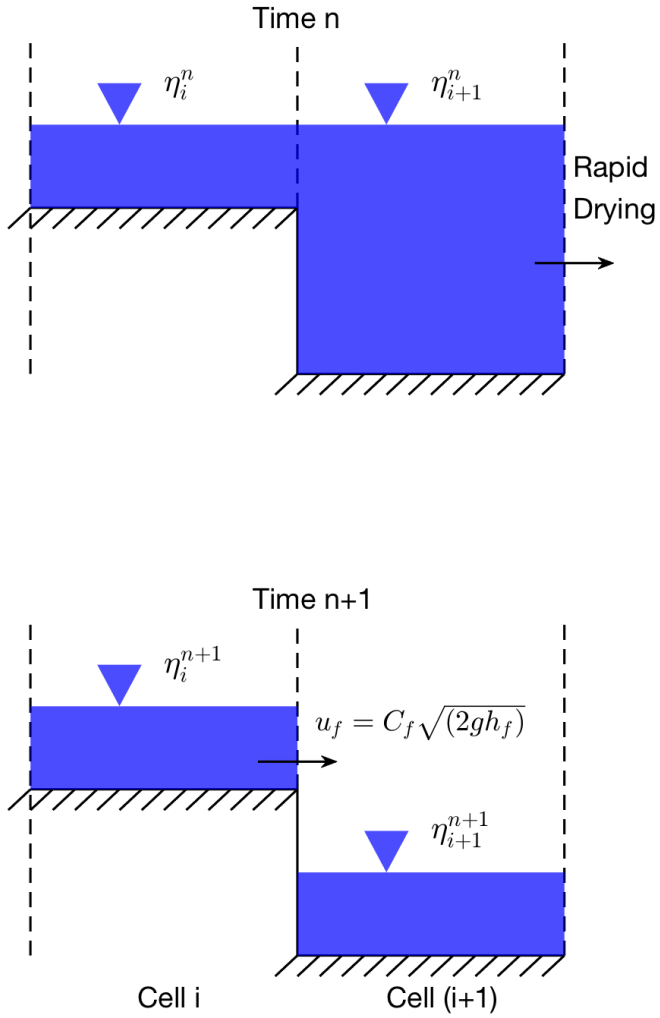

Figure 1: Rapid drawdown from (a) to (b) leaves water volumes in the uplands with a large driving pressure gradient. In (b), the steep surface gradient $\eta_i^{n+1} - \eta_{i+1}^{n+1}$ could cause unrealistically high velocity unless Eq. (8) is used to correct the velocity.

bottom boundary layers are effectively separated over a water column of some depth. However, for a sufficiently thin layer, both the wind-stress boundary layer and the bottom boundary layer will take up the entire water column, and simple linear superposition of their effects does not provide an adequate model of nonlinear interactions. That is, in the standard model the energy transfer from the wind is split between turbulent dissipation in the water column and acceleration of the near surface layer, but in a thin layer some portion of the wind effects are directly dissipated at the solid boundary. This issue is critical as simple superposition of standard bottom drag equations and wind-forcing models leads to absurd accelerations of thin-layer flows. To the best of our knowledge, this issue has not been discussed in the literature and there are no empirical data sets looking at the boundary layer interactions at the scales that are typical of tidal marshlands. Ideally, the τ_w model should be independent of the layer thickness and the τ_b model should account for the increased dissipation associated with the interaction of boundary layers. However, maintaining the standard τ_w and increasing τ_b requires a delicate balancing act otherwise the wind-driven velocity tends become unrealistically large. In the absence of data, we found the most practical approach was to provide an exponential decrease in the wind $C_{D(w10)}$ for water depths below a h_{bw}, which can be thought of as a wind buffer layer thickness – similar to but independent of h_{bd} for the drag. Formally we have $C_{D(wb)} = C_{D(w10)} \exp\left\{-\alpha \left(h_{bw} - h\right) h_{bw}^{-1}\right\}$ where α is a decay coefficient. For the present work we used $h_{bw} = 0.1$ m and $\alpha = 10$.

2.6 Instabilities and the nonlinear advection term

Incipient instabilities in a simulation typically appear as anomalously-large local velocities. In the time-marching algorithm, the nonlinear advection term typically amplifies the anomaly and propagates the instability to adjacent cells. Ideally, a model would never see such an anomaly or would reduce the time step to stabilize any anomaly. It seems generally impossible to ensure that a complex marsh model will be entirely free of instability, and reducing the model time step is simply impractical. Our solution is to sacrifice local fidelity of the discrete equations in order to suppress the growth incipient instabilities – we do this by limiting the nonlinear terms in the momentum solution. We define a nonlinear term limiter with a low cutoff (L_c) and a high cutoff (H_c). For a grid cell where $\text{CFL}_A > H_c$, the local nonlinear term is completely suppressed. For a cell where $L_c < \text{CFL}_A < H_c$, the discrete nonlinear terms are linearly reduced, i.e. for $N = u\partial u/\partial x$, the reduced nonlinear term is a simple linear decay over the cutoff range: $N_R = N\left(H_c - \text{CFL}_A\right)/\left(H_c - L_c\right)$. In the present work $L_c = 0.5$ and $H_c = 0.7$. The limiter ensures that the high CFL_A at a few points in space/time are not amplified by nonlinearity, which typically then allows the anomaly to be dissipated in the following free-surface solution.

2.7 Advection discretization and channel scales

First order schemes for coarse grid scales: In general, the literature deprecates the use of 1st-order upwind spatial discretization schemes as too diffusive for practical use. We agree with this philosophy in general, but in the specific application to 2D modeling of a channelized marshes we find higher-order schemes can distort the channel connectivity. Ideally, every channel in a marsh would be discretized by 8 or 10 grid cells across its width, allowing development of horizontal boundary effects and a meaningful ability to use a 3rd-order upwind discretization stencil. As a practical matter, such a discretization would drive the grid mesh down to ~ 0.1 m, requiring a time step less than 10^{-2} seconds and an impractical (for today's computers) computational time for modeling months (or even days) of marsh hydrodynamics. Once we are forced to a relatively coarse mesh, as is common in many geophysical problems, we encounter practical difficulties in applying a higher-order upwind stencil. *Where a channel is represented with only one or two grid cells across its width and has convoluted S-turns along its length, a higher-order upwind stencil requires extensive exception handling to ensure that the selected scalar values represent the values in the channel and not in the nearby shallows.* Otherwise, the modeled scalar flux in the channel can be driven by out-of-channel values that are entirely unrealistic.

Example of problems with higher-order schemes: To illustrate this problem, consider Fig. 2 where an 180 m $\times$ 180 m channel area at a coarse grid resolution of 30 m $\times$ 30 m is presented (see §2.8 for further details). This area is divided into shallow (brown) and deep (blue) regions to illustrate typical marsh channels on a coarse mesh. It can be seen that the 1st-order upwind stencil (red dots) are guaranteed to include only in-channel values. In contrast, 3rd-order schemes (white circles)

include values in shallow cells that are unlikely to represent either the correct momentum or salinity in the channel. An interpolation stencil in 2D with depth-dependent weighting for the nine upwind cells is a theoretical higher-order solution to this challenge. However, the key difficulty for a 2D stencil is that a channelized area requires extensive exception handling for blocked cell-edges, which will be computationally expensive.

Effects on diffusion: An unfortunate consequence of the use of the 1st-order stencil is that numerical diffusion will be greater than the physical κ of Eq. (3) under most flow conditions. Thus, we expect the model to diffuse any sharp salinity gradients in the marsh, which must be considered in interpreting results.

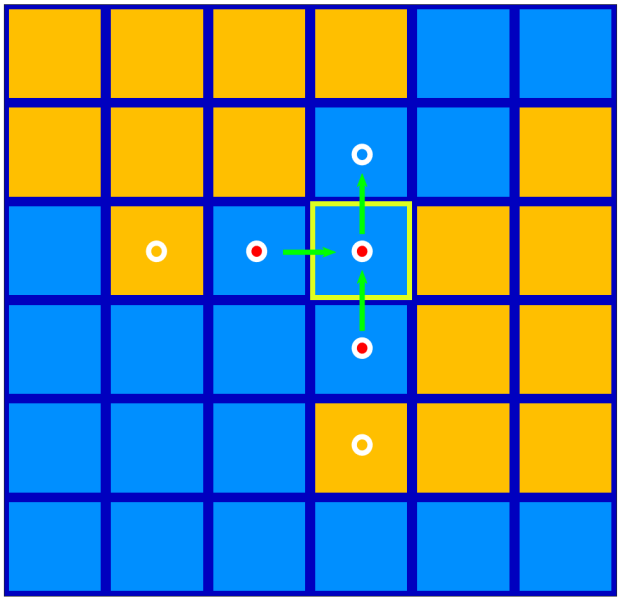

Figure 2: Stencils for 1st-order upwind (red dots) and 3rd-order upwind (white circles) schemes applied on one 30×30 m grid cell (yellow box). The brown indicates shallow areas whose scalar concentrations may be significantly disconnected from the deeper (blue) channels. The green arrows represent the major fluxes in/out of the target cell.

2.8 Bathymetry edge processing for connectivity

Difficulties of fine-resolution modeling: Creating an adequate bathymetry for a marsh requires trade-offs between structural accuracy and practical computability. Modeling directly using the (e.g.) 1×1 m resolution raster bathymetry that is often available is theoretically possible, but would generally require more than 10^8 grid cells and $\Delta t < 1$ s for any large simulation. The latter implies more than 3.0×10^7 steps per year of simulation. With a numerical model using several hundred floating point operations per grid cell per time step, we would require $O(10^{18})$ floating point operations for a year of simulation. To achieve reasonable simulation times would require a supercomputer in the petaflop range. Although such computers exist, they are not yet readily available to the majority of the scientific community. Furthermore, for larger marsh and delta systems the computational scales required for such high-resolution modeling simply are beyond what we can presently handle.

Upscaling fine-resolution data: For the present work, we developed up-scaled raster bathymetries following the approach in Hodges (2015) using a median filter to create a coarse-grid raster and a fine-scale (1 m) representation of the resolvable "background" topography In general, the

filtered bathymetry at the coarse-grid scale is missing connectivity at < 0 m elevation between two depressions in the marsh. The difference between the background topography and the original fine-resolution topography is used to identify contiguous objects that are not represented in the coarse-grid bathymetry but should have large-scale effects. These can be described as "positive" objects that represent blocking features higher than the coarse-grid bathymetry and "negative" objects that represent unresolved channels. The method for using positive objects to create "cell edge" features at the boundary between two raster cells is described in detail in Hodges (2015). A modification of this approach is used herein for negative objects, which are identified as channel grid cells with the bottom elevation adjusted from the median filter value to the median of the negative object. An additional step is taken to find locations where two channel cells are only diagonally connected (i.e. they do not share a common cell face). The bottom is adjusted in a cell perpendicular to the diagonal to create resolved channel bends that maintain connectivity.

Creating channel connectivity in upscaled mesh: The negative object method effectively takes any channel that is narrower than the model grid and broadens it to the grid scale to ensure connectivity. This approach maintains connectivity at coarse-grid scales at the cost of physical fidelity in the channel cross-sectional area. To allow a balance between connectivity and fidelity, we ignore identified channels that take less than r fine grid cells in a coarse grid cell, where r is the grid-coarsening ratio (e.g. $r = 15:1$ for a 15×15 m grid developed from 1×1 m data). This approach improves the connectivity at the coarse grid scale, but some connectivity for small channels are not restored. Developing intelligent and robust automated approaches to ensuring good channel connectivity of fine-scale effects within the coarse model mesh remains an ongoing challenge. A detailed example of the approach for the Nueces Bathymetry is provided in Appendix C.2.8.

3 Simulation of subgrid topographic effects

3.1 Overview

Subgrid vs. edge-based approaches: A challenge for practical modeling of any river delta is that winding narrow channels and embankments may only be visible in topography using a fine grid resolution, e.g., the 1×1 m scale available in many Texas lidar datasets. However, at coarser grid scales such features disappear in the averaging of fine-scale topography, as discussed in §2.8. Ideally, a model run at a coarse grid scale should be able to represent the effects of known finer-scale features within the coarse-grid model solution (i.e., without actually solving the fine-scale momentum and continuity equations). Studies of the Nueces River Delta showed averaging the fine-scale topography in grid coarsening can result in extremely poor representation of flux connectivity; to address this issue Hodges (2015) developed a "edge blocking" approach for grid coarsening to represent narrow embankments at grid scales wider than the actual embankment. The blocking approach was inverted and extended to narrow channels to ensure path connectivity in Z. Li and Hodges (2019b), as discussed in §2.8 and Appendix C. These simple edge-based approaches represent the net effects of fine-scale topography at the coarse scale in blocking/channelizing flow, but do not represent the flow dynamics associated with fine-scale topography. The "edge" approach is purely a topographic processing technique and can be contrasted with more sophisticated "subgrid" topography models. A subgrid model is one that uses an alteration of the momentum and/or continuity equations to directly represent effects of internal topography in the simulation, e.g., Defina, D'Alpaos, and Matticchio (1994), Bates (2000), Yu and Lane (2006b), Sanders, Schubert, and Gallegos (2008), Guinot, Sanders, and Schubert (2017) – and by the present authors in Z. Li and Hodges (2019a). Our goal in the present work is to evaluate whether the two approaches, *edge* and *subgrid*, provide similar or different results. The subgrid method of Z. Li and Hodges (2019a) is more computationally costly than the edge methods of Hodges (2015) or Z. Li and Hodges (2019b), but provides a more sophisticated subgrid model that automatically maintains surface connectivity, wetting/drying patterns and conserves storage volume during the grid coarsening process. This new subgrid model is an option in the *FrehdC* model and TDHM.

Outline of §3: In the remainder of this section, the subgrid geometry definitions are provided in §3.2, the necessary changes to the *FrehdC* discretization in the numerical method are presented in §3.3, the time-varying update of geometry is discussed in §3.4, and a new idea for block-checking that represents internal features is proposed in §3.5. Model results comparing the TDHM for the edge method and the subgrid method are provided in §3.6.

3.2 Subgrid geometry definitions

Before presenting the governing equations and discretization schemes of the subgrid-enhanced *FrehdC* model, it is useful to define the subgrid geometry variables that describe the high-resolution characteristics of a coarse grid. Consider a coarse grid cell (i, j) in a 2D domain with dimensions Δx by Δy, which contains $\Lambda \times \Psi$ high-resolution (subgrid) cells. Let Ω to represent the domain of cell (i, j) and Γ its boundary. The size of one subgrid cell is $\delta x \times \delta y$, where $\Lambda\, \delta x = \Delta x$, and $\Psi\, \delta y = \Delta y$. Figure 3 shows an example of a coarse grid cell with $\Lambda = \Psi = 4$. Each subgrid cell is labeled using (λ, ψ), where $1 \leq \lambda \leq \Lambda$ and $1 \leq \psi \leq \Psi$.

Cell elevations and volumes: The bottom elevation of a subgrid cell is denoted as $z_{i,j,\lambda,\psi}$. The coarse grid cell $\Omega_{i,j}$ is characterized by a single value of surface elevation, $\eta_{i,j}$. A single value for bottom elevation ($Z_{i,j}$) is defined as:

$$Z_{i,j} = \min_{\lambda,\psi \in \Omega} \left(z_{i,j,\lambda,\psi} \right) \tag{9}$$

The use of *min* function ensures the cell is identified as "wet" (i.e., contains some water), even when only a single of the (λ, ψ) subgrid cells is below the free surface. For regions with frequent wetting and drying, this definition is necessary to represent the inundation area and flux paths. The volume of cell $\Omega_{i,j}$ is defined as:

$$V_{i,j} = \sum_{\lambda,\psi \in \Omega} \max\left(\eta_{i,j} - z_{i,j,\lambda,\psi}, 0\right) \delta x\, \delta y \tag{10}$$

where the *max* function ensures that dry subgrid cells are not counted as negative volumes. If no subgrid topography exists, Eq. (10) simply reduces to $V_{i,j} = H_{i,j} \Delta x \Delta y$ (where $H_{i,j} = \eta_{i,j} - Z_{i,j}$ is the depth).

Face areas: Similarly, we may define the cell face areas as illustrated in Fig. 3. For example, the face areas normal to the x-axis on the plus and minus sides of $\Omega_{i,j}$ are:

$$\begin{aligned}
(A_X)_{i+\frac{1}{2},j} &= \sum_{k=1}^{\Psi} \max\left(\eta_{i,j} - z_{i,j,\Lambda,k}, 0\right) \delta y \\
(A_X)_{i-\frac{1}{2},j} &= \sum_{k=1}^{\Psi} \max\left(\eta_{i,j} - z_{i,j,1,k}, 0\right) \delta y
\end{aligned} \tag{11}$$

The face areas normal to the y-axis on the plus and minus sides of $\Omega_{i,j}$ are:

$$\begin{aligned}
(A_Y)_{i,j+\frac{1}{2}} &= \sum_{k=1}^{\Lambda} \max\left(\eta_{i,j} - z_{i,j,k,\Psi}, 0\right) \delta x \\
(A_Y)_{i,j-\frac{1}{2}} &= \sum_{k=1}^{\Lambda} \max\left(\eta_{i,j} - z_{i,j,k,1}, 0\right) \delta x
\end{aligned} \tag{12}$$

and the face area on the top face of the grid cell is:

$$(A_Z)_{i,j} = \sum_{\lambda,\psi \in \Omega} \epsilon_{i,j,\lambda,\psi} \delta x\, \delta y \tag{13}$$

$$\epsilon_{i,j,\lambda,\psi} = \begin{cases} 1, & \eta_{i,j} > z_{i,j,\lambda,\psi} \\ 0, & \eta_{i,j} \leq z_{i,j,\lambda,\psi} \end{cases} . \tag{14}$$

Labels for position in space: For use in discrete equations, the subgrid variables V, A_X, A_Y and A_Z are labeled by its (i, j) indices, which are the coordinates of its center. For example, we can also write $(A_X)_{i,j}$ to represent the face area normal to the x-axis centered at (i, j), or $V_{i+\frac{1}{2},j}$ to represent the cell volume centered at $(i + \frac{1}{2}, j)$. These subgrid variables are introduced into the discrete governing equations as illustrated in the following section.

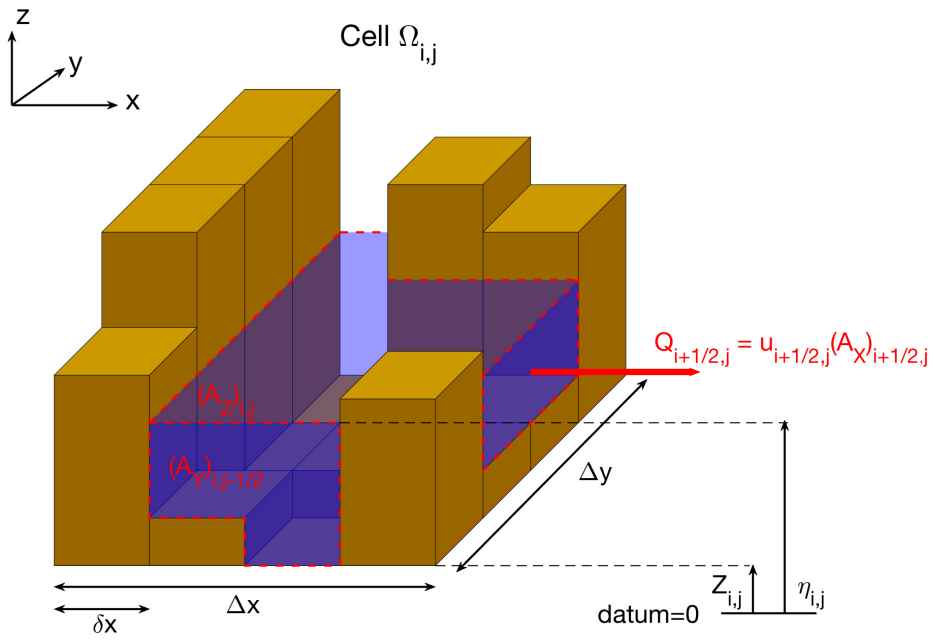

Figure 3: An illustration of the subgrid variable definitions using a coarse grid cell that contains 4×4 subgrid cells.

3.3 Subgrid discretization

Governing equations: The 2D depth-integrated free surface equation, momentum equations, and the scalar transport equation can be written in an integral form similar to Sanders et al. (2008):

$$\frac{\partial}{\partial t}\int_{\Omega}\eta\, d\Omega + \int_{\Gamma}\boldsymbol{u}\cdot\boldsymbol{n}\, dA = 0 \tag{15}$$

$$\int_{V}\left(\frac{\partial \boldsymbol{u}}{\partial t} + (\boldsymbol{u}\cdot\boldsymbol{n})\frac{\partial \boldsymbol{u}}{\partial \boldsymbol{x}}\right) dV = \int_{\Gamma} g\eta\boldsymbol{n}\, dA + \int_{\Gamma}\boldsymbol{\tau_{\nu}}\cdot\boldsymbol{n}\, dA + \int_{\Omega}\boldsymbol{\tau_{b}}\, d\Omega \tag{16}$$

$$\frac{\partial}{\partial t}\int_{V} C\, dV + \int_{\Gamma}(\boldsymbol{u}\cdot\boldsymbol{n})C\, dA = \int_{\Gamma}\boldsymbol{\tau_{\kappa}}\cdot\boldsymbol{n}\, dA \tag{17}$$

where η is the free surface elevation, $\boldsymbol{u} = [u, v]^T$ are depth-averaged velocities, $\boldsymbol{x} = [x, y]^T$ are the corresponding Cartesian axes, $\boldsymbol{n}$ is the normal unit vector to a flux-surface Γ, $\boldsymbol{\tau_b}$ is the bottom stress, $\boldsymbol{\tau_{\nu}}$ is the viscous stress, C is the scalar concentration, and $\boldsymbol{\tau_{\kappa}}$ is the scalar diffusion term. An infinitesimal volume inside the grid cell is dV with infinitesimal cell face areas dA, which can be written as $dA = h(\Gamma)\, d\Gamma$ where $h(\Gamma)$ is the depth function along the cell boundary. The density is assumed to be a constant.

Bottom stress and turbulence: The bottom stress and viscous stress are defined as:

$$\boldsymbol{\tau_b} = \frac{1}{2}C_D\,\boldsymbol{u}|\boldsymbol{u}| \tag{18}$$

$$\boldsymbol{\tau_{\nu}} = \left[\nu\frac{\partial \boldsymbol{u}}{\partial x}, \nu\frac{\partial \boldsymbol{u}}{\partial y}\right]^T \tag{19}$$

where ν is the eddy viscosity, and C_D is the drag coefficient defined as:

$$C_D = \frac{g\hat{n}^2}{\bar{H}^{\frac{1}{3}}}, \quad \bar{H} = \frac{V}{\Delta x \Delta y} \tag{20}$$

In Eq. (20), $\hat{n}$ is the Manning's roughness coefficient, which is assumed to be a constant in the present study. The scalar diffusion terms are computed as:

$$\boldsymbol{\tau_{\kappa}} = \left[\kappa\frac{\partial C}{\partial x}, \kappa\frac{\partial C}{\partial y}\right]^T \tag{21}$$

where κ is the eddy diffusivity. We use $\kappa = \nu = 10^{-4}$ m^2 s^{-1} because the *FrehdC* model has been shown to be insensitive to eddy viscosity for shallow estuaries and tidal marshes (Z. Li & Hodges, 2019b). Indeed, it can be argued that any depth-averaged coarse-grid hydrodynamic model will be insensitive to eddy viscosity in a marsh simulation because bottom drag and form drag associated with torturous channelization will dominate the effects of horizontal shear at the low velocities that are typical of such systems (Arega & Sanders, 2004). Although dispersion at channel bends could have strong effects on the flow field (Begnudelli, Valiani, & Sanders, 2010), in narrow coastal channels there often lacks sufficient grid resolution to fully resolve the bends, which makes numerical dissipation to be the dominant process (Z. Li & Hodges, 2019b). A detailed study on the relations between eddy diffusion, numerical diffusion and dispersion, especially under the existence of subgrid-scale topography, is beyond the scope of the present study, but it deserves further investigation in the future. Unlike some existing 2D subgrid models that are shock-capturing (e.g. Guinot, Delenne, Rousseau, & Boutron, 2018), *FrehdC* does not include any specific treatments regarding shock waves because flow in coastal marshes is generally slow. Inundation is often tidal-driven, which occurs at longer time scales than flash floods. Highly irregular topography and existence of vegetation further decelerates propagation of inundation extent, making shock-capturing a secondary task.

Free-surface equation: The solution algorithm of *FrehdC* uses the semi-implicit approach of Casulli and Cattani (1994), where the free surface gradient is discretized with a θ-method weighted implicit scheme. However, the nonlinear advective terms are discretized using first-order upwind as discussed in §2.7. Using a finite-volume method, the free surface equation, Eq. (15), is discretized

with subgrid-derived areas as:

$$\eta_{ij}^{n+1}(A_Z)_{ij}^n + \Delta t \Bigg[u_{i+\frac{1}{2},j}^{n+1}(A_X)_{i+\frac{1}{2},j}^n - u_{i-\frac{1}{2},j}^{n+1}(A_X)_{i-\frac{1}{2},j}^n + v_{i,j+\frac{1}{2}}^{n+1}(A_Y)_{i,j+\frac{1}{2}}^n - v_{i,j-\frac{1}{2}}^{n+1}(A_Y)_{i,j-\frac{1}{2}}^n \Bigg] = \eta_{ij}^n(A_Z)_{ij}^n + \Delta t I_{ij}^{n+\frac{1}{2}} \tag{22}$$

where, $I_{i,j}$ is the volumetric flow rate of the inflow boundary condition, n represents time level when appears as superscript. The above applies a time-linearization of the subgrid areas, e.g., the A_X^n is a coefficient of the u^{n+1}, which is similar to the time-linearization of geometry (Δz) that appears in many conventional semi-implicit schemes (Hodges, 2004).

Momentum equation: The momentum equation, Eq. (16), is discretized with respect to a staggered-grid volume $\Omega_{i+\frac{1}{2},j}$ as (for brevity, only the momentum equation in x direction is derived):

$$u_{i+\frac{1}{2},j}^{n+1} = g\Delta t \frac{(A_X)_{i+\frac{1}{2},j}^n}{V_{i+\frac{1}{2},j}^n} K_{i+\frac{1}{2},j}^n (\eta_{i,j}^{n+1} - \eta_{i+1,j}^{n+1}) + K_{i+\frac{1}{2},j}^n E_{i+\frac{1}{2},j}^n \tag{23}$$

where $K_{i+\frac{1}{2},j}^n$ is the inverse of the coefficient of implicit velocity u^{n+1} that appears due to time-linearization of the drag term to maintain stability during flow reversals (see §2.3), and $E_{i+\frac{1}{2},j}^n$ contains all the explicit terms. Specifically, these are:

$$K_{i+\frac{1}{2},j}^n = \left(1 + \frac{(A_Z)_{i+\frac{1}{2},j}^n}{2V_{i+\frac{1}{2},j}^n} C_{Dx}|\boldsymbol{u}| \right)^{-1} \tag{24}$$

$$E_{i+\frac{1}{2},j}^n = u_{i+\frac{1}{2},j}^n + \Delta t \left(\frac{\nu (A_X)_{i+\frac{1}{2},j}^n}{V_{i+\frac{1}{2},j}^n} \left(\frac{\partial u}{\partial x}|_{i+1,j} - \frac{\partial u}{\partial x}|_{i,j} \right) \right) + \Delta t \left(\frac{\nu (A_Y)_{i+\frac{1}{2},j}^n}{V_{i+\frac{1}{2},j}^n} \left(\frac{\partial u}{\partial y}|_{i+\frac{1}{2},j+\frac{1}{2}} - \frac{\partial u}{\partial y}|_{i+\frac{1}{2},j-\frac{1}{2}} \right) \right) - \Delta t \left(u\frac{\partial u}{\partial x} + v\frac{\partial u}{\partial y} \right)_{i+\frac{1}{2},j} \tag{25}$$

Time stepping: At each time step, the velocities u^{n+1} and v^{n+1} from Eq. (23) and the corresponding y-momentum equation are substituted into Eq. (22), forming a five-diagonal linear system for the free surface elevations:

$$\eta_{i,j}^{n+1} \Big[(A_Z)_{i,j}^n + (G_{xp})_{i,j}^n + (G_{xm})_{i,j}^n + (G_{yp})_{i,j}^n + (G_{ym})_{i,j}^n \Big] - \eta_{i+1,j}^{n+1}(G_{xp})_{i,j}^n - \eta_{i-1,j}^{n+1}(G_{xm})_{i,j}^n - \eta_{i,j+1}^{n+1}(G_{yp})_{i,j}^n - \eta_{i,j-1}^{n+1}(G_{ym})_{i,j}^n = \eta_{i,j}^n(A_Z)_{i,j}^n + \Delta t I_{ij}^{n+\frac{1}{2}} - \Delta t \Big[E_{i+\frac{1}{2},j}^n + E_{i-\frac{1}{2},j}^n + E_{i,j+\frac{1}{2}}^n + E_{i,j-\frac{1}{2}}^n \Big] \tag{26}$$

where the matrix coefficients are defined as:

$$(G_{xp})_{i,j}^n = g\Delta t^2 \frac{\left((A_X)_{i+\frac{1}{2},j}^n \right)^2}{V_{i+\frac{1}{2},j}^n} K_{i+\frac{1}{2},j}^n$$

$$(G_{xm})_{i,j}^n = g\Delta t^2 \frac{\left((A_X)_{i-\frac{1}{2},j}^n \right)^2}{V_{i-\frac{1}{2},j}^n} K_{i-\frac{1}{2},j}^n$$

$$(G_{yp})_{i,j}^n = g\Delta t^2 \frac{\left((A_Y)_{i,j+\frac{1}{2}}^n \right)^2}{V_{i,j+\frac{1}{2}}^n} K_{i,j+\frac{1}{2}}^n$$

$$(G_{ym})_{i,j}^n = g\Delta t^2 \frac{\left((A_Y)_{i,j-\frac{1}{2}}^n \right)^2}{V_{i,j-\frac{1}{2},j}^n} K_{i,j-\frac{1}{2}}^n. \tag{27}$$

In *FrehdC*, this linear system is solved by applying conjugate gradient method with symmetric successive over-relaxation preconditioner (available through Skalicky (2019)). The η^{n+1} from solution of Eq. (26) are substituted into Eq. (23) and a similar y-momentum equation to get updated velocities u^{n+1} and v^{n+1}.

Scalar transport: The scalar transport equation (Eq. 17) is discretized using finite-volume method. At the x-plus face, the net scalar mass m_c across the face is:

$$(\Delta m_c)^{n+1}_{i+\frac{1}{2},j} = \Delta t (A_X)^{n+1}_{i+\frac{1}{2},j} \left[u^{n+1}_{i+\frac{1}{2},j} C^n_{i,j} + \kappa \frac{\partial C}{\partial x}|_{i+\frac{1}{2},j} \right]. \tag{28}$$

Summing mass fluxes on all four faces and allowing sources/sinks of mass provides:

$$\begin{aligned}(m_c)^{n+1}_{i,j} = (m_c)^n_{i,j} + (\Delta m_c)^{n+1}_{i-\frac{1}{2},j} - (\Delta m_c)^{n+1}_{i+\frac{1}{2},j} + (\Delta m_c)^{n+1}_{i,j-\frac{1}{2}} \\ -(\Delta m_c)^{n+1}_{i,j+\frac{1}{2}} + source - sink.\end{aligned} \tag{29}$$

The updated scalar concentration is

$$C^{n+1}_{i,j} = \frac{(m_c)^{n+1}_{i,j}}{V^{n+1}_{i,j}}. \tag{30}$$

3.4 Subgrid geometry update

The subgrid geometry variables defined in §3.2 are all functions of the free-surface elevation. Ideally, their values should be updated simultaneously with the free-surface elevation to maintain mass conservation (Casulli, 2009). In practice, the geometry time-linearization discussed in §3.3 allows a simple linear implicit solver to be used for the free-surface solution. A pre-stored approach (Wu et al., 2016) is adopted herein for the update computation. At the solution start we initialize an array that contains pre-defined free surface elevations and their corresponding subgrid geometry; i.e., an array indexed by $\eta_{pd} = [\eta_{min}, \eta_{min} + \Delta\eta, \eta_{min} + 2\Delta\eta, \ldots, \eta_{max}]$, where η_{min} and η_{max} are based on expected maximum and minimum values for the system. For each η in η_{pd}, the corresponding subgrid geometry variables are computed and stored. For each time step, when the new free surface elevation $\eta^{n+1}_{i,j}$ is computed, we search in η_{pd} for $(\eta_{pd})_K \leq \eta^{n+1}_{i,j} \leq (\eta_{pd})_{K+1}$ and interpolate the subgrid variables between $(\eta_{pd})_K$ and $(\eta_{pd})_{K+1}$. For computational efficiency in searching in the pre-defined array of surface elevations, our algorithm begins from the last known interval $[(\eta_{pd})_K, (\eta_{pd})_{K+1}]$. If η^{n+1} does not fall within in this interval, we continue by searching neighbor intervals. This strategy significantly reduces the computation costs compared to an arbitrary search over $[\eta_{min}, \eta_{max}]$.

3.5 Block checking for internal features

Problems with too much connectivity: In §3.2, the cell face areas are defined using only the high-resolution data that is coincident with the cell faces, which naturally creates a water blockage if all the subgrid cells are dry along a face. However, a water-blocking feature in the interior of a cell cannot be directly represented by the cell face areas using the subgrid geometry as defined above. For example, we can imagine a case where $(A_X)_{i+\frac{1}{2},j} > 0$ and $(A_X)_{i-\frac{1}{2},j} > 0$ combined with $(A_X)_{i,j} = 0$, which would allow flow from the $i-1, j$ cell to the $i+1, j$ cell through the i, j cell because the the $(A_X)_{i,j}$ does not appear in the discrete equations. Thus, an additional algorithm is required to locally-alter the subgrid geometry and account for internal blocking effects. This is similar to the problem addressed in Hodges (2015) where the interior blocking height of subgrid geometry across a coarse-grid cell was identified and the feature was "snapped" to the nearest face – the result was a static face geometry that included effects of interior blockages, which was accomplished as a pre-processing step to a hydrodynamic model. Herein, we develop an approach that accomplishes a similar task, but is integrated in the approach for the hydrodynamic solution through direct effect on the A_X and A_Y.

Block-checking algorithm: Internal blocking is handled through a discrete analysis of subgrid geometry at each of the $(\eta_{pd})_K$ elevations in the pre-stored subgrid geometry array. A five-step process is used to modify the A_X and A_Y on each face. That is, the face areas at a given $(\eta_{pd})_K$ retain their values computed by the faces unless an effective interior blockage is detected, in which case the appropriate face area is set to zero. The process for each coarse-grid cell is:

1. At each pre-defined surface elevation, $(\eta_{pd})_K$, create a binary wet/dry map within a coarse grid cell that contains $\Lambda \times \Psi$ subgrid cells.
2. Cycle through each of the $(\eta_{pd})_K$, computing steps 3 - 5 below and modifying the subgrid geometry array.
3. Identify the single largest fully-connected wet patch in this coarse grid cell at this elevation. Mark the remainder of this cell as dry.
4. If the intersection between the wet patch and a coarse cell face at this elevation is zero, this face is blocked and has a subgrid face area of zero.
5. For two adjacent coarse grids both with nonzero areas on their common face at the same elevation, if the intersection of their wet subgrid indices on this face is an empty set, their common face area is zero.

In the present implementation this algorithm is used only at the start of the simulation to pre-store the effects of internal blocking. However, the algorithm could be easily introduced within the hydrodynamic time-stepping loop to allow dynamic modification of subgrid geometry (erosion or aggradation), issues that are worthy of further investigation.

Example of block-checking: An example of the block-checking technique is shown in Fig. 4a, where the water regions (blue) are divided by the land (brown), forming a river channel from left to right that is (mostly) not connected to the surrounding marshes. Following Eqs. (11) and (12), at $r = 15$ without block-checking the river bank would only be partially identified and blocked – as shown by the light blue faces that are the only subgrid faces with zero areas. Thus, näive application of the subgrid definitions in §3.2 will allow imaginary flow paths between the channel and its surrounding marshes. The new block-checking method identifies the red faces as additional blocked faces based on the high-resolution topography of the interior of each coarse-grid cell, which fully delineates the channel banks at an $r = 15$ coarsening as shown in Fig. 4a.

Limits of block-checking: However, the block-checking method does not allow coarsening to arbitrarily large r, as illustrated in Fig. 4b for $r = 30$. As the coarsening ratio increases there is an increasing likelihood that multiple unconnected flow paths could exist in a single coarse grid cell, but the block-checking method (Step 3) is limited to considering only the largest inundation area in a grid as the "true" connected region of a single cell. This approach inherently blocks other flow paths because only one velocity is allowed to exist on each face. In Fig. 4c, one cell from Fig. 4b (delineated by a green box) is examined in detail. The *top* panel shows the binary wet/dry map (Step 1) of the original cell, which contains two disconnected water regions *A1* and *A2*. Comparing to Fig. 4b, we found that *A2* belongs to the river channel and *A1* is located in its surrounding marshes. The *bottom* panel of Fig. 4c shows the wet/dry map after performing Step 3, where *A2* is turned into land because its area is less than *A1*. This leads to blocking of the east face (through Step 4) and the south face (through Step 5) of the target cell, which interrupts channel connectivity.

Despite the failure behavior of the block-checking method at large r, it still shows advantages over naïve upscaling and the edge identification method by Hodges (2015) in maintaining surface connectivity. It should be noted that model dependency on r varies for different domains, so to improve applicability over a variety of domains, the proposed block-checking method could be combined with some quantifications that reflect the "complexity" of topography, which is a topic that deserves further investigation.

3.6 Comparison of results for subgrid vs. edge method

Test case: Herein, the TDHM is run using (i) a 20×20 m grid developed using the *edge* techniques of §2.8, and (ii) with a 20×20 m grid that uses conventional topographic averaging but includes data for the *subgrid* approach described in §3.2 – 3.5. The *edge* simulations can be considered to be the minimum representation needed to capture flow blocking/channelization by fine-scale features. A comparison of the results allows us to examine the overall impact of the *subgrid* model on the simulation. However, the present work cannot validate the *subgrid* model for TDHM as we lack sufficient field data for comparison. Potential sensor locations for validation are discussed in §4.4. The new *subgrid* algorithm is based upon the difference between known high-resolution topographic data (e.g., 1×1 m lidar) and the coarser resolution that is practical for modeling. In these tests, we

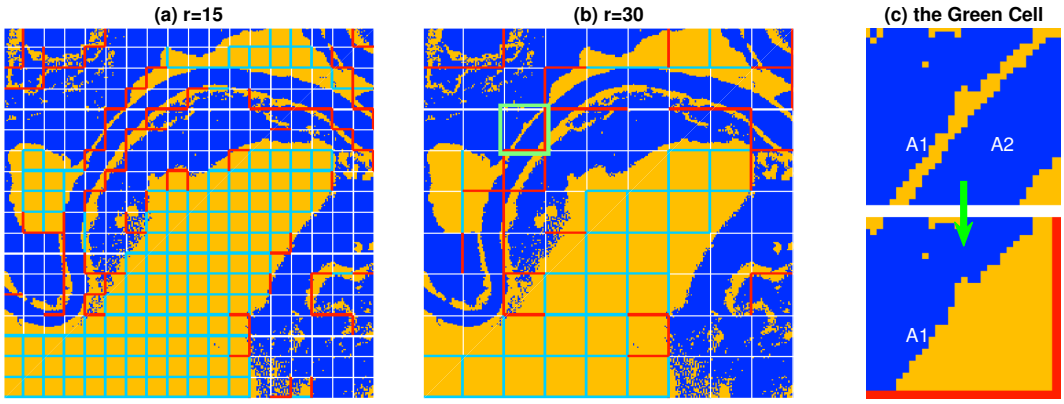

Figure 4: (a)-Internal blocking implemented over a coarse-grid map with 15 $\times$ 15 fine-grid resolution ($r = 15$) in each coarse cell. The fine-grid cells are a binary wet/dry map for a given η level (blue is wet, brown is dry). Light blue lines indicate blocked cell faces ($A = 0$) based on face-only subgrid cells using Eqs. (11) and (12). The red lines are additional blockages attributable to interior geometry using the block-checking method. (b)-The same region but with $r = 30$. (c)-The green cell in (b) examined in detail to show how channel connectivity is interrupted at large r, where *top* panel is the wet/dry map after performing Step 1, *bottom* panel is the wet/dry map after performing Step 3 (only 1 largest wet patch is retained.)

use 20×20 m coarse grid, which allows faster run times than the 10×10 m grid used in Z. Li et al. (2017). For consistency in evaluation, we applied the channel identification algorithms of Z. Li et al. (2017) on the finer 1×1 m grid and then separately upscaled to the coarser 20×20 grid using both (i) *edge* techniques (Hodges, 2015; Z. Li & Hodges, 2019b) and (ii) *subgrid* techniques (Z. Li & Hodges, 2019a). In the following, the two simulations using different topographic approaches are denoted by SB (subgrid) and EG (edge/channel identification).

Boundary forcing conditions: Similar to simulations in §4, tide, wind and river stage data are used as boundary conditions. Initial surface elevation and salinity are spatially-variable using linear interpolation between north and south initial boundary values. Both EG and SB scenarios are run for 10-day simulations starting from Sept. 10, 2017.

Prediction of inundated area: The key performance difference between the EG and SB model can be evaluated by the instantaneous inundated area of the model (i.e., the area of all cells that are wet at any time step). This metric is useful as the main difference between the bathymetry in EG and SB is that the EG forces an obstructions to block an entire grid edge whereas the SG allows partial blockage of the flow area across a grid edge. Thus, the SG is expected to allow flow through edges at times when the EG model would be blocked. The time-evolution of instantaneous inundation areas for EG and SB scenarios are shown in Fig. 5. The SB scenario provides a greater inundation area, which indicates it is better able to represent the narrow channels in the Trinity Delta. Because the EG can only represent an edge as either flow or blocked at the 20 m scale, it cannot adequately capture many of the narrow flow paths. Furthermore, the SB algorithm has a more sophisticated approach to partially-wet cells in the shallow regions, which are assessed as completely dry in the EG bathymetry.

Salinity distribution: The spatial distribution of salinity for the EG and SB simulations after 10 days of simulation are shown in Figs. 6 and 7 respectively. The EG simulation is limiting the rate of intrusion of salinity into the lower delta, and also limiting the rate of freshwater supply from the upper river – arguably the *edge* method prioritizes blockages over channelization. The SB simulation shows both the freshwater and salinity fluxes reach deeper into the delta, indicating the *subgrid* method prioritized channelization over blockage.

Figure 8 shows the difference of predicted salinity ($S_{SB} - S_{EG}$) averaged over the 10-day simulation period. Throughout the delta the paths of negative difference illustrate the enhanced connectivity provided by the *subgrid* method. Note that with the *edge* method, the blockages in the delta tends to force water downstream in the main channel, which leads to a larger brackish water signature

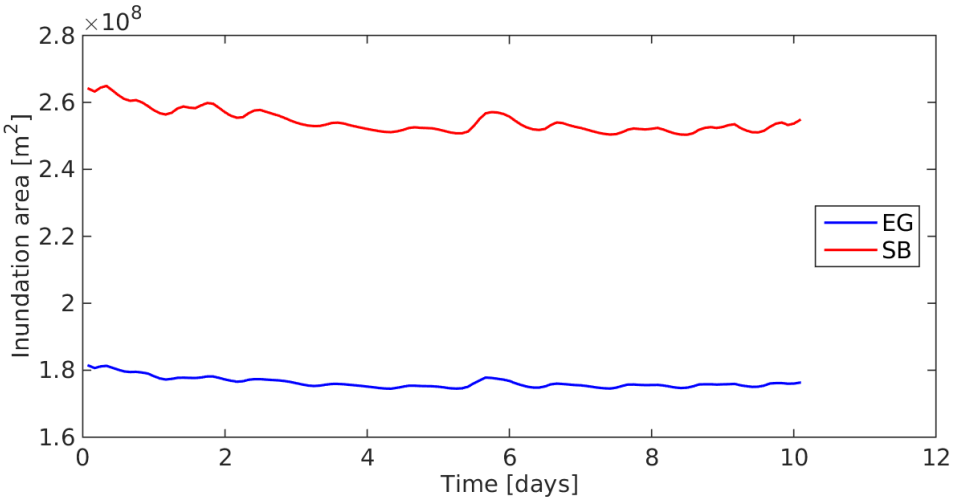

Figure 5: Instantaneous inundation areas for simulations with the *edge*-method (EG) and *subgrid* (SB).

in northeastern Trinity Bay in Fig. 6. This region corresponds to a region of net positive salinity difference in Fig. 8. Furthermore, in Fig. 8 we can discern the effects of different inundation extents – i.e., effects that are expected from Fig. 5. The shallow regions next to the Trinity River near the Lake Anahuac and Lake Charlotte have large positive salinity differences due to different inundation patterns between the EG and SB scenarios – i.e., "dry" cells are defined as zero salinity, so where the SB simulation is wet and the EG simulation is dry, any non-zero salinity in the SB shows up as a positive difference.

Interestingly, for the shallow marsh near the Horse Island Bayou the mean salinity difference is negative – i.e., net greater flushing, which might appear to contradict a comparison of Figs. 6 and 7 that show greater instantaneous salinity intrusion in the *subgrid* method. However, what we are seeing is that the instantaneous representation of Fig. 7 indicates the ability of the high-salinity bay water to more easily move further up into the delta with the *subgrid* method, and it will similarly be more easily drawn back out (and with reduced mixing) when the tidal flux is outward. In contrast, Fig. 6 illustrates a more diffuse mixing front in the *edge*-method. The comparison of the mean difference over time in Fig. 8 thus shows that the net difference is that the *edge*-method overpredicts salinity in this area due to the overall slower movement of freshwater through the delta.

Limitations of the present work: As we lack a comprehensive set of field observations, it is impossible (at this time) to say whether or not the *subgrid* method is better than the *edge* method. However, the substantial differences between the simulations and the more sophisticated solution approach used in the *subgrid* method make it appear to be the better option. It seems likely that the *edge* method blocks flows that should be moving through the delta. It remains to be seen whether the *subgrid* method is approximately correct or if it under- or over-estimates the flows.

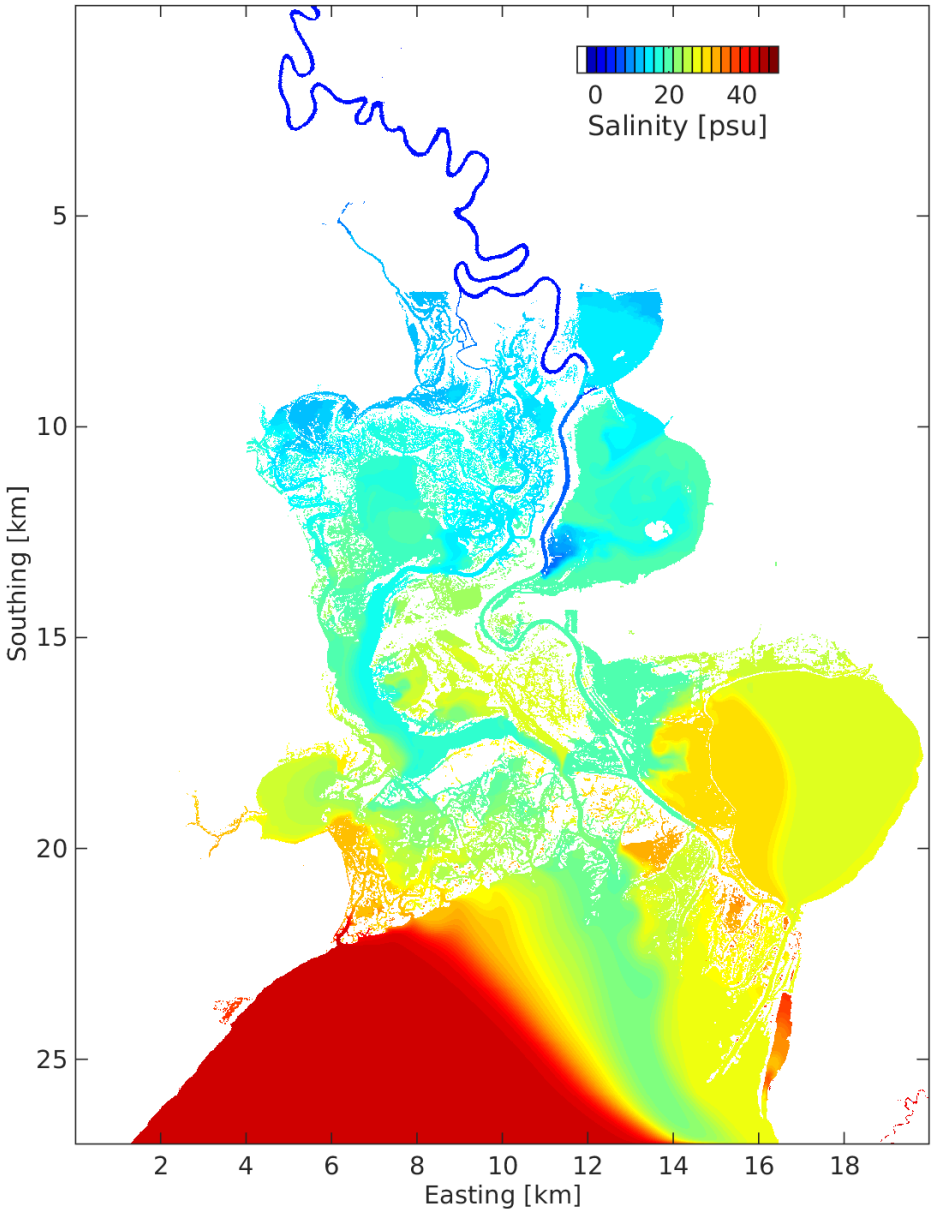

Figure 6: Instantaneous *edge*-method (EG) modeled salinity on Sept. 20, 2017 after 10 days of simulation.

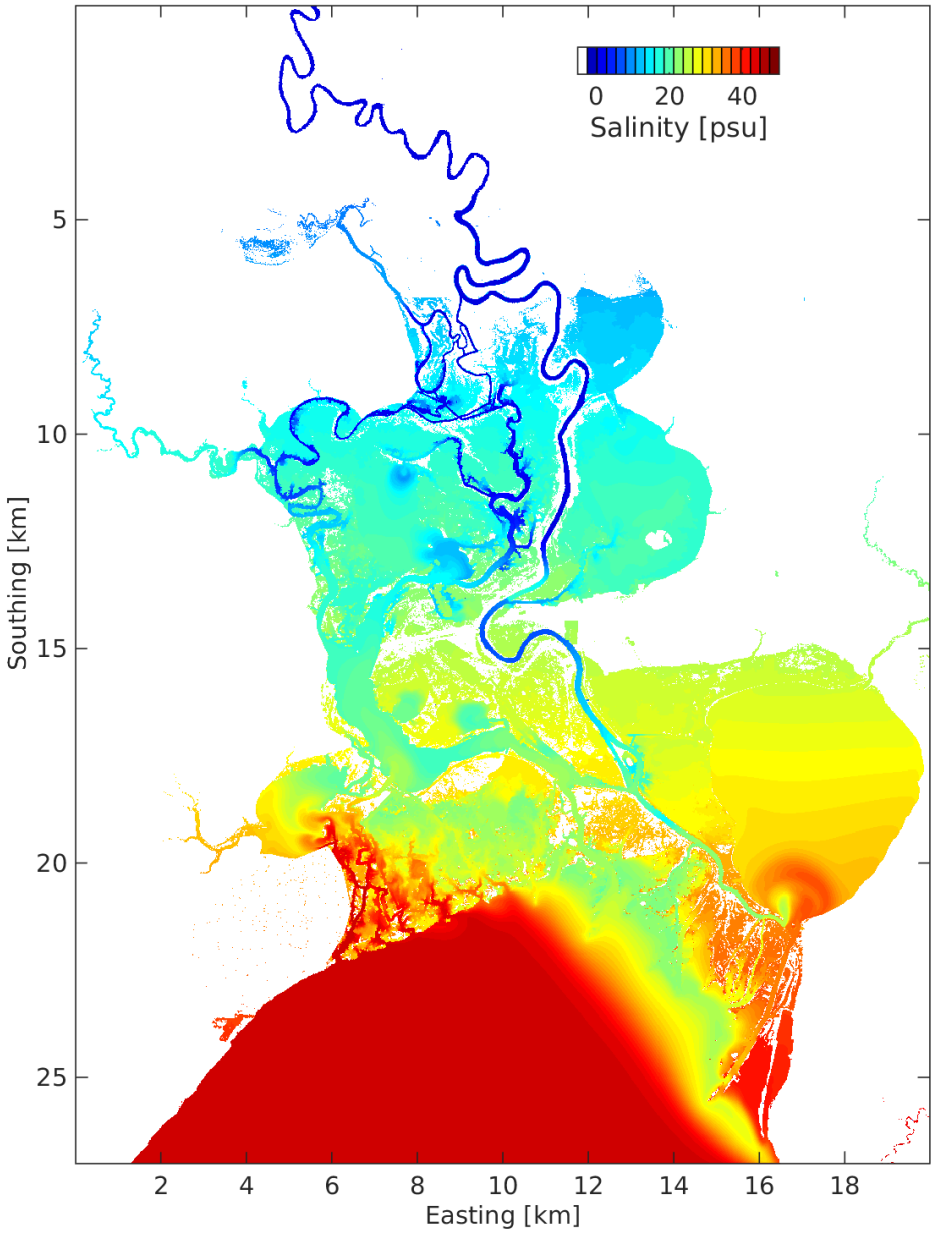

Figure 7: Instantaneous *subgrid*-method (SB) modeled salinity on Sept. 20, 2017 after 10 days of simulation.

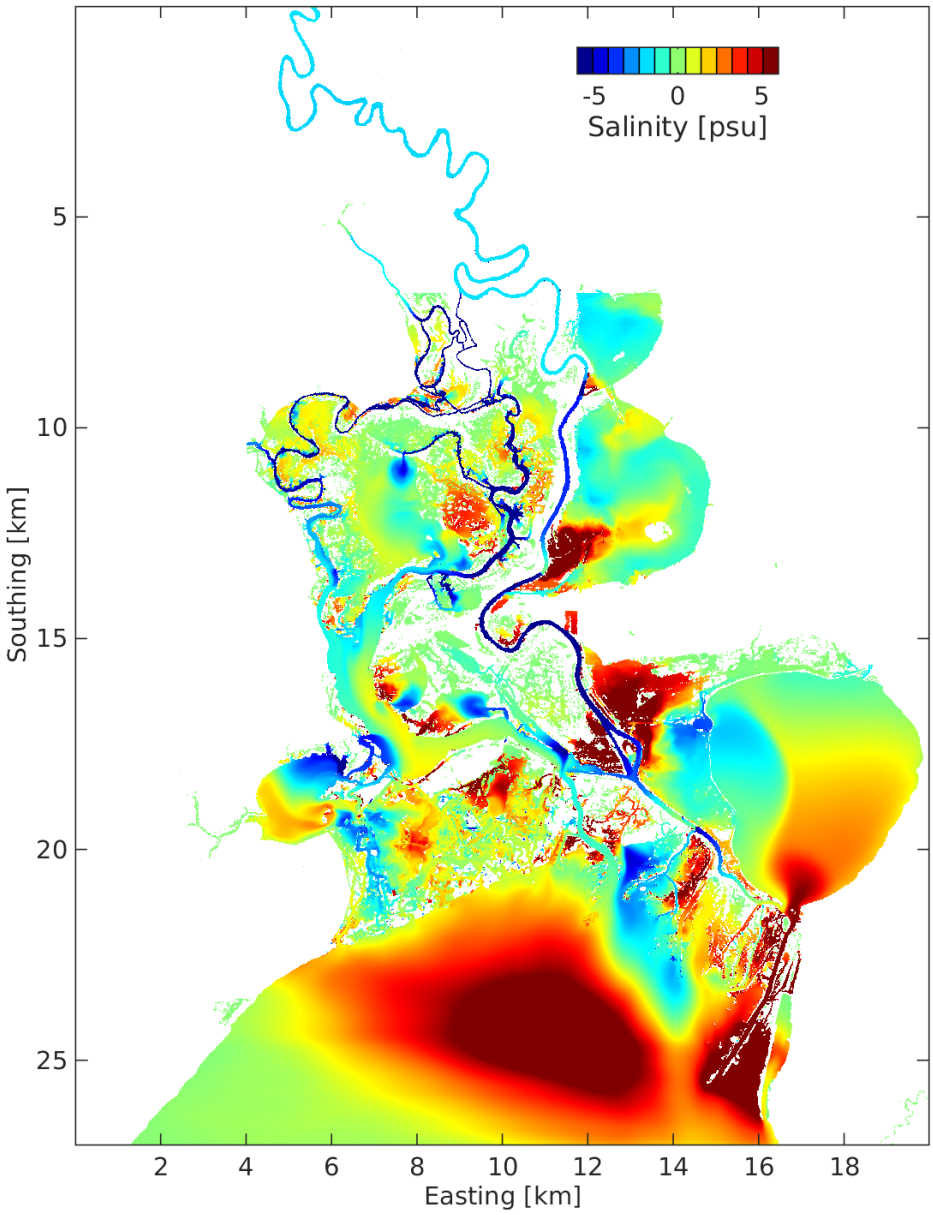

Figure 8: Mean difference of *subgrid*-method and *edge*-method of modeled salinity ($S_{SB} - S_{EG}$) over entire 10-day simulation period. Note that color scale is over small range than Figs. 6 and 7

4 TDHM model sensitivity to boundary conditions

4.1 Overview

A challenge for modeling a complex system such as the Trinity River Delta is obtaining sufficient data for model validation. In general, sensors deployed into the field without considering preliminary model results might be located where the model response is relatively insensitive to changes in the forcing. Sensors in such locations will have relatively little value in validating the model as there will be too many forcing conditions that lead to similar model outcomes. Thus, it is useful to understand the model sensitivity to changes in boundary forcing and identify locations that are particularly sensitive.

Outline for §4: In the remainder of this section, the model setup for sensitivity tests are presented (§4.2), the results of sensitivity tests are discussed (§4.3), and recommended sensor locations for validating the model are provided (§4.4).

4.2 Model setup

Topography and mesh: For the sensitivity tests, the *FrehdC* model is run on 30×30 m topography that is generated from the 1×1 m lidar data of the Trinity Delta. The grid-coarsening process is similar to that described in Appendix B and Z. Li et al. (2017), where a combined use of automatic and manual channel identifications helps to maintain surface connectivity of narrow river channels. Unfortunately, we do not have comprehensive survey data to accurately represent the inundated water areas that are missing from the lidar survey. To complete the dataset we assigned uniform bottom elevations of -0.5 m below NAVD88 datum for all the grid cells that were inundated during the lidar survey. This depth likely underestimates the depth in many larger channels; however, as a matter of modeling judgement it is better to globally underestimate these depths (especially for smaller channels) as the model grid tends to provide too much connectivity. The complete 30×30 m resolution grid for the Trinity Delta is shown in Fig. 9.

Boundary forcing conditions: The TDHM is driven by tides in Trinity Bay (northern section of Galveston Bay), river stage in the Trinity River and wind stress all over the model domain. In Figure 9 the open (bay) boundary is along the south edge of the domain, and is forced with water level data measured at the NOAA tide & currents station 8770613, Morgans Point, Barbours Cut, Texas. The north (river) boundary in Fig. 9 uses river stage data measured at USGS gage 08067100 Trinity River near Moss Bluff. This gage has a 15 minute sampling interval. The wind speed and direction data are taken from USGS gage 08067252 Trinity River at Wallisville, which also has a 15 minute sampling interval. The wind data is forced uniformly over the entire domain in Fig. 9.

Initial conditions: For initial conditions, the imposed water surface elevation is computed as a linear distribution from the initial river stage at the north to the initial tidal elevation at the south. The initial salinity field is also distributed linearly from 0 psu at the river to 45 psu at the bay[1]. This relatively high salinity was selected as the bay boundary condition to provide the broadest reasonable variability for sensitivity testing. Beginning with a spatially-distributed initial salinity allows flow features at any location to be characterized by the change in salinity, which removes the need for model spin-up in conducting sensitivity tests. The initial water velocities are set to zero throughout the domain.

Time period for simulations: Sensitivity tests for the TDHM are run for 20-day simulations starting from Sept. 10, 2017 with a time step $\Delta t = 1$ s. The TDHM is actually stable for significantly larger time steps, but the subgrid simulations in Section 3 require a small time step for validation. The time steps both with and without the subgrid method are kept at the small value to enable a consistent comparison of model performance.

Perturbations of boundary conditions used for sensitivity tests: The sensitivity tests are performed by changing the boundary conditions at the south tidal boundaries, north river boundary, and

[1]Note that for hydrodynamic modeling psu (practical salinity units) is an identical measure to ppt (parts per thousand).

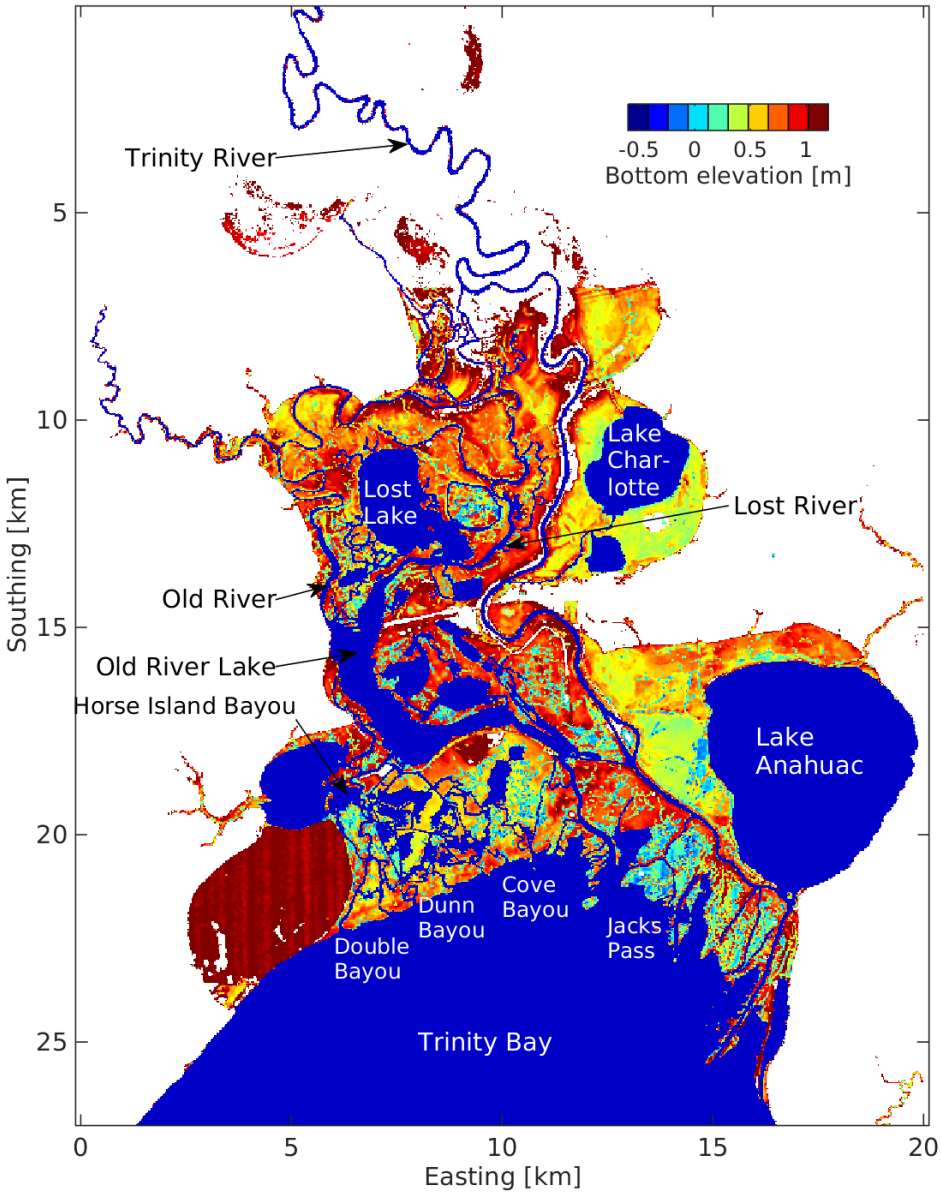

Figure 9: Trinity River Delta topography at 30×30 m used for the sensitivity test of the TDHM (relative to NAVD88 datum).

wind speeds across the domain, then evaluating the differences in predicted salinity. Three changes were made to boundary conditions:

1. Increase/decrease baseline tidal elevation by 0.1 m at the south boundary (maintaining observed tidal amplitudes).
2. $2\times$ and $0.5\times$ observed wind speed.
3. Increase/decrease river stage by 0.1 m at the north river boundary.

Note that in these sensitivity tests the upstream river boundary is forced by stage height rather than inflow, which is appropriate for the low inflow conditions during the testing period.

4.3 Results of sensitivity tests

Sensitivity to tidal forcing: The 20-day averaged difference in modeled salinity (S) between two tide scenarios ($S_{\text{high tide}} - S_{\text{low tide}}$) is shown in Fig. 10. The stronger tide enhances salt intrusion, which is indicated by the positive salinity difference. The difference is particularly large in Trinity Bay, Old River Lake, Horse Island Bayou, and the marshland in between. The salinity responses in the northern parts of the domain (e.g., Lost Lake, Lake Charlotte) are relatively insensitive to tidal elevation. However, salinity in the main stem of the Trinity River is significantly affected by tide up to 20 km upstream because of the relatively weak river inflow during the simulated time period.

Sensitivity to wind speed: The difference in modeled salinity caused by increasing/decreasing the applied wind speed is shown in Fig. 11. Under the tested conditions, the change of the applied wind speed from 1/2$\times$ to 1$\times$ to 2$\times$ the observed speeds (while maintaining observed wind direction) leads to higher salinity in the western marshlands between Trinity Bay and Horse Island Bayou. Lower salinity is detected east of Jacks Pass. The northern interior of Trinity Delta is only mildly affected by increases in wind speed because flow the short fetch in winding channels limits the ability of the wind to influence the transport.

Sensitivity to river stage: The difference in modeled salinity caused by increasing/decreasing the river stage is shown in Fig. 12. Increasing river stage leads to decreasing salinity in the upstream reaches of the Trinity River and through some of the upper channels of the delta, but has negligible effects over most of the domain. During the low-flow period simulated in these sensitivity tests the salinity response in the studied area was most sensitive to the changes in the baseline tidal elevation and less sensitive to changes in wind speed or river stage.

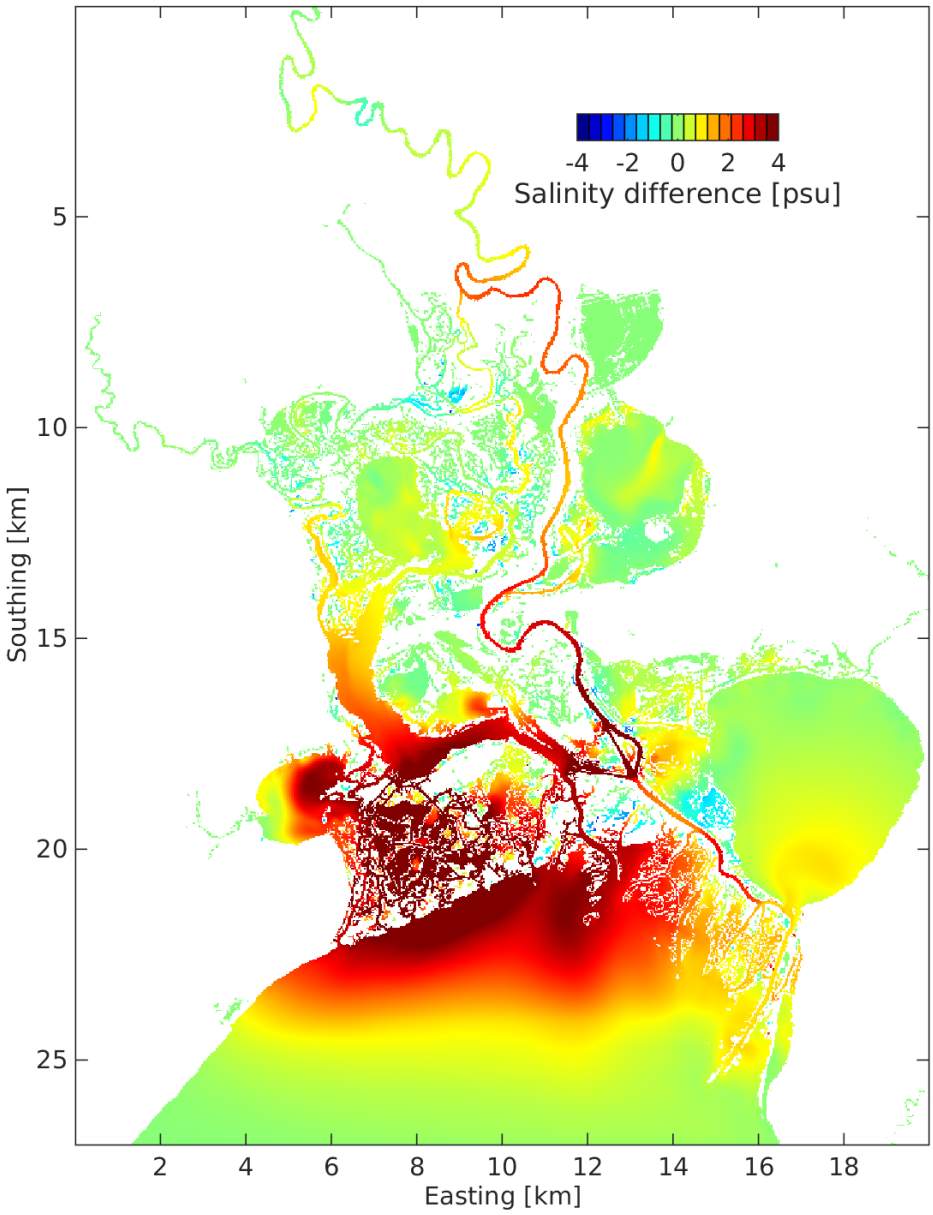

Figure 10: Sensitivity analysis for tide: difference in modeled salinity between two tide scenarios (increase/decrease tidal elevation by 0.1 m), averaged over 20 days.

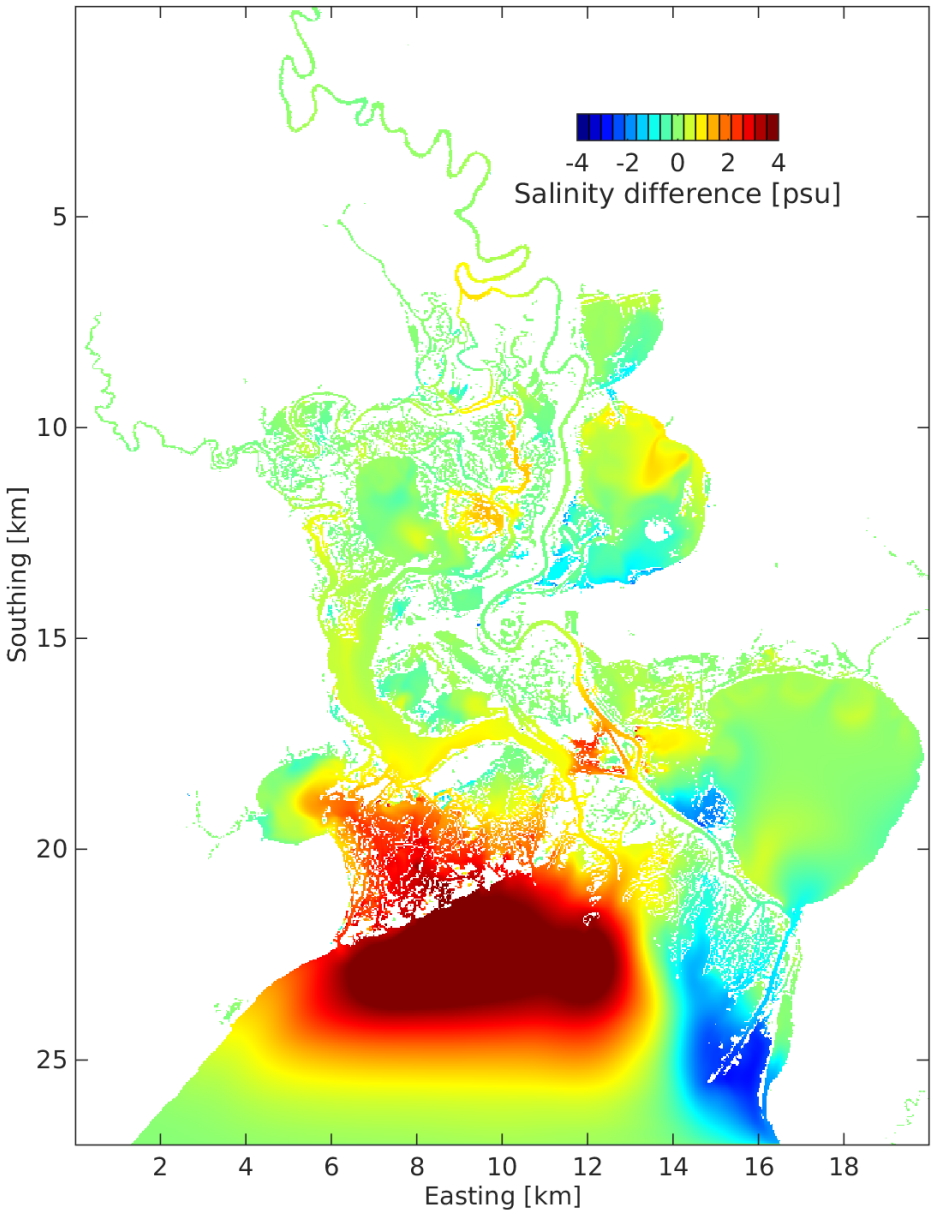

Figure 11: Sensitivity analysis for wind: difference in modeled salinity between two wind scenarios ($2\times$, $0.5\times$ observed wind speed), averaged over 20 days.

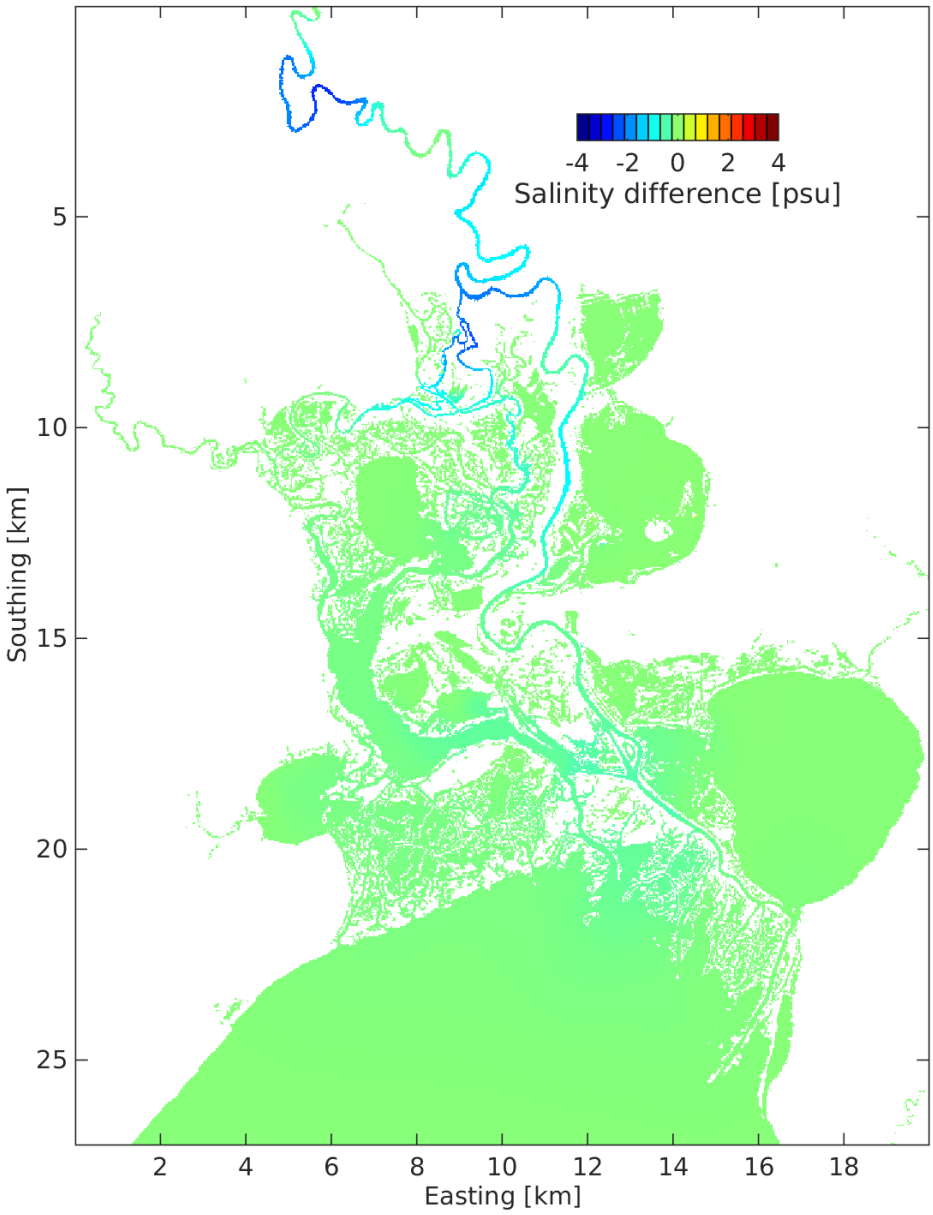

Figure 12: Sensitivity analysis for river stage: difference in modeled salinity between two river stage scenarios (increase/decrease stage by 0.1 m), averaged over 20 days.

4.4 Proposed sensor locations for surface water hydrodynamics

The above sensitivity analyses can be used to provide insights into how future field data collection might be organized to provide data for model validation and/or calibration. In Figures 10-12, the main stream of the Trinity River and the shallow marshes near the Trinity Bay are generally sensitive to changes in the boundary conditions. The Lake Charlotte, Lost Lake, north parts of the Old River and the Lost River show relatively low sensitivity, indicating relatively poor surface connectivity at these locations. Large discrepancies between model results and field data are expected at these locations (Z. Li & Hodges, 2019b).

Based on our analyses, we propose 16 locations should be considered for a comprehensive field monitoring program, as illustrated in Fig. 13. These locations can be grouped as follows:

1. Main stem of Trinity River: Sites 1, 2, 3, 7, 12, 16. These sites are needed to monitor loss/gain of river flow through identifiable branches.
2. Near Trinity Bay: Sites 13, 14, 15. These sites are needed to validate the boundary conditions used to represent Trinity Bay.
3. Old River and Lost River: Sites 4, 5, 6. These represent upper delta areas that are not strongly affected by the boundary conditions. These sites are needed to validate model performance in areas where the surface connectivity is relatively poor and source/sink to groundwater might be a major control on fluxes.
4. Old River Lake: Sites 8, 9, 10, 11. These sites are needed to validate model performance in areas where the salinity is likely to see some of the steepest gradients and largest swings in value.

Presently, we do not recommend sensors for surface water in (i) the shallow marsh between the Old River Lake and Trinity Bay, (ii) Lake Charlotte or (iii) Lake Anahuac. These locations appear to be hydraulically isolated from both the river and the bay (see §A for detailed discussion). However, sensors in these areas might be needed for future groundwater studies.

The sites selected above provide greater detail on the fate of inflows and the salinity dynamics across the breadth of Trinity Delta than can be obtained from the present USGS gaging stations, which are focused on the main stem river.

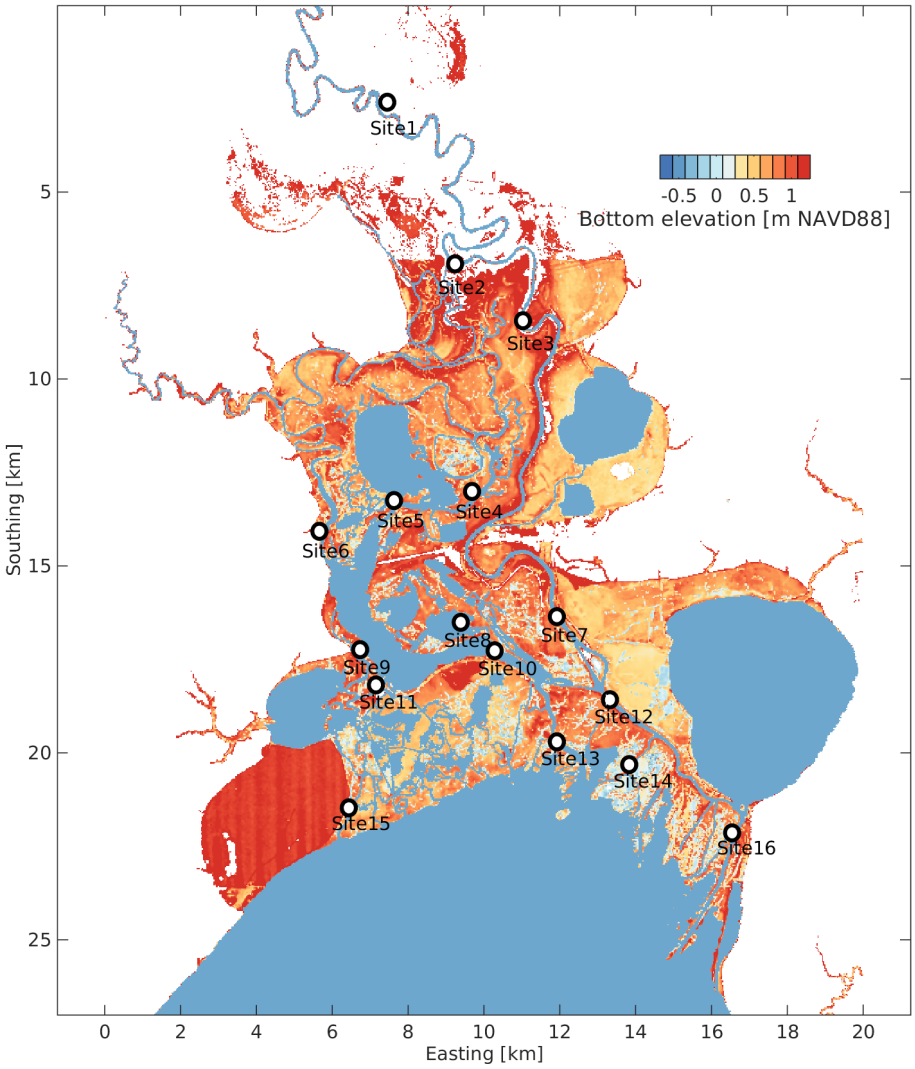

Figure 13: Proposed locations for deploying sensors and collecting field data for model calibration and validation.

5 Surface-subsurface exchange

5.1 Overview

As part of developing the TDHM, the *FrehdC* model has been directly coupled with a near-surface groundwater model to simulate flow exchange between the surface and the subsurface domain. Subsurface storage and flux paths can be a cause for discrepancies in observed surface water budgets in a surface water model (e.g., Niu, Shen, Li, & Phanikumar, 2014). The present study is limited to a development of the coupled hydrodynamic model. Full testing and validation of the model requires future field data collection and model-data comparisons.

Investigation of groundwater models: As part of this effort, we examined two popular groundwater models that could be coupled with FrehdC: ParFlow (Kollet & Maxwell, 2006) and MODFLOW (Hughes, Langevin, & Banta, 2017). Unfortunately, ParFlow requires implicit coupling between the surface and the subsurface domains, i.e. equations for both domains are put into one system of equations and are solved simultaneously. Thus, to couple *FrehdC* with ParFlow would require either (i) extracting the subsurface part of ParFlow and coupling with the semi-implicit solver in *FrehdC*, or (ii) writing a new version of *FrehdC* within the ParFlow models structure. Neither option was considered practical within the scope of the present contract. In contrast, MODFLOW is a better candidate for coupling as it can be done with an explicit solution (i.e., aligning data on the n time steps without implicit linking of a matrix solution). However, MODFLOW is written in Fortran, which is difficult to directly integrate with *FrehdC* due to the difference in data structures (row-major in C versus column-major in Fortran). We determined that it would be possible to create an effective coupling between the models that works in a parallel implementation and does not have high overhead associated with data transfer; however, such code development is a non-trivial endeavor and beyond the funds and time available within the present project. Thus, to fulfill Task 3 of the contract we wrote a groundwater module directly in *FrehdC*. This approach does not provide all the capabilities of models such as MODFLOW or ParFlow, but is a starting point for TWDB to consider for future endeavors.

Outline of §5: In the remainder of this section, the numerical model for the coupled groundwater is described (§5.2), the setup for tests of the groundwater model are presented (§5.3), and results from simulations with the coupled model are provided (§5.4). Note that validation of the groundwater model requires: (i) future work to evaluate the sensitivity of the model to its forcing and setup, and (ii) analyses to identify potential locations for groundwater sensors that would be effective in model validation.

5.2 Model description

Governing equations: The groundwater module in *FrehdC* solves the saturated 3D Darcy's Law. For a coarse cell with finite volume, the governing equation can be written as:

$$S_s V \frac{\partial h}{\partial t} = \sum (KA\nabla h) + Q \tag{31}$$

where, S_s is the specific storage, h is head, K is hydraulic conductivity, V and A are subsurface cell volume and face area, and Q is the source term. The specific storage is calculated as:

$$S_s = \gamma(\beta_s + \phi\beta_w) \tag{32}$$

where γ is the specific weight of water, ϕ is porosity, β_s is the compressibility of solids and β_w is the compressibility of water. Following the conventions used in MODFLOW (Hughes et al., 2017), a "conductance" is defined to further simplify the equations. The conductance between two grid cells is:

$$C = \frac{KA}{\ell} \tag{33}$$

where ℓ is the distance between the center of two cells. With the definition of conductance, the volumetric flow rate between cell i and cell $i+1$ can be calculated as:

$$Q_{i+\frac{1}{2}} = K_{i+\frac{1}{2}} A_{i+\frac{1}{2}} \frac{h_{i+1} - h_i}{\Delta x} = C_{i+\frac{1}{2}} \left(h_{i+1} - h_i\right). \tag{34}$$

Discrete form of equations: Using the concept of conductance, Eq. (31) can be discretized with respect to cell (i, j, k) (assume constant ϕ and K):

$$\begin{aligned}\Big[S_s V_{i,j,k} + \Delta t \left(C_{i+\frac{1}{2},j,k} + C_{i-\frac{1}{2},j,k} + C_{i,j+\frac{1}{2},k} + C_{i,j-\frac{1}{2},k} + C_{i,j,k+\frac{1}{2}} + C_{i,j,k-\frac{1}{2}}\right)\Big] h^{n+1}_{i,j,k} \\ -\Delta t \Big(C_{i+\frac{1}{2},j,k} h^{n+1}_{i+\frac{1}{2},j,k} + C_{i-\frac{1}{2},j,k} h^{n+1}_{i-\frac{1}{2},j,k} + C_{i,j+\frac{1}{2},k} h^{n+1}_{i,j+\frac{1}{2},k} \\ + C_{i,j-\frac{1}{2},k} h^{n+1}_{i,j-\frac{1}{2},k} + C_{i,j,k+\frac{1}{2}} h^{n+1}_{i,j,k+\frac{1}{2}} + C_{i,j,k-\frac{1}{2}} h^{n+1}_{i,j,k-\frac{1}{2}}\Big) \\ = S_s V_{i,j,k} h^{n}_{i,j,k} + \Delta t Q^{n}_{i,j,k} \qquad (35)\end{aligned}$$

The above provides a seven-diagonal linear system that can be solved with many existing solvers (e.g., the pre-conditioned conjugate gradient method used in *FrehdC*).

Boundary conditions: The bottom and side boundaries of the subsurface domain are assumed impervious, where $C = 0$ is enforced. The top boundary is connected to the surface domain. Surface-subsurface exchange is modeled as a volumetric flow rate Q_{ss} between the two domains, which is calculated as:

$$Q_{ss} = \frac{K_z A}{\ell_{ss}} \left(h_{surf} - h_{sub}\right) \qquad (36)$$

where K_z is the vertical hydraulic conductivity (the K used in the present study does not vary in space and time, but may vary in different directions), h_{surf} is the depth of the surface water, h_{sub} is the head of the top subsurface cell that is connected to the surface domain. $\ell_{ss} = 0.5\Delta z$ is half of the thickness of the top subsurface cell (de Rooij, 2017).

5.3 Model setup

Mesh and topography: The coupled surface-subsurface model is tested on the Trinity Delta at 50×50 m resolution (Fig. 14) without using the subgrid method of §3 for surface water modeling. The coarser grid resolution and neglect of subgrid effects are appropriate simplifications for testing the model operation, but future studies to validate the coupled model will require using the subgrid method and one of the finer resolution grids that we have prepared for the Trinity Delta. The 50×50 m topography is generated from 1 m lidar data, with grid-coarsening using the minimum value of all 50×50 fine grid cells – which prioritizes flow paths over blockages. This approach tends to overestimate grid storage and fluxes, but ensures adequated surface connectivity is obtained (which can be a problem for coarser grid resolutions). This task in the present contract is only for preliminary model development, so tests herein are to examine whether this groundwater model produces differences in the overall evaluation of water budget and salinity transport and should not be taken as a quantitative (or even qualitative) study of the fluxes.

Unknown variability of submerged topography: An inherent problem with the lidar topography used in the TDHM model is that we lack comprehensive data on submerged bottom elevations (see discussions in Appendices A and B). Furthermore, the upscaling to the 50×50 m resolution tends to smooth the topographic variability. To provide a more complex test of the groundwater model, we added *ad hoc* variability to the submerged water areas at the coarse model resolution. This was accomplished using kriging interpolation. For the Trinity River and the Old River, the elevations were interpolated from the limited field survey collected in the prior project as discussed in Appendix B and Z. Li et al. (2017). For the Trinity Bay (where field data is not available) bottom elevations are set to *ad hoc* (reasonable) values. The Lake Anahuac region is removed from the model domain because evidence has shown limited surface connectivity between this lake and the Trinity River (Section A). However, in future modeling should investigate whether this region affects groundwater fluxes

Vertical layers in groundwater model: A total of 30 layers are used in the vertical direction, ranging from -13 m to $+2$ m above datum (NAVD88) with a constant layer thickness of 0.5 m.

Initial and boundary conditions: The initial and boundary conditions for the surface water domain are similar to the ones used in testing the subgrid model in §3. Initial head and salinity in the subsurface domain are both zero. The hydraulic conductivity in x and y directions are set to $10^{-6} m/s$, whereas in vertical direction it is $10^{-7} m/s$. These values are chosen to allow quick

response of the subsurface domain. Depending on the soil condition, the field values for the hydraulic conductivities could be much smaller. The porosity is set to 0.4.

Simulation time period: The coupled surface-subsurface model is run starting from Oct. 1, 2017 for a 20-day simulation.

5.4 Model results

Change in subsurface head: Figure 15 shows the change of subsurface head with time along cross-section X1, which is the black line on Fig. 14. Downward propagation of head can be seen, with the highest propagation speed near $x = 12$ km because of a large depth. Horizontal transport is also observed, but is much weaker because of lower gradients in the horizontal directions.

Change in subsurface salinity: Figure 16 shows the change of salinity in the subsurface domain. Compared to head, vertical transport of salinity occurs at much lower speeds. This phenomenon is common for coastal aquifers, where effects of salt intrusion during over-bank floods could last several years (e.g. Yang, Zhang, Yu, Graf, & Michael, 2018). The use of impervious boundaries and negligence of evaporation makes it more difficult for salinity to enter the subsurface domain. However, the relatively quick response to surface salinity can be found for the top subsurface layer. For example, a decrease of salinity in the top layer occurs from 240 h to 480 h near $x = 13$ m is due to a decrease in modeled surface salinity (not shown).

Volume from surface into groundwater: Figure 17 shows relative volume loss of the surface domain into groundwater, which is calculated as:

$$r_V = \frac{V_s - V_{ss}}{V_s} \tag{37}$$

where V_s is the total surface water volume when simulating the surface flow only, and V_{ss} is the total surface water volume when simulating both surface and subsurface flows. The maximum volume loss is about 0.04% for the entire Trinity Delta. This value is expected to increase if the present groundwater solver is replaced with a variably-saturated solver because of strong evaporation along the Texas coast. The volume loss shows oscillatory behavior with both positive and negative values, indicating surface-subsurface exchange is a two-way process and is affected by tidal force.

Net effect of groundwater model on salinity: The difference in predicted salinity with/without the groundwater model is shown in Fig. 18, where negative values indicate the surface-only model produces lower salinity. The salinity difference has spatial variability, with net negative values generally found in the Old River Lake and downstream of the Trinity River. These values indicate that salinity storage in the groundwater could play a role in the temporal variability of salinity across the system.

Computational costs of the groundwater solver: Including the groundwater module for TDHM (at $\Delta x, \Delta y = 50$ m with 30 subsurface layers) increases the total computational cost by $25\times$ the cost of the surface-water only model. To effectively use the coupled model at the finer grid scales required for accurate modeling of surface water transport (10×10 m) will require a number of model improvements. Firstly, the coupled model needs to be ported to a supercomputer and efficiently parallelized. Secondly, an adaptive model time step for the surface/groundwater coupling needs to be introduced so that the groundwater time step can take advantage of the slower transport rates. Finally, it would be useful to introduce a coarser horizontal grid for groundwater model to reduce the overall computational burden.

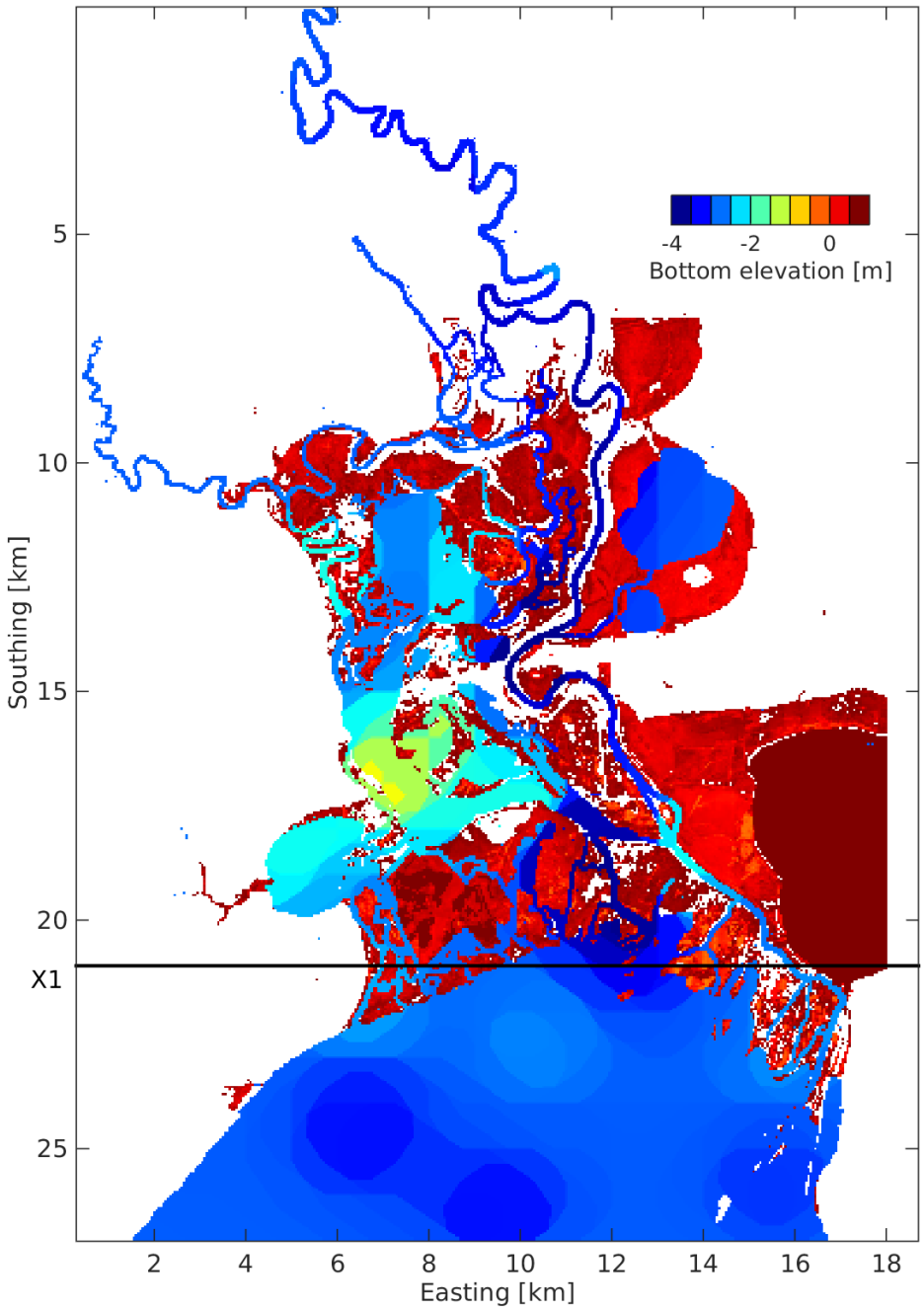

Figure 14: Topography and coupled surface-subsurface model domain for testing the coupled surface-subsurface model. The black line is the cross-section X1 where model outputs are examined.

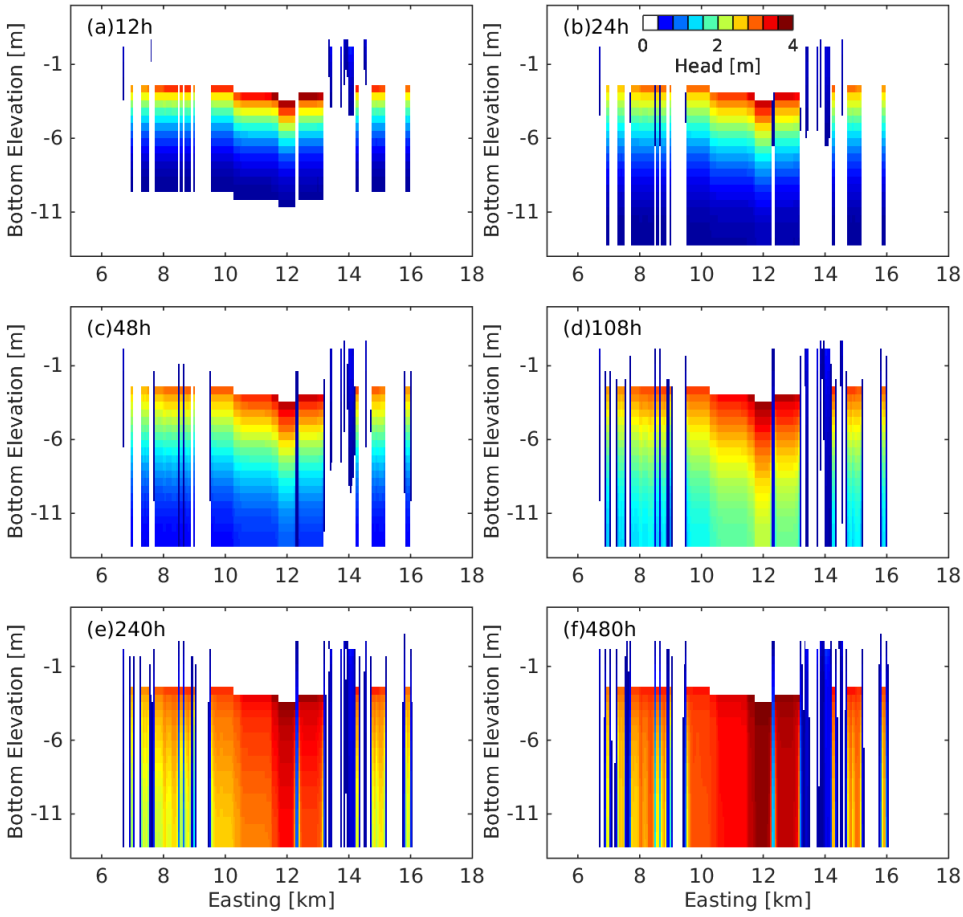

Figure 15: Modeled head along cross-section $X1$

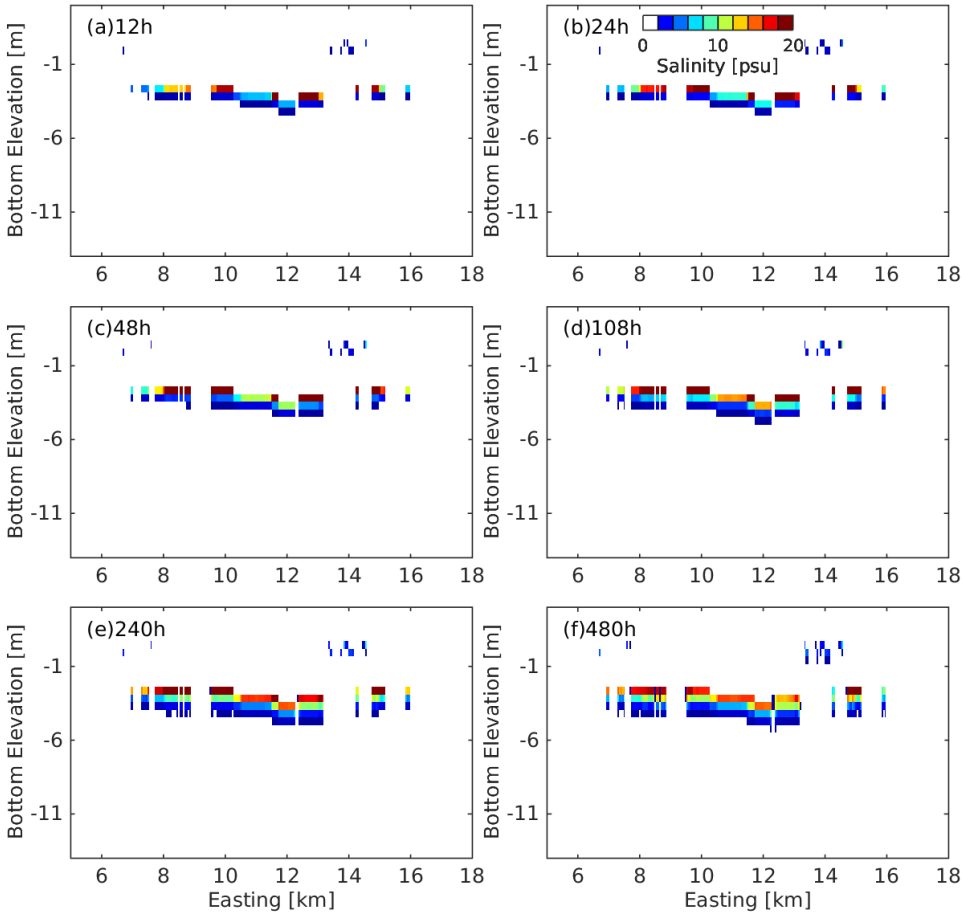

Figure 16: Modeled salinity along cross-section $X1$

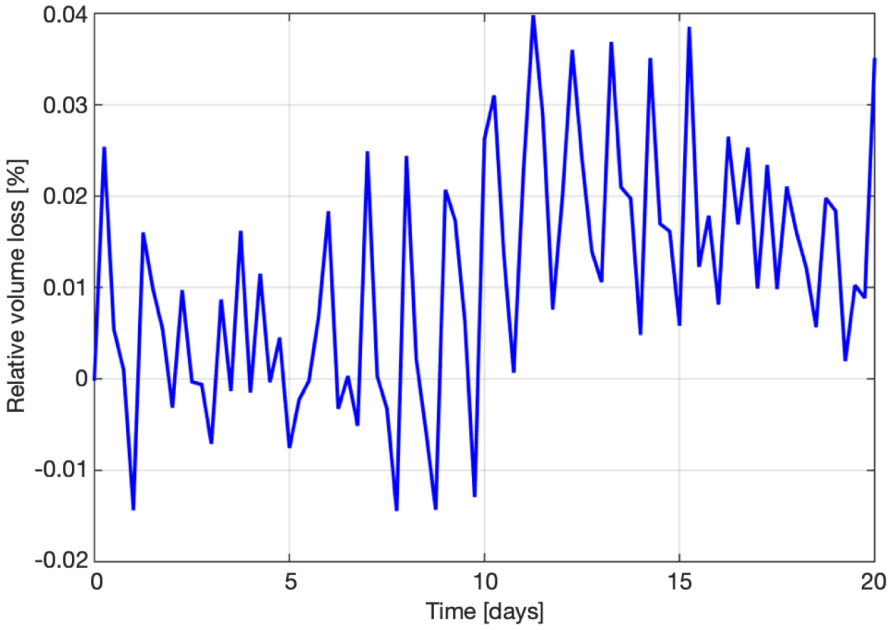

Figure 17: Relative loss of surface water volume to subsurface (r_V, see Eq. 37).

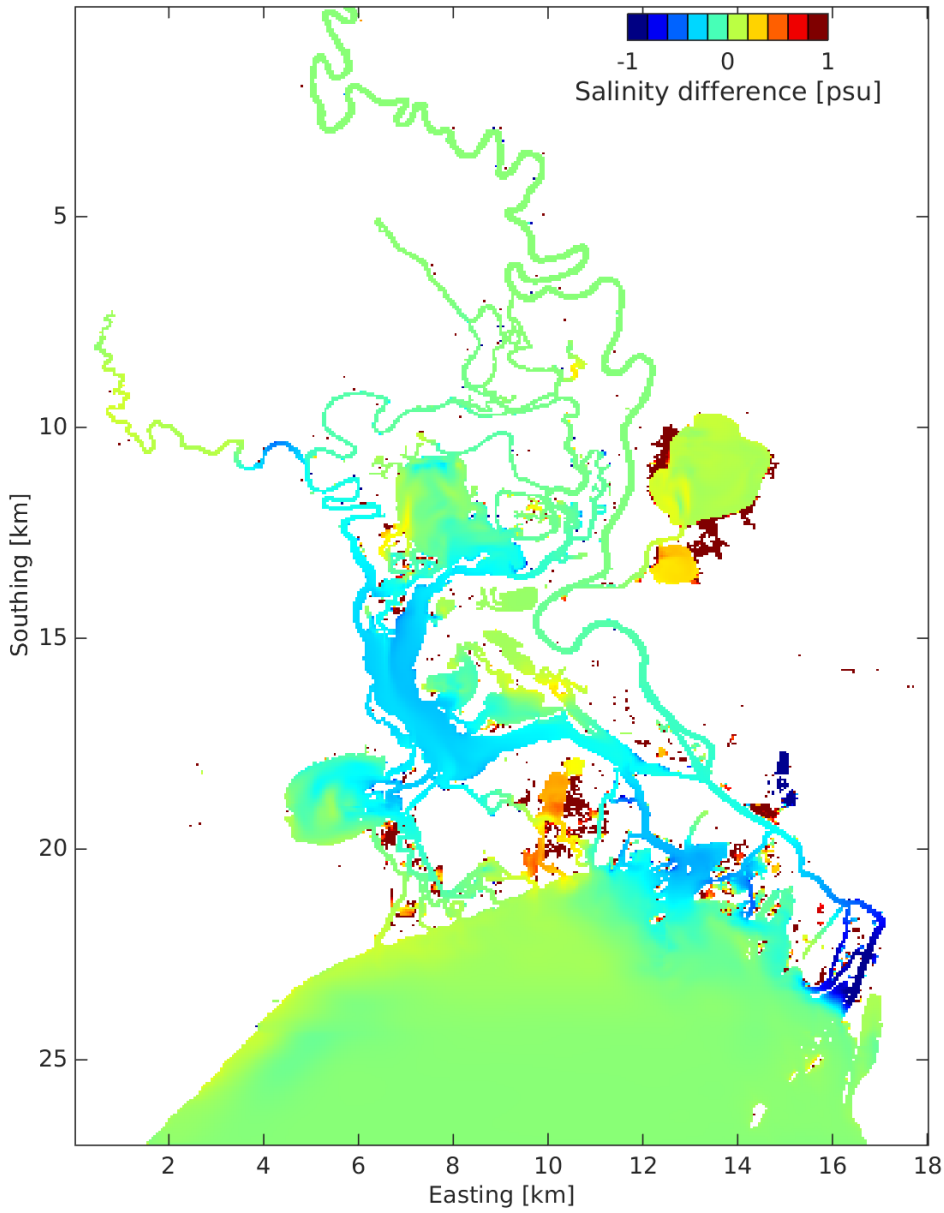

Figure 18: Difference in surface salinity between simulations without/with groundwater solver averaged over 20 days. Negative values indicate lower salinity in surface-water only model.

6 Discussion and conclusions

Completion of contracted tasks: This project provides the second stage in developing and testing the Trinity Delta Hydrodynamic Model (TDHM) – building on the progress in Z. Li et al. (2017), which is also provided in Appendix B. Three contracted tasks were completed: (i) implementing subgrid algorithm to allow simulating effects of subgrid-scale topography, §3; (ii) testing sensitivity of model results to changes in boundary conditions, §4; and (iii) developing new code to use the TDHM for coupled surface-subsurface simulations §5.

Development and test of the subgrid method: The subgrid method designed by Z. Li and Hodges (2019a) was tested on the Trinity Delta (see §3 and Appendix D) and compared to the edge-based method of Hodges (2015). A comparison between test scenarios with/without applying the subgrid method reveals significant difference in predicted inundation area and salinity. At a practical coarse grid resolution of 20 m, many narrow river channels are cut off on conventional coarse-grid bathymetry. The subgrid method is able to resolve the small scale topographic features during grid coarsening, which maintains surface connectivity at coarse resolution. As a result, test scenarios with subgrid method predict intrusion of both ocean water and river water into the interior of the Trinity Delta – a phenomenon that is not observed in conventional coarse-grid simulations. The present results indicate that subgrid method is an improvement over the edge-based method in representing connectivity, but there remains an open question as to the practical maximum grid scale that can be used with the subgrid method and the TDHM. Answering this question will require a comprehensive field campaign that gather surface and groundwater data.

Sensitivity tests and proposed sensor locations: In §4, the sensitivity studies showed effects of relatively small changes in boundary conditions tend to be spatially localized. High sensitivity to the tidal boundary condition is found at regions closed to the Trinity Bay as well as in the main stem of the Trinity River. The larger open-water expanses (Trinity Bay and lakes within the delta) are strongly affected by wind speed, whereas the narrow channels do not have significant fetch and have only a weak response to wind. Only the upper sections of the Trinity River are strongly affected by changes in river stage in the present tests, which were focused on a weak inflow regime. Our analysis of the sensitivity tests is used to propose potential locations for field sensors (Fig. 13) that could be used to validate the model.

Saturated groundwater model: A saturated groundwater model was developed and coupled to the *FrehdC* model for TDHM as presented in §5. This coupled model allows simulation of surface-subsurface exchange. An implicit solution to the 3D Darcy's Law is used to calculate the head distribution in the subsurface domain. Surface-subsurface exchange is modeled as a volumetric source term in the mass conservation equations. The coupled model is tested on the Trinity Delta, which provides reasonable prediction of head propagation and salinity transport from surface into the subsurface domain. The comparison between simulations with/without groundwater model reveals slight different salinity and surface volume, meaning that surface flow and salinity are affected by subsurface processes, but more field data is required to fully quantify the change in model results and evaluate the role of groundwater flow. This difference is expected to increase in more realistic scenarios where unsaturated groundwater flow is considered. Although the coupled model is functional, it presently cannot be run at the finer grid scales required for correctly representing surface water connectivity. Developing a coupled model that can effectively run seasonal to annual simulations will require rewriting the model to handle (i) adaptive time stepping, (ii) coarse-fine grid communication between groundwater and surface water, and (iii) efficient parallelization on a supercomputer.

Potential importance of the coupled surface-groundwater model with subgrid bathymetry: The distribution of salinity in surface water through the Trinity River Delta is often controlled by narrow channels through the marshes. Narrow dikes and small dams isolate many shallow marshes and large lakes from the rest of the Trinity Delta – such areas might only connected by groundwater or during overbank flooding. To correctly model the salinity distribution requires capturing surface and connectivity and blockage across small scales and the subsurface connectivity that bypasses such blockages or enhances existing connectivity. The subgrid model improves our ability to capture the small-scale surface water connectivity at practical model scales and the groundwater model provides a means of capturing the groundwater connectivity and transport.

Preliminary processing of new lidar data: A new lidar dataset of the Trinity Delta became available midway through this project. Although not a part of the tasking under the present contract, we have completed a preliminary analysis of the new data, as discussed in Appendix A.

Open questions and issues: Collecting adequate field data to further develop and validate the TDHM remains a challenging problem. There are three types of data where further work is needed:

1. More detailed bathymetric surveys of channels within the Trinity River Delta, including both multi-beam survey of larger channels and single-beam survey of smaller channels. These need to provide enough data to make reasonable estimates of submerged elevations in channels where data is unavailable.
2. Long-term (24+ month) monitoring of water surface elevations, temperature, and salinity and a wide range of locations throughout the Trinity River Delta. This monitoring should be based on the sensor locations developed in §4.4 with further consultation of researchers and agencies who have been conducting field studies of the Trinity River Delta.
3. Long-term (24+ month) groundwater monitoring for head and salinity. The present project did not include sufficient time to explore the sensitivity of the coupled groundwater model to determine good locations for groundwater monitoring. It is suggested that either further modeling should be done, and/or experts in groundwater contacted to discuss locating sensors.

There remains an open question as to whether the best approach to future work with the TDHM is to improve the existing groundwater model, or to take the time to couple TDHM to MODFLOW for a fully-functioning coupled model. The decision as to which approach makes the most sense depends on the timescales over which the TWDB sees the coupled model being used. If the TDHM is envisioned as an ongoing management model that will be more widely disseminated, then spending the time to link to MODFLOW would be worthwhile. However, if the TDHM is seen as a research model that will only be of local use, then it probably makes more sense to upgrade the directly-coupled groundwater model that was written in this project.

Appendices

A Higher resolution lidar data

A new lidar dataset of the Trinity Delta at higher resolution (0.35 m compared to 1 m in the old data) became available in 2017. This dataset provides more information on the topography and surface connectivity of the model domain. Figure 19 shows the new data set averaged to 2 m resolution (finer resolutions cannot be readily printed at this scale). The new lidar data provides significantly more detail in the topography of the dry areas of the delta, but does not provide any new information on bathymetry for inundated areas. Note that the inundated areas have the same vertical stripe features discussed in the processing of the prior lidar data set (Z. Li et al., 2017). It is interesting to note that Lake Anahuac has higher surface elevation than the majority of the domain (e.g., Trinity Bay, Trinity River, Old River), indicating that Lake Anahuac is not hydraulically connected to the delta, and can be removed from the surface water simulation domain. Detailed examination revealed that the flow path between Lake Anahuac and the Trinity River is cut off by narrow dams/dikes that are not visible on the earlier 1 m lidar dataset. Similar small hydraulic features appear to exist at multiple locations in the Trinity Delta. Thus, the surface connectivity of the model domain could be affected by the operation modes of these dams, which leads to a potential source of uncertainty for the TDHM model. Similarly, in Fig. 19, a small region in the shallow marsh between the Trinity Bay and the Old River Lake has lower surface elevations than its surroundings, which indicates this region is also isolated from the rest of the Trinity Delta by narrow levees. These observations emphasizes the significance of resolving small-scale water-blocking features at practical coarse grid resolutions. Future refinement of the TDHM should include an inventory of all the hydraulic features that affect the delta, delineation of isolated regions, and ensuring that upscaling in the subgrid method accurately reflects these features.

Note that before this new lidar data set can be used, it must be processed through the techniques developed in Z. Li et al. (2017) to set the bottom elevations for the inundated areas. The dataset will also need to be processed to remove artificial blockages associated with overhanging trees, bridges, or other artifacts.

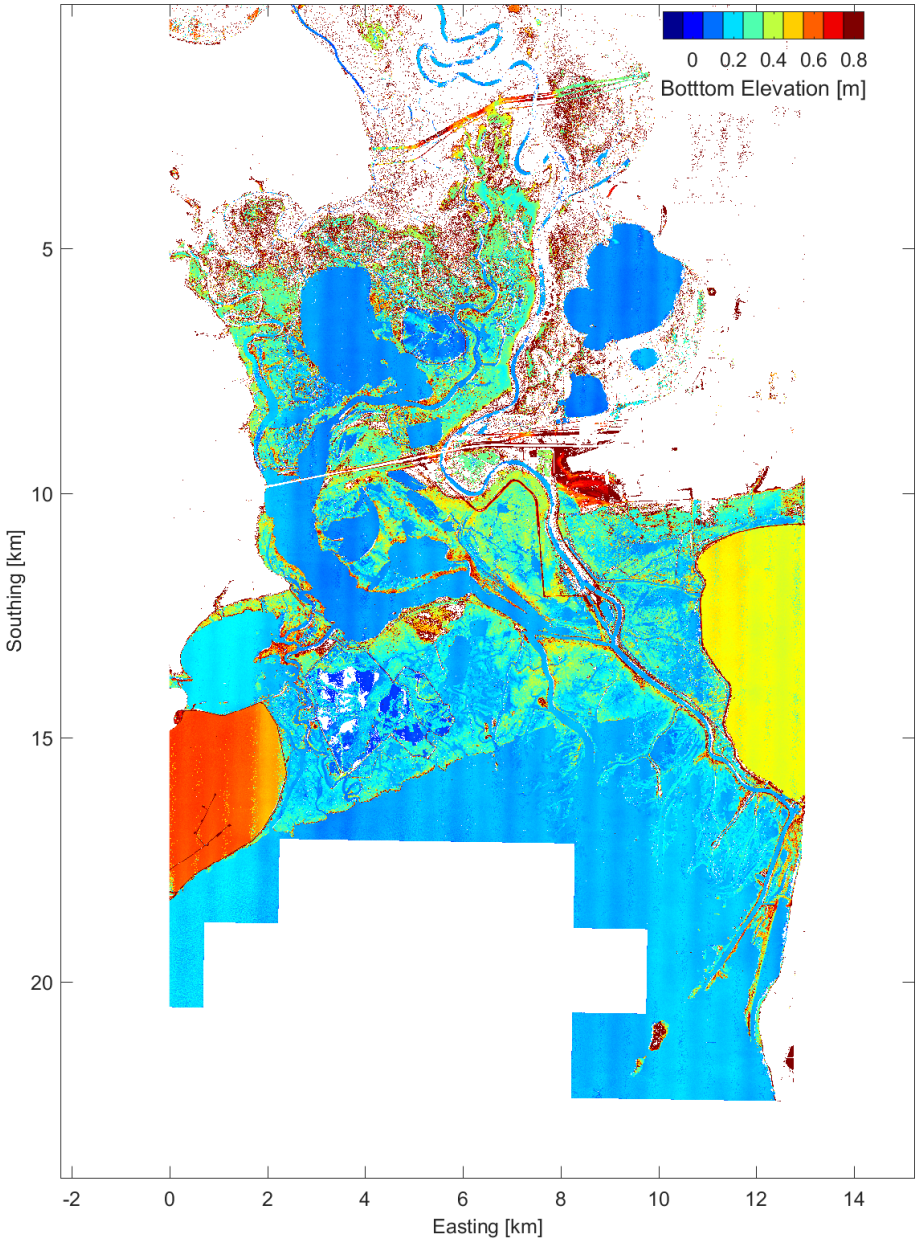

Figure 19: New lidar data of the Trinity Delta (data available at 0.35 m resolution but displayed at 2 m resolution).

B Hydrodynamic model development for the Trinity River Delta

For convenience to the reader, following appendix provides the text and figures of the final project report for the prior contract (2016-2018), which initiated the TDHM. Modifications have been made for consistent cross-references as an appendix to the present report.

Report Title: **Hydrodynamic model development for the Trinity River Delta**

Authors: Zhi Li, Paola Passalacqua, Ben R. Hodges

Submitted to:
Texas Water Development Board
Final report under contract no. 1600011928
July 19, 2018

Executive Summary

A hydrodynamic model (the newly-written *FrehdC*) has been constructed to investigate mismatch of flow between different measurement locations across the Trinity Delta and provide the foundations for the Trinity Delta Hydrodynamic Model (TDHM). The model bathymetry is generated from lidar data with extensive analyses as described in this report. The available lidar data does not contain trustworthy values regarding the bottom elevation in submerged areas of the delta, so a limited ground-truth field survey was conducted. Two methods are used to separate the water regions and the land regions in the lidar data such that estimated bottom elevations can be assigned to the water regions to maintain surface connectivity in the model. These methods are (i) an automatic clustering algorithm that identifies the water areas by their color from a GoogleEarth satellite image, and (ii) a manual delineating method that identifies additional channel connectivity in Photoshop. Two hydrodynamic simulations were executed with the bathymetries created by these two methods. Comparison between the two simulations shows different patterns regarding surface wave propagation and salinity transport because the automatic clustering algorithm fails to identify many narrow channels in the mid-to-upper delta. This comparison indicates the significant impact of the bathymetry processing on simulation results. The potential of *FrehdC* in modeling the hydrodynamics of the Trinity Delta has been shown. However, for the model to be used to solve realistic problems will require (i) more bathymetry data for submerged regions than was collected in this project, (ii) analysis and processing of comprehensive boundary condition data for inflows, tidal elevation and winds, and (iii) an additional field data collection program throughout the delta for model calibration and validation. Finally, it should be noted that the *FrehdC* model does not (at this time) include algorithms representing the slow, near-surface groundwater flows that are likely to affect water movement through the delta.

B.1 Introduction

Mismatch of river discharge between Romayor gage (08066500) and Wallisville gage (08067252) has been previously detected based on data collected by the U.S. Geological Survey (USGS). To improve understanding of the timing and spatial distribution of Trinity River water entering the Trinity Bay, a two-dimensional (2D) hydrodynamic model, the Trinity Delta Hydrodynamic Model (TDHM), is being developed to model transport and exchange through this region. Such models require extensive input data, including detailed bathymetry information, initial conditions for water surface elevations, and boundary conditions on flows and depths. This report summarizes the preliminary work required for model construction, which included three tasks:

1. Mobilizing lidar data and analysis of “not-a-number" (NaN) elements.
2. Field work for limited checking of NaN elements and bathymetry in some channels.
3. Analysis of landscape data and development of a hydrodynamic model.

Model bathymetry is created by upscaling (i.e., coarsening) lidar data to a grid resolution that is practical for hydrodynamic modeling. This task requires extensive analyses to ensure that data errors in the lidar data are not translated into the model bathymetry. The high-resolution lidar data of the Trinity Delta topography contains many NaN elements in regions containing deep channels and lakes because the red laser light used in the survey does not penetrate water. These regions were carefully analyzed to assess the reliability of the lidar data. A field survey was executed to validate the lidar

data at several locations of interest. After generating a high-resolution (1×1 m) model bathymetry that encompasses the best available knowledge, a hydrodynamic model was developed and tested at a coarser grid resolution (10×10 m) that is practical for large-scale modeling. The test simulations used approximate initial and boundary conditions to investigate effects of different bathymetry processing options. This work sets the stage for more extensive model development.

This report is arranged as follows: Section B.2 describes the procedures to process the lidar data (Task 1). Section B.3 introduces the field survey and validation of the lidar data with the survey data (Task 2). Section B.4 illustrates the selection, construction of the numerical model as well as the preliminary simulation results (Task 3). Section B.5 summarizes the findings and discusses possible future improvements of the current study.

B.2 Lidar data processing

B.2.1 Creating a Digital Elevation Model (DEM) from lidar data

The two lidar datasets used in this project were obtained from Federal Emergency Management Agency (FEMA) surveys and processing: *FEMA2006*[2], which provides 1.4 m resolution raster data over the lower delta, and *FEMA2011*[3], which has approximately 1.0 m resolution for Liberty area. The coverage areas of these data are shown in Fig. 20, where the grid represents the available data subsets. The focus area for this study (yellow box in Fig. 20) encompasses 39 subsets from the *FEMA2006* dataset and 70 subsets from the *FEMA2011* dataset. For the *FEMA2006* dataset, each subset (corresponding to one data file) covers an area of about 4×5 km. These subsets were concatenated by matching the latitudes and longitudes at the boundaries. To meld the *FEMA2006* and *FEMA2011* datasets, a 1×1 m gridded mesh was defined over the study area. The *FEMA2006* data were interpolated onto this raster grid using the MATLAB *interp2* function. As the *FEMA2011* data points (given by latitude and longitude) were not uniformly distributed over space, the data from the 70 files were projected to the 1×1 m gridded mesh based on latitude and longitude bounding coordinates of each grid cell. Where multiple data points shared a single grid cell, the median of these points was used as the cell elevation. Where a cell had no data points, a NaN value was assigned. An area at the southern edge the study area is not available in the lidar coverage area and was assigned NaN values in the raster grid.

B.2.2 Noise removal and water body identification

A noise removal process is required before the rasterized lidar data can be used to generate the model bathymetry. Using one subset of the *FEMA2006* dataset as an example, the lidar data (interpolated to 1×1 m) can be found in Fig. 21, where three types of noise exists.

1. No data points (as represented by white blocks in Fig. 21).
2. Vertical stripes are found on large lakes, ponds and lagoons. These stripes are likely noise associated with the data collection flight path where the laser beam is reflected from the water surface.
3. Patchwork triangular blocks in some channels appear to be the remnant of interpolation methods (triangulated irregular network, TIN) applied in lidar data processing prior to data storage in *FEMA*. These features can be taken as an indication that few direct measurements were made in these channels.

Unfortunately, all the water areas in Fig. 21 (and throughout the Trinity data) typically belong to one of the three noise categories. Thus, there is no trustworthy information about the water depth within the *FEMA* data sets. However, the lidar data for the land seems reliable (and has been spot-checked over limited extent, see Section B.3). For further processing, the land regions and the water regions were separated within the dataset. To continue with the present model development without a comprehensive bathymetric survey, all water regions have been assigned a value of -1.0 m. This preserves connectivity of the channels visible at the lidar resolution, but likely misrepresents the

[2]FEMA, 2006, FEMA 2006 140cm Lidar, Texas Natural Resources Information System, `https://tnris.org/data-catalog/entry/fema-2006-140cm`

[3]FEMA, 2011, FEMA 2011 1m Parker Lidar, Texas Natural Resources Information System, `https://tnris.org/data-catalog/entry/fema-2011-1m-parker`

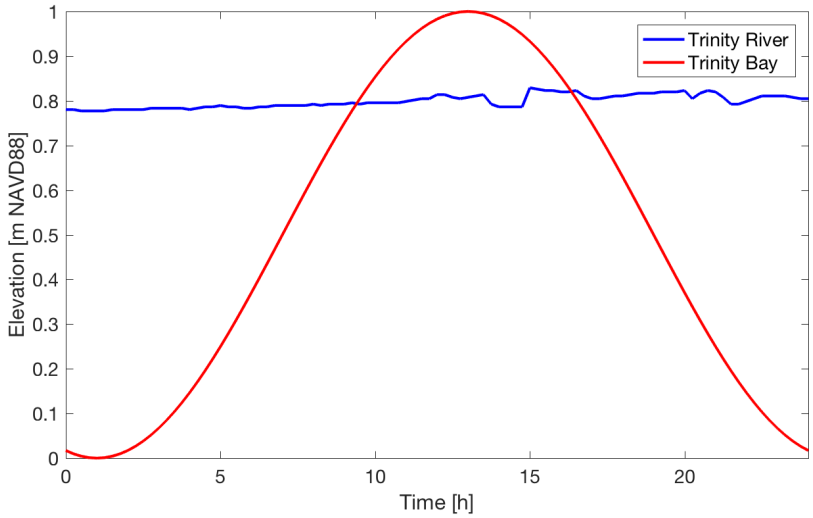

Figure 20: Scope of the lidar data. The red grids are the *FEMA2006* dataset. The blue grids are the *FEMA2011* dataset. The solid red and solid blue boxes are boundaries of data used in TDHM. The yellow box is the computation domain. (Source: Esri, DigitalGlobe, GeoEye, Earthstar Geographics, CNES/Airbus DS, USDA, USGS, AeroGRID, IGN, and the GIS User Community)

actual water depth in many areas. If reliable bathymetric measurements for submerged regions can be provided in the future, the affected regions are easily identified and an algorithm to integrate the new data into the dataset can be developed.

To separate the water regions from the land regions, the *kmeans* algorithm (e.g., Arthur & Vassilvitskii, 2007) was applied in conjunction with GoogleEarth satellite images. The *kmeans* approach is an image clustering algorithm commonly used in unsupervised machine learning. This approach uses an iterative process, grouping the pixels with similar properties (e.g., color) together until a cost function converges. More insights of this algorithm can be found in description of the function *kmeans* in the MATLAB Statistics and Machine Learning Toolbox. The present application of *kmeans* to discriminate between land and water requires the following workflow:

1. Obtain the GoogleEarth image that covers the region of the lidar data, called *imgA*.
2. Using the lidar data as a reference, correct the distortion in the satellite image by matching the scales of the objects in *imgA* and the lidar data. This task is accomplished with the MATLAB functions *cpselect* and *fitgeotrans*. The result (for one data section) is Fig. 22, called *imgB*
3. Crop the distortion-fixed GoogleEarth image to get a portion of the image that matches the corresponding lidar data, called *imgC*. Selecting the regions to crop depends on the subjective judgement of the modeler, so some errors are expected.
4. Apply the *kmeans* algorithm on *imgC*. For the sample area shown the algorithm identifies 20 clusters from *imgC*. The resulting clustered map is shown as Fig. 23, called *imgD*.
5. The *imgD* pixels have values ranging from 1 to 20. Using *imgC* as a reference, the pixels indices that represent water areas are identified. In the example, it is clear that two shades of red colors and three shades of blue represent water. This step also depends on subjective judgement.
6. Finally, the water area pixels in the corresponding lidar data are replaced by a uniform bottom elevations (-1.0 m in this example), which provides the automatic (AU01) processed bathymetry at 1×1 m resolution, as Fig. 24.

As can be seen from Fig. 24, the majority of the water areas have been successfully identified. The wide channels and large lakes are sufficiently delineated. However, this method produced some extraneous water areas on the left of the figure that appear to be farmland or pasture. This approach

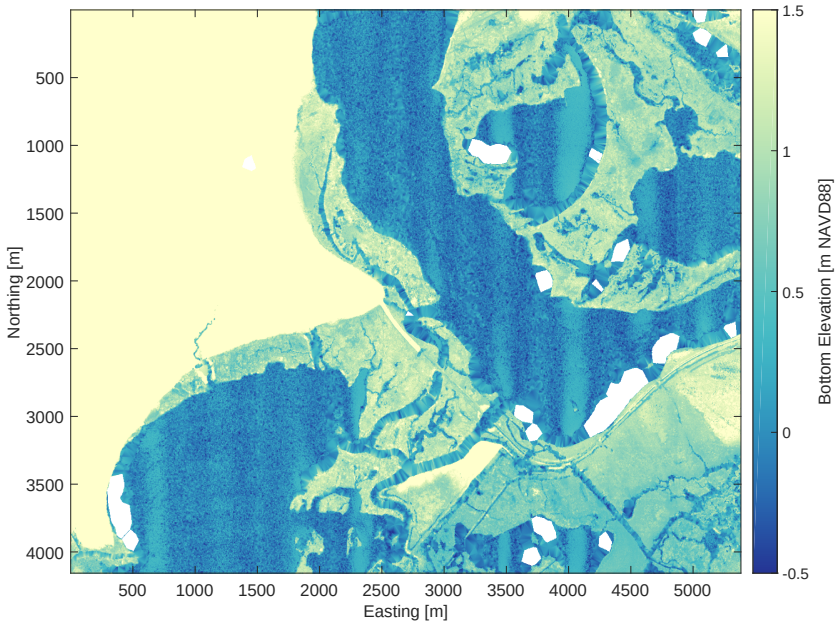

Figure 21: A subset of the raw lidar data from the *FEMA2006* dataset.

also failed to identify some narrow channels. The main reason for these deficiencies is in the overall quality of the satellite image. The *kmeans* algorithm clusters the image based on colors, which must be separable in the satellite image. It is likely that the use of multiple satellite images taken at different times of the year (or in different years) could be used to improve this approach. Detailed review of the results show that at some locations the channels in the satellite image and the lidar data have horizontal location mismatches of up to 10 m. This occurs because (i) the distortion correction algorithms that match these datasets are approximations and do not create a precise overlay, and (ii) there can be transitional color features at the channel edges that affect the precision of its representation in the clustering algorithm.

The water-body identification procedure is applied for the entire study area to generate the high-resolution (1×1 m) bathymetry model, which is described in detail in Section B.4.

Figure 22: GoogleEarth satellite image after distortion correction

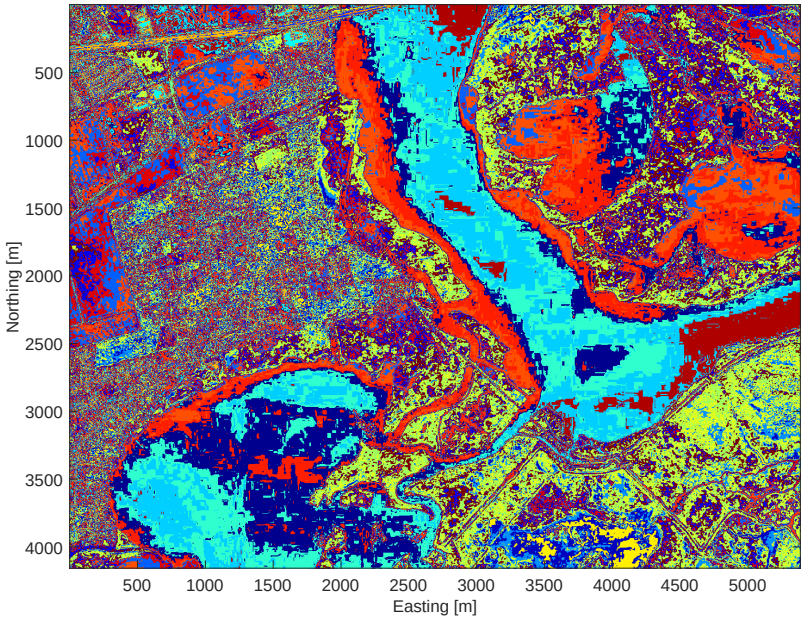

Figure 23: Clustered map of the distorting-corrected GoogleEarth image after cropping

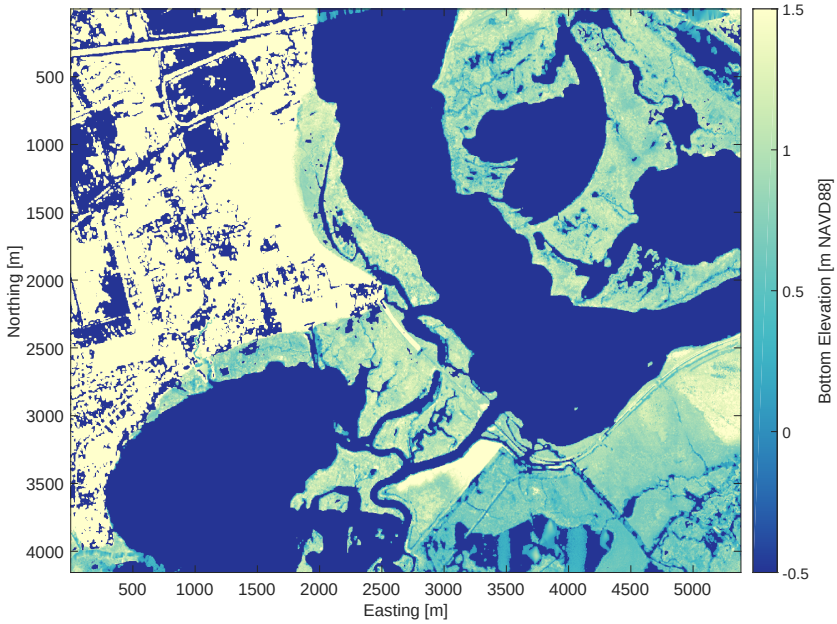

Figure 24: AU01 bathymetry created with automatic processing techniques from lidar data and clustered map.

B.3 Validation with field survey measurements

Although the clustering method successfully separated most of the land and the water regions, data for the water depth are lacking. A field trip organized by the Texas Water Development Board (TWDB) and the Trinity River Authority (TRA) was executed from Dec. 18th to Dec. 21st of 2016 to collect field data for validating the lidar data. The route of the field survey is shown in Fig. 25. Water depth is measured along main stream of the Trinity River as well as part of the Lost River. Several land elevations were also measured to examine the possible noise produced in the lidar data due to vegetation canopies. These field data are compared with the lidar data so that the reliability of the lidar data can be evaluated.

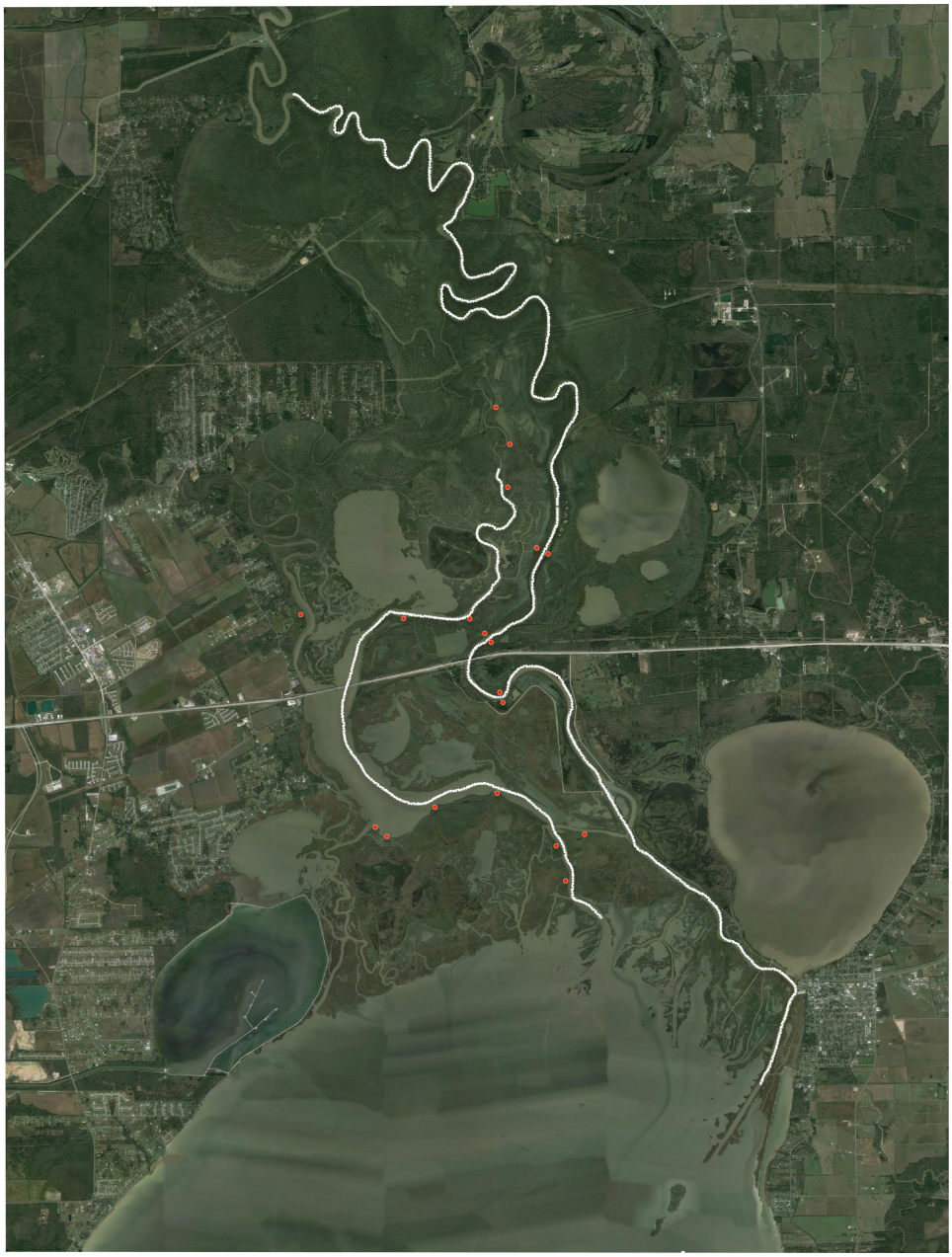

Figure 25: Route of the Trinity Delta field survey. The water depth was measured along the white path. The land elevation was measured at the red dots.

The surveyed water depths were converted into bottom elevations for the river channels. The survey depths have a mean of -3.296 m (NAVD88) and a median of -2.986 m, whereas none of the lidar data show deeper values than -0.5 m. Thus, the survey confirms that the *FEMA* dataset for submerged regions is not trustworthy.

To validate the land elevation, the median of the lidar data in a 50×50 m region (water areas excluded) centered at each of the land-validation locations (red dots in Fig. 25) were computed as a best estimate of the lidar land elevation. This value is compared with multiple field survey measurements that were taken at the same location. The absolute errors between the surveyed land elevations and the lidar results are shown in Fig. 26. Both the mean and the median of the absolute error are within 0.4 m, which provides a baseline for estimating uncertainty in the topography.

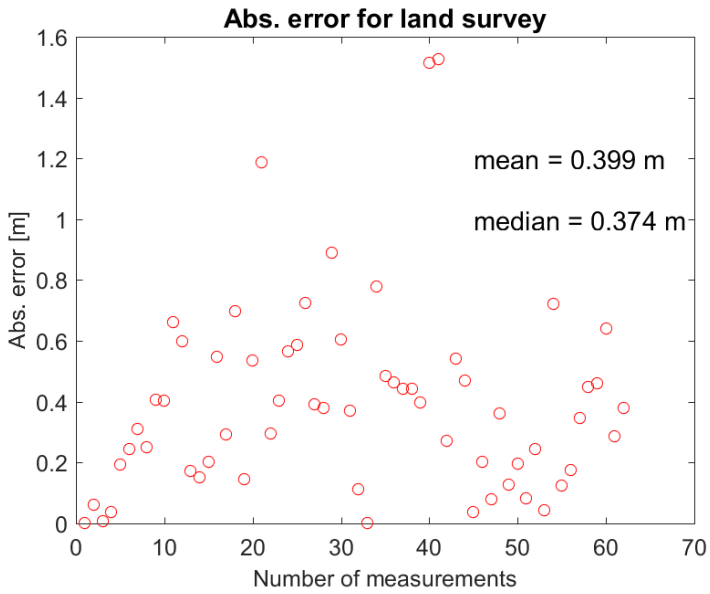

Figure 26: Absolute error of field surveyed land elevation and lidar data

B.4 Preliminary development of TDHM

B.4.1 Hydrodynamic model selection

The Frehd and SUNTANS hydrodynamic models were proposed as candidates for modeling of the Trinity Delta. The Frehd model is built on structured Cartesian grids, which are easy to use with the lidar dataset and has been successfully applied in a similar study in the Nueces River Delta (Ryan & Hodges, 2011). However, the Frehd model is computationally expensive for the larger Trinity Delta region as it is written as a set of MATLAB scripts. The SUNTANS model is compiled C code that is fast and parallelizes (Fringer, Gerritsen, & Street, 2006), but constructing the required high quality unstructured mesh with wetting and drying turned out to be laborious and time-consuming. The advantages of the two models were combined by rewriting the Frehd model in the C programming language and enabling parallel computing via the Message Passing Interface (MPI). In this way, the numerical model (referred as "*FrehdC*") retains the ease-of-use of the original Frehd model at a significantly reduced computational cost.

FrehdC solves the 2D depth-integrated free-surface Navier-Stokes equations with nonhydrostatic pressure and density gradients neglected. The solution algorithm is a hybrid finite-difference/finite-volume semi-implicit scheme that follows the methods originally designed by Casulli (Casulli & Cattani, 1994; Casulli & Cheng, 1992) with updates for turbulence modeling, accuracy, and stability (Hodges, 2015; Hodges et al., 2000; Hodges & Rueda, 2008; Rueda et al., 2007; Wadzuk & Hodges, 2009). The model is fundamentally mass conservative and allows the advective Courant-Friedrichs-Lewy (CFL) number to be slightly greater than unity in limited time/space areas without causing catastrophic instabilities. Furthermore, the barotropic CFL (associated with surface waves) can be significantly larger than unity across the entire domain while retaining a stable solution. When running in parallel mode, the computational domain is divided into equal subdomains by the number of computational threads. The subdomains communicate with each other by sharing the variables along their common boundaries. Ideally, linearly-increased speedup can be obtained with an increasing number of threads, but in practice the speedup is limited by overhead costs associated with a large number of threads. When executing with four threads, the *FrehdC* code is approximately 10 times faster than the original Frehd. This speed-up is due to both the parallelization and the computational efficiency of a compiled C code compared to MATLAB. The *FrehdC* was compiled on Mac Pro OSX El Capitan system (version 10.11.6) with Intel Xeon processor (64 GB memory).

FrehdC models wetting and drying processes directly through the free surface solution, which follows the semi-implicit algorithm designed by Casulli and Cheng (1992). This approach allows dry cells to transition into wet cells based where the depth goes from zero to a positive value in the free-surface solution. To avoid both instabilities and the small time steps required for extremely small depths, a minimum depth threshold ($h_{min} = 10^{-3}$ m) is used. Where the local depth is below the threshold, a formerly wet cell is designated as a dry cell and the water surface elevation is set equal to the bottom bathymetry elevation. Dry cells remain in the computational domain but do not incur computational costs until they become wet. To ensure scalar transport (e.g., salinity) remains conservative, *FrehdC* limits the propagation of the wetting front in a single time step so that a newly-wet cell must be adjacent to an existing wet cell. As is typical of wetting/drying algorithms, the need to truncate very small depths and limit the wet front propagation speed leads to minor non-conservation of mass. This mass loss is tracked during the solution so that the user can be sure the solution is not degraded.

B.4.2 Modeling scenarios

The AU01 digital elevation model (Section B.2) at 1×1 m resolution has 5.39×10^8 grid cells and would require a model time step of less than 0.1 seconds for stability. This scale of computation is not practical without use of high-performance supercomputers, which were not used in this study. For practical modeling on a desktop workstation the AU01 bathymetry was coarsened to 10×10 m by median filtering, which provides the AU10 digital elevation model that is shown in Fig. 27. This grid resolution has acceptable computational costs for short-period simulations (56 hours of wall-clock time for a one-day simulation using eight computational threads), but longer-term simulations on a desktop computer will likely require further coarsening of the grid. For example, a 20×20 m grid would have only 25% of the grid cells of the AU10 grid and allow a time step twice as long, which would require about 12.5% of the computational time of the AU10 grid. Thus, we expect that an AU20 bathymetry could be run at least $3\times$ faster than real time. Similarly, an AU30 bathymetry

should run approximately $12\times$ faster than real time. Obtaining even faster run times would require either coarser bathymetric resolution or moving the computation to a supercomputer.

Although generating the AU10 bathymetry is straightforward and mostly automated, it introduces significant noise into the channel connectivity. The major channels are clearly identified but many secondary channels remain hidden. Thus, the AU10 bathymetry is unlikely to reproduce the correct surface connectivity needed to understand transport through the delta. To address this problem, a second bathymetry was created by using manual channel adjustments, resulting in the MA10 bathymetry shown in Fig. 28. The manual adjustments were made with Adobe Photoshop software using the GoogleEarth satellite images as a reference. The primary and secondary channels were delineated by hand on the AU10 data in Photoshop and the problematic noise features (discussed in Section B.2.2) were removed. Unfortunately, this approach cannot (at this time) be reproduced with an automated method. Obtaining a more accurate bathymetric map with high-resolution channel connectivity remains a challenge in the absence of a complete on-the-ground survey of the channel depths.

The *FrehdC* model requires initial conditions for the water depth throughout the domain and boundary conditions for the inflow and tidal boundaries. In addition, extensive field data is needed for model calibration and validation. Unfortunately, only the water level and flow rate data from a few USGS flow gages along the Trinity River and tidal elevations within Galveston Bay are available. In totality, these available data are inadequate for simulating, calibrating, and validating any specific real-world flow scenario. Thus, the *FrehdC* model has been tested using idealized initial and boundary conditions to evaluate the capabilities and limitations of the model with the AU10 and MA10 bathymetries.

Dirichlet boundary conditions (prescribed values for free-surface elevation) are used for both the south boundary in Trinity Bay and the north boundary of the Trinity River. The north boundary is defined using the water level measured at USGS 08067100, Trinity River near Moss Bluff (15 min sampling interval). The south boundary is defined as a sine wave representing an idealized tidal oscillation (Fig. 29). The model is initiated with a spatially-uniform free surface elevation ($\eta = 0$ m, NAVD88) and zero velocities. These test simulations are designed to examine the stability and efficiency of the model: investigating the physical details of the hydrodynamics and the transport processes is reserved for future studies. For simplicity and computational efficiency, the tested scenarios do not include a model spin-up period. Note that the initial surface matches the tidal boundary condition on the south but is discontinuous at the north boundary, which is a physically unrealistic initial condition. For practical future simulations, the initial surface elevation should be sloping to provide a continuous match to boundary conditions on both sides. Salinity is used as a passive scalar in the simulations to visualize net transport. Our modeling period is only one day (from Jan. 2nd to Jan. 3rd of 2017), which is much shorter than the residence time of the Trinity delta, so a spatially-varied salinity initial condition is set to help visualize short-term transport. The initial salinity field increases from north to south at an interval of 5 psu for every 3950 m. The salinity at the north boundary is 0 psu, while at the south boundary it is 40 psu. The wind speed and direction measured at USGS 08067252, Trinity River at Wallisville, are used to compute the wind stress (15 min sampling interval), which is assumed spatially-uniform across the model domain. During the modeling period, an east wind dominates with an average wind speed of 3.12 m/s. Other required model parameters for testing are listed in Table. 1.

Parameter	Value	Description
Δt [s]	1	time step
Δx [m]	10	grid size
Δy [m]	10	grid size
ν [$\mathrm{m^2 s^{-1}}$]	0.0001	eddy viscosity
C_D	0.01	bottom drag coefficient
h_D [m]	0.001	minimum depth allowed
N_p	6	number of threads

Table 1: *FrehdC* model parameters for idealized tests

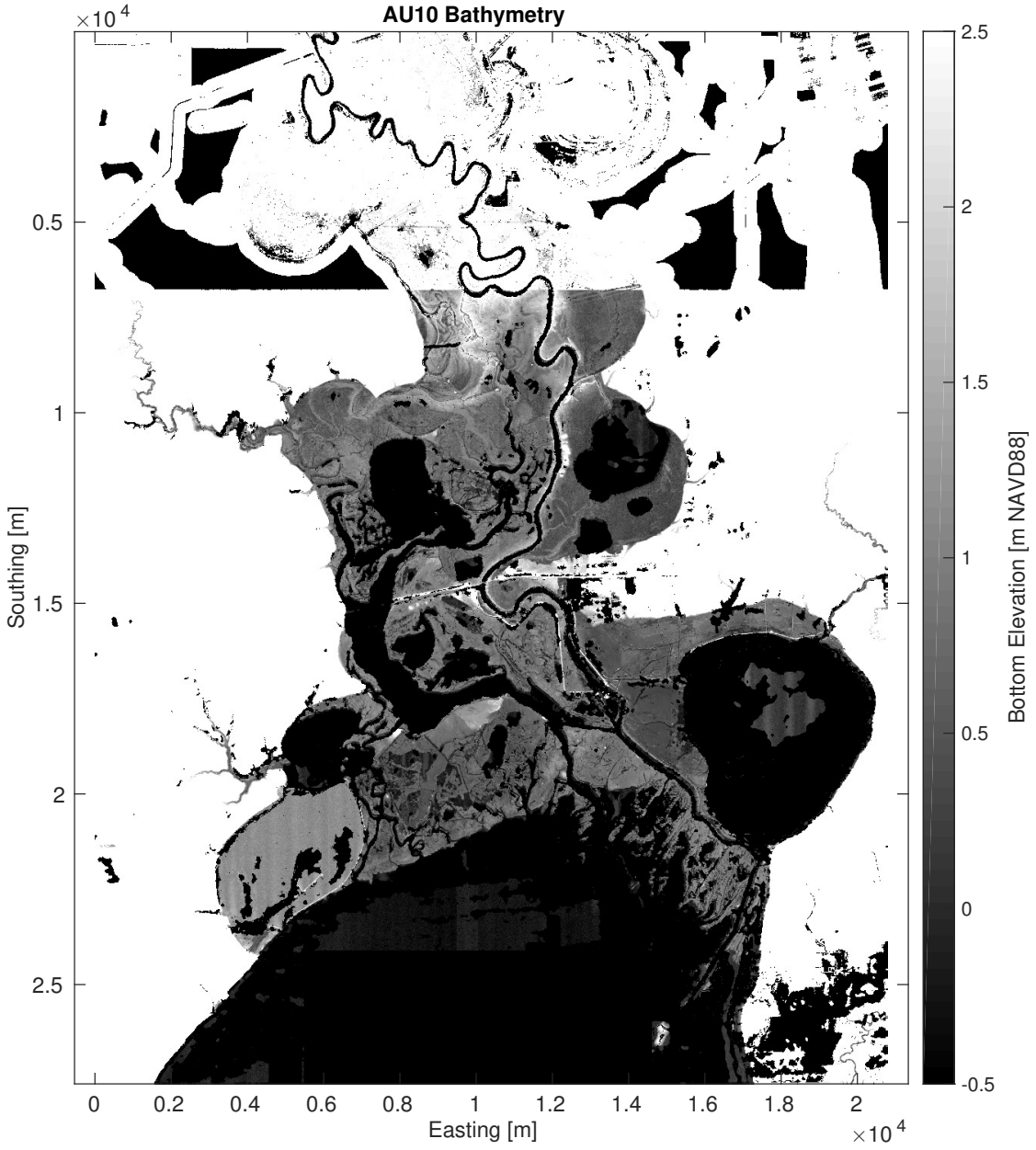

Figure 27: The AU10 bathymetry for the Trinity Delta created using the automatic clustering method. Black indicates water pixels where -1.0 m was assigned as the bottom elevation.

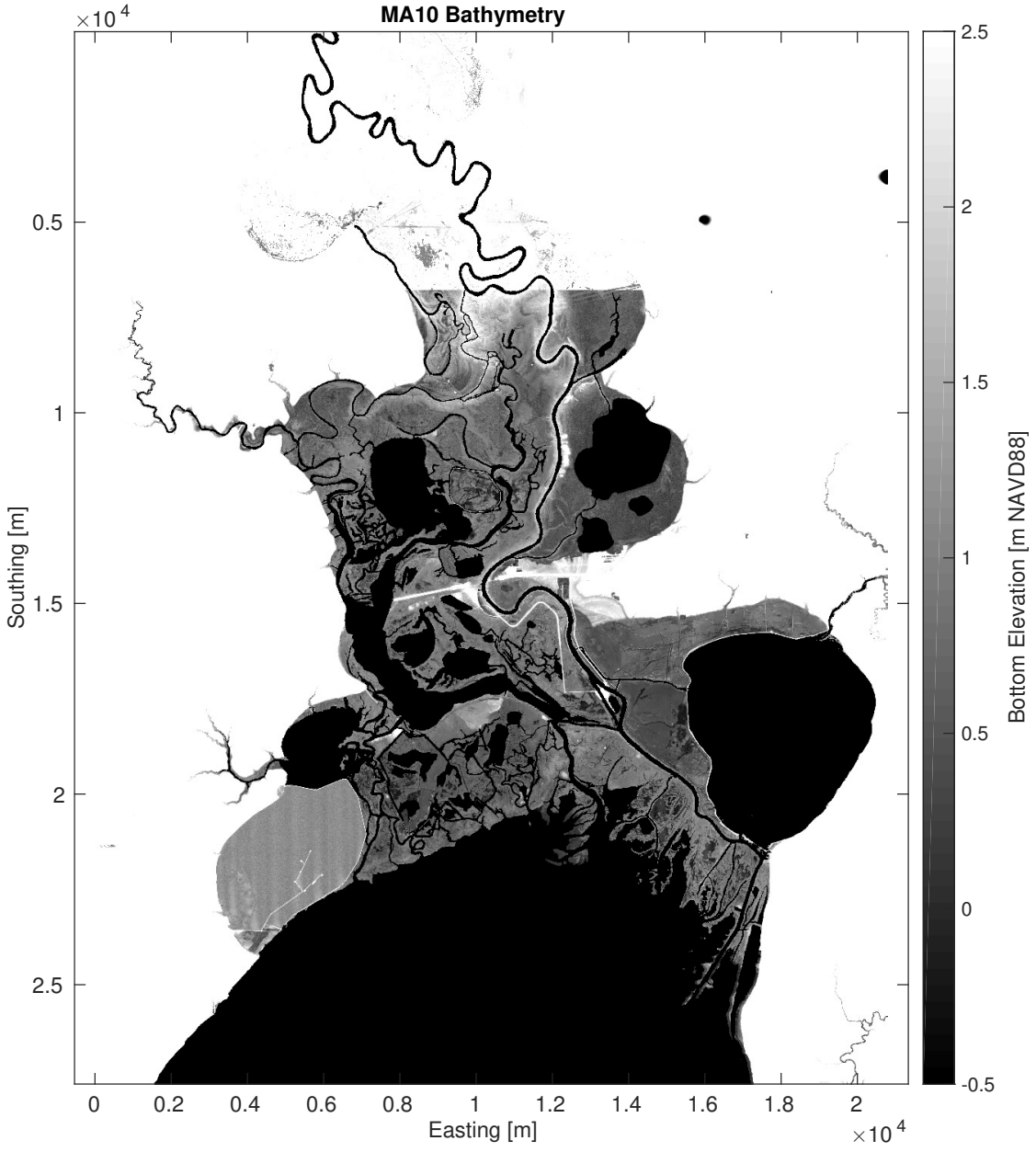

Figure 28: The MA10 bathymetry for the Trinity Delta created with manual adjustment for narrow channels. Black indicates water pixels where -1.0 m was assigned as the bottom elevation.

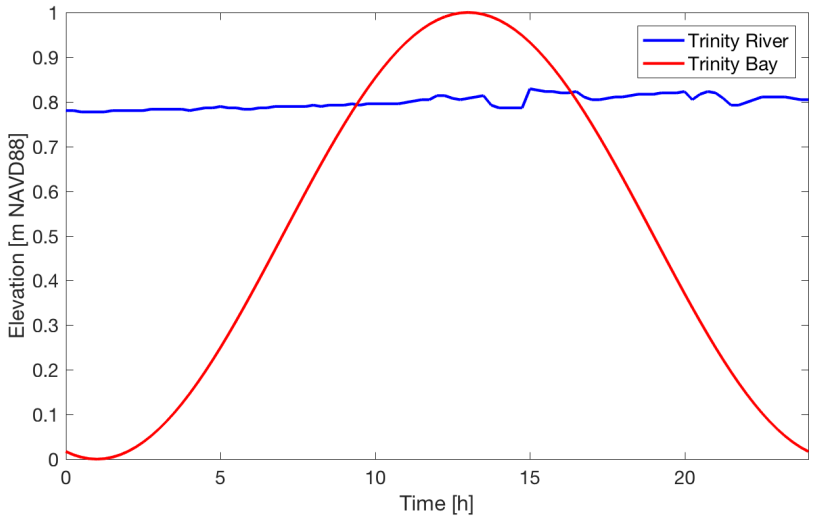

Figure 29: Boundary conditions at the south (Trinity Bay) and north (Trinity River) edges of the simulation domain

B.4.3 Model results

Figure 30 shows the modeled free surface elevation for the MA10 bathymetry at four selected times. Figure 31 shows the similar modeled free-surface elevation for the AU10 bathymetry that was generated by an automatic process without manual interference. In comparing these results, it can be seen that the AU10 tends to build up higher water surface elevations in the lower-to-middle delta. Arguably, this is because the lack of connectivity of the small channel network in the AU10 bathymetry for the middle-to-upper delta. These small channels are effectively the relief valve that allows water from the lower delta to be pushed inland, and lack of these paths in the AU10 bathymetry causes the water to accumulate in the lower delta. These results indicate the overall importance of the small channels in the flow physics. Despite their small size, they have a visible effect on the inundation patterns.

Figure 32 shows the modeled salinity using the MA10 bathymetry. Tidally-driven transport into the Trinity Delta is clearly observed. The lower part of the delta experiences relatively significant dispersion and mixing. In the upper part of the delta, the salinity field varied more slowly. Freshwater in the upstream river pushes both downstream and into the delta through upstream channels.

Figure 33 shows the modeled salinity for the AU10 simulation. A major difference between the MA10 and AU10 simulations is the downstream extent of freshwater, which is significantly further in the AU10 bathymetry. This result is consistent with the surface elevation results, where the lack of connectivity to small channels in the upper delta allows higher water elevations in the main river channel upstream, which leads to a more significant surface gradient that drives freshwater further downstream in the main channel. However, it is difficult to draw conclusions from these comparisons as a non-conservation warning for scalar concentrations was produced in the simulation with AU10 bathymetry. The precise reason for conservation failure is not yet known, but is likely due to incompatibility between the Frehd scalar limiter and the MPI algorithm, which requires further investigation.

These preliminary model results indicate that the different bathymetry processing techniques have a significant impact on transport within the delta. Specifically, the complex narrow channel network in the mid-to-upper delta receives and stores a significant volume of water, and neglecting these volumes can lead to overpredicted surface water elevation in the lower delta. Correctly representing both the surface connectivities and overall volumes of these channels is thus important and is a challenge to the lidar data processing techniques and the coarsening of the bathymetry to produce a computationally-practical model.

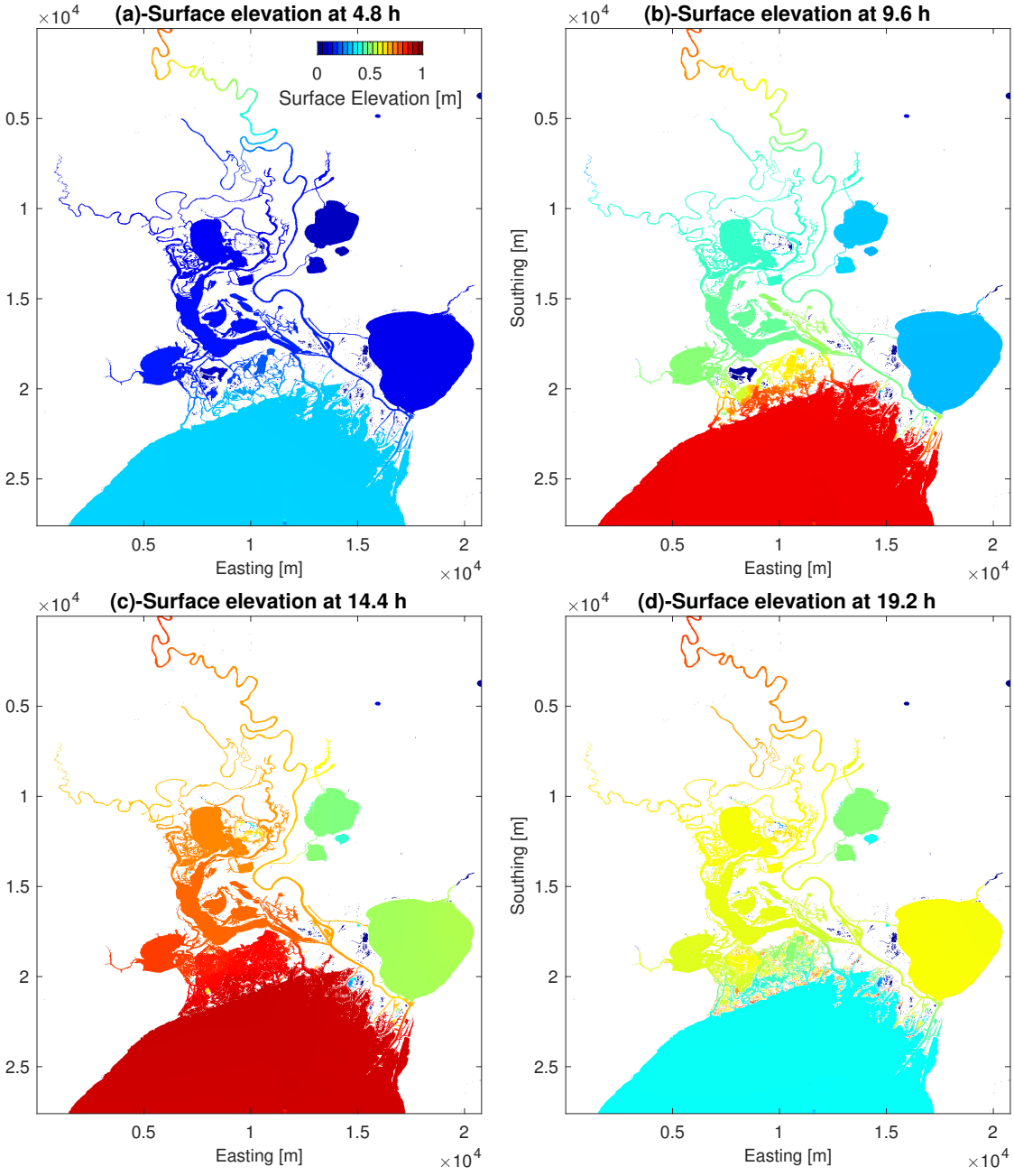

Figure 30: Modeled surface elevation for the MA10 bathymetry at 4.8, 9.6, 14.4 and 19.2 hours after model starts, which corresponds to 20%, 40%, 60% and 80% of the total simulation time.

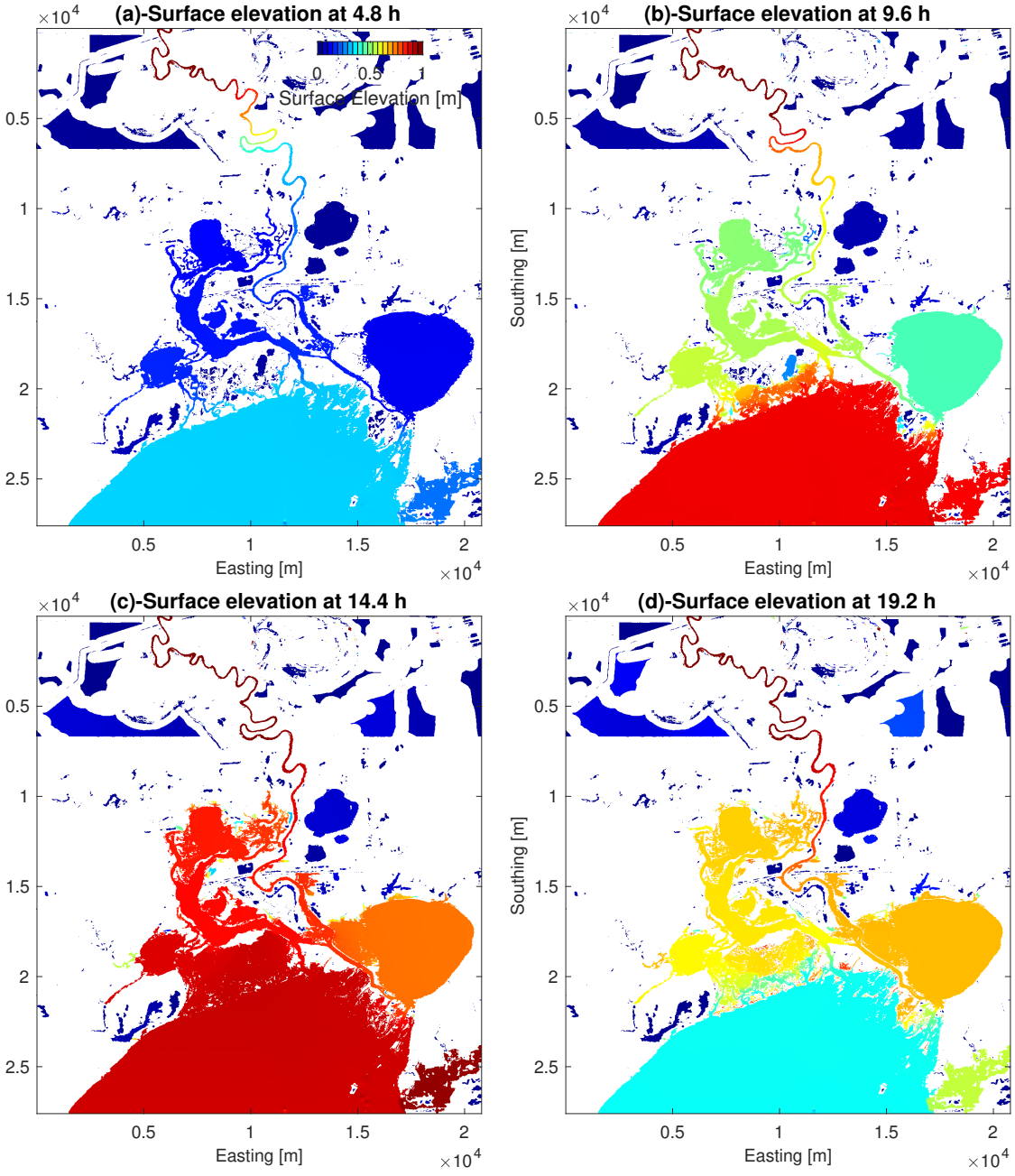

Figure 31: Modeled surface elevation for the AU10 bathymetry at 4.8, 9.6, 14.4 and 19.2 hours after model starts, which corresponds to 20%, 40%, 60% and 80% of the total simulation time.

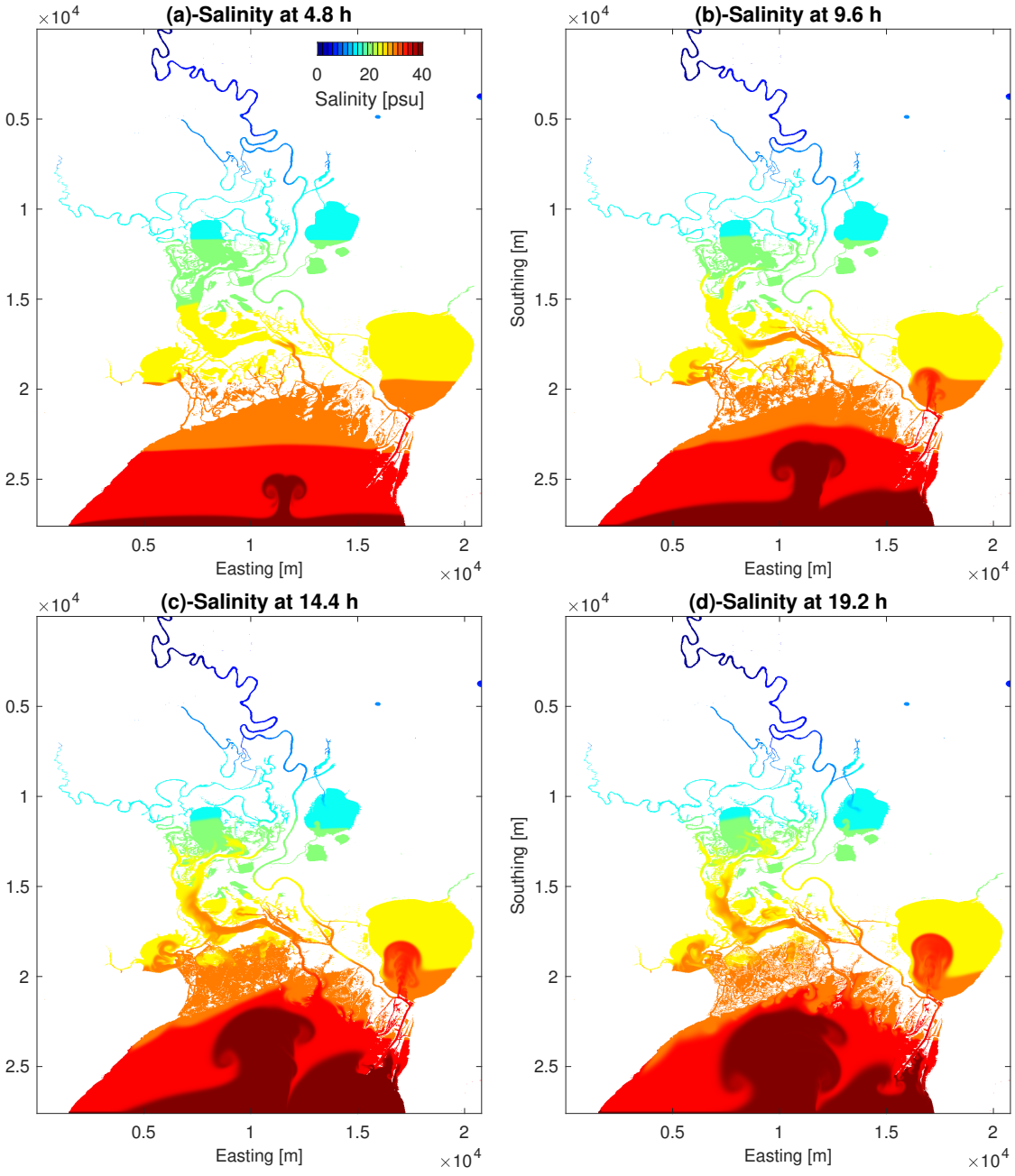

Figure 32: Modeled salinity for the MA10 bathymetry at 4.8, 9.6, 14.4 and 19.2 hours after model starts.

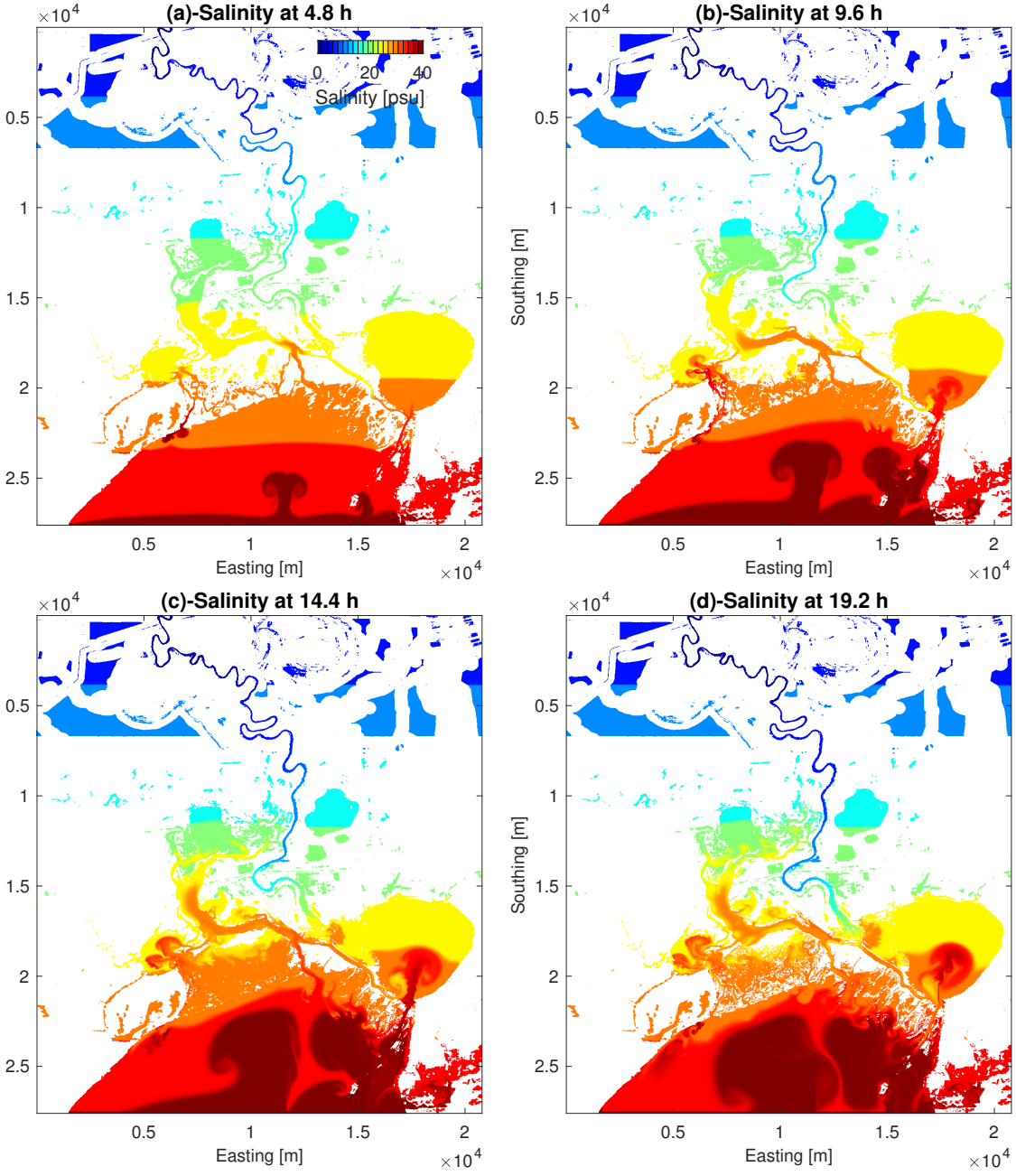

Figure 33: Modeled salinity for the AU10 bathymetry at 4.8, 9.6, 14.4 and 19.2 hours after model starts.

B.5 Summary and future tasks

This project developed a bathymetric model for the Trinity Delta using the best-available data at 1×1 m resolution. A hydrodynamic model of the delta at 10×10 m grid resolution has been developed and tested. Preliminary results show that the bathymetric representation of small-channel connectivity and volume in the middle-to-upper delta may significantly influence the simulated water surface elevations and transport in the delta. Correctly representing these channels in the model remains a challenge because (i) the model runs on a 10×10 m grid, which overestimates some channels and cannot represent others, and (ii) the *FEMA* lidar datasets do not include reliable bathymetry in any of the submerged areas, including the small channels. Methods to better represent the effects of small channels at coarse grid scales are presently being developed.

Translating lidar topography into an adequate model bathymetry for a river delta is a complex task that requires judgement of the analyst and some manual adjustments. Automated approaches that assist in this effort and reduce the amount of manual processing have been developed herein, but as yet these cannot be entirely relied on to discriminate between submerged and unsubmerged topography in the *FEMA* lidar data. A key roadblock to automated analyses is the quality of the satellite photographs used for image discrimination. It is likely that higher quality and/or multi-spectrum images could be effectively used for improving the processing. However, no amount of processing can overcome the lack of adequate data in the submerged portions of the system.

Extending the present model to represent a particular simulation period will require more extensive data for calibration, validation, and boundary conditions. The prior TWDB deployment of CTD (conductivity, temperature and depth) sensors across wide swaths of the Nueces River Delta (Schoenbaechler, Negusse, & Guthrie, 2014) is a prototype for the type of deployment needed in the Trinity Delta. However, it should be noted that fluxes of near-surface groundwater across the Trinity Delta are likely to affect the total water storage, residence time, and surface-water flows through the system. The *FrehdC* model does not presently include groundwater storage/flux computations, although this feature could be readily added. More challenging than adding the groundwater fluxes to the model is the effort required for collecting adequate data to calibrate and validate groundwater effects.

C Model instability and channel connectivity for 2D coastal marsh simulations

For the convenience of the reader, the following appendix provides the text and figures for portions of this study that were published in Z. Li and Hodges (2019b). Modifications have been made for consistent cross-references as an appendix to the present report. Note that the model development documented in this paper used the Nueces Delta as a test case rather than the Trinity Delta due to the availability of field data in the former. The model developments tested on the Nueces Delta were incorporated into the TDHM.

Article Title: **Model instability and channel connectivity for 2D coastal marsh simulations**

Authors: Zhi Li, Ben R. Hodges

Published in:
Environmental Fluid Mechanics
19:1309-1338 (2019)
https://doi.org/10.1007/s10652-018-9623-7

Abstract

Reduced freshwater inflow into a coastal marsh can result in environmental stress through episodic hypersalinity. Hydrodynamic models can be used to evaluate salinity-control strategies when freshwater supplies are constrained by climate or increasing urban demands. However, there remain significant scientific, engineering, and technical barriers to correctly modeling salinity transport in such systems. In particular, the numerical instability at the wetting/drying front caused by strong wind stress and steep surface gradient and the inappropriate representation of the complex channels at practical computational scales are unsolved problems. This study documents recent achievements in modeling the time-space evolution of shallow marsh salinity using the Fine Resolution Environmental Hydrodynamic model (Frehd) applied to the Nueces River Delta (Texas, USA). The 2D depth-integrated model is tested across a variety of bathymetric representations derived from high-resolution lidar data to evaluate the effects of grid refinement and a variety of bathymetry processing methods. Novel treatments are proposed and tested to suppress unrealistic velocities and scalar concentrations caused by rapid wetting/drying and strong wind stress. The model results are compared with the field data collected at 12 spatially-distributed locations across the marsh, yielding good model-data agreements for free surface elevation and reasonable agreements for salinity. Analyses of results indicate that the critical difficulty for capturing salinity transport is in correctly representing connectivity effects (both blocking and channel features) at fine scales on the coarse grid without overestimating fluxes. Modeled water surface elevations are relatively robust to poor representation of connectivity whereas the salinity distribution is strongly affected, particularly at key choke points. This study defines a set of future challenges in developing automated methods for evaluating and preserving geometric connectivity at practical model grid resolution.

Acknowledgements

This work has been supported by the Texas Water Development Board under interagency cooperation contracts 1400011719 and 1600011928. Field work was conducted by the TWDB with funding from the US Army Corps of Engineers.

C.1 Introduction

Hydrologic modification of river flows and sea level rise are combined threats to the viability of many freshwater/saltwater marsh ecosystems (e.g. Herbert et al., 2015; Snedden, Cretini, & Patton, 2015; Watson et al., 2016). Both effects push upstream the salt/fresh mixing zones, often into narrower, confined areas with inhospitable geomorphology of steeper gradients and incised channels. Marsh systems are critical for many estuarine and coastal species that have limited salinity tolerance as juveniles, so the upstream migration and reduction in brackish marsh areas will potentially reduce nursery habit and impact the ecosystem balance both offshore and within the estuary itself. Understanding and quantifying the salinity exchange in these systems with field data alone is difficult due to the myriad of flow pathways, which necessarily requires numerous sensors distributed widely

over the marsh that are emplaced for months to years. Numerical models thus become popular tools aiding in marsh salinity research.

The present work is motivated by difficulties encountered in modeling salinity transport in a shallow marsh, the Nueces River Delta (Texas, USA). This shallow marshland (with depth on the order of 1 m) is located northwest of Nueces Bay, an extension of Corpus Christi Bay along the Texas coast (Fig. 34). The main channel through the marshes and down to Nueces Bay is known as the Rincon Bayou, which was separated from the Nueces River main stem. Because Nueces Bay is micro-tidal (typical daily range of 0.3 m), the tidal flux into the delta is insufficient to turn the marshland into a simple well-flushed saltwater system. Instead, the combination of limited freshwater inflows, poor tidal flushing, and high evaporation rates results in inverse estuary effects that have caused episodic hypersalinity in the upper marsh (Alexander & Dunton, 2002). Infrastructure efforts to improve freshwater flushing (see Fig. 34) have included physically modifying connectivity of the system with the Nueces Overflow Channel (NOC), the Rincon Bayou Overflow Channel (ROC) and directly pumping freshwater into the delta through the Rincon Bayou Pipeline (Hill, Tunnell, & Nicolau, 2015). The pumping system is an unusual step in marsh restoration, and is capable of delivering 3.7×10^6 m^3 d^{-1} (3000 ac-ft per day) of freshwater from just upstream of the Calallen dam (Fig. 34) on the Nueces main stem to the upper end of the Rincon Bayou. Field studies show that the pumping system is effective in flushing hypersalinity through the main channels of the Rincon Bayou (Del Rosario & Montagna, 2018; Hill et al., 2015). However, there remain open questions as to the best flow rates, pumping durations, and event timing to optimize the effect of the fresh water available that have to be answered with the assistance of numerical modeling.

Numerical models for coastal marshes require three increasingly challenging levels of reliability: (i) the model must be numerically stable, (ii) the surface flux connectivity should be reasonably represented, and (iii) the net salinity transport should provide residence time and salinity distributions that are statistically similar to observations. In deep estuaries with limited wetting/drying, model stability and path connectivity requirements are often easily satisfied, so research has focused on the third requirement (e.g., studies on residence time Silva, Marti, and Imberger (2014), tidal intrusion Ralston, Geyer, and Lerczak (2010), turbulence closures and high-order schemes Chua and Fringer (2011)). However, for shallow coastal marshes with frequent wetting/drying the first two requirements are challenging in themselves. In terms of model stability, it is well-recognized that modeling the wetting/drying of marshland can affect the maximum size of the stable time step and hence the practicality of a model (Ip et al., 1998; Murillo, Garcia-Navarro, & Burguete, 2009). We have also identified (as discussed herein) a range of other issues that affect model stability including the interaction of small depths (which cannot be neglected in a marsh) and wind-driven fluxes that send conventional modeling algorithms unstable or produce unrealistic velocities unless extraordinarily small time steps are taken. As to connectivity, it has been demonstrated that it is a non-trivial task to produce a bathymetry at a practical modeling resolution (e.g., 15×15 m) that maintains the continuity of blocking features (e.g., levees) that are evident at 1×1 m lidar data (Hodges, 2015). This idea is extended to the challenges of representing channels, or in general any small but hydraulically important topographical feature that might not be fully captured by the model grid. Failure to correctly capture the channels and blockages can interrupt surface connectivity and to completely different hydrodynamic behaviors (Cea & French, 2012; Torres & Styles, 2007; Wang et al., 2009).

With reference to the three requirements of coastal marsh models discussed above, the focus of the present work is in developing practical approaches for handling the model stability and system connectivity problems with salinity transport used as a means of evaluating the effectiveness of the methods. We use a high-resolution hydrodynamic model for the Nueces Delta to demonstrate the efficacy of our new methods and evaluate how spatial resolution affects the model results. This system was selected because of its importance in a real-world water management problem and the availability of a data set with 15 months of salinity and depth measurements at broadly-distributed locations (Schoenbaechler et al., 2014).

The modeling methods used herein are presented in §C.2, including a brief introduction of the Frehd hydrodynamic and transport model (§C.2.2). The approach to wetting/drying is found in §C.2.4; a novel method for wind-driven thin-layer flows is found in §C.2.5 and approaches to handle bathymetric connectivity at various scales are presented in §C.2.8. These specific issues are often given little attention in the numerical literature when a model is presented, but are critical to the performance in modeling marsh systems. The model setup for the Nueces Delta test case is illustrated in §C.3, which includes descriptions of the field-data collection (§C.3.1) as well as the tested model

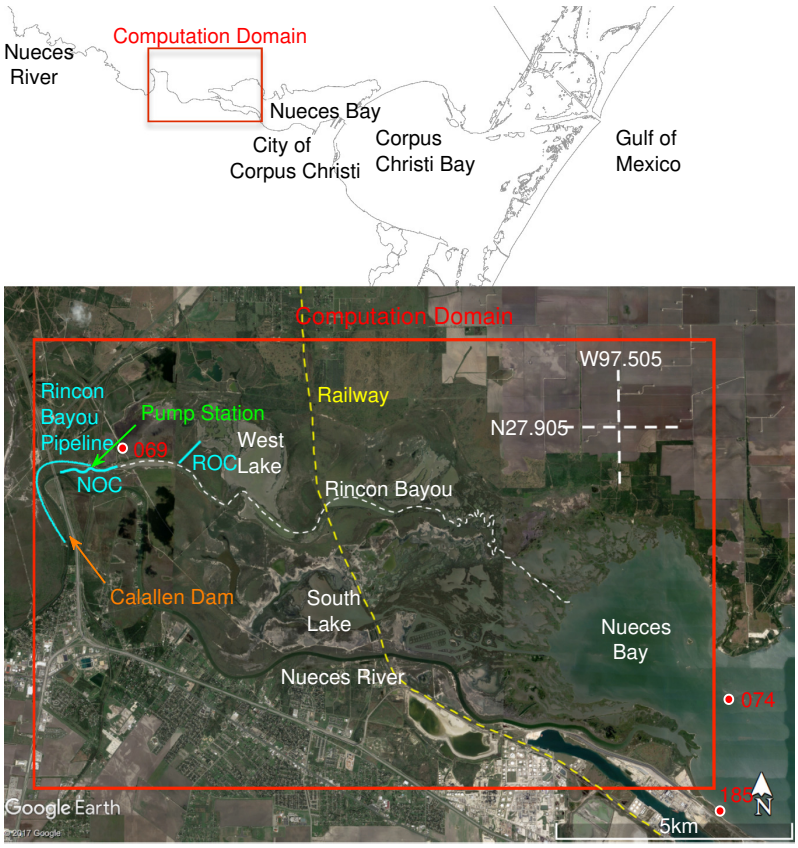

Figure 34: Nueces Delta study site with locations of the Rincon Overflow Channel (ROC), Nueces Overflow Channel (NOC) and Rincon Bay Bayou Pipeline. Sites 069, 074, 185 are long-term monitoring stations. Note that West Lake and South Lake are actually periodically-inundated tidal flats rather than lakes. Texas coastline from ArcGIS online, satellite image from Google Earth.

scenarios with different conditions for stability treatment (§C.3.2), spatial resolution and channel delineation (§C.3.3). The simulation results are analyzed in §C.4 by comparing to extensive field observations across the delta. The major findings are summarized in the conclusion, §C.5. Minor aspects such as the model spin-up and calibration are presented in the Appendix.

C.2 Numerical Methods

C.2.1 Overview

This study uses a numerical model that is driven by and compared to a suite of observations of the delta and surroundings. The model is an updated version of the Nueces Delta Hydrodynamic Model (NDHM) (Ryan & Hodges, 2011). The NDHM is a 2D version of the 3D Fine Resolution Environmental Hydrodynamic Model, which we call "Frehd" for readability. This model is a descendent of TRIM (Casulli & Cattani, 1994) and ELCOM (Hodges et al., 2000) semi-implicit models with optional adaptions for 2nd-order accuracy (Hodges, 2004; Hodges & Rueda, 2008; Rueda et al., 2007), non-hydrostatic effects (Wadzuk & Hodges, 2009) and edge-blocking in complex topography (Hodges, 2015). A brief description of the model foundations is provided in §C.2.2.

In general, the semi-implicit numerical method is unconditionally linearly stable for any barotropic (wave speed) Courant-Friedrich-Lewy (CFL_B) number, and is conditionally stable in the advective CFL_A Casulli and Cattani (1994). Practical experience has shown that momentum stability is retained for $\mathrm{CFL}_A > 1$ in limited space-time locations as long as the the majority of the domain is at $\mathrm{CFL}_A < \sqrt{2}/2$ and care is taken with the nonlinear terms. The discrete scalar advection, Eq. (40), is an explicit finite-volume advance that strictly requires $\mathrm{CFL}_A < 1$ everywhere for both mass

conservation and stability. In general, the semi-implicit approach for momentum is robust to an occasional high-CFL$_A$ transient as the implicit free surface solution serves to damp and re-distribute effects of localized instabilities. Similarly, smaller perturbations of scalar concentrations caused by localized hydrodynamic instabilities can be neglected if they do not grow and scalar distributions remain within physical ranges. Unfortunately, the combination of thin layers, wind-driven flows, and wetting/drying across a marsh can lead to high velocities (both real and unreal) in a simulation that can develop into catastrophic instability. In our experience, trying to reduce the global time step to maintain stability in a high-resolution marsh simulation results in absurdly small time steps that are simply impractical for the seasonal-to-annual time frames that are of interest. We have investigated approaches to using local subtime-stepping in lakes (Hodges, 2014) and broader estuaries (Hajduk et al., 2018) but to date have not been able to efficiently implement these approaches in the coastal marsh simulations. In the present work we focus on measures to identify and address the causes of instabilities rather than refining the time step to resolve the flow. Our philosophical argument for this approach is that resolving the flow associated with instabilities in a marsh is of little importance given their localized time/space locations – especially in consideration of the uncertainty and approximations of the system geometry at practical model grid scales. Thus, we seek methods to prevent instabilities by constraining the solution with physically plausible bounds. We have identified three key sources of instability and developed measure to address each: (i) instability caused by flow reversal, §C.2.3, (ii) instability due to wetting/drying §C.2.4, and (iii) instability due to wind-driven thin layers §C.2.5. These measures are necessary, but not entirely sufficient to ensure stable solutions, so we have added an *ad hoc* approach to truncating nonlinear terms (§C.2.6) to prevent a locally-high CFL from being propagated forward in time.

Simulating system connectivity in a channelized marsh is an interesting challenge as we often have finer-resolution digital elevation models (e.g., lidar) than we can practically represent in a simulation. The relative coarseness of the mesh has implications for the advective discretization, which can be readily solved as discussed in §C.2.7. More difficult is ensuring that a (relatively) coarse model mesh has a reasonable representation of the channel connectivity, flow areas, and blockages – i.e., a question of upscaling to maintain hydrodynamics and transport. In §C.2.8 we apply a concept of positive and negative objects that can be identified and modeled with automated processes. This approach provides some success, as discussed in §C.4, but there remains a number of outstanding issues (see §C.5).

C.2.2 Model foundations

The NDHM is a semi-implicit, volume-conservative implementation of the depth-integrated, hydrostatic Navier-Stokes (shallow water) equations on a rectilinear (structured) Cartesian grid. Momentum is:

$$\frac{\partial u_j}{\partial t} + u_k \frac{\partial u_j}{\partial x_k} = -g\frac{\partial \eta}{\partial x_j} + \frac{\partial}{\partial x_k}\left(\nu \frac{\partial u_j}{\partial x_k}\right) + \frac{\tau_{wj} - \tau_{bj}}{\rho h}, \quad : \quad j,k \in \{1,2\} \tag{38}$$

where η is the free surface elevation, u_j are depth-averaged velocities, x_j are the corresponding Cartesian axes, h is the depth, ρ is the local density, ν is an eddy viscosity, and τ_{wj}, τ_{bj} are the wind and bottom stress boundary conditions in the x_j direction. Note that the discretization of the boundary stresses has effects on model stability, as discussed in §C.2.3, below.

For Eq. 38, the depth at a grid cell center is defined as $h = \eta - b$, where b is the local bottom elevation above a baseline (herein NAVD88). Although Frehd includes governing equations for 3D flow and baroclinic forcing, herein the depth-integrated effect of salinity on density is neglected as it does not significantly contribute to advective fluxes in a shallow marsh. The momentum equations are closed by the depth-integration of the kinematic boundary condition applied to continuity (Casulli, 1999), resulting in

$$\frac{\partial \eta}{\partial t} + \frac{\partial h u_k}{\partial x_k} = 0 \tag{39}$$

Salinity transport is modeled with a standard advection-diffusion equation for incompressible flow:

$$\frac{\partial C}{\partial t} + u_k \frac{\partial C}{\partial x_k} = \frac{\partial}{\partial x_k}\left(\kappa \frac{\partial C}{\partial x_k}\right) \tag{40}$$

where C is the salt concentration (kg/m^3) and κ is the turbulent diffusivity. Although the baseline Frehd model includes a variety of turbulence closures, for simplicity the NDHM uses a uniform, constant, small value of $\nu = 10^{-4} m^2/s$. This simplification is reasonable where numerical diffusion associated with low-order advection scheme (see §C.2.7) provides significant horizontal mixing (Gross et al., 1999; Wang et al., 2009). Furthermore, for shallow estuaries, fluxes could be controlled by bottom stress and topographical restrictions rather than horizontal shear in the velocity field. In keeping with this simple approach, for the salinity we use $\kappa = \nu$, which is equivalent to setting the turbulent Schmidt number to unity.

Frehd follows the approach of Casulli (1990) in using uniform Cartesian grid cells with an Arakawa-C stencil where the governing equations are solved for velocities on cell faces whereas surface elevations and scalar concentrations are solved on cell centers. The bathymetry is represented as a standard "z-level" system where the bottom elevation at the cell center is considered a uniform value across the entire cell. A finite-volume formulation is used in continuity (Eq. 39) and scalar transport (Eq. 40) so that volume and scalar mass are conserved to numerical precision (the latter as long as $\mathrm{CFL}_A < 1$). The advection terms are finite-difference discretizations, so the overall method is a hybrid finite difference/volume approach. The details of the Frehd discretization are similar to the semi-implicit approach described in Casulli (1990) and Casulli and Cattani (1994), except where otherwise noted herein.

Frehd includes several choices for nonlinear terms in advection, Eq. (38), and scalar transport, Eq. (40). The choice of discretization is inherently tied to the bathymetric resolution, and is discussed in §C.2.7, below. The diffusion terms for momentum and scalar diffusivity are discretized with central difference stencils.

For time-marching, Frehd offers the choice of the standard semi-implicit "theta method" (Casulli & Cattani, 1994) that is almost (but not quite) 2nd-order accurate (Hodges, 2004), or a predictor-corrector method that is fully 2nd-order (Hodges & Rueda, 2008). In keeping with 1st-order upwind scheme (see §C.2.7), herein we use a simple 1st-order $\theta = 1$ method, which is a 3-step method consisting of (1) a non-conservative, explicit-Euler approximation of the velocity time advance, (2) an implicit solution of the free surface elevation (continuity) time advance, and (3) a finite-volume correction of the velocity field to ensure flux conservation, stability, and consistency with continuity (Gross et al., 2002).

C.2.3 Stability and flow reversals

As is common in shallow-water models, we model the bottom stresses with a standard drag relationship such that the stress in the x_j direction is

$$\tau_{bj} = \frac{1}{2} C_D \, \rho u_j \sqrt{u_1^2 + u_2^2} \quad : \quad j \in \{1, 2\} \tag{41}$$

where C_D is a drag coefficient. The wind stress in the direction of the wind is modeled as

$$\tau_w = C_{D(w10)} \, \rho_a \left(\vec{U}_{w10} - \vec{U}_\eta \cos\beta \right)^2 \tag{42}$$

where $\vec{U}_{w10}$ is the wind speed measured at 10 m above the surface, $\vec{U}_\eta$ is the water speed at the surface, β is the angle between the wind direction and the water direction, $C_{D(w10)}$ is a drag coefficient based on the 10 m wind measurement height, and ρ_a is the air density. The wind drag in the x_1 and x_2 directions is found from

$$\tau_{w1} \quad = \tau_w \cos\omega \qquad \tau_{w2} \quad = \tau_w \sin\omega \tag{43}$$

where ω is the angle from the x_1 axis to the wind direction.

One of the issues that does not seem to be addressed in the literature is the destabilizing effect that boundary stresses can have in a reversing flow. In the semi-implicit momentum solution of Casulli (1990) the boundary stresses are defined in terms of the time n values, which implies that the drag between time n and $n + 1$ steps in the implicit solution must oppose the time n flow direction. However, when the flow reverses direction during a time step the explicit drag is effectively an input of momentum, which is destabilizing (i.e., it does not oppose the time $n + 1$ flow direction and is hence anti-dissipative). Although this problem is unlikely to lead to catastrophic instability in simulations of a large-scale estuarine flow where reversals have a long time-scale, it can be a

vexing issue in a shallow, wind-driven marsh where reversals are small in spatial-scale and short in time-scale. To fix this problem, the bottom drag term is time-linearized and solved implicitly as part of the free-surface solution. Specifically, the bottom drag term in Eq. (38) is represented as

$$\frac{\tau_{bj}}{\rho h} = \frac{C_D\, u_j^{n+1} \left([u_1^n]^2 + [u_2^n]^2 \right)^{1/2}}{2h^n} \quad : \quad j \in \{1, 2\} \tag{44}$$

where n superscripts indicate data at the known time level and $n+1$ superscripts are the unknown solution time level. This approach is similar to time-linearization ideas developed by Patankar (Burchard et al., 2003; Patankar, 1980). Time-linearization ensures that the bottom drag is always in opposition to the velocity direction at time $n+1$ by moving the drag term from the $\mathbf{b}$ side of $\mathbf{Ax} = \mathbf{b}$ to the $\mathbf{A}$ side in the matrix inversion step of the semi-implicit method (see Casulli (1990) for further details of the semi-implicit matrix). This approach guarantees the net effect of drag term is *always* in opposition to the time $n+1$ velocity and thus is always dissipative. Note that simply discretizing drag as an implicit term without this time-linearization is possible, but it creates a nonlinear term of $\left(u^{n+1}\right)^2$ that destroys the simple linear solution technique at the heart of the semi-implicit method (Casulli, 1990). Failure to use implicit drag discretization can destabilize the solution during flow reversals, which is a particular problem for wind-driven flows in a marsh.

C.2.4 Wetting and drying

Wetting and drying of tidal flats is always a challenge for numerical modeling and has a wide literature (e.g., Candy, 2017; Martins et al., 2018; Medeiros & Hagen, 2013; Teng et al., 2017). Wetting/drying methods are typically somewhat *ad hoc* and related to the underlying numerical discretization techniques. In the semi-implicit approach, dry cells do not cause instability as they simply imply $\eta^{n+1} = \eta^n = b$ if there are no fluxes into a cell (R. T. Cheng et al., 1993). However, a wetting/drying challenge for the semi-implicit theta-method is that the theory (Casulli & Cattani, 1994) does not constrain the implicit solution of η relative to the bottom elevation b, so it is entirely possible to have a time step where a wet grid cell starting with $\eta^n > b$ will end with $\eta^{n+1} < b$. This unphysical condition is typically remedied with an *ad hoc* clamping of $\eta^{n+1} = b$ to create a dry cell. Unfortunately, as the original solution of $\eta^{n+1} < b$ is volume conservative, such clamping inherently causes non-conservation of volume, which cascades to non-conservation of scalars.

A related problem is that real-world wetting/drying involves thin layers where the flow is strongly affected by the local bottom slope; however, the z-level grid system only represents the dynamic effects of the larger-scale bottom slope between grid cells and does not directly consider the volume effects of the slope within a grid cell itself. Thus, during the model drying process a rapid drawdown can create the conditions shown in Fig. 35 where water on the upstream tidal flats has a dramatically different free surface elevation. If the free surface gradient between the two cells is used as the momentum source for the flow (as in the standard solution algorithm), then extreme unrealistic velocities are produced. The result is typically $\eta^{n+1} < b$ in the next time step and a large loss of conservation. We solve this problem through an *ad hoc* approach that treats the flow from the upland as though it is similar to flow over weir (Tracy, 1957) where the velocity is given by

$$u_f = C_f \sqrt{2gh_f} \tag{45}$$

where u_f is the velocity across the cell face, C_f is an empirical coefficient (herein 0.7) and h_f is the water depth at the face. The u_f computed from time n data can be used directly in the discretization of the free surface evolution (removing the dependency on the free surface pressure gradient across the face), which ensures that the velocity remains limited to physically reasonable values and the drying step to $\eta < b$, if it occurs, will be small.

Rapid wetting can cause a problem similar to rapid drying. For efficient computation of scalar transport, wetting should ideally occur with a wet/dry front that moves less than Δx in a time step (i.e., wetting only dry cells that are adjacent to wet cells), otherwise, the scalar computation must be subtime-stepped to ensure stability. However, the semi-implicit method is stable for $\text{CFL}_B > 1$, which implies that water can appear in a dry cell that is *not* adjacent to the wet/dry front. These non-adjacent wetting cells typically have very thin layers containing little volume or scalar mass, so the simplest *ad hoc* approach is to maintain these cells as dry until the wet/dry front moves adjacent, which is accomplished with a $\text{CFL}_A < 1$ limiter for movement of the wet/dry front. This approach

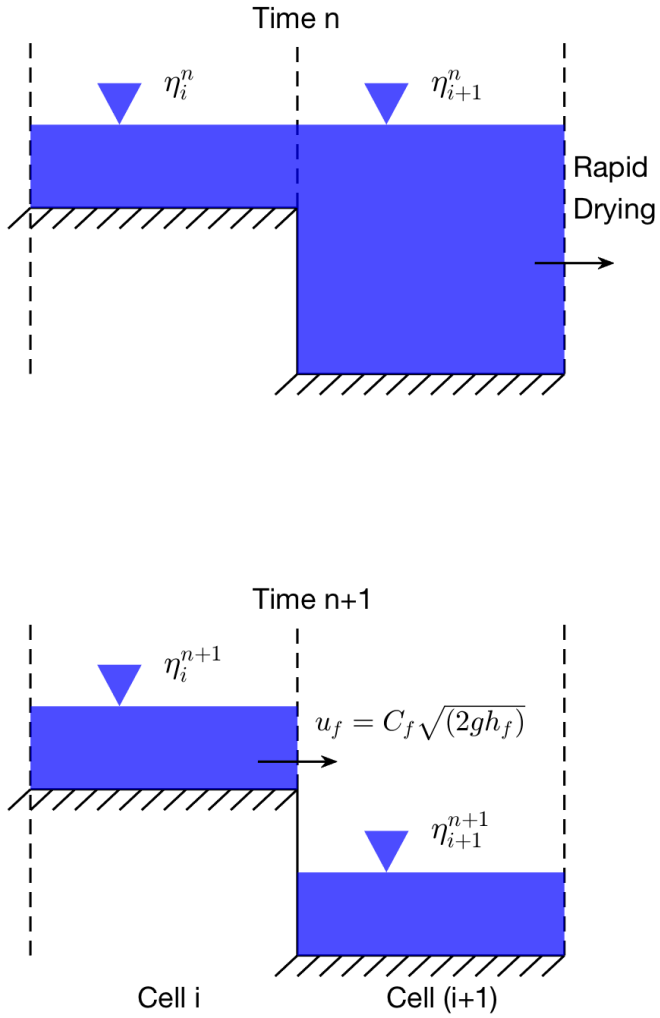

Figure 35: Rapid drawdown from (a) to (b) leaves water volumes in the uplands with a large driving pressure gradient. In (b), the steep surface gradient $\eta_i^{n+1} - \eta_{i+1}^{n+1}$ could cause unrealistically high velocity unless Eq. (45) is used to correct the velocity.

necessarily is non-conservative (similar to other aspects of wet/dry algorithms), but the volumes lost in the tested simulations are negligible.

Finally, to prevent wetting and drying from becoming a computational burden as $h \to 0$, we set a minimum depth such that $h < h_{min}$ results in $\eta = b$ and a small loss of volume. The present work uses $h_{min} = 10^{-3}$ m.

C.2.5 Thin layers and drag

As water layers get thinner, i.e., $h \to 0$, the bottom drag of Eq. (41) requires an increasing value of C_D to represent the nonlinearly-increasing drag as the flow evolves toward laminar. That is, a Reynolds number defined as $uh\nu^{-1}$ is expected to decrease as the layer thins and result in an increasing C_D (Bricker et al., 2005; Chao et al., 2008; Spitz & Klinck, 1998). We use a simple buffer layer approach for this problem, similar to Chou et al. (2015); Ip et al. (1998); Wang et al. (2009); Zheng et al. (2003). For our implementation, a drag buffer layer thickness (h_{bd}) is defined such that $h < h_{bd}$ provides a linearly-increasing drag from the standard value to a maximum value as $C_{D(b)} = (C_{Dmax} - C_D)\,(h_{bd} - h)\,h_{bd}^{-1}$. Herein the $C_{Dmax} = 1.0$ and $h_{bd} = 0.1$ m.

The wind acting on thin-layer flows creates further challenges. The empirical wind stress relationship of Eqs. (41) and (42) are based upon data where the wind and bottom boundary layers are effectively separated over a water column of some depth. However, for a sufficiently thin layer, both the wind-stress boundary layer and the bottom boundary layer will take up the entire water column, and simple linear superposition of their effects does not provide an adequate model of nonlinear interactions. That is, in the standard model the energy transfer from the wind is split between turbulent dissipation in the water column and acceleration of the near surface layer, but in a thin layer some portion of the wind effects are directly dissipated at the solid boundary. This issue is critical as simple superposition of standard bottom drag equations and wind-forcing models leads to absurd accelerations of thin-layer flows. To the best of our knowledge, this issue has not been discussed in the literature and there are no empirical data sets looking at the boundary layer interactions at the scales that are typical of tidal marshlands. Ideally, the τ_w model should be independent of the layer thickness and the τ_b model should account for the increased dissipation associated with the interaction of boundary layers. However, maintaining the standard τ_w and increasing τ_b requires a delicate balancing act otherwise the wind-driven velocity tends become unrealistically large. In the absence of data, we found the most practical approach was to provide an exponential decrease in the wind $C_{D(w10)}$ for water depths below a h_{bw}, which can be thought of as a wind buffer layer thickness – similar to but independent of h_{bd} for the drag. Formally we have $C_{D(wb)} = C_{D(w10)} \exp\left\{-\alpha\,(h_{bw} - h)\,h_{bw}^{-1}\right\}$ where α is a decay coefficient. For the present work we used $h_{bw} = 0.1$ m and $\alpha = 10$.

C.2.6 Instabilities and the nonlinear advection term

Incipient instabilities in a simulation typically appear as anomalously-large local velocities. In the time-marching algorithm, the nonlinear advection term typically amplifies the anomaly and propagates the instability to adjacent cells. Ideally, a model would never see such an anomaly or would reduce the time step to stabilize any anomaly. It seems generally impossible to ensure that a complex marsh model will be entirely free of instability, and reducing the model time step is simply impractical. Our solution is to sacrifice local fidelity of the discrete equations in order to suppress the growth incipient instabilities – we do this by limiting the nonlinear terms in the momentum solution. We define a nonlinear term limiter with a low cutoff (L_c) and a high cutoff (H_c). For a grid cell where $\text{CFL}_A > H_c$, the local nonlinear term is completely suppressed. For a cell where $L_c < \text{CFL}_A < H_c$, the discrete nonlinear terms are linearly reduced, i.e. for $N = u\partial u/\partial x$, the reduced nonlinear term is a simple linear decay over the cutoff range: $N_R = N\,(H_c - \text{CFL}_A)\,/\,(H_c - L_c)$. In the present work $L_c = 0.5$ and $H_c = 0.7$. The limiter ensures that the high CFL_A at a few points in space/time are not amplified by nonlinearity, which typically then allows the anomaly to be dissipated in the following free-surface solution.

C.2.7 Advection discretization and channel scales

In general, the literature deprecates the use of 1st-order upwind spatial discretization schemes as too diffusive for practical use. We agree with this philosophy in general, but in the specific application to 2D modeling of a channelized marshes we find higher-order schemes can distort the channel connectivity. Ideally, every channel in a marsh would be discretized by 8 or 10 grid cells across

its width, allowing development of horizontal boundary effects and a meaningful ability to use a 3rd-order upwind discretization stencil. As a practical matter, such a discretization would drive the grid mesh down to ~ 0.1 m, requiring a time step less than 10^{-2} seconds and an impractical (for today's computers) computational time for modeling months (or even days) of marsh hydrodynamics. Once we are forced to a relatively coarse mesh, as is common in many geophysical problems, we encounter practical difficulties in applying a higher-order upwind stencil. *Where a channel is represented with only one or two grid cells across its width and has convoluted S-turns along its length, a higher-order upwind stencil requires extensive exception handling to ensure that the selected scalar values represent the values in the channel and not in the nearby shallows.* Otherwise, the modeled scalar flux in the channel can be driven by out-of-channel values that are entirely unrealistic.

To illustrate this problem, consider Fig. 36 where an 180 m $\times$ 180 m area in the Nueces Delta at 30 m $\times$ 30 m resolution is presented (see §C.2.8 for further details). This area is divided into shallow (brown) and deep (blue) regions to illustrate typical marsh channels on a coarse mesh. It can be seen that the 1st-order upwind stencil (red dots) are guaranteed to include only in-channel values. In contrast, 3rd-order schemes (white circles) include values in shallow cells that are unlikely to represent either the correct momentum or salinity in the channel. An interpolation stencil in 2D with depth-dependent weighting for the nine upwind cells is a theoretical higher-order solution to this challenge. However, the key difficulty for a 2D stencil is that a channelized area requires extensive exception handling for blocked cell-edges, which will be computationally expensive.

An unfortunate consequence of the use of the 1st-order stencil is that numerical diffusion will be greater than the physical κ of Eq. (40) under most flow conditions. Thus, we expect the model to diffuse any sharp salinity gradients in the marsh, which must be considered in interpreting results.

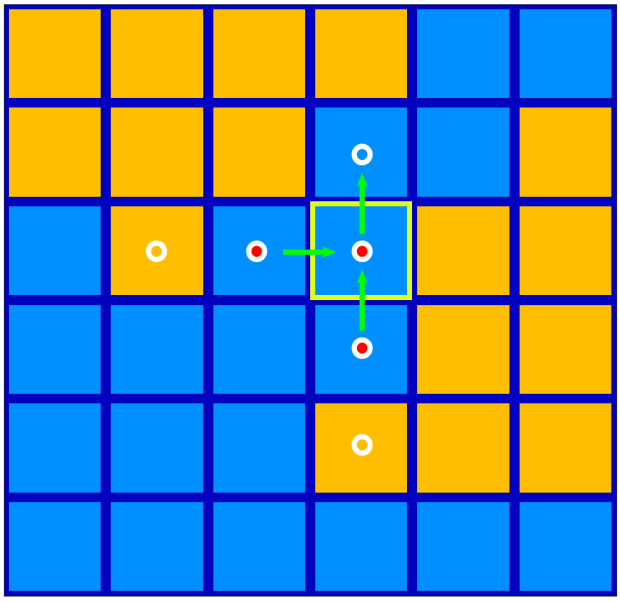

Figure 36: Stencils for 1st-order upwind (red dots) and 3rd-order upwind (white circles) schemes applied on one 30 $\times$ 30 m grid cell (yellow box). The region shown is the Nueces Delta at the intersection between the Rincon Bayou and the Rincon Overflow Channel (ROC) where brown indicates shallow areas whose scalar concentrations may be significantly disconnected from the deeper (blue) channels. The green arrows represent the major fluxes in/out of the target cell.

C.2.8 Bathymetry processing for connectivity

Creating an adequate bathymetry for a marsh requires trade-offs between structural accuracy and practical computability. Modeling directly using the 1×1 m resolution raster bathymetry available for the Nueces Delta is theoretically possible, but would require 7.5×10^7 grid cells and $\Delta t < 1$ s, i.e. more than 3.0×10^7 steps per year of simulation. With a numerical model using several hundred floating point operations per grid cell per time step, we would require $O(10^{18})$ floating point operations for a year of simulation. To achieve reasonable simulation times would require a supercomputer in the petaflop range. Although such computers exist, they are not yet readily available to the majority of the scientific community. Furthermore, for larger marsh and delta systems the computational scales required for such high-resolution modeling simply are beyond what we can presently handle.

For the present work, we developed up-scaled raster bathymetries at 15×15 m and 30×30 m grid resolution. The methodology follows the approach in Hodges (2015) using a median filter to create a coarse-grid raster and a fine-scale (1 m) representation of the resolvable "background" topography, as shown in Fig. 37(a) and (b). It is clear that the filtered bathymetry at the coarse-grid scale is missing connectivity at < 0 m elevation between two depressions in the marsh. The difference between the background topography and the original 1 m fine-resolution topography is used to identify contiguous objects that are not represented in the coarse-grid bathymetry but should have large-scale effects. These can be described as "positive" objects that represent blocking features higher than the coarse-grid bathymetry and "negative" objects that represent unresolved channels. The method for using positive objects to create "cell edge" features at the boundary between two raster cells is described in detail in Hodges (2015). A modification of this approach is used herein for negative objects, which are identified as channel grid cells with the bottom elevation adjusted from the median filter value to the median of the negative object. An additional step is taken to find locations where two channel cells are only diagonally connected (i.e. they do not share a common cell face). The bottom is adjusted in a cell perpendicular to the diagonal to create resolved channel bends that maintain connectivity.

The negative object method effectively takes any channel that is narrower than the model grid and broadens it to the grid scale to ensure connectivity. Clearly, this approach maintains connectivity at coarse-grid scales at the cost of physical fidelity in the channel cross-sectional area. To allow a balance between connectivity and fidelity, we ignore identified channels that take less than r fine grid cells in a coarse grid cell, where r is the grid-coarsening ratio (e.g. $r = 15 : 1$ for the 15×15 m grid developed from 1×1 m data). The result, shown in Fig. 37(c), improves the connectivity at the coarse grid scale compared to the median-filtered bathymetry of Fig. 37(b), but it is clear that some connectivity at < 0 m elevation has not been restored. Developing intelligent and robust automated approaches to ensuring good channel connectivity of fine-scale effects within the coarse model mesh remains an ongoing challenge. In the interim, we have identified key choke points in the marsh that are poorly resolved by the algorithm and restored connectivity by manually adjusting the coarse-grid elevations, as shown in Fig. 37(d). The complete 30×30 m bathymetry for the Nueces Delta computational domain is shown in Fig. 38.

C.3 Model Setup

C.3.1 Field data

Field data is used for both boundary conditions and calibration. Locations of long term data collection sites used for boundary conditions are shown in Fig. 34. We take the tidal forcing, wind forcing, and upstream pumping to be fundamental processes that are represented with the best available data and are not perturbed in the test cases. Tidal elevations are applied along the open boundary across the width of Nueces Bay on the east side of the domain in Fig. 38. The tidal data was obtained from Station 185 (Nueces Bay) in the Texas Coastal Ocean Observation Network (TCOON[4]), which is located on the south edge of Nueces Bay just outside the computational domain. Salinity data for tidal inflows used TCOON Station 074 (SALT03) which is approximately midway between the north and south shores of Nueces Bay and less than 1 km outside the computational boundary. Wind speed and direction data were obtained from measurements at TCOON Station 069 (Nueces Delta Weather Station). We applied spatially-uniform values for all boundary conditions as there are no available

[4] `https://cbiweb.tamucc.edu/TCOON/`

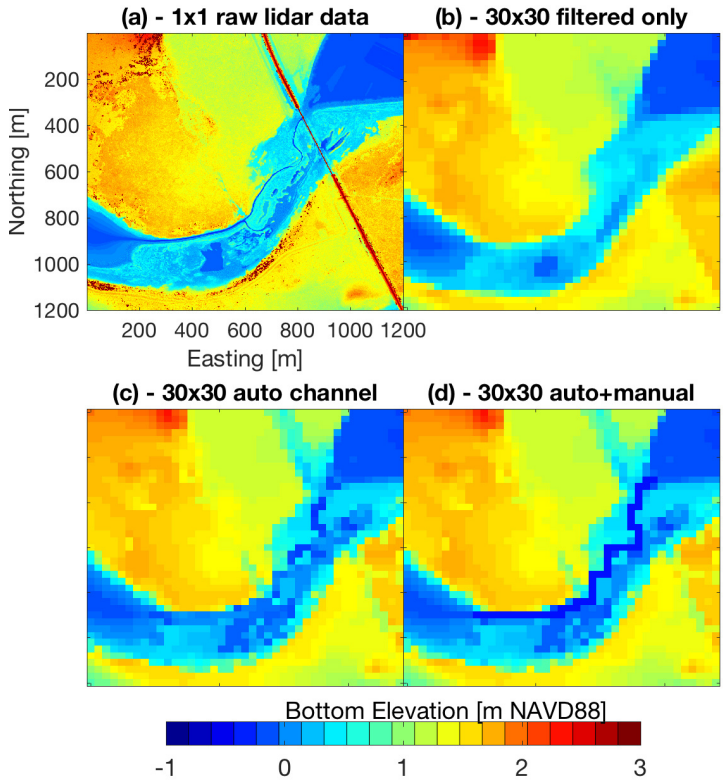

Figure 37: Bathymetry processing for small section of Nueces Delta: (a) 1 by 1 m lidar data; (b) median filter applied to create coarse grid; (c) after adding automatic channel algorithm; (d) addition of manual channel identification. ote that a narrow channel in the center of (a) is totally smoothed on (b). The surface connectivity is blocked. Only with the manual channel identification (d) we can reconstruct the surface connectivity.

data sources for spatial heterogeneity at the scales of the computational domain. The upstream boundary of the Rincon Bayou was modeled as a fixed water-blocking edge, which represents a swing gate separating the Bayou from the main stem of the Nueces River (Tunnell & Lloyd, 2011). Freshwater inflows were added as a volumetric source term with zero salinity at the pump outlet location (Fig. 34). The pump flow rates were obtained from the Nueces River Authority[5].

Texas Water Development Board (TWDB), with funding from the US Army Corps of Engineers, conducted a field campaign to measure salinity, water temperature, and water depth at 14 field monitoring stations in the Nueces Delta from August, 2012, through October, 2013. These stations are named Nueces1through Nueces14, with locations shown on Fig. 38. All sampling was with automated logging stations at 15 minute intervals. The water velocity was also measured with ADCPs at two locations in the delta, but these data were not used in the present study. Free-surface elevations (relative to NAVD88) were computed from the measured data by TWDB. The free-surface elevation and the salinity are used herein for model-data comparison. Note that field data measured at Nueces13 and Nueces14 have not been used herein as the data were not coherent with data from other stations. These sensors were along the same channel leading to Nueces12, so their data should have been very similar but showed unexplainable discrepancies. We believe that either these sensors malfunctioned or their placement was not correctly recorded in the metadata.

Analysis of field data (not shown) indicates that upstream salinities at all stations except Nueces1 are episodically higher than any salinities observed in Nueces Bay (station 185) over the course of the field study. The implication is that upstream hyper-salinities result from some combination of (i) direct evaporation from surface water, (ii) release of salt that has been concentrated in porewater

[5] http://www.nueces-ra.org/CP/CITY/rincon/

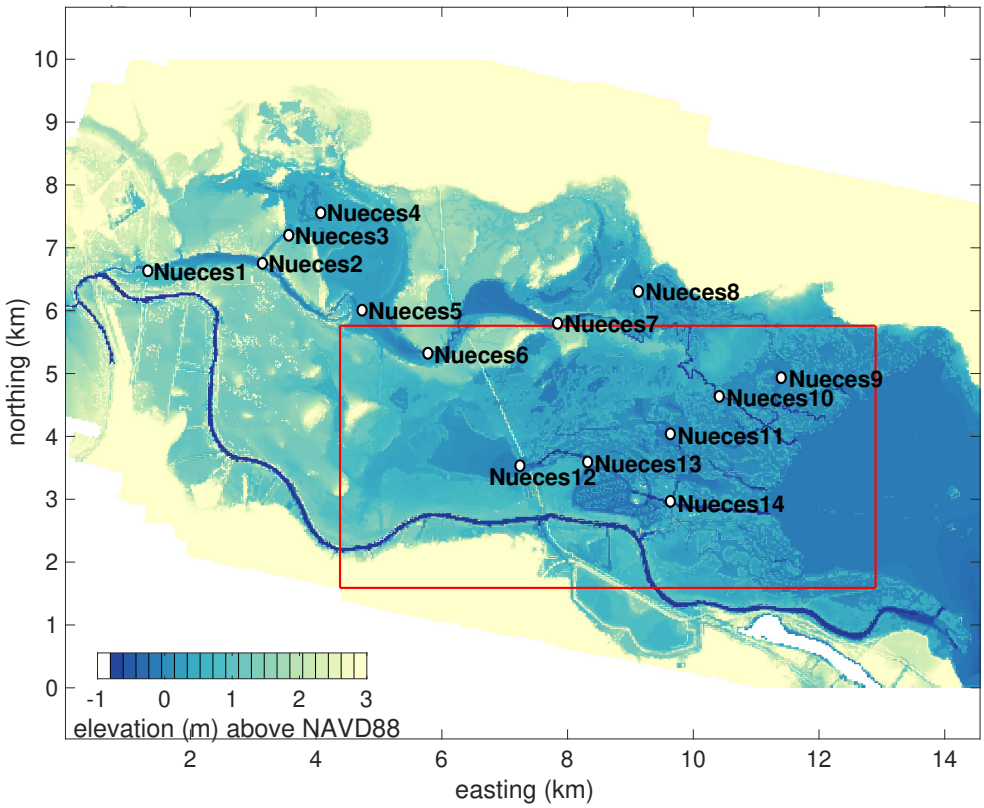

Figure 38: The 30 by 30 meters bathymetry used for NDHM. The locations of 14 field monitoring stations were labeled. More details of these stations can be found in §C.3.1. The red box is the computation domain for the stability test.

around plant roots by transpiration, or (iii) release of salt that is concentrated in the drying of episodically-flushed tidal flats. The complexities of these processes creates a modeling challenge. The development of porewater salinities through transpiration has been documented for the Nueces Delta (Stachelek & Dunton, 2013), but we do not have enough data to parameterize its scales or release rates across the landscape. Similarly, evaporation and salt storage in tidal flats is known to be an issue in other systems (Alvarez, Carol, & Dapena, 2015; Zhang, Li, & Lockington, 2014), but we do not have adequate data to evaluate whether it is significant in the Nueces Delta. The direct evaporation from surface water is arguably more tractable through the heat budget methods typically applied in coastal or lake/reservoir models (e.g. (Wunderlich, 1972)), but thin water layers in the marsh tends to develop unphysical temperature extrema due to the difficulty in adequately estimating the bottom reflection that limits the effective shortwave absorption. Furthermore, we found that modeling evaporation across the marsh with simple empirical formulas such as Penman's equation (McMahon, Peel, Lowe, Srikanthan, & McVicar, 2013; Penman, 1948) significantly overestimates salinity (results not shown). Given these complexities, evaluating evaporation models is reserved for future work, and the mismatch between model and observed hyper-salinities herein provides an indicator of these unknown and unmodeled processes. During our study period (Feb. 1, 2013 to Jun. 30 2013), precipitation had relatively insignificant effects on salinity (results not shown) and therefore is also neglected.

C.3.2 Stability test scenarios

To evaluate the performance of the novel stability treatments described from §C.2.3 to C.2.5, five model scenarios have been executed on a small section of the Nueces Delta bathymetry (shown as the red box in Fig. 38). Field tide and wind data measured at TCOON Station 185 and 069 were applied as boundary conditions. The initial salinity and the tidal salinity were both fixed to 35 psu, so a perfectly conservative model will have no salinity changes inside the domain. However, local

violation of $\text{CFL}_A > 1$ is expected to cause non-conservation of salinity. The reference scenario uses all the novel treaments to prevent possible instability and unrealistic salinity. The other four scenarios are executed by turning off one of the treatments at a time to examine if this treatment helps to maintain stability and conservation. The four treaments to be turned off are (1) the weir equation for rapid drawdown (§C.2.4, named *Drying*), (2) the CFL limiter for rapid wetting (§C.2.4, named *Wetting*), (3) the implicit treatment of the bottom drag term (§C.2.3, named *Drag*) and (4) the wind thin-layer model (§C.2.5, named *Wind*). These test scenarios are evaluated by estimating the total amount of salt lost as well as the mean CFL_A over the entire simulations. The salt loss is normalized (divided) by the loss in the reference simulation for ease of comparison. Note that the impacts of the tested treatments also depend on the bathymetry, boundary conditions and simulation configurations. To make sure all four treatments produce non-trivial results, we intentionally chose a large time step ($\Delta t = 120s$) such that even the reference simulation did not exactly conserve salinity. However, as shown in §C.4.1, the salt loss was orders of magnitudes greater in test cases without the stability treatments.

C.3.3 Full Nueces Delta test scenarios

A key goal of this paper is to quantify how different bathymetry processing methods affect the model skill in predicting surface water elevations and salinity distributions at practical grid resolutions for a coastal marsh. We have developed a suite of six scenarios using different grid resolutions and bathymetry processing techniques, as shown in Table 2. The baseline simulation (*A30*) uses all the bathymetric treatments at a grid resolution of 30×30 m, which allows for rapid simulations (approximately $20\times$real time on a desktop computer). The "no treatment" case with a 30×30 m grid (*N30*) uses only the median filtered bathymetry, e.g. Fig. 37(b). The 15×15 m cases (*A15, EC15*) were the smallest practical resolution for this study as they ran at only $2\times$real time. Pairwise comparison of scenarios, as listed in Table 3, allows us to distinguish between effects of different processing techniques. Because the designation of manual channels in *A30* and *A15* is inherently subjective, we decided to interpolate the manual channels from the *A30* bathymetry to the *A15* bathymetry to allow the effect of the grid resolution to be analyzed without introducing further manual intervention. The long-term *A30* simulation was analyzed from Feb. 1, 2013 to Jun. 30, 2013 to examine seasonal variation of the salinity. Other scenarios were modeled from Jun. 1, 2013 to Jun. 30, 2013, during which several pumping events occurred. The baseline model parameters for *A30* scenario are listed in Table 4. Issues of model spin-up and drag calibration are discussed in Appendices A and B, respectively.

Table 2: Description of test scenarios for different bathymetry processing methods

Label	grid size	cell edge	auto. channels	manual channels
A30	30m	Yes	Yes	Yes
N30	30m	No	No	No
C30	30m	No	Yes	No
EC30	30m	Yes	Yes	No
A15	15m	Yes	Yes	Yes
EC15	15m	Yes	Yes	No

Table 3: List of pairwise comparisons. The first column is the corresponding figure numbers showing the results.

Figure No.	Pairs compared	Interest of study
Fig. 41	*A30* : *EC30*	Effect of manual channels
	EC30 : *C30*	Effect of edges
	C30 : *N30*	Effect of auto channels
Fig. 45	*A30* : *A15*	Effect of grid refinement
	A15 : *EC15*	Effect of 15m manual channels

Table 4: Baseline model parameters

Parameter	Value	Description
$\Delta t[s]$	20	time step
$\Delta x[m]$	30	grid size
$\Delta y[m]$	30	grid size
$F[m]$	60	median filter size for grid coarsening
$dH[m]$	0.2	minimum object identification height Hodges (2015)
$\nu[m^2/s]$	0.0001	eddy viscosity
$\kappa[m^2/s]$	0.0001	eddy diffusivity
$h_{bw}, h_{bd}[m]$	0.1	thin layer model depth
C_D	0.01	bottom drag coefficient
C_{Dmax}	1	maximum drag coefficient in thin layer
α	10	decay rate of thin layer wind stress
$h_{min}[m]$	0.001	minimum depth allowed
C_f	0.7	weir coefficient
L_c	0.5	low cutoff for nonlinear term limiter
H_c	0.7	high cutoff for nonlinear term limiter

C.4 Results

C.4.1 Model stability

As the semi-implicit method with $\theta = 1$ is strongly dissipative of free-surface oscillations, none of the stability test simulations described in §C.3.2 cause the classic infinitely-increasing free surface oscillations that are the signature of catastrophic instability. However, local instabilities lead to non-conservation in the salinity field that can be readily analyzed. The normalized salt loss for the stability tests can be found in Fig. 39. All four tested treatments are needed for the model to maintain reasonable global salinity conservation. The reference simulation has an average loss of 0.003% of salt mass over the course of 5 simulation days, amounting to an average global change in salinity of less than 3.3×10^{-4} psu. Most notable in Fig. 39 is the dramatic effect of the *Drag* treatment that increases salinity non-conservation by more than six orders of magnitude. Analysis of the CFL_A over the course of the simulations, Table 5, indicates that the effect of switching from the implicit drag term (*Reference*) to the explicit drag term (*Drag*) causes large changes in the velocity field, which cascades to the non-conservation shown in Fig. 39. It can be seen that removing the *Drying*, *Wetting* and *Wind* treatments have smaller hydrodynamic effects, but still cause global salinity non-conservation increase of several orders of magnitude.

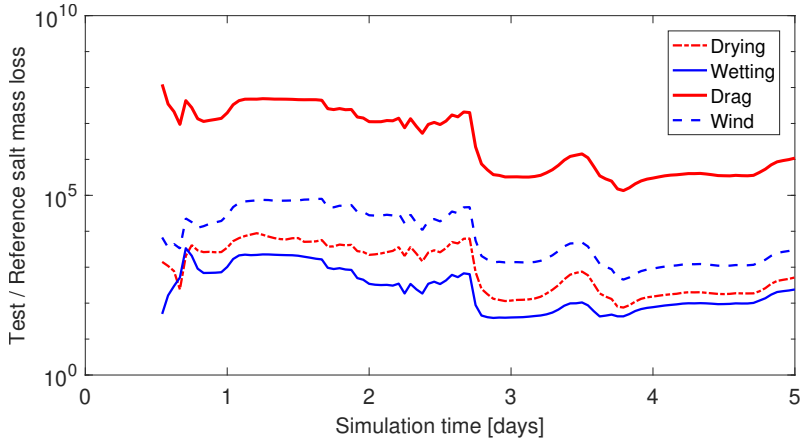

Figure 39: Ratio of total salt loss between tested scenarios and the reference scenario for five-day simulations.

Table 5: Time-average of spatial max, mean and standard deviation of CFL_A for five stability test scenarios

Scenario	Max.	Mean	Std. Deviation
Reference	1.5845	0.1392	0.1307
Drying	2.3956	0.1394	0.1319
Wetting	1.5846	0.1392	0.1307
Drag	261.2825	3.3215	18.6116
Wind	1.6790	0.1410	0.1308

C.4.2 Long-term modeling

The baseline long-term model results are provided by the *A30* case including all the bathymetric treatments. The daily-averaged model-data comparison of free surface elevation and salinity from Feb. 1, 2013 to Jun. 30, 2013 are shown in Fig. 40. For the free surface elevation (left column), the model and field data generally have good agreement. The agreement is excellent in most of the lower delta (Nueces9, Nueces10, Nueces12), which is expected due to proximity to the tidal boundary. At Nueces11 the model systematically overestimates free surface by a small amount. Although we generally hesitate to use model results to question field data, the good agreement at other stations in the lower delta indicates there is likely a bias in the field sensor vertical datum at Nueces11. The surface elevation agreements in the upper delta stations are not quite as good, but are still reasonable given the complexity of the marsh system. The largest error appears to be an underrepresentation of the water volume retained near Nueces2 between days 140 and 180, which includes pumping events (discussed below). These results likely indicate the model is allowing slightly greater flow rates out of the upper delta than observed in the field, a predictable consequence where the real flow path is narrower than that represented in the coarse-grid bathymetry. Note that blank areas in the field data indicate malfunctioning sensors.

The salinity results (right column in Fig. 40) show that the sudden drop in salinity due to pumping events is clearly captured at most upper delta stations. Hyper-salinity observed prior to pumping at Nueces3, Nueces4, and Nueces6 is not captured in the model, which can be explained by the neglect of evaporation etc. (as discussed in §C.3.1). At all other stations, model results are of similar scales as the field data, but with weaker oscillations. This smoothing effect is due to (i) numerical diffusion associated with the 1st order upwind scheme (Gross et al., 1999), and (ii) the use of the 30×30 m grid, which is not able to capture the subgrid scale features. We do not have a confirmed explanation for the anomalous sustained decline in observed salinity at Nueces10 between day 60 and day 80, which is neither captured in the model nor visible in nearby sensors Nueces8 and Nueces11. Overall, the model shows reasonable agreement in daily averages for both salinity and water surface elevations throughout the marsh for the baseline *A30* case. The increased discrepancies towards the upper delta indicate that bathymetry and surface connectivity have impact on model results as expected, which are investigated in §C.4.3 and §C.4.4.

C.4.3 Effects of bathymetry treatments

To compare the various bathymetry treatments we focus on a 30-day time frame (Jun. 1, 2013 to Jun. 30) and use hourly rather than daily-averaged data. The results for the *A30*, *EC30*, *C30* and *N30* scenarios are shown in Fig. 41. For the sites in the lower marsh (Nueces7 – Nueces12) and the first sensor in the Rincon Bayou upper marsh near the railroad dike (Nueces6), we see that only case *N30* (no treatment) has any substantial difference from the observed surface elevation. These results indicate that the critical requirement for obtaining the correct water surface elevation across the lower delta is the automatic channel identification, which is common to the *C30*, *EC30*, and *A30* cases. The no-treatment *N30* cannot capture the hourly hydrodynamics in the lower delta, but does provides a somewhat reasonable approximation of longer-term trends. In the upper marsh (Nueces1 – Nueces5) the *N30* case is again very poor and is, in many cases, simply flat-lined at the bottom elevation (i.e. no water). That is, the no-treatment condition of *N30* using a simple median filtered 30×30 bathymetry results in bottom elevations that are higher than the observed water at some of the sensor sites. Furthermore, the tidal oscillations are essentially lost in all the *N30* results, indicating that simple filtering to the coarse grid converts the channelized flow in the marshes into sheet flow that rapidly dissipates the tidal energy in the model.

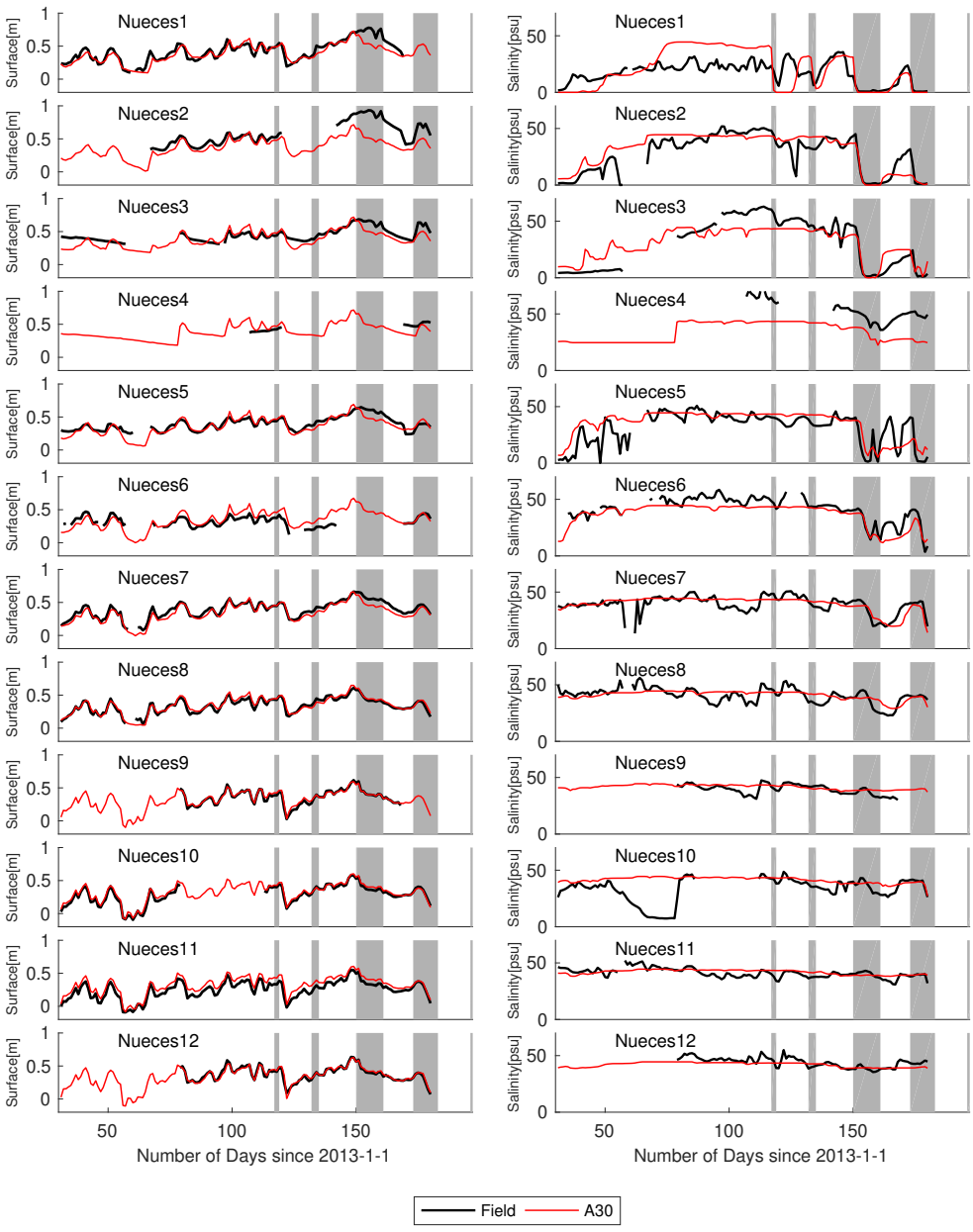

Figure 40: Daily-averaged modeled and measured surface elevation (left) and salinity (right) at 12 stations from Feb. 1, 2013 to Jun. 30, 2013 (*A30* scenario). Shaded areas represent pumping periods

The *C30*, *EC30* and *A30* scenarios produced similar surface elevations at all stations except Nueces1. They all have good model-data agreements at lower delta stations (Nueces8 – Nueces12) close to the tidal boundary, but the differences increase moving upstream in the marsh. These results are consistent with the expected accumulation of error associated with shallower flows and more complex topography in the uplands. Nueces1 shows an interesting result where the *C30* and *A30* scenarios capture the tidal oscillations of the water surface shown in the field data, but the *EC30* scenario does not. These results illustrate an important complexity in the interaction between automatic channel identification (*C30*), cell edges (*EC30*), and the manual channel identification (*A30*) in modeling marsh connectivity. Figure 42 shows a high-resolution view of the three model bathymetries in the vicinity of Nueces1. Note that the *C30* bathymetry has connections to the main channel in the east and to the floodplain in the south that are *not* blocked by the channel embankments, which can be identified as cell edges in *EC30*. Thus, it can be expected that simple automatic channel identification without cell edges will overpredict flooding in this area. However, the automated cell edge identification causes blocking of a key flow path at the eastern end of this channel section, which leads to the poor performance of *EC30* upstream of the blockage. The manual channel identification that reduces the bottom elevation in a single cell for *A30* resolves this issue.

For salinity in Fig. 41, again the *N30* simulation is inadequate across all cases, indicating that simple coarse-grid filtering of the bathymetry to 30×30 m does not provide an reasonable representation of the connectivity through the marsh. In contrast to the surface elevations results, there is significant divergence in the predictions of the salinity for the different topographic treatments. In the upper marsh (Nueces1), the *A30* with all the topographic treatments shows the strongest salinity signal and matches the overall salinity trend as well as daily oscillations. The other stations in the upper marsh illustrate some of the challenges in modeling evolution of a conserved scalar in convoluted channels. From Nueces1, the flow downstream splits at Nueces2 to travel either through the ROC towards Nueces3 and Nueces4 or down the Rincon Bayou to Nueces5. Flood tides and wind-driven fluxes can reverse these flow directions. When the freshwater pumping operation ends at day 162, the field data shows a slow salinity rise across Nueces2, Nueces3, and Nueces4, with a highly variable pattern at Nueces5. In contrast, the model results (excluding *N30*) show a rapid oscillatory rise of salinity, which becomes relatively constant at Nueces2 and Nueces3. The relatively quick response of the model (compared to field data) at Nueces3 is likely due to (i) the topography-adjusted channels simply allow too much reverse flow rather than slower mixing, and/or (ii) the wind parameterization driving a larger flux in the model. The highly-variable salinity in the field observations at Nueces5 indicates the real world has dynamic mixing features of salt and fresh water that simply are not represented at the resolvable model scales. Modeled salinity in the lower delta, Nueces9, Nueces11, and Nueces12, are smoothed relative to the field observations, indicating the horizontal salinity gradients are being lost in the lower delta such that the model produces a relatively well-mixed system. The similar phenomenon is observed in Inoue, Park, Justic, and Wiseman Jr. (2008); Zacharias and Gianni (2008). However, we see that the main channel through the lower delta (Nueces10) retains some of the oscillatory salinity characteristic.

Further insight into the model performance is provided by taking a Fast Fourier Transform (FFT) of the free surface displacement at upstream and downstream stations, which should show a power spike at $\sim 0.04\ \mathrm{h}^{-1}$ where tidal oscillations are significant. As shown in Fig. 43, both model (*A30*) and field data show a clear tidal signature of similar amplitude at the mid-delta site Nueces7, but at the upper delta site, Nueces2, the tidal signature is entirely missing from the field data, while still detectable (albeit smaller) in the model results. These results indicate that the model does not have sufficient damping of the barotropic mode through the upper delta. This effect likely results from narrower channels being widened to 30 m, which is inherent in the automatic channel algorithm. Note that although tidal oscillation is absent at Nueces2, we can clearly observe the oscillation at Nueces1 from Fig. 41. This result is likely indicative of leaking from the main stem of the river through the upstream swing gate that is normally closed. Note that such leakage would also be a contributor to salinity mismatch in the upper delta.

C.4.4 Effects of grid refinement

To provide qualitative insight on how grid resolution affects the modeled spatial distribution of salinity, contours at an instant in time are shown in Fig. 44. The selected time (Jun. 12, 2013, 12:00AM) corresponds to the end of an 11-day freshwater pumping event. The sub-figures focus on the West Lake where the *EC30* and *EC15* scenarios show distinct salinity patterns. The high-resolution model

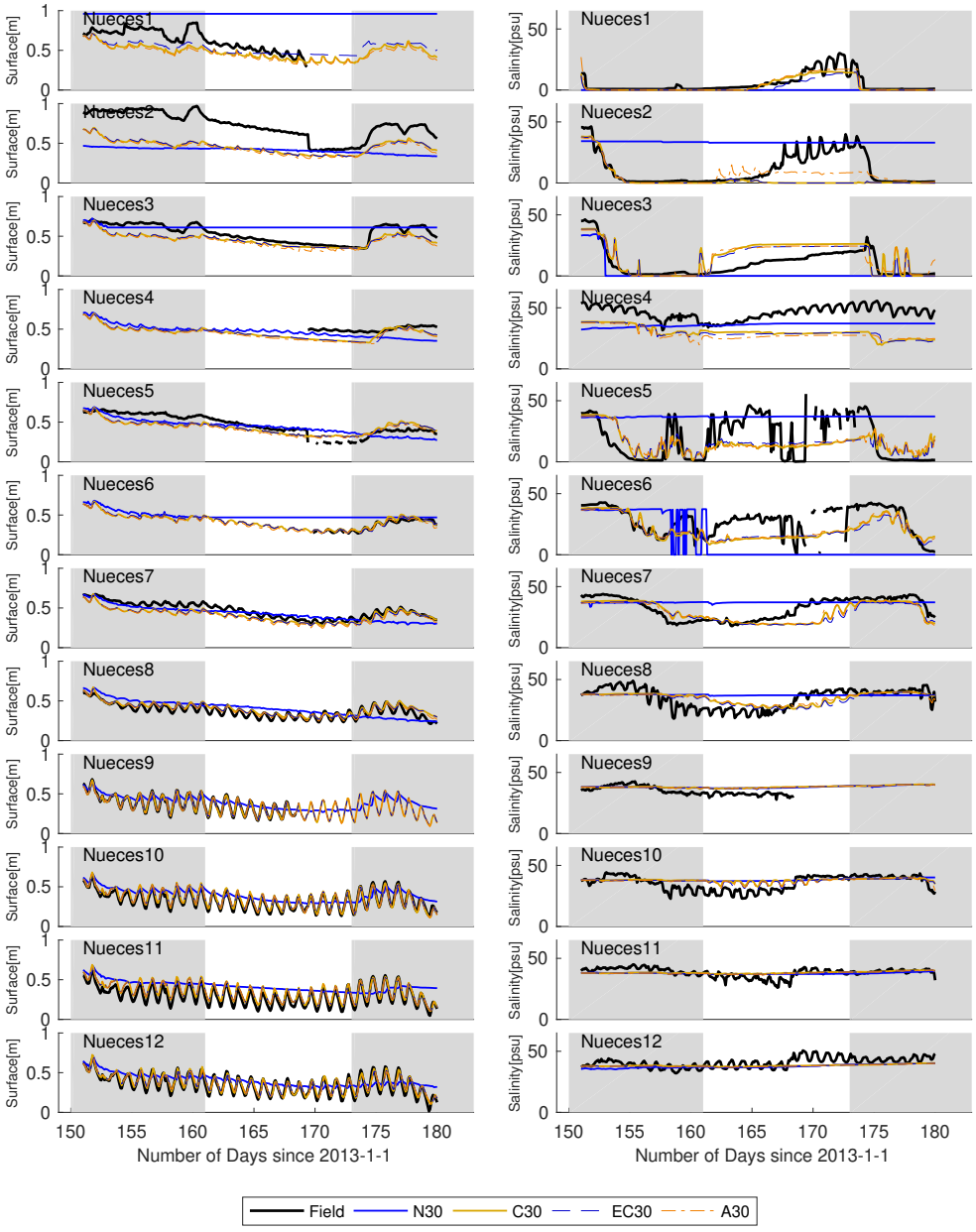

Figure 41: Hourly modeled and measured surface elevation and salinity at 12 stations from Jun. 1, 2013 to Jun. 30, 2013 for different bathymetry processing methods. The left column is the free surface elevation. The right column is salinity. Shaded areas represent pumping periods

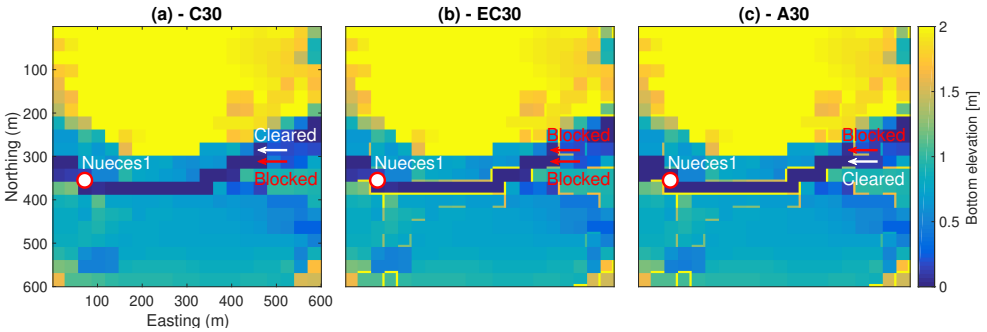

Figure 42: Bathymetry treatments *C30*, *EC30* and *A30* near Nueces1 that result in surface elevation discrepancies. The surface connectivity between Nueces1 and the lower delta is maintained for *C30* and *A30*, but not for *EC30* (where both flow paths are blocked). The narrow lines between adjacent grid cells represent the cell edges, whose elevations are referred to the colorbar. White arrows indicate cleared flow path; red arrows indicate blocked flow path. The natural downstream flow is from left to right.

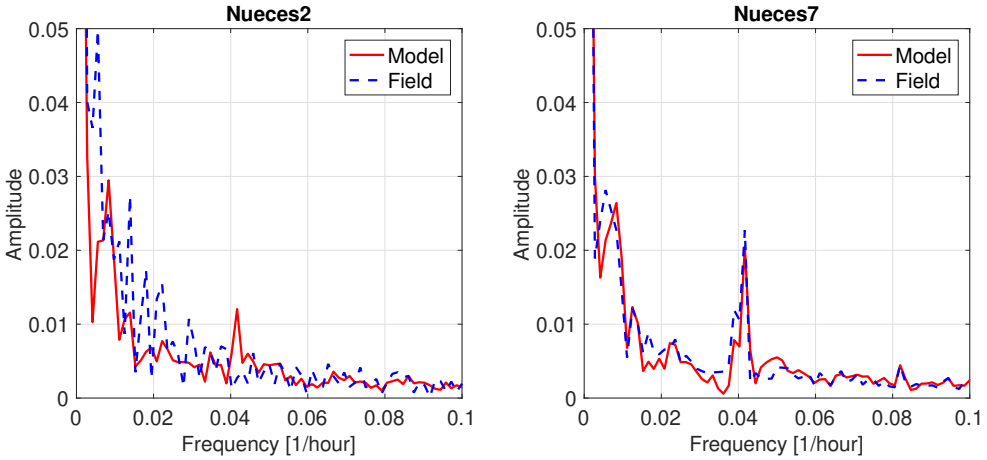

Figure 43: Amplitude of FFT at upstream (Nueces2) and downstream (Nueces7) stations for field and *A30* model results. The model results capture the tidal frequency (the peaks near frequency of 0.04) at both stations, but the field data only show tidal frequency at Nueces7.

(Fig. 44(b)) creates blockage in the middle of the West Lake, which prevents lateral mixing between the high-salinity water and the pumped water, causing a trapped region of high-salinity water between the middle and upper deltas. The *EC30* scenario (Fig. 44(a)), on the contrary, shows well-mixed salinity in the West Lake. This is a clear evidence that different grid resolutions lead to difference surface connectivity patterns, which results different spatial distribution of salinity. Figure 44(c) shows the salinity of the entire model domain (*EC30* with the Nueces Bay masked out). The middle to lower delta has relatively uniform salinity as observed from Fig. 41.

Quantitative comparisons of field and model results at different grid resolutions using the *A30*, *EC30*, *A15* and *EC15* scenarios are shown in Fig. 45. For the surface elevation, with a few exceptions, the $2\times$ grid refinement does not significantly affect the differences between the modeled and observed. The most notable exception is Nueces1, where the *EC15* and *A15* cases track remarkably better for surface elevation during the pumping periods, but then completely miss the salinity throughout the simulation. For the coarse grid simulations, the frequency analysis (Fig. 43) indicates that tidal oscillations are effectively damped at Nueces2, and therefore the field observations of tidal oscillations further upstream at Nueces1 are a sign of backflow leakage through the NOC (see Fig. 34) from the tidally-influenced main river stem. Thus, the tidal oscillations in the *A30* model (which does *not* allow NOC backflow) indicate that the coarse-grid model has too much downstream connectivity. However, this interpretation creates a conundrum – if the coarse grid allows too much upstream flow,

why does it compare better with salinity at Nueces1? The likely answer is in the release of salt bound up in the soils or porewaters of the West Lake tidal flats (Nueces4) that are not represented in the model. Note that the observed salinity at Nueces4 is consistently higher than its neighbors Nueces3 and Nueces5, which is expected for a local salt source. Furthermore, the observations downstream at Nueces5 show strong oscillations indicating frontal mixing that can be interpreted as pumped (fresh) water comes from Rincon Bayou is mixing with high-salinity water from West Lake. With this interpretation, the observed slow rise in salinity in the upper delta after day 160 is primarily attributable to salt released from West Lake being gradually mixed upstream through the ROC rather than water fluxed upstream from the lower delta. Thus the salinity results in the upper delta with the 30×30 m models are the "right" answers for the wrong reasons – i.e. an overestimation of upstream tidal and wind-driven fluxes. In the 15×15 m simulations, since the surface connectivity across the West Lake is blocked (Fig. 44), salinity in the West Lake is not transported further upstream, making the salinities for 15×15 m consistently lower than for the 30×30 m scenarios at Nueces1 through Nueces4. We may conclude that neither grid resolution preserves the 1×1 m surface connectivity – with the 30 m grid overestimates the connectivity downstream of the Rincon Bayou and the 15 m grid underestimates the connectivity across the West Lake.

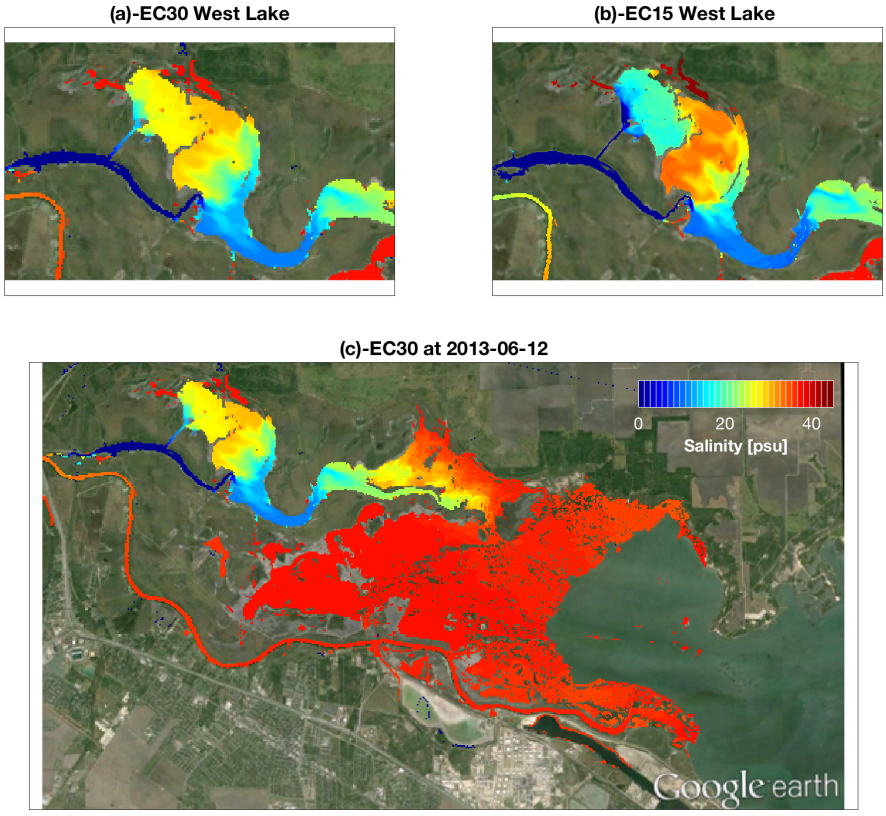

Figure 44: Modeled salinity in the marsh at 12:00 AM, Jun. 12, 2013. (a) is salinity in the West Lake for the *EC30* scenario, (b) is salinity in the West Lake for the *EC15* scenario, (c) is salinity of the entire model domain for the *EC30* scenario. Note that the open bay hydrodynamics are included in the model, but salinities in the bay are suppressed for clarity. We can observe the longitudinal salinity gradient in the Rincon Bayou, the well-mixed salinities in the lower delta (possibly due to numerical diffusion) and the distinct surface connectivities in the West Lake.

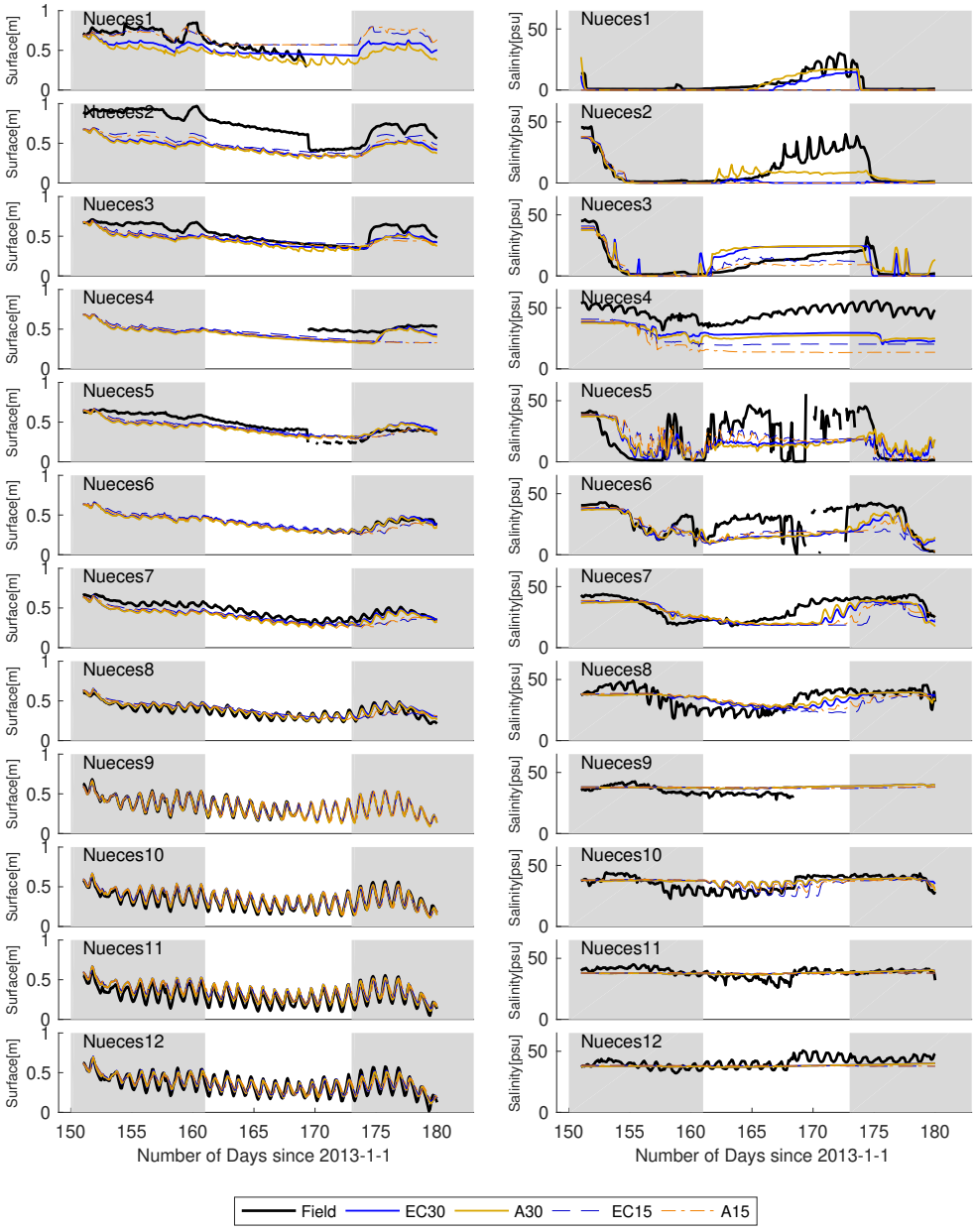

Figure 45: Grid refinement comparison of hourly modeled and measured surface elevation (left) and salinity (right) from Jun. 1, 2013 to Jun. 30, 2013. Shaded areas represent freshwater pumping periods.

C.5 Discussion and Conclusions

The hydrodynamics and salinity transport in a shallow coastal wetland, the Nueces Delta, have been modeled using a 2D depth-integrated numerical model (NDHM) that is designed to handle wetting/drying, thin-layer flows, wind-driven fluxes, and coarse-grid approximations of fine-resolution connectivity. The goal of the present study is to examine if these new algorithms could help to maintain stability and surface connectivity, which are critical challenges that have to be overcame before salinity transport processes in shallow marshes can be modeled and studied. The model results are compared with field data measured at multiple locations in the computation domain on both tidal and sub-tidal time scales. The effects of grid resolution and various bathymetry processing methods are assessed. The major findings are:

1. The approaches used to handle flow reversal (§C.2.3), rapid wetting/drying (§C.2.4) and the thin-layer drag models (§C.2.5) are effective in maintaining hydrodynamic stability and limiting scalar non-conservation caused by high CFL effects, without requiring subtime stepping.

2. The NDHM is able to produce good model-data agreements for both tidal and sub-tidal free surface elevation in the lower delta, which is closer to the Nueces Bay open boundary. In the upper delta, subgrid topography causes poor surface connectivity and poor results at practical grid resolutions if the bathymetry processing does not explicitly account for subgrid-scale features (channels and blockages).

3. Automatic channel and edge identification from subgrid data provides significant improvement over an untreated coarse-grid bathymetry. Manual channel identification, although time-consuming, further improves the representation of bathymetry on a coarse grid.

4. One drawback in representing fine-scale connectivity at a coarse resolution is that broadening a fine-scale channel to the resolved coarse-grid resolution predictably leads to overestimation of fluxes. It seems likely that either some form of automated spatial adjustment through a drag coefficient or through use of subgrid flow areas is needed to compensate for this effect.

5. The NDHM provides satisfactory model-data agreements for sub-tidal salinity variations, although there is some question as to whether the upstream propagation of high-salinity water is overestimated at 30×30 resolution with the full bathymetry treatment. The downstream propagation of a salinity mixing front during freshwater pumping is qualitatively captured, but quantitative agreement is difficult to obtain due to missing salt sources (e.g. evaporation, porewater salinity).

6. A modest $2\times$ refining of the model grid provides greater insight, albeit at a $10\times$ increase in computational time. The comparison across grid scales shows that the "better" answer for upper delta salinity at the 30×30 m grid scale is likely due to excessive upstream salinity flux taking the place of neglected salinity sources.

7. Simple grid refinement, unless carried out to an extremely fine scale, does not necessarily eliminate bathymetric errors. This effect is illustrated by the $2\times$ grid refinement that interrupts surface connectivity upstream in the West Lake, indicating that an even finer grid is required to represent fluxes through the choke point in this region.

Overall, the model results are promising and show that a coarse-grid model has the potential to capture the fluxes of the salt/fresh water interface in a coastal marsh without requiring micro-resolution and supercomputing resources. Errors in modeled salinity come from multiple aspects such as unresolved bathymetry, inadequate field data, and omitted source terms. It has been shown that shallow-marsh model construction should follow the three requirements proposed in §C.1, where maintaining stability and surface connectivity are critical challenges and prerequisites for salinity modeling. With the stability issue being properly handled in this study, the key future tasks for improving such models are (i) developing improved automated approaches that correctly represent flow connectivity/blockages along with the resistance of fine-scale features project up to the coarse-grid scale, and (ii) developing algorithms and approaches for modeling salinity storage and exchange between surface water, porewater, soil, and plants.

C. Appendix 1. Model spin up

The "spin-up" time for a model is the simulation time that it takes for the results to be independent of the initial conditions. Spin-up for a fresh/salt marsh simulation is inherently challenging. Unless the sampling period includes a complete flush of the system, we cannot start from a "clean slate" of zero salinity and expect to reach the actual salinity distribution by some date. In contrast, the hydraulic memory of the velocity and elevation fields is relatively short and can be approximated by the time it takes for an increase in tidal elevation to be seen throughout the domain, which allows uniform conditions to be readily applied as a starting guess. To examine the spin-up behavior of the NDHM, we conducted test simulations starting two weeks apart (from Nov. 15 and Dec. 1, 2012 respectively) to evaluate when the model results are independent of the initial starting date. The start date was chosen based on availability of field data and to ensure sufficient spin-up time prior to the pump operations in summer. Note that during the winter, the secular water elevations in the Nueces and Corpus Christi Bay systems are declining towards a semi-annual low in January (Ward, 1997), and it can be expected that spin-up times during other stages of the secular cycle might be different. For the spin-up simulations, the NDHM was started from quiescent water ($u_j = 0, j \in \{1, 2\}$) with a uniform free-surface elevation equal to the tidal boundary condition. The initial condition for salinity was computed using the ordinary kriging method[6], in which the salinity field was interpolated based on measurements from the 12 stations at the beginning of the model start date.

We consider an adequate spin-up time as the interval when the residual (difference between 2 simulation results) is less than 2 psu for salinity and 0.002 m for free surface. Using this metric, the spin-up times as well as a final salinity residual after 60 days from Dec. 1, 2012 are listed in Table 6. As expected, the spin-up times for free surface elevation are significantly shorter than that for salinity. The poorest result was at Nueces4 in the upstream tidal flat known as West Lake (Fig. 34) that is poorly flushed during the secular low tidal period in winter. In contrast, the locations in the Rincon Bayou main channel and marsh areas close to the open boundary (e.g., Nueces1, 5, 6, 7, 9, 10 and 11) see more consistent flushing through the winter and hence the spin-up times are much shorter. As a conservative measure, all data analyses herein is based on model results after 60 days of spin-up time.

Table 6: Spin-up time for free surface elevation, salinity and 60-day residual for salinity at each TWDB station. The 60-day residuals for free surface elevation are all on the order of 10^{-4} m or less.

Station	Spin-up [days]		Res. [psu]	Station	Spin-up [days]		Res. [psu]
No.	free surf.	salinity	salinity	No.	free surf.	salinity	salinity
Nueces1	6	8	0	Nueces7	6	40	0.40
Nueces2	6	17	0.42	Nueces8	6	50	1.18
Nueces3	10	58	1.43	Nueces9	<1	28	0.52
Nueces4	10	>60	6.58	Nueces10	1	40	0.55
Nueces5	6	20	0.44	Nueces11	<1	35	0.29
Nueces6	6	20	0.44	Nueces12	1	50	1.36

C. Appendix 2. The irrelevance of global drag calibration

Model calibration for a 2D shallow-water model is generally accomplished by adjusting either coefficients of a turbulence model (e.g. ν) or drag (C_D) that control energy dissipation (Ralston et al., 2010; Yuan, Lin, & Falconer, 2007). This is typically conducted using global values: the calibration problem cannot be reasonably constrained if every model grid cell has an independent C_D and field data is available at limited locations. Our analyses (not shown) indicate the NDHM results are relatively insensitive to the choice of a global ν or C_D. The minor variability of results obtained in our calibration exercise does not allow rejection of the hypothesis that our *a priori* selected baseline values are acceptable. Similar conclusions have been reached by other researchers for simulations with complex bathymetries (Cea, French, & Vazquez-Cendon, 2006; Rayson, Gross, & Fringer, 2015).

Arguably, there are two principal reasons for the insensitivity of the model to calibration: (i) the numerical dissipation associated with our 1st-order upwind advection scheme (Chua & Fringer, 2011; Gross et al., 1999), and (ii) the "topographic" dissipation associated with the convoluted channels

[6] `https://www.mathworks.com/matlabcentral/fileexchange/29025-ordinary-kriging`

in a marsh. We have not seen this latter topic specifically addressed in the literature, but it follows from simple consideration of how momentum turns a corner with the hydrostatic approximation. In the real world, the pressure gradients at a channel bend serve to redirect momentum, i.e. the dp/dx_1 required to slow momentum in the x_1 direction increases the pressure p on the outer edge of the channel, and results in dp/dx_2 that accelerates the flow in the x_2 direction around the bend. Thus, streamwise momentum is not lost around a corner, but is smoothly transferred from x_1 to x_2 coordinate directions through the pressure gradients and nonlinear terms. Indeed, the 1D Saint-Venant equations for channel flow are essentially the mathematical embodiment of this idea (Hodges & Liu, 2014). However, when a narrow channel bend is represented by a single set of grid cells in a 2D hydrostatic model, only a small part of the momentum change in the x_1 direction will be recovered in the hydrostatic pressure and returned to the x_2 direction. The fundamental problem is that insufficient grid resolution at the channel scale creates an inability to have smooth transition of pressure gradients and nonlinear terms between coordinate directions. Thus, every bend in a narrow channel causes the flow to stop its streamwise acceleration in the x_1 direction and restart the streamwise acceleration in the x_2 direction. If the marsh system were strongly nonlinear with high channel velocities, then increased grid resolution would be necessary for a reasonable approximation of the fluxes. However, velocities in the marsh channels are slow and only weakly nonlinear, so relatively coarse grid resolution of the channels is an acceptable trade-off for computational efficiency. The main consequence is that the topographic dissipation from channel bends plays a major role in dissipation of energy, which makes C_D, ν, and drag calibration nearly irrelevant.

It can be argued that a depth-dependent drag model (e.g., Chezy-Manning $C_D = g\hat{n}^2 h^{-1/3}$, where $\hat{n}$ is Manning's n) would be an appropriate baseline model. However, our calibration exercises showed that field data could not adequately discriminate between competing models. Thus, we appeal to Occam's Razor and use the simplest possible drag model. This model is a baseline uniform C_D that is only depth-dependent in thin layers (as discussed in §C.2.5) where the depth dependency has a clear impact. Nevertheless, we do not consider this the final answer. Results with the automated channel bathymetry treatment (discussed below) indicate that some form of spatially-distributed drag might be useful, although it is not clear that simple depth-dependency such as Chezy-Manning is necessarily the solution. We speculate that a local drag coefficient might be linked to the approximations made in the channel connectivity algorithm and calibrated with some form of global coefficient. This idea remains an area of ongoing research.

D Modeling subgrid-scale topographic effects on shallow marsh hydrodynamics and salinity transport

For the convenience of the reader, the following appendix provides the text and figures for portions of this study that were published in Z. Li and Hodges (2019a). Modifications have been made for consistent cross-references as an appendix to the present report. Note that the model development documented in this paper used the Nueces Delta as a test case rather than the Trinity Delta due to the availability of field data in the former. The model developments tested on the Nueces Delta were incorporated into the TDHM.

Article Title: **Modeling subgrid-scale topographic effects on shallow marsh hydrodynamics and salinity transport**

Authors: Zhi Li, Ben R. Hodges

Published in:
Advances in Water Resources
129:1-15 (2019)
https://doi.org/10.1016/j.advwatres.2019.05.004

Abstract

A 2D depth-integrated subgrid hydrodynamic model (*FrehdC*) is designed to simulate effects of subgrid-scale topography on flow and scalar transport in shallow coastal marshes using computationally-efficient grid cells that are coarser than many of the channelized paths through the marsh. The subgrid-scale topography is parametrized into four depth-dependent variables (subgrid cell volume and three subgrid face areas) that characterize the high-resolution features of coarse grid cells. These variables are pre-stored in a table and embedded into the governing equations as model inputs to scale cell storage, mass and momentum fluxes across cell faces. A block-checking procedure is designed to automatically preserve high-resolution surface connectivity during grid-coarsening. By testing on both synthetic domain and real marshes, this new model is able to approximate fine-grid simulation results of surface elevation, inundation area, flow rate and salinity with less computational cost.

D.1 Introduction

High-resolution topographic data obtained from lidar, typically at a 1 m scale, are difficult to directly use in a fine-resolution hydrodynamic model for an extensive marsh system due to the small model time step and large number of computational cells that would be required. For example, a 10×10 km marsh would require 10^8 grid cells and a time step of less than 10 s. Using a highly-efficient computational model with 100 floating point operations per time step per grid cell would requires a petaflop supercomputer with terabytes of memory to achieve practical computation speeds of $100\times$ faster than real time. While such computers exist, they are typically not available for scientists and engineers studying flow and transport through marshlands. Thus, to effectively use high-resolution data, some form of grid-coarsening scheme must be employed. The challenge of handling known (but unresolved) bathymetry complicates the challenge of handling unknown (or poorly-known) bottom roughness (Wang et al., 2009).

Unfortunately, a coarse grid cannot directly represent many of the small but hydrodynamically-important topographical features that are evident in lidar data (e.g., Hodges, 2015). Grid coarsening (or topographic upscaling) usually involves filtering the high-resolution data to get approximations of the bottom elevations, which introduces errors in hydrodynamic modeling of the flow depths that in turn affects the modeled velocities and fluxes (Cea & French, 2012). Furthermore, subgrid-scale channels and water-blocking ridges are often widened or smoothed on coarse grids, which leads to (i) overestimated flow rates in channels that are widened, (ii) underestimated resistance where surface roughness is smoothed (Cea, Legout, Darboux, Esteves, & Nord, 2014), (iii) erroneous surface connectivity and (iv) different flow patterns (either channelized flow or shallow sheet flow) due to shifts in the wetting/drying front (Sullivan et al., 2015; Torres & Styles, 2007).

These problems have been previously noted and subgrid methods have been developed by a number of researchers to represent high-resolution topographic effects on coarse grids (e.g., Bates, Marks, &

Horritt, 2003; Casas, Lane, Yu, & Benito, 2010; D'Alpaos & Defina, 2007; Duan, Liu, Chen, & Zhu, 2017; Guinot, 2012; Guinot et al., 2018; Hodges, 2015; Jan, Coon, Graham, & Painter, 2018; Kim, Sanders, Famiglietti, & Guinot, 2015; Loftis, Wang, DeYoung, & Ball, 2016; Neal, Schumann, & Bates, 2012; Ozgen, Liang, & Hinkelmann, 2016; Ozgen, Teuber, Simons, Liang, & Hinkelmann, 2015; Ozgen, Zhao, Liang, & Hinkelmann, 2016; Sanders & Schubert, 2019; Stelling, 2012; Viero & Valipour, 2017; Volp, van Prooijen, & Stelling, 2013; Yu & Lane, 2006b, 2006a). Of interest for the present work are methods using artificial porosity to scale the volumetric flow rates in/out of the grid cells. As proposed by Defina et al. (1994), artificial porosity can be treated as a function of the free surface elevation as well as the high-resolution topography. By multiplying porosity into the governing equations, the high-resolution topographic information is embedded into coarse-grid models. However, dependency between artificial porosity and surface elevation introduces another nonlinearity to the governing equations. Early attempts used empirical relationship between porosity and depth for linearization (Defina, 2000), which showed good performance on simple idealized topography (Bates, 2000). A recent approach by Wu et al. (2016) used pre-stored porosity parameters calculated for all possible surface elevations in a look-up table. Model porosity was updated for each grid at each time step by searching in the table. Since the pre-stored porosities are calculated from high-resolution data, the method can be used on domains with complex topography where empirical relationships do not hold. Casulli (2009) developed an algorithm to solve the mildly nonlinear system produced by porosity-depth coupling with minimal additional computational cost and ensured conservation of mass in the free surface solution. This method was proven to improve the model performance on sections of the Elbe river (Platzek, Stelling, Jankowski, Patzwahl, & Pietrzak, 2016; Sehili, Lang, & Lippert, 2014). Artificial porosity has also been used for modeling urban floods (where buildings are difficult to represent) with an "integral porosity (IP) model" (Sanders et al., 2008). This approach embeds volumetric and anisotropic areal porosities in the governing equations. Although anisotropy of areal porosity was proven necessary, the IP model was subsequently shown to be sensitive to mesh design (Guinot, 2017a). Further improvement on the IP model was made by correcting the flux terms (referred as "DIP model") that alleviated dependencies on the mesh (Guinot, 2017b; Guinot et al., 2017). Nevertheless, a practical application involving a levee-breach flow through a residential neighborhood showed that the DIP model cannot capture the full distribution of velocity directions and magnitude that are resolved by finer resolution models. Furthermore, the DIP mesh must be strategically placed so that the cell edges intersect with water-blocking structures, otherwise the effects of these structures will not be correctly reflected from areal porosity.

Despite the noted progress in subgrid methods, a key unsolved problem is the lack of a method that automatically preserves high-resolution surface connectivity during grid coarsening. In the present study, surface connectivity refers to the network of flux paths through a marsh system, which is controlled by channels and blockages in topography. Connectivity is generally increased when a channel is widened by grid coarsening. However, grid coarsening can also interrupt surface connectivity where it eliminates narrow channels from the high-resolution topography. This effect has been noted to be a function of a coarsening ratio (r), which is defined as the ratio of the coarse-grid length scale to the fine-grid length scale. Wu et al. (2016) has reported unreasonable model results when $r > 4$ due to interrupted connectivity. Z. Li and Hodges (2019b) showed that poor representation of surface connectivity caused significant discrepancies between modeled salinity fluxes and observations in a coastal marsh. Identifying small but hydraulically-important topographical features that must be represented to maintain adequate surface connectivity remains a challenging task. Yu and Lane (2011) detected water-blocking features and added artificial walls to maintain surface connectivity by hand, which was time and labor-consuming. Chen, Evans, Djordjevic, and Savic (2012) used a multi-layer method, solving the model equations for the two regions bisected by the water-blocking feature separately. But for general marsh topography where the use of multiple layers (more than two) is expected, this approach could severely increase computational cost. Neal et al. (2012) used a subgrid method that simulates effects of narrow channels in floodplains, but it requires characterization of channel geometry. For coastal marshes with frequent wetting/drying, it is not easy to separate the domain into distinct "channels" and "floodplains". Hodges (2015) designed an automatic channel and cell edge identification method to detect small-scale water-blocking features, but some narrow channels still needed to be manually identified in practical applications (Z. Li & Hodges, 2019b). A recent study on urban floods (Sanders & Schubert, 2019) also emphasized the needs of automatically detecting small-scale topographic features.

Many subgrid methods have been developed for flood modeling where free surface elevation and inundation area are the variables of interest. In contrast, the coarse-grid effects on scalar transport

processes (e.g., salinity) have not been extensively studied. Scalar transport modeling typically has greater uncertainties than modeling surface elevation (Aizinger, Proft, Dawson, Pothina, & Negusse, 2013; Inoue et al., 2008; Wang et al., 2009) because scalar error is inherently accumulative over the residence time scale of the modeled system and does not have a feedback effect. In contrast, by definition for slow-moving marsh waters the errors leading to local accumulations (or deficits) in surface elevations must also lead to changes in the surface gradients with neighbor cells, which in turn induce errors in the local fluxes that will counteract the accumulation (or deficit) of surface elevation. Furthermore, modeling advective scalar transport in shallow marshes requires accurate reproduction of the velocity field, which is more sensitive to grid-coarsening errors than is surface elevation (Mazzolari, Trigo-Teixeira, & Araujo, 2015). It has been shown that a subgrid model with minimal surface error could still contain large errors for the modeled flux (Shin, 2016).

The present study is an outgrowth of efforts to understand the effectiveness of freshwater inundation in reducing salinities across tidal marshes of the Nueces River Delta (Texas, USA), as described in Z. Li and Hodges (2019b). We previously identified two key issues that limited the existing models (i) stability of numerical methods for wetting/drying fronts, and (ii) obtaining correct connectivity at the practical model grid resolution. The former was addressed in new methods proposed in Z. Li and Hodges (2019b), and herein we examine how the new subgrid model improves the representation of marsh connectivity and salinity (scalar) transport. The new method (§D.2) borrows the concept of artificial porosity and uses a pre-store of high-resolution topographic information similar to Wu et al. (2016). The relationships between the coarse and the fine grid are stored as a group of subgrid variables (similar to artificial porosity), which saves computation efforts (§D.2.1). The governing equations are discretized by including the subgrid variables as parameters (§D.2.2). An automatic checking routine is designed to effectively capture narrow water-blocking features (§D.2.4). Model results are evaluated with respect to surface elevation, inundation area, and salinity through comparisons with high-resolution simulation results and field data (§D.3). The advances and limitations of the proposed model are summarized in §D.5.

D.2 Methods

The new subgrid method is implemented in a two-dimensional (2D), depth-integrated solution of the shallow-water equations. The numerical methods for the solution are a hybrid finite-volume/difference approach developed from the three-dimensional (3D) Fine Resolution Environmental Hydrodynamic Model (Frehd), which is a descendent of TRIM (Casulli & Cattani, 1994) and ELCOM (Hodges et al., 2000) models. The 3D Frehd model was written in Matlab scripting to develop and test new algorithms for 3D flow and transport in natural environments (Hodges, 2004, 2014, 2015; Hodges & Rueda, 2008; Rueda et al., 2007; Wadzuk & Hodges, 2009). For seasonal-to-annual simulations, the serial Matlab implementation of Frehd is too slow for more than 10^4 grid cells and does not parallelize well – the code structure was designed to allow implementation and testing of new algorithms, which hampers parallel solution efficiency. The basic Frehd algorithms for 2D have been rewritten in the C programming language to improve computation efficiency. Parallelization is achieved using the Message Passing Interface (MPI), where the entire model domain is divided into sub-domains of equal sizes. A range of 1 to 32 threads are used for the simulations performed in the present study. Good scaling property is observed within this range (results not shown because parallelization is not the focus of the present study). This new 2D version is named *FrehdC*.

D.2.1 Subgrid geometry definitions

Before presenting the governing equations and discretization schemes of the *FrehdC* model, it is useful to define the subgrid geometry variables that describe the high-resolution characteristics of a coarse grid. Consider a coarse grid cell (i, j) in a 2D domain with dimensions Δx by Δy, which contains $\Lambda \times \Psi$ high-resolution (subgrid) cells. Let Ω to represent the domain of cell (i, j) and Γ its boundary. The size of one subgrid cell is $\delta x \times \delta y$, where $\Lambda\, \delta x = \Delta x$, and $\Psi\, \delta y = \Delta y$.

Figure 46 shows an example of a coarse grid cell with $\Lambda = \Psi = 4$. Each subgrid cell is labeled using (λ, ψ), where $1 \leq \lambda \leq \Lambda$ and $1 \leq \psi \leq \Psi$. The bottom elevation of a subgrid cell is denoted as $z_{i,j,\lambda,\psi}$. The coarse grid cell $\Omega_{i,j}$ is characterized by a single value of surface elevation, $\eta_{i,j}$. A single value for bottom elevation ($Z_{i,j}$) is defined as:

$$Z_{i,j} = \min_{\lambda,\psi \in \Omega} \left(z_{i,j,\lambda,\psi} \right) \tag{46}$$

The use of *min* function ensures the cell is identified as "wet" (i.e., contains some water), even when only a single of the (λ, ψ) subgrid cells is below the free surface. For regions with frequent wetting and drying, this definition is necessary to represent the inundation area and flux paths. The volume of cell $\Omega_{i,j}$ is defined as:

$$V_{i,j} = \sum_{\lambda,\psi \in \Omega} \max\left(\eta_{i,j} - z_{i,j,\lambda,\psi}, 0\right) \delta x \, \delta y \tag{47}$$

where the *max* function ensures that dry subgrid cells are not counted as negative volumes. If no subgrid topography exists, Eq. (47) simply reduces to $V_{i,j} = H_{i,j}\Delta x \Delta y$ (where $H_{i,j} = \eta_{i,j} - Z_{i,j}$ is the depth).

Similarly, we may define the cell face areas as illustrated in Fig. 46. For example, the face areas normal to the x-axis on the plus and minus sides of $\Omega_{i,j}$ are:

$$\begin{aligned}
(A_X)_{i+\frac{1}{2},j} &= \sum_{k=1}^{\Psi} \max\left(\eta_{i,j} - z_{i,j,\Lambda,k}, 0\right) \delta y \\
(A_X)_{i-\frac{1}{2},j} &= \sum_{k=1}^{\Psi} \max\left(\eta_{i,j} - z_{i,j,1,k}, 0\right) \delta y
\end{aligned} \tag{48}$$

The face areas normal to the y-axis on the plus and minus sides of $\Omega_{i,j}$ are:

$$\begin{aligned}
(A_Y)_{i,j+\frac{1}{2}} &= \sum_{k=1}^{\Lambda} \max\left(\eta_{i,j} - z_{i,j,k,\Psi}, 0\right) \delta x \\
(A_Y)_{i,j-\frac{1}{2}} &= \sum_{k=1}^{\Lambda} \max\left(\eta_{i,j} - z_{i,j,k,1}, 0\right) \delta x
\end{aligned} \tag{49}$$

and the face area on the top face of the grid cell is:

$$(A_Z)_{i,j} = \sum_{\lambda,\psi \in \Omega} \epsilon_{i,j,\lambda,\psi} \delta x \, \delta y \tag{50}$$

$$\epsilon_{i,j,\lambda,\psi} = \begin{cases} 1, & \eta_{i,j} > z_{i,j,\lambda,\psi} \\ 0, & \eta_{i,j} \leq z_{i,j,\lambda,\psi} \end{cases} \tag{51}$$

For use in discrete equations, the subgrid variables V, A_X, A_Y and A_Z are labeled by its (i, j) indices, which are the coordinates of its center. For example, we can also write $(A_X)_{i,j}$ to represent the face area normal to the x-axis centered at (i, j), or $V_{i+\frac{1}{2},j}$ to represent the cell volume centered at $(i + \frac{1}{2}, j)$. These subgrid variables are introduced into the discrete governing equations as illustrated in the following section.

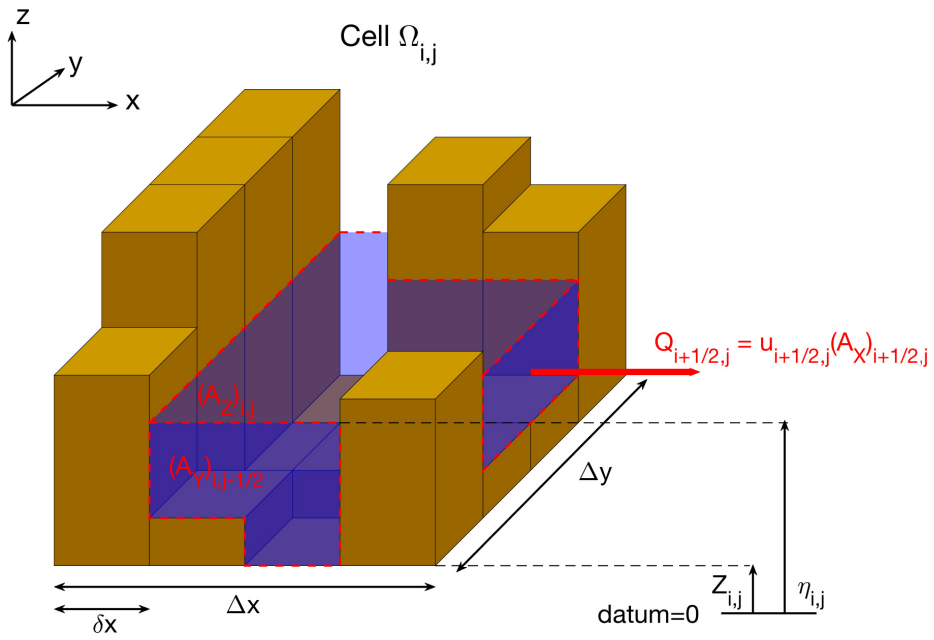

Figure 46: An illustration of the subgrid variable definitions using a coarse grid cell that contains 4×4 subgrid cells.

D.2.2 Governing equations

The 2D depth-integrated free surface equation, momentum equations, and the scalar transport equation can be written in an integral form similar to Sanders et al. (2008):

$$\frac{\partial}{\partial t}\int_{\Omega}\eta\, d\Omega + \int_{\Gamma}\boldsymbol{u}\cdot\boldsymbol{n}\, dA = 0 \tag{52}$$

$$\int_{V}\left(\frac{\partial \boldsymbol{u}}{\partial t} + (\boldsymbol{u}\cdot\boldsymbol{n})\frac{\partial \boldsymbol{u}}{\partial \boldsymbol{x}}\right) dV = \int_{\Gamma} g\eta\boldsymbol{n}\, dA + \int_{\Gamma}\boldsymbol{\tau_\nu}\cdot\boldsymbol{n}\, dA + \int_{\Omega}\boldsymbol{\tau_b}\, d\Omega \tag{53}$$

$$\frac{\partial}{\partial t}\int_{V} C\, dV + \int_{\Gamma}(\boldsymbol{u}\cdot\boldsymbol{n})C\, dA = \int_{\Gamma}\boldsymbol{\tau_\kappa}\cdot\boldsymbol{n}\, dA \tag{54}$$

where η is the free surface elevation, $\boldsymbol{u} = [u, v]^T$ are depth-averaged velocities, $\boldsymbol{x} = [x, y]^T$ are the corresponding Cartesian axes, $\boldsymbol{n}$ is the normal unit vector to a flux-surface Γ, $\boldsymbol{\tau_b}$ is the bottom stress, $\boldsymbol{\tau_\nu}$ is the viscous stress, C is the scalar concentration, and $\boldsymbol{\tau_\kappa}$ is the scalar diffusion term. An infinitesimal volume inside the grid cell is dV with infinitesimal cell face areas dA, which can be written as $dA = h(\Gamma)\, d\Gamma$ where $h(\Gamma)$ is the depth function along the cell boundary. The density is assumed to be a constant.

The bottom stress and viscous stress are defined as:

$$\boldsymbol{\tau_b} = \frac{1}{2}C_D\,\boldsymbol{u}|\boldsymbol{u}| \tag{55}$$

$$\boldsymbol{\tau_\nu} = \left[\nu\frac{\partial \boldsymbol{u}}{\partial x}, \nu\frac{\partial \boldsymbol{u}}{\partial y}\right]^T \tag{56}$$

where ν is the eddy viscosity, and C_D is the drag coefficient defined as:

$$C_D = \frac{g\hat{n}^2}{\bar{H}^{\frac{1}{3}}}, \quad \bar{H} = \frac{V}{\Delta x \Delta y} \tag{57}$$

In Eq. (57), $\hat{n}$ is the Manning's roughness coefficient, which is assumed to be a constant in the present study. The scalar diffusion terms are computed as:

$$\boldsymbol{\tau_\kappa} = \left[\kappa\frac{\partial C}{\partial x}, \kappa\frac{\partial C}{\partial y}\right]^T \tag{58}$$

where κ is the eddy diffusivity. We use $\kappa = \nu = 10^{-4} m^2 s^{-1}$ because the Frehd model has been shown to be insensitive to eddy viscosity for shallow estuaries and tidal marshes (Z. Li & Hodges, 2019b). Indeed, it can be argued that any depth-averaged coarse-grid hydrodynamic model will be insensitive to eddy viscosity in a marsh simulation because bottom drag and form drag associated with torturous channelization will dominate the effects of horizontal shear at the low velocities that are typical of such systems (Arega & Sanders, 2004). Although dispersion at channel bends could have strong effects on the flow field (Begnudelli et al., 2010), in narrow coastal channels there often lacks sufficient grid resolution to fully resolve the bends, which makes numerical dissipation to be the dominant process (Z. Li & Hodges, 2019b). A detailed study on the relations between eddy diffusion, numerical diffusion and dispersion, especially under the existence of subgrid-scale topography, is beyond the scope of the present study, but it deserves further investigation in the future. Unlike some existing 2D subgrid models that are shock-capturing (e.g. Guinot et al., 2018), *FrehdC* does not include any specific treatments regarding shock waves because flow in coastal marshes is generally slow. Inundation is often tidal-driven, which occurs at longer time scales than flash floods. Highly irregular topography and existence of vegetation further decelerates propagation of inundation extent, making shock-capturing a secondary task.

The solution algorithm of *FrehdC* uses the semi-implicit approach of Casulli and Cattani (1994), where the free surface gradient is discretized with a θ-method weighted implicit scheme. However, the nonlinear advective terms are discretized using first-order upwind as discussed in Z. Li and Hodges (2019b). Using a finite-volume method, the free surface equation (Eq. 52) is discretized with

subgrid-derived areas as:

$$\eta_{ij}^{n+1}(A_Z)_{ij}^n+\Delta t\Bigg[u_{i+\frac{1}{2},j}^{n+1}(A_X)_{i+\frac{1}{2},j}^n-u_{i-\frac{1}{2},j}^{n+1}(A_X)_{i-\frac{1}{2},j}^n$$
$$+v_{i,j+\frac{1}{2}}^{n+1}(A_Y)_{i,j+\frac{1}{2}}^n-v_{i,j-\frac{1}{2}}^{n+1}(A_Y)_{i,j-\frac{1}{2}}^n\Bigg]=\eta_{ij}^n(A_Z)_{ij}^n+\Delta tI_{ij}^{n+\frac{1}{2}} \tag{59}$$

where, $I_{i,j}$ is the volumetric flow rate of the inflow boundary condition, n represents time level when appears as superscript. The above applies a time-linearization of the subgrid areas, e.g., the A_X^n is a coefficient of the u^{n+1}, which is similar to the time-linearization of geometry (Δz) that appears in many conventional semi-implicit schemes (Hodges, 2004).

The momentum equation (Eq. 53) is discretized with respect to a staggered-grid volume $\Omega_{i+\frac{1}{2},j}$ as (for simplicity, only the momentum equation in x direction is derived):

$$u_{i+\frac{1}{2},j}^{n+1}=g\Delta t\frac{(A_X)_{i+\frac{1}{2},j}^n}{V_{i+\frac{1}{2},j}^n}K_{i+\frac{1}{2},j}^n(\eta_{i,j}^{n+1}-\eta_{i+1,j}^{n+1})+K_{i+\frac{1}{2},j}^nE_{i+\frac{1}{2},j}^n \tag{60}$$

where $K_{i+\frac{1}{2},j}^n$ is the inverse of the coefficient of implicit velocity u^{n+1} that appears due to time-linearization of the drag term to maintain stability during flow reversals (Z. Li & Hodges, 2019b), and $E_{i+\frac{1}{2},j}^n$ contains all the explicit terms. Specifically, these are:

$$K_{i+\frac{1}{2},j}^n=\left(1+\frac{(A_Z)_{i+\frac{1}{2},j}^n}{2V_{i+\frac{1}{2},j}^n}C_{Dx}|\boldsymbol{u}|\right)^{-1} \tag{61}$$

$$E_{i+\frac{1}{2},j}^n=u_{i+\frac{1}{2},j}^n+\Delta t\left(\frac{\nu(A_X)_{i+\frac{1}{2},j}^n}{V_{i+\frac{1}{2},j}^n}(\frac{\partial u}{\partial x}|_{i+1,j}-\frac{\partial u}{\partial x}|_{i,j})\right)$$
$$+\Delta t\left(\frac{\nu(A_Y)_{i+\frac{1}{2},j}^n}{V_{i+\frac{1}{2},j}^n}(\frac{\partial u}{\partial y}|_{i+\frac{1}{2},j+\frac{1}{2}}-\frac{\partial u}{\partial y}|_{i+\frac{1}{2},j-\frac{1}{2}})\right)-\Delta t\left(u\frac{\partial u}{\partial x}+v\frac{\partial u}{\partial y}\right)_{i+\frac{1}{2},j} \tag{62}$$

At each time step, the velocities u^{n+1} and v^{n+1} from Eq. (60) and the corresponding y-momentum equation are substituted into Eq. (59), forming a five-diagonal linear system for the free surface elevations:

$$\eta_{i,j}^{n+1}\Big[(A_Z)_{i,j}^n+(G_{xp})_{i,j}^n+(G_{xm})_{i,j}^n+(G_{yp})_{i,j}^n+(G_{ym})_{i,j}^n\Big]$$
$$-\eta_{i+1,j}^{n+1}(G_{xp})_{i,j}^n-\eta_{i-1,j}^{n+1}(G_{xm})_{i,j}^n-\eta_{i,j+1}^{n+1}(G_{yp})_{i,j}^n-\eta_{i,j-1}^{n+1}(G_{ym})_{i,j}^n=$$
$$\eta_{i,j}^n(A_Z)_{i,j}^n+\Delta tI_{ij}^{n+\frac{1}{2}}-\Delta t\Big[E_{i+\frac{1}{2},j}^n+E_{i-\frac{1}{2},j}^n+E_{i,j+\frac{1}{2}}^n+E_{i,j-\frac{1}{2}}^n\Big] \tag{63}$$

where the matrix coefficients are defined as:

$$(G_{xp})_{i,j}^n=g\Delta t^2\frac{\left((A_X)_{i+\frac{1}{2},j}^n\right)^2}{V_{i+\frac{1}{2},j}^n}K_{i+\frac{1}{2},j}^n$$
$$(G_{xm})_{i,j}^n=g\Delta t^2\frac{\left((A_X)_{i-\frac{1}{2},j}^n\right)^2}{V_{i-\frac{1}{2},j}^n}K_{i-\frac{1}{2},j}^n$$
$$(G_{yp})_{i,j}^n=g\Delta t^2\frac{\left((A_Y)_{i,j+\frac{1}{2}}^n\right)^2}{V_{i,j+\frac{1}{2}}^n}K_{i,j+\frac{1}{2}}^n$$
$$(G_{ym})_{i,j}^n=g\Delta t^2\frac{\left((A_Y)_{i,j-\frac{1}{2}}^n\right)^2}{V_{i,j-\frac{1}{2},j}^n}K_{i,j-\frac{1}{2}}^n \tag{64}$$

In *FrehdC*, this linear system is solved by applying conjugate gradient method with symmetric successive over-relaxation preconditioner (available through Skalicky (2019)). The η^{n+1} from solution of Eq. (63) are substituted into Eq. (60) and a similar y-momentum equation to get updated velocities u^{n+1} and v^{n+1}.

The scalar transport equation (Eq. 54) is discretized using finite-volume method. At the x-plus face, the net scalar mass m_c across the face is:

$$(\Delta m_c)^{n+1}_{i+\frac{1}{2},j} = \Delta t (A_X)^{n+1}_{i+\frac{1}{2},j} \left[u^{n+1}_{i+\frac{1}{2},j} C^n_{i,j} + \kappa \frac{\partial C}{\partial x}|_{i+\frac{1}{2},j} \right] \tag{65}$$

Summing mass fluxes on all four faces and allowing sources/sinks of mass provides:

$$\begin{aligned}(m_c)^{n+1}_{i,j} = (m_c)^n_{i,j} + (\Delta m_c)^{n+1}_{i-\frac{1}{2},j} - (\Delta m_c)^{n+1}_{i+\frac{1}{2},j} + (\Delta m_c)^{n+1}_{i,j-\frac{1}{2}} \\ -(\Delta m_c)^{n+1}_{i,j+\frac{1}{2}} + source - sink\end{aligned} \tag{66}$$

The updated scalar concentration is

$$C^{n+1}_{i,j} = \frac{(m_c)^{n+1}_{i,j}}{V^{n+1}_{i,j}} \tag{67}$$

D.2.3 Subgrid geometry update

The subgrid geometry variables defined in §D.2.1 are all functions of the free-surface elevation. Ideally, their values should be updated simultaneously with the free-surface elevation to maintain mass conservation (Casulli, 2009). In practice, the geometry time-linearization discussed in §D.2.2 allows a simple linear implicit solver to be used for the free-surface solution. A pre-stored approach (Wu et al., 2016) is adopted herein for the update computation. At the solution start we initialize an array that contains pre-defined free surface elevations and their corresponding subgrid geometry; i.e., an array indexed by $\eta_{pd} = [\eta_{min}, \eta_{min} + \Delta\eta, \eta_{min} + 2\Delta\eta, \ldots, \eta_{max}]$, where η_{min} and η_{max} are based on expected maximum and minimum values for the system. For each η in η_{pd}, the corresponding subgrid geometry variables are computed and stored. For each time step, when the new free surface elevation $\eta^{n+1}_{i,j}$ is computed, we search in η_{pd} for $(\eta_{pd})_K \leq \eta^{n+1}_{i,j} \leq (\eta_{pd})_{K+1}$ and interpolate the subgrid variables between $(\eta_{pd})_K$ and $(\eta_{pd})_{K+1}$. For computational efficiency in searching in the pre-defined array of surface elevations, our algorithm begins from the last known interval $[(\eta_{pd})_K, (\eta_{pd})_{K+1}]$. If η^{n+1} does not fall within in this interval, we continue by searching neighbor intervals. This strategy significantly reduces the computation costs compared to an arbitrary search over $[\eta_{min}, \eta_{max}]$.

D.2.4 Block checking for internal features

In §D.2.1, the cell face areas are defined using only the high-resolution data that is coincident with the cell faces, which naturally creates a water blockage if all the subgrid cells are dry along a face. However, a water-blocking feature in the interior of a cell cannot be directly represented by the cell face areas using the subgrid geometry as defined above. For example, we can imagine a case where $(A_X)_{i+\frac{1}{2},j} > 0$ and $(A_X)_{i-\frac{1}{2},j} > 0$ combined with $(A_X)_{i,j} = 0$, which would allow flow from the $i-1, j$ cell to the $i+1, j$ cell through the i, j cell because the the $(A_X)_{i,j}$ does not appear in the discrete equations. Thus, an additional algorithm is required to locally-alter the subgrid geometry and account for internal blocking effects. This is similar to the problem addressed in Hodges (2015) where the interior blocking height of subgrid geometry across a coarse-grid cell was identified and the feature was "snapped" to the nearest face – the result was a static face geometry that included effects of interior blockages, which was accomplished as a pre-processing step to a hydrodynamic model. Herein, we develop an approach that accomplishes a similar task, but is integrated in the approach for the hydrodynamic solution through direct effect on the A_X and A_Y.

Internal blocking is handled through a discrete analysis of subgrid geometry at each of the $(\eta_{pd})_K$ elevations in the pre-stored subgrid geometry array. A five-step process is used to modify the A_X and A_Y on each face. That is, the face areas at a given $(\eta_{pd})_K$ retain their values computed by the faces unless an effective interior blockage is detected, in which case the appropriate face area is set to zero. The process for each coarse-grid cell is:

1. At each pre-defined surface elevation, $(\eta_{pd})_K$, create a binary wet/dry map within a coarse grid cell that contains $\Lambda \times \Psi$ subgrid cells.
2. Cycle through each of the $(\eta_{pd})_K$, computing steps 3 - 5 below and modifying the subgrid geometry array.
3. Identify the single largest fully-connected wet patch in this coarse grid cell at this elevation. Mark the remainder of this cell as dry.
4. If the intersection between the wet patch and a coarse cell face at this elevation is zero, this face is blocked and has a subgrid face area of zero.
5. For two adjacent coarse grids both with nonzero areas on their common face at the same elevation, if the intersection of their wet subgrid indices on this face is an empty set, their common face area is zero.

In the present implementation this algorithm is used only at the start of the simulation to pre-store the effects of internal blocking. However, the algorithm could be easily introduced within the hydrodynamic time-stepping loop to allow dynamic modification of subgrid geometry (erosion or aggradation), issues that are worthy of further investigation.

An example of the block-checking technique is shown in Fig. 47a, where the water regions (blue) are divided by the land (brown), forming a river channel from left to right that is (mostly) not connected to the surrounding marshes. Following Eqs. (48) and (49), at $r = 15$ without block-checking the river bank would only be partially identified and blocked – as shown by the light blue faces that are the only subgrid faces with zero areas. Thus, näive application of the subgrid definitions in §D.2.1 will allow imaginary flow paths between the channel and its surrounding marshes. The new block-checking method identifies the red faces as additional blocked faces based on the high-resolution topography of the interior of each coarse-grid cell, which fully delineates the channel banks at an $r = 15$ coarsening as shown in Fig. 47a.

However, the block-checking method does not allow coarsening to arbitrarily large r, as illustrated in Fig. 47b for $r = 30$. As the coarsening ratio increases there is an increasing likelihood that multiple unconnected flow paths could exist in a single coarse grid cell, but the block-checking method (Step 3) is limited to considering only the largest inundation area in a grid as the "true" connected region of a single cell. This approach inherently blocks other flow paths because only one velocity is allowed to exist on each face. In Fig. 47c, one cell from Fig. 47b (delineated by a green box) is examined in detail. The *top* panel shows the binary wet/dry map (Step 1) of the original cell, which contains two disconnected water regions *A1* and *A2*. Comparing to Fig. 47b, we found that *A2* belongs to the river channel and *A1* is located in its surrounding marshes. The *bottom* panel of Fig. 47c shows the wet/dry map after performing Step 3, where *A2* is turned into land because its area is less than *A1*. This leads to blocking of the east face (through Step 4) and the south face (through Step 5) of the target cell, which interrupts channel connectivity.

Despite the failure behavior of the block-checking method at large r, it still shows advantages over naïve upscaling and the edge identification method by Hodges (2015) in maintaining surface connectvity, which will be verified in §D.3. It should be noted that model dependency on r varies for different domains, so to improve applicability over a variety of domains, the proposed block-checking method could be combined with some quantifications that reflect the "complexity" of topography, which is a topic that deserves further investigation.

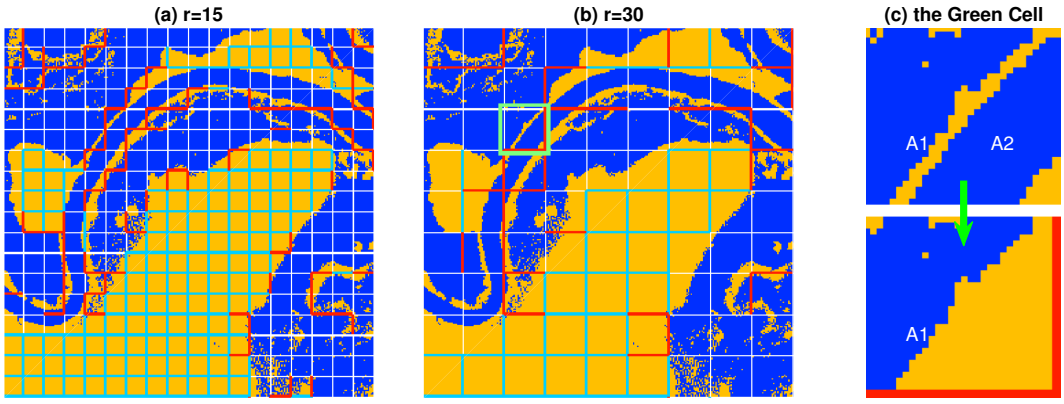

Figure 47: (a)-Internal blocking implemented over a coarse-grid map with 15×15 fine-grid resolution ($r = 15$) in each coarse cell. The fine-grid cells are a binary wet/dry map for a given η level (blue is wet, brown is dry). Light blue lines indicate blocked cell faces ($A = 0$) based on face-only subgrid cells using Eqs. (48) and (49). The red lines are additional blockages attributable to interior geometry using the block-checking method. (b)-The same region but with $r = 30$. (c)-The green cell in (b) examined in detail to show how channel connectivity is interrupted at large r, where *top* panel is the wet/dry map after performing Step 1, *bottom* panel is the wet/dry map after performing Step 3 (only 1 largest wet patch is retained.)

D.3 Test cases and Results

The new subgrid methods are tested on three bathymetries: (i) an idealized channel, (ii) a highly-resolved portion (170 hectare) of a narrow waterway at the west end of the Nueces Delta – the Upper Rincon Bayou (URB) – and (iii) a larger portion (2178 hectare) of the Nueces Delta (the Upper Nueces Delta, UND). To understand the effects of the subgrid model we generate a range of model bathymetries to use for comparisons. The baseline comparison cases (*M*) use a $2\Delta x$ median filter for upscaling topography as described in Hodges (2015). The *M* simulations are a naïve grid-coarsening that is applied without any consideration of subgrid features in the upscaling or in the numerical solution. The second set of comparison cases are *MB* cases – median filter with block-checking – which use the approaches of Hodges (2015) and Z. Li and Hodges (2019b) to upscale topography as edge blocking and channelization, but do not include the new subgrid model described above. The test cases with the new subgrid model (§D.2.1-D.2.3) are labeled the *S* test cases. test cases using the new subgrid model together with the new block-checking method (§D.2.4) are named *SB*. Note that the letter *B* indicates the use of a block-checking method to identify small-scale water-blocking features, but identification processes are different for *MB* and *SB*. The former comes from Hodges (2015) and the latter follows §D.2.4. The difference between tested scenarios are summarized in Table. 7.

Table 7: List of differences among tested scenarios.

Scenario label	M	MB	S	SB
Median filter	Yes	Yes	No	No
Edge/channel identification (Hodges, 2015)	No	Yes	No	No
Subgrid variables (§D.2.1-D.2.3)	No	No	Yes	Yes
Block-checking (§D.2.4)	No	No	No	Yes

D.3.1 Idealized channel

The Idealized Channel bathymetry uses a uniform flat bottom (with bottom elevation 0.5 m) with a varying-width wide channel (50 to 120 m width) connected internally by a narrow channel (5 m wide) and accompanied by two non-submerged vertical walls as illustrated in Fig. 48. The forcing boundary condition for this test case is a sinusoidal tide (range from 0.8 to 1.2 m above the $z = 0$ bottom, with a period of 6 h) along the open boundary of the model domain. The initial surface elevation is uniform at the tidal elevation for $t = 0$. The initial velocities are all zero. The initial scalar concentrations (herein salinity) are created with a piecewise constant function that can be visualized in Fig. 48, which makes it easy to observe instantaneous flow patterns all over the domain. The salinity at the tidal boundary is fixed to a constant value of 25 psu.

For Idealized Channel test cases we apply a grid-coarsening ratio of $r = 10$ ($\Delta x = 10$ m), which is the point where the narrow channel and the walls are entirely lost in the *M* coarse grid but still appear in the *MB* grid. However, the *MB* overestimates the interior wall heights and the width of the narrow channel. The modeled salinity transport in the Idealized Channel at $t = 7$ h is shown in Fig. 49. The fine-grid simulation (Fig. 49a) shows the higher salinity wrapping around the unsubmerged walls and a small flux through the narrow channel. These features are qualitatively reproduced by the subgrid model (Fig. 49d). The coarse-grid simulation *M* (Fig. 49b) produces a significantly different transport result due to the loss of the interior walls and the narrow channel. The *MB* simulation (Fig. 49c) shows some effects of the walls, but allows greater flux through the narrow channel because the channel is widened to match grid size. Note that the blocking walls that are evident in the control solution do not appear in the visualization of the subgrid model results because the *min* function is used for bottom elevations (Eq. 46), but their effect is captured by the subgrid model as can be clearly seen in the sharp, rectilinear change in the salinity contour where the walls should be in Fig. 49d.

A quantitative evaluation of the subgrid model is performed by estimating the absolute error of salt flux over one tidal period across two cross-sections in the wide and narrow channel respectively (*X1* and *X2* as labeled in Fig. 49a). The fine-grid simulation is used as the “true solution" for computing error. As shown in Fig. 50, the *SB* simulations produce minimal errors among all test simulations for both channels. The interquartile ranges (IQR) for the subgrid simulations are also much smaller, indicating that the *SB* scenarios consistently outperform the other scenarios over the entire tidal

period. Error for the coarse-grid simulation *M* is not shown at *X2* because the narrow channel is completed ignored after filtering.

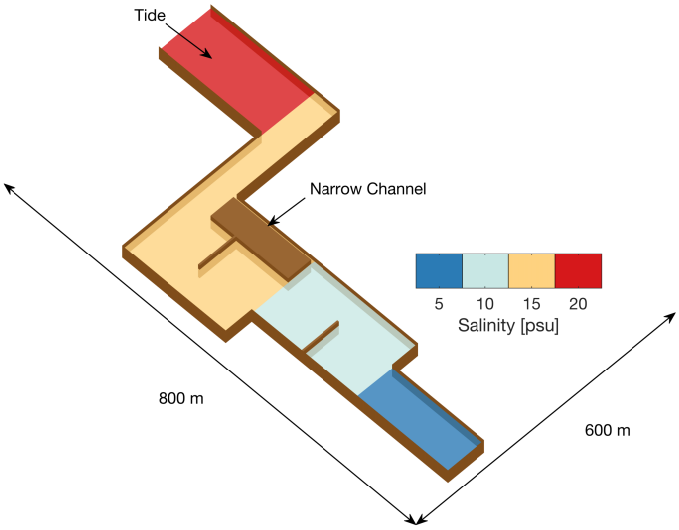

Figure 48: Idealized channel computational domain (presented at $1 \times 1m$ resolution). The initial condition for salinity is shown by the color scheme in the wet region. Vertical elevations are exaggerated for clarity.

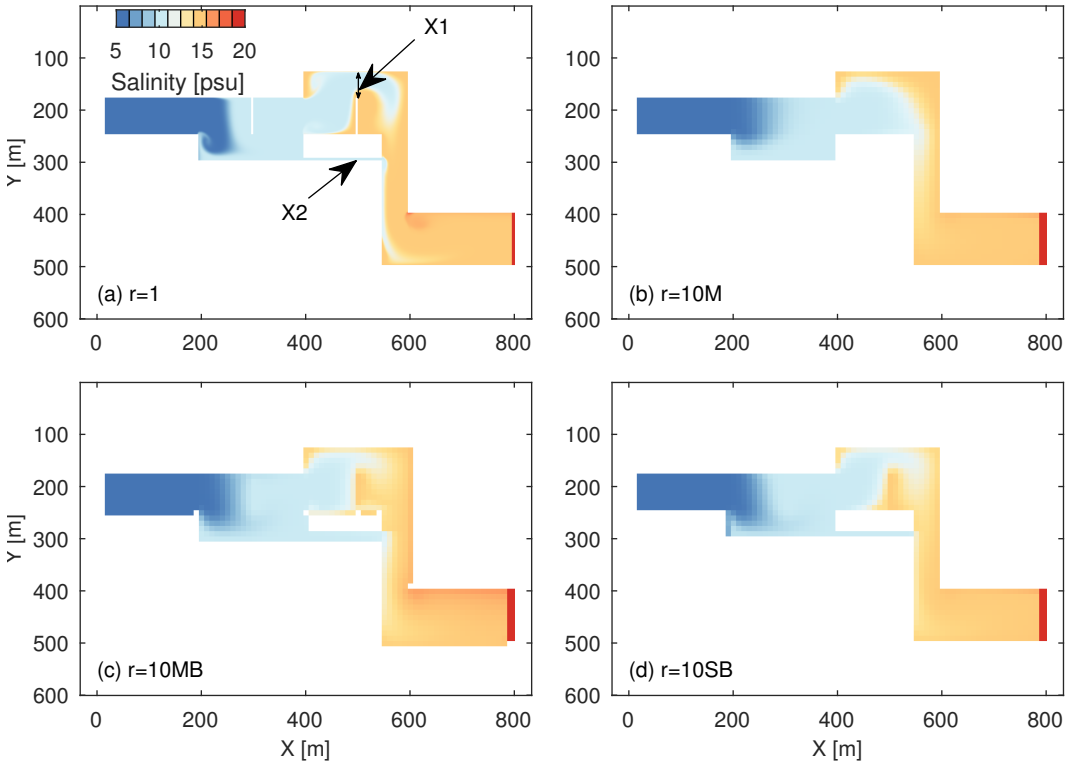

Figure 49: Modeled scalar concentration (salinity) at $t = 7$ h for the Simple Channel bathymetry. The channel cross-section *X1* and *X2* for computing salt flux error are labeled in (a). Labels of different scenarios are described in Table. 7.

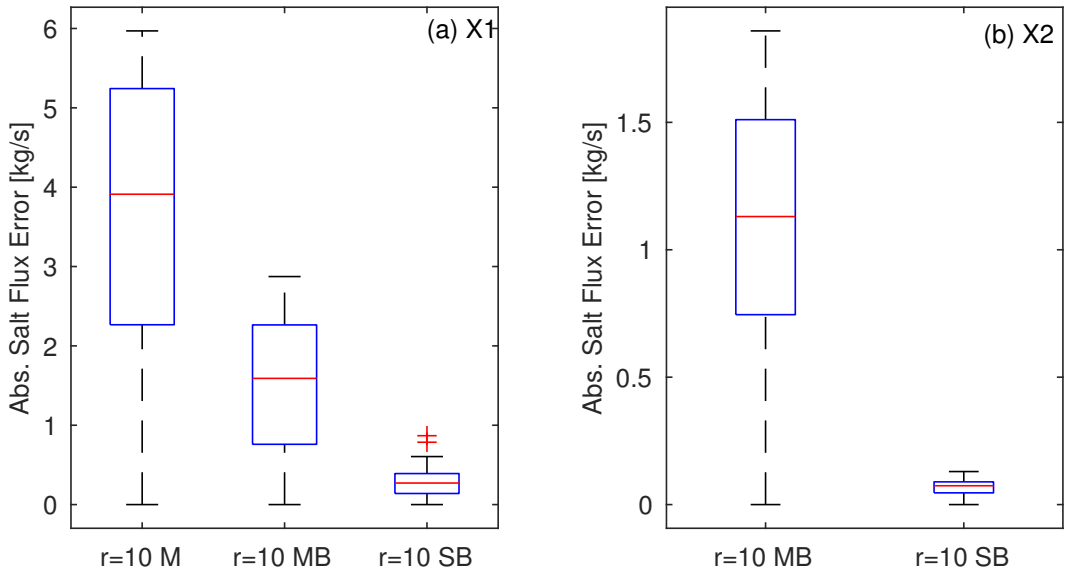

Figure 50: Absolute error of salt flux over one tidal period across cross-section *X1* and *X2* (Fig. 49).

D.4 The Upper Rincon Bayou (URB)

The two test cases with real-world bathymetry use a lidar data set from the Nueces River Delta along the Texas (USA) coast near the City of Corpus Christi. This data was previously used in studies of Hodges (2015); Z. Li and Hodges (2019b); Ryan and Hodges (2011), wherein further details can be found. The Nueces Delta is a shallow, micro-tidal river delta with limited freshwater inflows. The river now debouches through a main channel that is isolated from the delta and upstream dams have reduced overbanking events that previously flooded the system. Increasing episodes of hypersalinity became subject of a lawsuit and eventually an agreed order to mitigate the impact of the dams on the wetlands (Lloyd, Tunnell, & Everett, 2013). Towards this end, a pumping system was installed for controlled introduction of freshwater into the upstream end of the delta (Del Rosario & Montagna, 2018; Hill et al., 2015; Lloyd et al., 2013). The delta system has been subject of a number of studies and physical modifications over the past two decades.

The test bathymetry for the Upper Rincon Bayou (URB), shown in Fig. 51, is a small section extracted and slightly modified from the full 1×1 m data set. This is a section of the Rincon Bayou where the shallow depth and complex flow paths caused poor model-data agreement in a prior study (Z. Li & Hodges, 2019b). An artificial bay on the east end of the model domain is connected by a narrow channel to the Rincon Bayou to provide the tidally-driven forcing. The channel dimensions are similar to those in the Rincon Overflow Channel (ROC) that was created to improve flushing in the upper marsh (Dunton et al., 2000). The west end of the domain is blocked with a fixed wall. A sinusoidal tide (with range from 0.3 m to 0.7 m and period of 24 h) is added to the open boundary on the east for the URB test case.

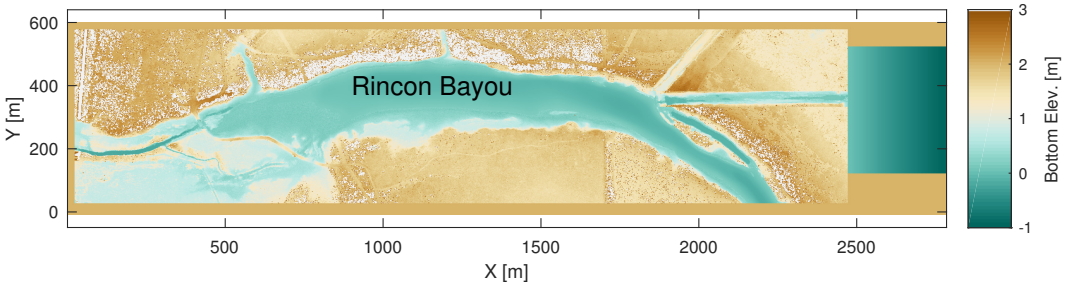

Figure 51: Bottom elevation of the Upper Rincon Bayou test case at 1×1 m resolution.

For the URB simulations, the control simulation uses $\Delta x = \delta x = 1$ m; the reference cases *MB* and the *SB* test simulations use grid coarsening with $r \in \{4, 8, 16, 32\}$, i.e., $\Delta x \in \{4, 8, 16, 32\}$ m. Since we have shown the effectiveness of *MB* over *M* in Fig. 50 and in Z. Li and Hodges (2019b), the subgrid model is only compared to *MB*. Figure 52 shows the surface elevations at $t = 34$ h for $r \in \{1, 16, 32\}$. Results at coarse resolutions are downscaled onto the high-resolution bathymetry following Sanders and Schubert (2019). The overall differences between the surface elevations in the control (1×1 m) simulation, the reference simulations (*MB*) , and the test simulations (*SB*) are small in magnitude – mostly a few cm across the majority of the domain. All the coarse-grid simulations tend to overestimate the surface elevation, with the *MB* scenarios having a more substantial disagreement than the *SB* scenarios. A clear quantitative difference is in the marginal wetland flooding that shows up as dark purple along the lower left edge of Fig. 52a. The dark purple indicates lower water surface elevation due to constricted connectivity between the bayou and this wetland area. All of the *SB* results preserve the reduced connectivity and lower water surface elevations. However, for the coarse-grid $r = 16$ scenario with *MB*, the connectivity to the wetland is increased and it floods to higher water surface elevations.

We can better understand this effect by examining areal flooding extent, as shown by the time evolution of the integrated inundation area in Fig. 53. For the *S* and *SB* scenarios, inundation area is simply the sum of subgrid face areas, A_Z. For an *MB* scenario performed at $r > 1$, two methods are used to estimate inundation area. The first method is based on the coarse-grid bathymetry at r, where all wet coarse cells have a surface area of $\Delta x \Delta y$ (Fig. 53a). The second method downscales the modeled surface elevation onto $r = 1$ fine-grid bathymetry (Sanders & Schubert, 2019) and sums the areas of the wet fine cells (Fig. 53b). For both methods, at $r = 8$, the disagreement in the *MB* begins to increase, and has significantly diverged from the other simulations at $r = 16$ and $r = 32$. In

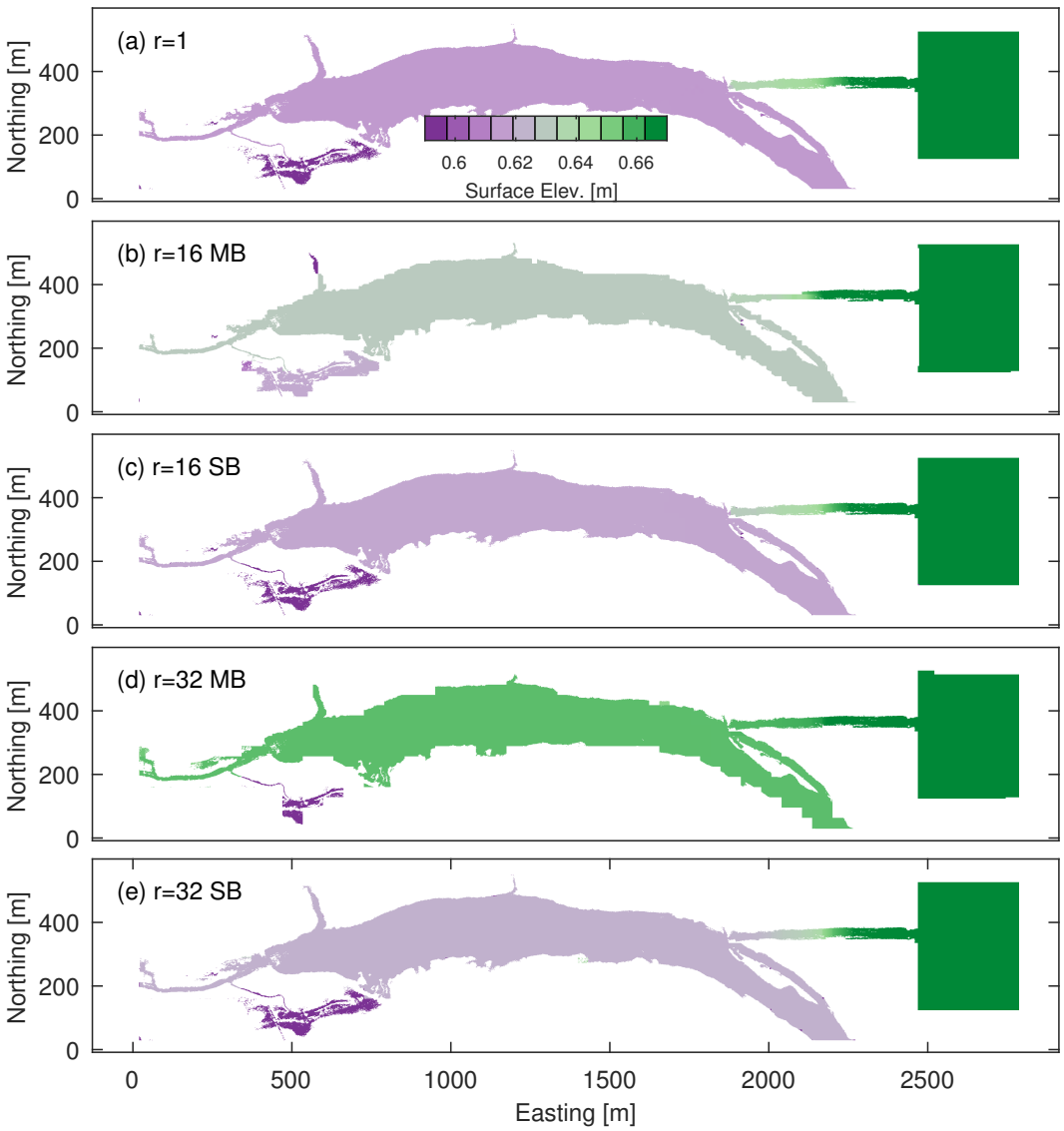

Figure 52: Water surface elevations for URB scenarios at $t = 34$ h ($r = 1, 16, 32$), when the tide is drawing down the water surface level. Labels of different scenarios are described in Table. 7.

contrast, the *SB* results at $r = 16$ and $r = 32$ remain quite similar to the control case. At $r = 16$, the *S* scenario generates higher errors than *SB*, but it still outperforms *MB*. The block-checking method (§D.2.4) prevents creation of unexisted new flow paths during grid-coarsening, whereas the use of minimum bottom elevation (Eq. 46) prevents removal of existing narrow flow paths. The comparison between *MB*, *S* and *SB* indicates both methods are important in maintaining surface connectivity when coarsening the shallow-marsh bathymetry.

More insights are obtained by analyzing the different behaviors of *MB* scenarios between Fig. 53a and b. The difference in inundation areas between the *MB* and *SB* scenarios are affected by three factors: (i) surface connectivity of key flow paths, (ii) surface area within the coarse grid cells (using A_Z versus $\Delta x \Delta y$), and (iii) predicted surface elevations. In Fig. 53a, the *MB* scenarios overestimate inundation area because the dominant factor here is (ii). In Fig. 53b, however, the effects of factor (ii) is removed because the surface area is calculated at fine scale. Underestimation of inundation area is thus caused by factor (i), where many deep subgrid cells near the wetting/drying front are smoothed on the *MB* bathymetries. Factor (iii) has negligible effects on the tested scenarios because the difference in predicted surface elevations are small (only a few centimeters, Fig. 52). With either

Fig. 53a or b, the results verify the effectiveness of the new subgrid method (*SB*) in maintaining high-resolution surface connectivity and inundation patterns at large r.

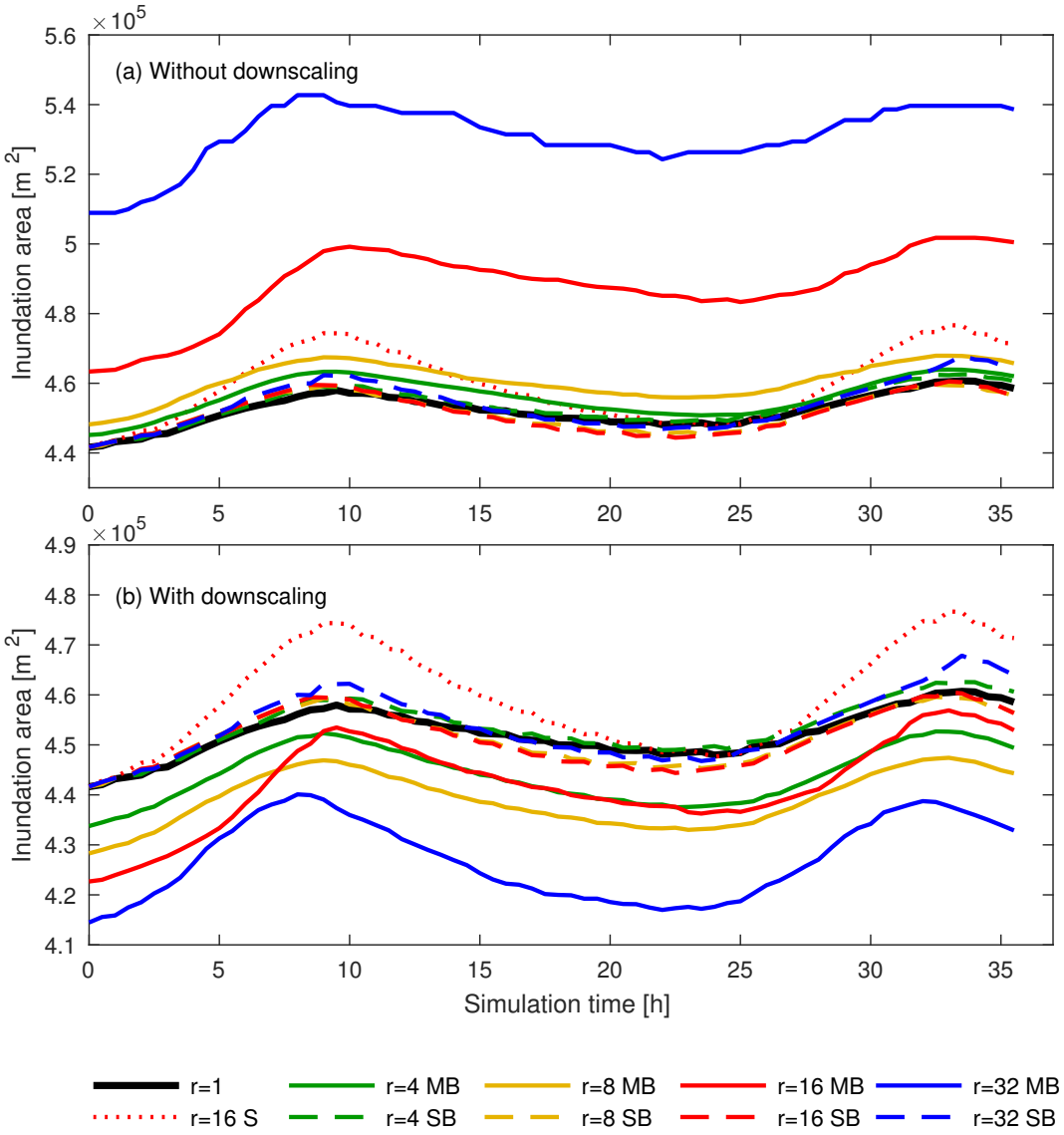

Figure 53: Inundation areas of the URB scenarios. For the *MB* scenarios, the inundation areas are calculated with respect to (a) the coarse grid bathymetry, and (b) the 1 m resolution fine grid bathymetry. Labels of different scenarios are described in Table. 7.

Quantification of flow rate error in the channel between the bay and the Rincon Bayou over one tidal period is provided in Fig. 54. Since we have shown that *SB* is superior over *S* in maintaining surface connectivity, the following analysis only focus on the difference between *SB* and *MB*. The *MB* scenarios show maximum error at $r = 32$ and decreasing error as r increases from 4 to 16. Since natural topography is spatially heterogeneous, grid-refinement does not necessarily reduce model error. The grid-coarsening method adopted (Hodges, 2015) involves filtering as well as edge and channel identification, so its ability to resolve high-resolution topography does not depend on r alone. Furthermore, grid-coarsening enhances numerical diffusion, which reduces flow rates. The reduction of model error for $r = 16$ *MB* may be caused by a balance between multiple error sources. Despite the complex behaviors of model error, two observations can be made regarding the proposed subgrid model. First, the *SB* model errors show weak dependency on r, which allows it to perform well at very coarse grid. In Fig. 54, the *MB* error abruptly increases at $r = 32$. The *SB* error, however, maintains a mild increase. Second, the *SB* errors produce smaller IQR than the *MB* scenarios, indicating stable

variations over the entire tidal period. This is an evidence that the *SB* error does not come from occasional balance between multiple sources, but from processes that are not simulated in the present subgrid model (e.g., topographical features in the cell interior). Although the *MB* simulation can produce a slightly smaller median error (e.g., at $r = 16$), it always has a larger interquartile range, indicating the subgrid model has better applicability over a variety of domains, coarsening ratios and flow characteristics.

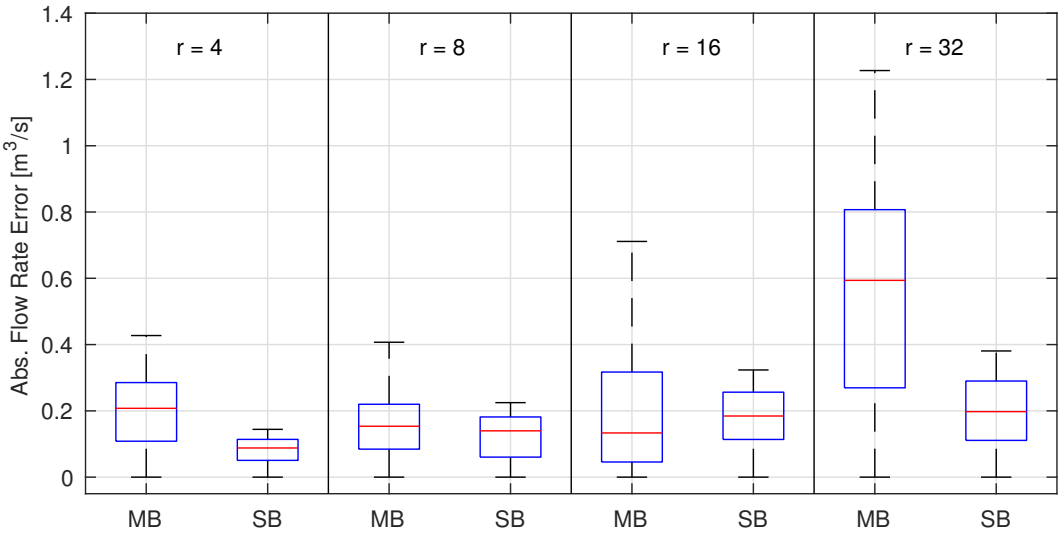

Figure 54: Statistics of the flow rate error in the channel connecting the Bay and the Rincon Bayou for the URB scenarios.

D.4.1 The Upper Nueces Delta (UND)

The Texas Water Development Board (TWDB) collected field data of water depth and salinity at 14 monitoring stations in the Nueces Delta, which enables us to test the subgrid model with realistic boundary conditions. The final test case – Upper Nueces Delta (UND) – uses a larger portion for the Nueces Delta, as shown in Fig. 55. The pump station where freshwater is introduced is noted at the left side of the figure. The region between the pump station and the Rincon Overflow Channel is the area extracted for the URB test case in Fig .51. Six of the 14 TWDB monitoring stations are located within this domain, which are labeled from Nueces1 to Nueces6. A 7th station is located at the east boundary, which is used to provide tidal and salinity boundary conditions. Other boundary conditions involved are wind data available at Texas Coastal Ocean Observation Network (TCOON, 2019), as well as pump inflow that is available from Nueces River Authority (NRA, 2019). Three cross-sections (*Y1* to *Y3*) are labeled in Fig. 55. Flow rates across these sections will be used as indicators for evaluating model performance. For the UND, running a multi-month simulation at $\delta x = 1$ m is impractical with our available computational power, so we use only coarser simulations along with field data for real-world evaluation of the model performance.

In modeling the Upper Nueces Delta (UND), the tested coarsening ratios are $r \in \{5, 10, 15, 30, 50, 75\}$. To avoid overlong spin-up at fine resolutions, we use a 45-day spin-up time from Apr. 1st to May 15th of 2013 at $r = 15$ followed by a 15-day spin-up at each tested value of r. Previously, the full Nueces Delta modeled at coarse resolution was shown to have a 60-day spin-up for salinity (Z. Li & Hodges, 2019b). The model results are reported for a 15-day period in the first half of June, 2013, which brackets an 11-day period during which the pumping system was providing a total of 10^6 m^3 freshwater into the upstream end of the delta (NRA, 2019).

Figure 56 shows a qualitative comparison of the salinity fields during pumping for $r \in \{5, 30, 50\}$. It can be seen that the three subgrid scenarios predict similar spatial distribution of freshwater, but as r increases, stronger numerical diffusion smooths salinity gradient at the interface of fresh and saline water. Compared to the *SB* scenario, the *MB* at $r = 5$ predicts more freshwater entering the West Lake via Rincon Overflow Channel (ROC) and less freshwater down through Rincon Bayou, but this difference is negligible compare to the differences at larger r. The *MB* at $r = 30$

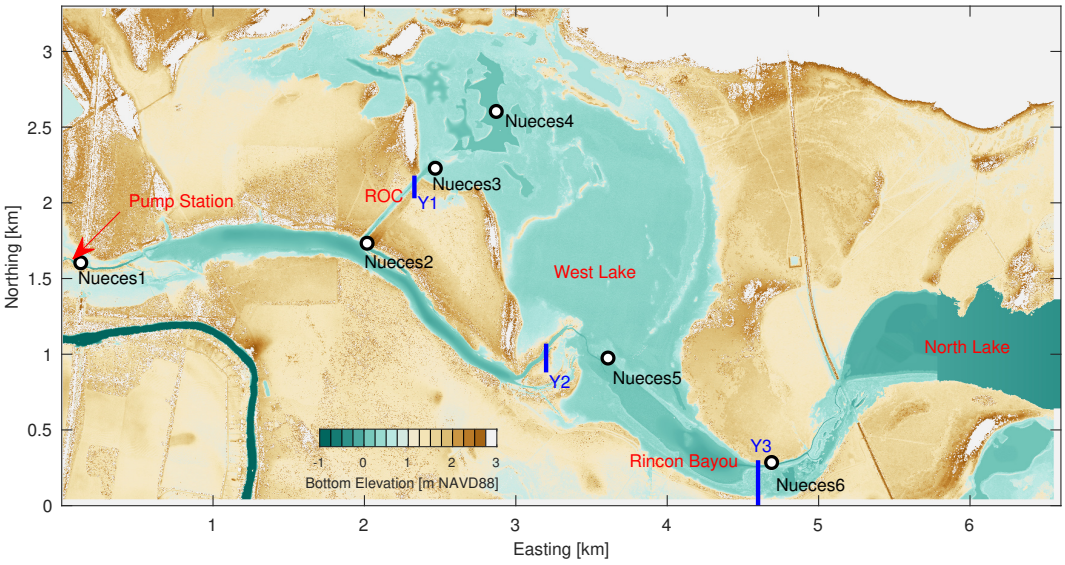

Figure 55: $1 \times 1m$ bathymetry of the Upper Nueces Delta (UND) test case. Locations of 6 field monitoring stations, the pump station and the Rincon Overflow Channel (ROC) are labelled. *Y1* through *Y3* are cross-sections where flow rates are evaluated and analyzed in §D.4.1.

underestimates pump flow in both channels, which is likely caused by an overestimation of volume as the *MB* grid-coarsening procedures are not volume-conservative. At $r = 50$, freshwater into the West Lake is completely omitted in *MB* scenario because the surface connectivity of the ROC is cut off. We may conclude that the subgrid model is relatively insensitive to r as it better approximates the high-resolution surface connectivity and salinity transport patterns at relatively large r ($r = 30, 50$) owing to the conservation of subgrid cell volume as well as the block-checking procedure.

A quantitative comparison of absolute values of flow rates (not flow rate errors) for all UND tested scenarios are given in Fig. 57 for the three cross-sections labeled in Fig. 55. Two main observations can be made:

1. For most values of r, the *SB* scenarios have relatively smaller IQRs than the *MB* scenarios and they show relatively weak dependency on r. This phenomenon is particularly obvious at *Y3* (Fig. 57c).
2. For $r \geq 50$, surface connectivity of the *MB* scenarios begins to be interrupted, which is reflected by a sudden decrease of median flow rate and IQR at *Y1*. This matches the observation from the salinity contour (Fig. 56e). The interruption of connectivity is also found for *SB*, but at a higher value of $r = 75$.

These two observations again indicate than compare to *MB*, the proposed subgrid model better preserves the high-resolution topographical characteristics (surface connectivity and volume) at large grid-coarsening ratios. The *SB* bathymetry is able to maintain surface connectivity at higher r than *MB*. Even if both scenarios maintain surface connectivity, using *MB* bathymetry overestimates flow rate due to expansion of channel width to match the grid size (Z. Li & Hodges, 2019b), which leads to higher IQR and strong dependency on r. However, since the cell volumes are also overestimated, given the same inflow rate from pumping, it decelerates salinity transport towards the West Lake because freshwater accumulates in the Rincon Bayou.

The modeled salinities are compared to the field data in Fig. 58 to provide further insights. It should be noted that although comparisons at all six stations in Fig. 55 can be made, they do not necessarily highlight the effectiveness of the subgrid method because the stations might be located in regions where variation of subgrid-scale topography is smooth and trivial, or other error sources might dominate. Figure 58 only shows results at Nueces3 and Nueces5 located near *Y1* and *Y2* (Fig. 55) where scalar patterns are strongly affected by subgrid topography. Results at other stations are provided as supplemental material. A detailed analysis of model-data agreements and other dominant error sources can be found in Z. Li and Hodges (2019b).

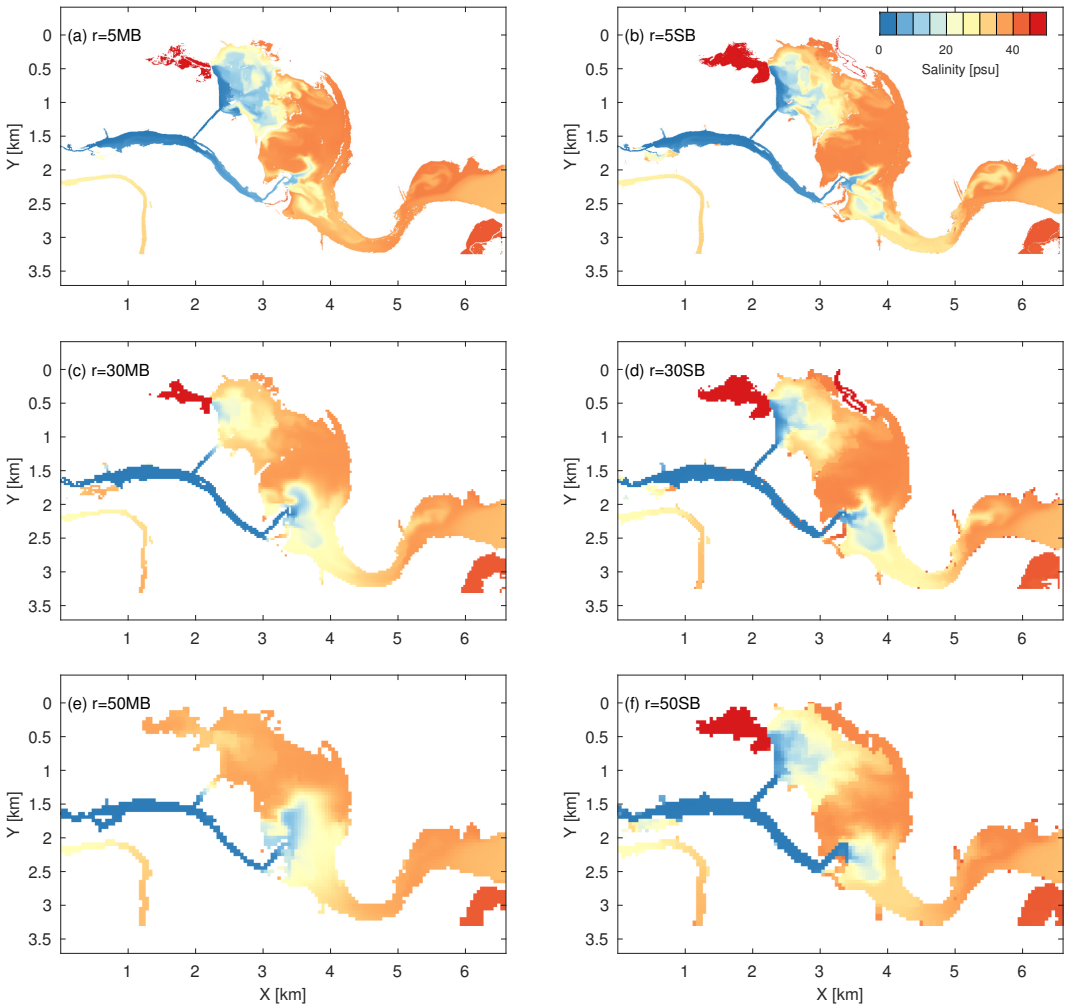

Figure 56: Spatial patterns of salinity for selected UND test scenarios at June 6th of 2013.

At Nueces3 (Fig. 58a), the decrease of salinity upon freshwater-pumping is successfully reproduced by all *SB* scenarios. But for the *MB* scenarios, salinity displays oscillatory behaviors at $r = 30, 50$. It implies weaker freshwater flushing, which is in agreement with Fig. 54. As stated above, this is caused by an overestimation of volume that slows down spreading of salinity. At Nueces5 (Fig. 58b), all test scenarios predict delayed response to freshwater pumping. It comes from a combination of errors such as bathymetry, boundary condition and possibly field data itself (Z. Li & Hodges, 2019b). Due to the complex nature of shallow marsh modeling, the subgrid model is not expected to correct all errors in one step, but it certainly provides improvements over existing *MB* models, especially at large r and at locations where surface connectivity is easily broken.

D.4.2 Computational cost

The key advantage of any subgrid method is in the ability to model a system faster than would be required at fine grid resolution. Thus, there is always a question as to how much additional cost is incurred by the subgrid algorithm itself. The effective computational cost of the subgrid algorithm can be evaluated by a speed-up ratio, $\Delta\tau_{\text{coarse}}/\Delta\tau_{\text{fine}}$, where $\Delta\tau$ is the computational time for a simulation and subscripts indicate the coarse and fine grid. Computational cost is evaluated for the URB scenarios by plotting the speed-up relative to 1 m simulation on Fig. 59. All scenarios shown in Fig. 59 are executed in serial with Intel Xeon Platinum 8160 (“skylake") nodes in Stampede2 at the Texas Advanced Computing Center. We use the same time step $\Delta t = 0.5s$ for the control cases and the test cases with different grid-coarsening ratios so that the relationship between cost

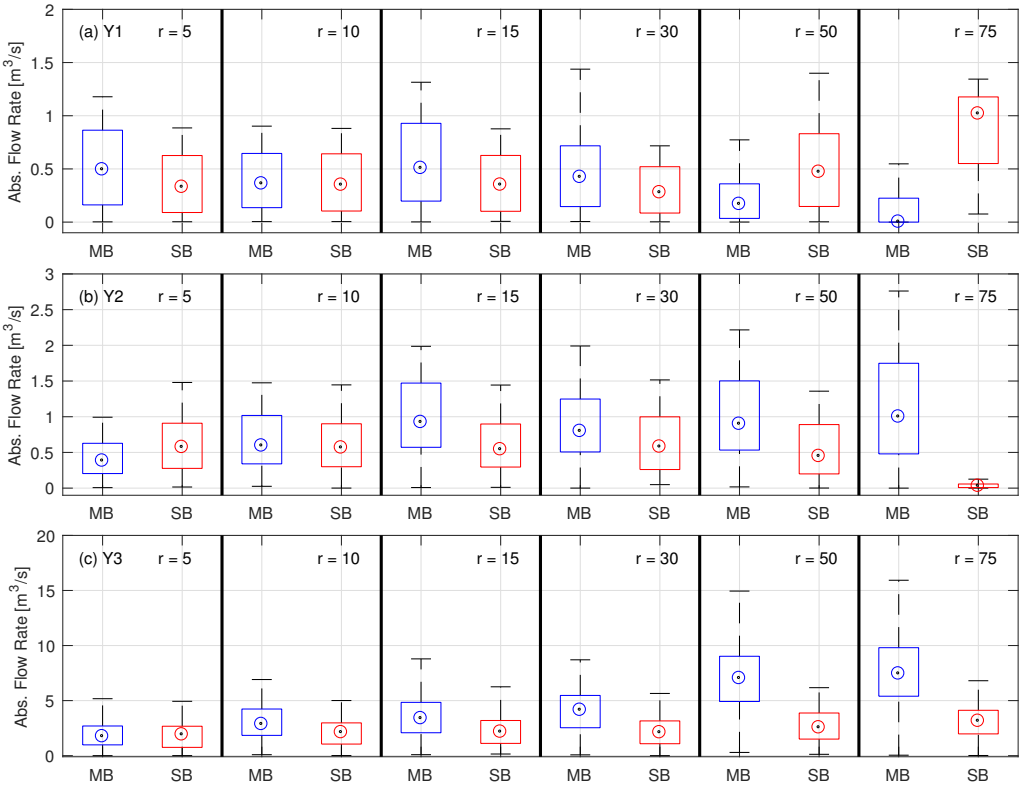

Figure 57: Statistics of absolute flow rates across *Y1* through *Y3* for tested Nueces Delta scenarios from May 30th to June 15th of 2013 (Note that this is not flow rate error because simulation at $\delta = 1$ m is not performed. The purpose of this figure is to show the *SB* scenarios have weak sensitivity to r, rather than showing that *SB* scenarios have low error).

and coarsening ratio is more clear. In practical applications, Δt for coarse-grid simulations can be further increased as long as the Courant-Friedrichs-Lewy (CFL) condition is met, so an additional test scenario is performed with $r = 8$ and a larger time step $\Delta t = 10s$. It can be seen from Fig. 59 that the subgrid scenarios generally have lower speed-ups compared with the corresponding *MB* scenarios. The reduction is caused by searching and interpolating among the pre-defined surface elevations, as well as increased number of wet cells for the *SB* scenarios (which is not equivalent to increased inundation area) due to the use of Eq. 46. Given this reduction in speed-up, adapting subgrid method is still much more efficient than performing a $2\times$ grid refinement even with the same time step Δt. By using a larger time step ($\Delta t = 10s$) the speed-up can be further increased.

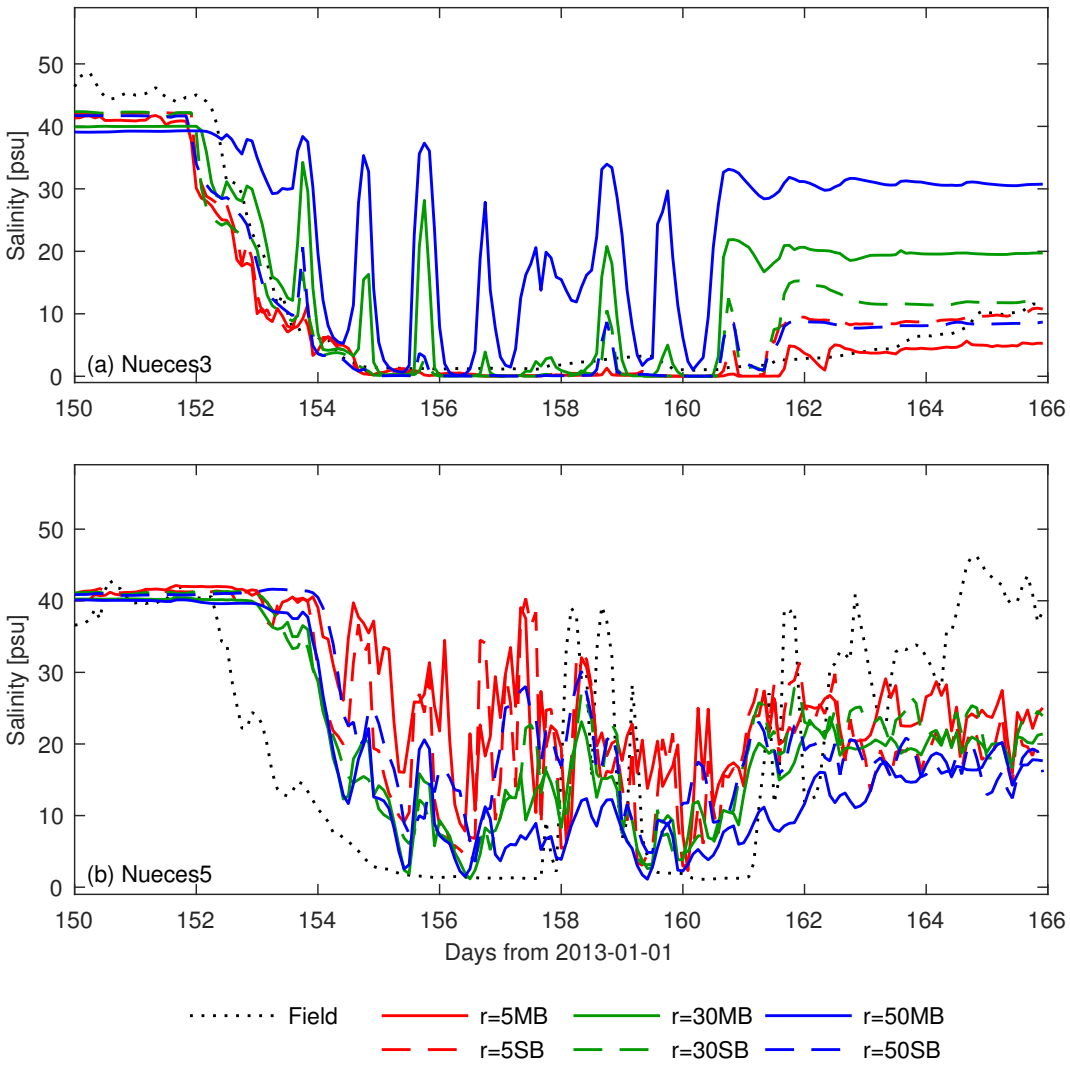

Figure 58: Comparison between modeled and measured salinity for selected test scenarios at Nueces3 and Nueces5.

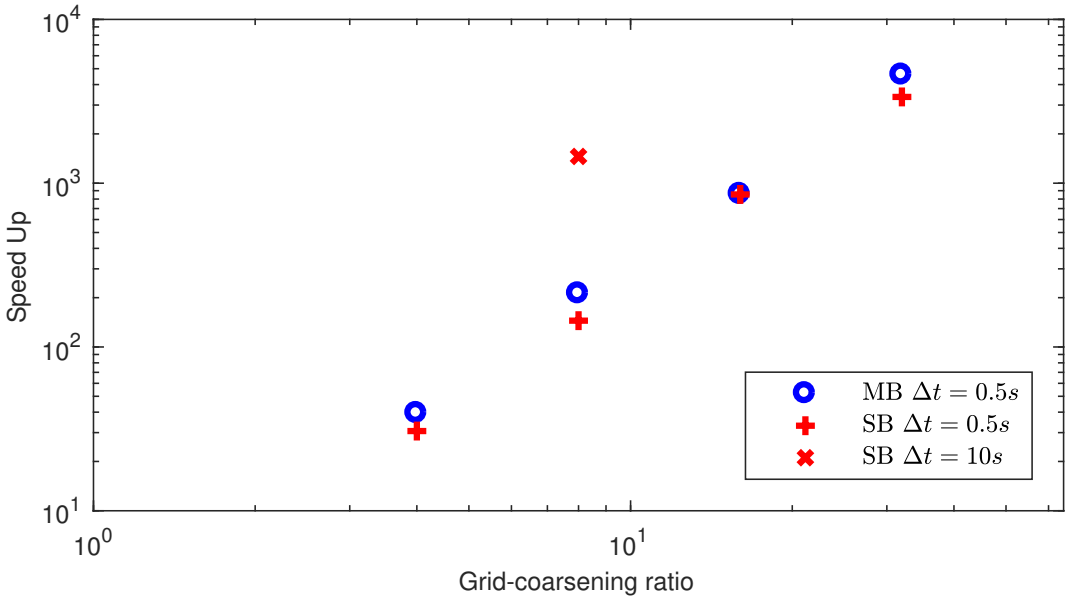

Figure 59: Speed-up of *MB* and *SB* scenarios tested on URB bathymetry. Speed-up values are calculated with respect to $r = 1$ scenario.

D.5 Conclusions

A method that simulates effects of subgrid-scale topography using practical coarse grids is designed and coded into the Fine Resolution Environmental Hydrodynamic Model (Frehd) for modeling hydrodynamics and salinity in shallow coastal wetlands. The proposed subgrid method parametrizes the subgrid-scale topography into four subgrid variables (subgrid cell volume and three subgrid face areas) that represent the high-resolution grid volumes and face areas. These variables are included in the continuity and momentum equations as parameters to scale mass/momentum storage and transport of coarse grids. An automatic block-checking method is developed to maintain high-resolution surface connectivity upon grid-coarsening.

The subgrid Frehd model (*FrehdC*), after parallelization, is evaluated using three test cases ranging from simple idealized channel bathymetry to real coastal-marsh bathymetry derived from lidar data. For all cases, compare to existing coarse-grid models, the surface elevation, inundation area, flow rate and salinity predicted by the subgrid model are closer to simulation results performed at finer resolutions. Model-data agreement for salinity is also improved with subgrid modeling. The subgrid simulation results show weak sensitivity to grid resolution, which means topographical features at finer scales are successfully captured. Compare to coarse-grid models, this resolution-independent behavior makes the subgrid model suitable for shallow marsh modeling at large grid-coarsening ratio (r) as long as the surface connectivity is not interrupted. Three key components that contribute to the advantages of the subgrid model are:

1. The use of minimum bottom elevation (Eq. 46), which guarantees accurate assessment of a cell's wet/dry status.
2. The conservation of cell volume during grid-coarsening (Eq. 47), which is critical in simulating salinity transport.
3. The automatic block-checking procedure (§D.2.4), which maintains high-resolution surface connectivity patterns at coarse grids.

Applying the subgrid method slightly increases computation cost compared to simulating on traditional coarse Cartesian grids, but it is still much more efficient than performing grid refinement. It should be acknowledged that there exists an upper limit for r beyond which surface connectivity is no longer maintained even with the block-checking method, but the range of applicable r values are proven larger than existing coarse-grid models.

Acknowledgement

The authors wish to thank the Texas Water Development Board for providing field data. This work has been supported by the Texas Water Development Board under interagency cooperation contracts 1400011719, 1600011928 and 1800012195.

E On modeling subgrid-scale macro-structures in narrow twisted channels

For the convenience of the reader, the following appendix provides the text and figures for portions of this study that are in press in the accepted paper Z. Li and Hodges (2020). Modifications have been made for consistent cross-references as an appendix to the present report. Note that the model development documented in this paper used the Nueces Delta as a test case rather than the Trinity Delta due to the availability of field data in the former. The model developments tested on the Nueces Delta were incorporated into the TDHM.

Article Title: **On modeling subgrid-scale macro-structures in narrow twisted channels**

Authors: Zhi Li, Ben R. Hodges

To be published in:
Advances in Water Resources
in press (2020)
https://doi.org/10.1016/j.advwatres.2019.103465

Abstract

Porosity-based subgrid topography models often fail to capture the effects of subgrid-scale topographic features in the interior of coarse grid cells. Existing approaches that modify bottom roughness or a drag coefficient are inadequate for macro-structures (large emergent or submerged obstacles) in subgrid-scale narrow twisted channels. Such structures partially block the cross-sectional area and provide enhanced topographic dissipation – effects that are not well represented by a drag coefficient that scales on a coarse-grid cell-averaged velocity and the cell volume. The relative alignment between mesh and flow further complicates this problem as it makes the subgrid model sensitive to mesh design. In the present study, three new approaches for simulating subgrid-scale macro-structures in narrow channels are proposed. The interior partial-blocking effect of structures is modeled as reduction of grid face-area. The sheltering of flow volumes around obstacles, which leads to topographic dissipation, is modeled by reducing the cell volume in the momentum equation (only). A mesh-shift procedure is designed to optimize mesh alignment for identifiable subgrid features. Combining the three subgrid methods improves the approximation of surface elevation and in-channel flow rate with a coarse-grid model. Tests are conducted for channelized flow using both synthetic domains and real marsh topography. The new methods reduce the overall mesh dependency of the subgrid model and provides stronger physical connection between effects of macro-structures and their geometry at coarse grid scales.

E.1 Introduction

Two-dimensional (2D) depth-integrated hydrodynamic models have been used to study salinity transport, evaluate hydrological modifications, and help restoring ecosystems at shallow estuaries and coastal marshes (e.g., Inoue et al., 2008; Matte, Secretan, & Morin, 2017; Zacharias & Gianni, 2008). The model domains are often characterized by frequent wetting/drying and complex flow paths of various spatial scales, which requires careful selection of an appropriate grid resolution that resolves important topographic features. Unfortunately, in practical applications the grid resolution is often limited by the available computational power. Modeling at coarse resolution (relative to the scales of smallest channels) leaves small-scale topographic features unresolved, leading to errors in modeled surface connectivity, inundation area, and flow rates (Z. Li & Hodges, 2019a, 2019b).

To improve results for practical coarse-grid simulations, subgrid topography models have been previously proposed to represent the large-scale effects of subgrid-scale features. Such models have been developed for efficient modeling of estuarine hydrodynamics (e.g. Sehili et al., 2014; Wu et al., 2016) and urban flooding (e.g., Guinot et al., 2017; Sanders et al., 2008). One popular type of subgrid models parametrizes the high-resolution topography as a “porosity" term similar to the approach for handling spatial hetereogeneity in groundwater models (e.g., Bates, 2000; Defina, 2000; Defina et al., 1994). Two types of porosities have been identified and used in the prior literature: the volumetric porosity (fraction of cell volume occupied by water) and the areal porosity (fraction of cell face area occupied by water). The former is used to adjust cell storage and the latter is used to adjust conveyance (i.e., flow rate) through cell faces (Sanders et al., 2008). Although porosity-based subgrid models can capture the changes of cell storage and flow conveyance across the cell faces, they ignore

the contribution from topographic features in the interior of a coarse cell. For general topography with wetting/drying, Z. Li and Hodges (2019a) designed a combined volume-area subgrid model that automatically preserves high-resolution surface connectivity, thereby allowing more than $30\times$ grid coarsening while maintaining complex connectivity patterns.

Arguably, the variability of structural scales in a marsh is fractal – from the winding of the channels themselves to the bank shapes and on down to the rocks, plants, stems, and leaves that affect fluid flow. We propose separating this structural space based on scales that can be modeled, scales that can be observed, and scales that are unknown. As a convenient set of equivalent definitions, a physical feature of length scale ℓ can be categorized as either (i) resolvable, (ii) macro-structure, or (iii) micro-structure. If we take a practical model grid scale as Δx (whereas topography data is available at a finer grid scale δx), the resolvable features are those of $\ell \geq \Delta x$ that can be directly represented in the model. The macro-structure features are those that are identifiable with available data between scales $\Delta x > \ell \geq \delta x$ and could be resolved in the model if we had sufficient computational power. The micro-structure are features $\ell < \delta x$ that are relatively unknown and constitute "roughness". For example, airborne lidar data readily provides $\delta x \sim 1$ m digital terrain that identifies physical structures over the wide expanse of a coastal marsh, but it is typically impractical to model hydrodynamics with today's computers at much less than a $\Delta x \sim 10$ m grid scale. Arguably, smaller-scale features such as plant topology are identifiable through structure-from-motion and land-based 3D lidar, but such methods are presently impractical over large areas and thus such features constitute micro-structure. The intersection of practical data collection scales and practical modeling scales set the boundaries between resolvable, macro-, and micro-scale features (Fig. 60).

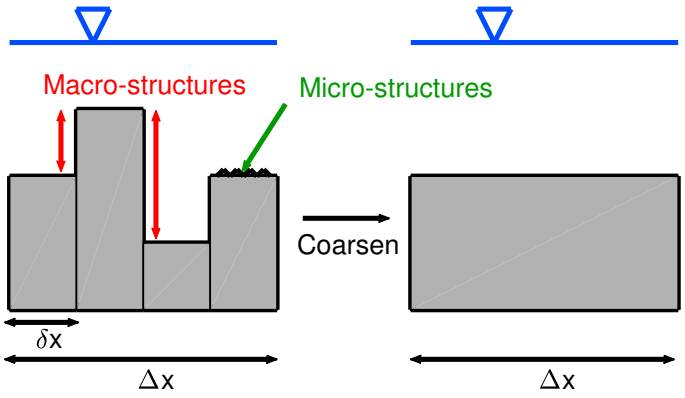

Figure 60: A coarse grid cell containing four subgrid macro-structures ($\Delta x/\delta x = 4$) whose effects must be represented on the Δx model grid

There are two major challenges associated with this conceptual model in a shallow 2D system: (i) upscaling of micro-structure drag, and (ii) upscaling of macro-structure flow effects. The two issues are closely related because the macro-structure channelizes flow and controls the subgrid spatial velocity distribution, which affects the micro-structure drag. The effects of micro-structures on an overlying shallow flow (at scale δx) are reasonably modeled using bottom roughness (e.g., Manning's n) that in 2D relates the depth-integrated drag force to the bottom stress characterized by the depth-averaged velocity – where both are considered only over a subgrid area $\delta x \times \delta x$. However, exact upscaling of the drag force from the δx subgrid scale to the coarse-grid Δx scale requires the subgrid spatial velocity distribution, which is unknown. Approximate upscaling is typically accomplished by introducing calibration parameters (Ozgen et al., 2015), assuming constant friction slope (Shin, 2016; Volp et al., 2013; Wu et al., 2016), or assuming a uniform flow direction at the δx scale (Duan et al., 2017). Unfortunately, in a shallow coastal marsh (as investigated herein) the spatial heterogeneity of subgrid channels cannot be adequately represented with the prior techniques. The underlying difficulty in this research area is that we do not have a comprehensive theory of fluid-structure interaction that provides the robustness of the kinetic energy/length scale relationship in turbulence modeling, e.g., as for plane jets and mixing layers in the ubiquitous $k-\epsilon$ turbulence model (Launder & Spalding, 1974). Thus, both the present and prior works rely on scalings that represent observable features and require the introduction of parameters that *cannot* be reduced to standard coefficients such as von Karman's κ or the C_μ, C_1, and C_2 that are standardized and used in $k-\epsilon$ subgrid models for a wide range of turbulence conditions.

Macro-structures are not necessarily random roughness elements and hence their anisotropic distribution affects the flow within a coarse-grid cell. For example, consider Fig. 61 that shows three coarse-grid cells with uniform bathymetry that is confounded by emergent macro-structure. These imaginary configurations are designed such that the volumetric porosity of the macro-structures are identical. Furthermore, as there are no edge blockages the face areal porosities are also identical. Nevertheless, it should be obvious that the different distributions of macro-structure will have significantly different effects on the overall flow through the coarse-grid cell. The cell in the left panel has an isotropic arrangement of the macro-structures, which generates similar resistance to incoming flow in both x and y directions. The middle panel is expected to have similar effects to the left panel for flow in the y direction, but has minimal resistance to flow in the x direction. Conversely, the right panel provides a preferential flow path in the y direction and slows flow in the x. An upscaling model needs to represent the anisotropic and heterogeneous effects of these structures on the flow field. The real-world problem becomes even more complicated as the macro-structures are rarely vertically uniform but have different horizontal areas at different vertical levels. Thus, changes in the water level (i.e., wetting/drying) can change the effective shape, drag, and flow connectivity through the macro-structure.

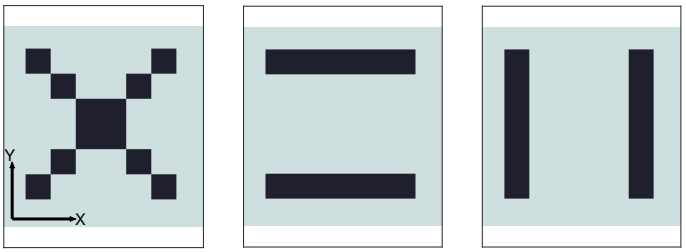

Figure 61: Theoretical arrangement of 12 emergent macro-structure elements in the interior of a coarse grid that would have significantly different flow effects. Light color represents the background topography and dark color represents emergent macro-structures. The three coarse grid cells have identical volumetric and areal porosities.

Prior subgrid models typically relate macro-structures to bottom stress and treat the coarse-grid drag coefficient C_D as a calibration parameter (e.g. Bruwier, Archambeau, Erpicum, Pirotton, & Dewals, 2017; Guinot et al., 2018, 2017; Ozgen, Liang, & Hinkelmann, 2016; Ozgen, Zhao, et al., 2016; Sanders et al., 2008). However, an effective theoretical linkage between a drag coefficient and the arbitrary 2D geometry of the macro-structures remains to be found. On the most fundamental level, if the size of a macro-structure is comparable to flow depth (the “low-submergence condition"), its bottom stress cannot be represented using Manning-type formulas (Cea et al., 2014; N. S. Cheng, 2015; Katul, Wiberg, Albertson, & Hornberger, 2002). Although other theories have been suggested for estimating drag coefficient – e.g., the use of turbulence mixing-layer theory (Casas et al., 2010) – a robust well-accepted alternative has not been found (Powell, 2014). Furthermore, macro-structures induce a variety of phenomena via mechanisms other than drag – e.g., sidewall obstructions (Azinfar & Kells, 2009) and momentum dissipation due to reflection of positive waves (Guinot et al., 2017) – that are not well-represented by a drag-law paradigm. Finally, it has been observed that the spatial heterogeneity of macro-structures cannot be fully captured through global calibration with one or two simple parameters (D’Alpaos & Defina, 2007; Horritt & Bates, 2001) and the complexity of geometry over an entire marsh make it impossible to obtain sufficient flow data for optimized local adjustment of calibration parameters (Z. Li & Hodges, 2019b).

To address the challenges discussed above, the present work builds on the subgrid blocking algorithm of Z. Li and Hodges (2019a), which preserves subgrid connectivity, and the porosity-based approaches of Guinot et al. (2017); Sanders et al. (2008) and Bruwier et al. (2017), which apply anisotropy in the porosity to represent coarse-grid interior and face-based effects. Herein we focus on sidewall macro-structures in the narrow twisted channels of shallow coastal marshes, where two issues (other than drag) associated with subgrid macro-structures are identified: (i) grid alignment and (ii) topographic dissipation. As a brief overview, the former issue arises because subgrid methods depend on the relationship between mesh faces and the macro-structures such that shifting the mesh can alter the number of macro-structure sub-elements in a given coarse-grid cell. To use this property to our advantage, a mesh-adjustment method is developed to rectilinearly shift the

uniform coarse-grid mesh into an optimum placement that provides the minimum number of cells that are "barely wet." The latter issue (topographic dissipation) is addressed in a new approach to coarse-grid upscaling of high-resolution topography (i.e., modifying formulation of the porosities) based on quantifications of the macro-structure geometry. The new methods are evaluated using both simple straight channels and real marsh channels. Compared to simple calibration using C_D, the new geometry-based representation of macro-structures provides a stronger physical connection between flow and topography, albeit at the additional complication of introducing a new parameter (γ, see §E.2).

A brief background of the numerical model, existing issues with topographic dissipation and grid alignment are provided in §E.2, together with description of the new subgrid methods that handles these issues. Test cases and results are described in §E.3. Discussions on model achievements, limitations and possible future directions are provided in §E.4. Our conclusions are presented in §E.5.

E.2 Methods

E.2.1 Hydrodynamic model

The present work builds on the subgrid method (SB) previously developed and implemented in the *FrehdC* model, which is explained in detail in Z. Li and Hodges (2019a) and briefly below. The *FrehdC* model is the C-language version of the Fine Resolution Environmental Hydrodynamic Model (*Frehd*), which was originally programmed in Matlab. The latter model inherits works by Hodges (2004, 2014, 2015); Hodges et al. (2000); Hodges and Rueda (2008); Z. Li and Hodges (2019b); Rueda et al. (2007); Wadzuk and Hodges (2009). The original *Frehd* code has been streamlined, parallelized, and reduced in options so that *FrehdC* efficiently solves the 2D depth-integrated free surface continuity equation, the momentum equations, and the scalar transport equation. These equations can be written in the volume-integrated form as:

$$\frac{\partial}{\partial t}\int_{\Omega}\eta d\Omega + \int_{\Gamma}\boldsymbol{u}\cdot\boldsymbol{n}dA = 0 \tag{68}$$

$$\int_{V}\left(\frac{\partial \boldsymbol{u}}{\partial t} + (\boldsymbol{u}\cdot\boldsymbol{n})\frac{\partial \boldsymbol{u}}{\partial \boldsymbol{x}}\right)dV = \int_{\Gamma} g\eta\boldsymbol{n}dA + \int_{\Gamma}\boldsymbol{\tau_{\nu}}\cdot\boldsymbol{n}dA + \int_{\Omega}\boldsymbol{\tau_{b}}d\Omega \tag{69}$$

$$\frac{\partial}{\partial t}\int_{V} C\,dV + \int_{\Gamma}(\boldsymbol{u}\cdot\boldsymbol{n})C\,dA = \int_{\Gamma}\boldsymbol{\tau_{\kappa}}\cdot\boldsymbol{n}\,dA \tag{70}$$

where η is the free surface elevation, $\boldsymbol{u} = [u, v]^T$ are depth-averaged velocities, $\boldsymbol{x} = [x, y]^T$ are the corresponding Cartesian axes, $\boldsymbol{n}$ is the normal unit vector, $\boldsymbol{\tau_b}$ is the bottom stress, $\boldsymbol{\tau_{\nu}}$ is the viscous stress, C is scalar concentration, $\boldsymbol{\tau_{\kappa}}$ represents scalar diffusion, dV is an infinitesimal volume inside the model domain (Ω) and dA is an infinitesimal face area, which can be written as $dA = h(\Gamma)d\Gamma$ where $h(\Gamma)$ is the depth function along a volume boundary Γ.

The bottom stress in Eq. (69) is modeled using:

$$\boldsymbol{\tau_b} = \frac{1}{2}C_D\,\boldsymbol{u}|\boldsymbol{u}| \tag{71}$$

$$C_D = \frac{g\tilde{n}^2}{\bar{H}^{\frac{1}{3}}} \tag{72}$$

$$\bar{H} = \begin{cases} \frac{V}{A_Z}, \text{with SB method} \\ \eta - z_b, \text{otherwise} \end{cases} \tag{73}$$

where C_D is the drag coefficient, $\tilde{n}$ is the constant Manning's roughness coefficient ($\tilde{n} = 0.03$ in this study). If the subgrid model is activated, $\bar{H}$ is the cell-averaged depth, V is the cell volume and A_Z is the free surface area. Both V and A_Z are computed from the high-resolution topography data as illustrated in Z. Li and Hodges (2019a). If the subgrid model is turned off, then $\bar{H} = H = \eta - z_b$, where z_b is the bottom elevation of a grid cell. Although physical viscosity and diffusion are important processes in a shallow marsh, they are predominantly determined by physics at the subgrid scale and are dominated by the numerical dissipation and diffusion in a coarse-resolution model (Z. Li & Hodges, 2019a, 2019b). As such, we focus our new methods on handling the critical issue of macro-scale effects of advection and reserve the study of macro-scale dissipation and diffusion as a subject for future research.

In traditional structured-grid models without subgrid topography (e.g., Hodges et al., 2000), a grid cell is typically described by a uniform bottom elevation z_b and grid sizes Δx, Δy, such that the horizontal water surface area at any free-surface elevation (η) is $\Delta x \Delta y$, the cell volume is $(\eta - z_b)\Delta x \Delta y$, and the cell face areas are $(\eta - z_b)\Delta y$ and $(\eta - z_b)\Delta x$. Arguably, the next level of complexity for modeling topography with a structured grid is that invoked by our SB method, where the grid cell topography is described using four subgrid variables that are all discrete functions of η: cell volume $V(\eta)$, surface area $A_Z(\eta)$, and side face areas $A_X(\eta)$, $A_Y(\eta)$. Similar to the artificial porosities used in other subgrid models (e.g., Guinot et al., 2018; Ozgen, Liang, & Hinkelmann, 2016), these variables are calculated from high-resolution topographic data over the range of possible values of η.

Following Casulli (1990), Casulli and Cattani (1994), and Z. Li and Hodges (2019a), Eqs. (68) and (69) can be written in discretized forms with embedded subgrid variables. For simplicity in exposition, these can be presented for the inviscid 1D case as:

$$\eta_i^{n+1}(A_Z)_i^n = \eta_i^n(A_Z)_i^n + \Delta t \left(u_{i-\frac{1}{2}}^{n+1}(A_X)_{i-\frac{1}{2}}^n - u_{i+\frac{1}{2}}^{n+1}(A_X)_{i+\frac{1}{2}}^n \right) \tag{74}$$

$$u_{i+\frac{1}{2}}^{n+1} = -g\Delta t K_{i+\frac{1}{2}}^n \frac{(A_X)_{i+\frac{1}{2}}^n(\eta_{i+1}^{n+1} - \eta_i^{n+1})}{V_{i+\frac{1}{2}}^n} + K_{i+\frac{1}{2}}^n E_{i+\frac{1}{2}}^n \tag{75}$$

where i is the cell center index, $i + \frac{1}{2}$ indicates variables stored at cell faces, n represents the time level when appears as superscript (different from Manning's $\tilde{n}$), K and E represent an inverse drag term and an explicit momentum source term that can be written as:

$$E_{i+\frac{1}{2}}^n = u_{i+\frac{1}{2}}^n - \Delta t u_{i+\frac{1}{2}}^n \frac{u_{i+\frac{1}{2}}^n - u_{up}^n}{\Delta x} \tag{76}$$

$$K_{i+\frac{1}{2}}^n = \left(1 + \Delta t \frac{C_D(A_Z)_{i+\frac{1}{2}}^n \sqrt{(u_{i+\frac{1}{2}}^n)^2}}{2V_{i+\frac{1}{2}}^n} \right)^{-1} \tag{77}$$

In Eq. (76), the first-order upwind scheme is used for the advective stencil as higher-order stencils are restricted by insufficient grid resolution in narrow channels (Z. Li & Hodges, 2019b). The variable u_{up}^n is the velocity at an upwind face, which could be $u_{i-\frac{1}{2}}^n$ or $u_{i+\frac{3}{2}}^n$ depending on the flow direction. It should be noted that following Z. Li and Hodges (2019a), the volumes in momentum (Eqs. 75, 77) are "staggered", i.e., they are defined at the cell faces. This leads to different volumes in x and y directions ($V_{i+\frac{1}{2},j}$ versus $V_{i,j+\frac{1}{2}}$) for a 2D stencil. For simplicity in notation, in the following sections we use $V_X = V_{i+\frac{1}{2},j}$ and $V_Y = V_{i,j+\frac{1}{2}}$ to represent the volumes in x, y directions for calculating momentum transport. This staggered volume approach does not affect mass conservation because the cell volume for calculating cell storage is still defined at a cell center.

Following the standard semi-implicit approach (e.g., Casulli, 1990), Eq. (75) is substituted into Eq. (74) to generate a linear system for η^{n+1}. Back-substitution of the linear solution into Eq. (75) provides the updated u^{n+1}. Subgrid variables are updated using η^{n+1} at each time step and hence are treated explicitly (e.g., A_X^n during the $n \to n+1$ solution step), which is consistent with the explicit treatment of Δz in Casulli and Cattani (1994) as discussed in Hodges (2004). Scalar transport is simulated as advective (first-order upwind) and diffusive transport of scalar mass flux, which guarantees mass conservation.

Two features introduced in the Z. Li and Hodges (2019a) SB method and used herein are (i) a "block-checking" algorithm that reconstructs the subgrid-scale water-blocking features that are smoothed during grid coarsening, and (ii) setting the bottom elevation of a coarse grid to be the minimum bottom elevations of all its subgrids. The block-checking algorithm eliminates extraneous flow paths that are created due to removal of blocking features in upscaling the grid. Using the minimum bottom elevation is a complementary function as it ensures that actual flow paths are *not* removed during upscaling. As a result, the high-resolution connectivity patterns are preserved in Z. Li and Hodges (2019a) at a large grid-coarsening ratio ($r = \Delta x / \delta x \gg 1$). Compared to structured-grid models that do not parameterize subgrid-scale topography, Z. Li and Hodges (2019a) showed the SB method provides a better approximation of surface elevation, inundation area, flow rate, and salinity at coarse grid resolution. The SB method is used as a baseline for improvement in the present work.

E.2.2 Partial blocking and topographic dissipation

Background

The underlying hypothesis of the present work is that the SB subgrid method, as discussed above, can be further improved by simulating the effects of interior macro-structures on the local flow field. Our contention is that one key feature missing in the SB (and other subgrid) method is the tendency of interior macro-structures to contract/expand cross-sectional areas of narrow channels. Such changes create shelter areas (e.g., recirculation zones) in which flow decelerates, leading to an increased velocity gradient across the channel breadth. This phenomenon can be viewed as enhanced "topographic dispersion" of momentum. By applying the SB method at coarse resolution, only one velocity is allowed to exist on each cell face (Guinot et al., 2018), which implies any velocity gradient in the cell interior will be smoothed, resulting "topographic dissipation" – i.e., the integrated kinetic energy of the average velocity, $\bar{u}^2 A$, is less than that implied by the velocity profile $\int u^2 \, dA$. The concept of topographic dissipation is applicable beyond recirculation zones and will be a factor wherever there are substantial real-world velocity gradients across a coarse-grid cell. Unless narrow channels are substantially wider than the coarse-grid scale, upscaling high-resolution topography will always lead to insufficient grid resolution across a channel breadth. Thus, the complex geometry of channel boundaries is an important component of the subgrid macro-structures that affect flow (Horritt, Bates, & Mattinson, 2006). Twists and turns of channel boundaries as well as subgrid-scale sidewall obstacles (e.g., bridge piers or natural contraction/expansion of channels) lead to non-uniform velocity distributions and topographic dissipation.

An example of flow at a highly-resolved grid cell that cannot be correctly resolved at a coarse grid (an hence implies topographic dissipation) is shown in Fig. 62a, where a coarse $r = 100$ mesh is overlapped with high-resolution simulation results in a straight channel with a sidewall obstacle (the macro-structure) that contracts cross-sectional area. A recirculation zone is found downstream of the macro-structure where the channel width expands. The high velocities are observed around the channel centerlines and away from the macro-structure, low velocities are observed in the recirculation zone. The expected physical result is stronger momentum transport around the centerline (conveniently referred to as the "advection zone") accompanied by weaker momentum transport in the recirculation zone and turbulent mixing at the interface of the two zones (Han, Mignot, & Riviere, 2017). For illustrative purposes, we can ignore the turbulent mixing layer and consider frictionless inviscid flow in two distinct zones (advection and recirculation zones) in a coarse grid cell, as shown in Fig. 62b. Here we model the flow as only in the x direction. Recall that momentum equation (Eq. 69) in x direction can be written in the form of the Newton's second law:

$$a_x = \frac{\sum F_{bx}}{\rho V_X} = \frac{\sum \left(F_{bx}\right)_{\text{adv}} + \sum \left(F_{bx}\right)_{\text{rec}}}{\rho \left(V_{X(\text{adv})} + V_{X(\text{rec})}\right)} \tag{78}$$

where F_{bx} is the barotropic force acting on volume V_X in x direction and subscripts "adv" and "rec" indicate values in the advective and recirculation zones, respectively. The recirculation zone generated due to the macro-structures has negligible mean velocity as the macro-structure exerts reaction forces against incoming flow thereby canceling the barotropic force, which is an argument similar to that used for the interior pressure term of Ozgen, Liang, and Hinkelmann (2016); Sanders et al. (2008). It is thus reasonable to neglect the barotropic force on the recirculation zone and rewrite the Newton's law as:

$$a_x = \frac{\sum \left(F_{bx}\right)_{\text{adv}}}{\rho \left(V_{X(\text{adv})} + V_{X(\text{rec})}\right)} \leq \left(a_x\right)_{\text{adv}} = \frac{\sum \left(F_{bx}\right)_{\text{adv}}}{\rho V_{X(\text{adv})}} \tag{79}$$

The above implies that topographic dissipation is caused by uniformly distributing the force $\sum (F_{bx})_{\text{adv}}$ over the volume of the entire coarse cell. Thus, a coarse cell with interior change of cross-sectional area can be characterized by considering the advection zone alone, and neglecting the recirculation zones that have minimal participation to the momentum transport. This effect can be achieved by replacing (e.g.) $V_{i+1/2}$ and $(A_X)_{i+1/2}$ in momentum and continuity, Eqs. (74) and (75) by the advective volume and advective cross-sectional area. The former is used to constrain excessive topographic dissipation and the latter is used to represent a "partial blocking" effects caused by the reaction forces. Unlike complete blocking of channel's cross section, which has been handled in Z. Li and Hodges (2019a), partial blocking does not completely eliminate surface connectivity but reduces channel conveyance as part of the cross section is blocked by the macro-structure.

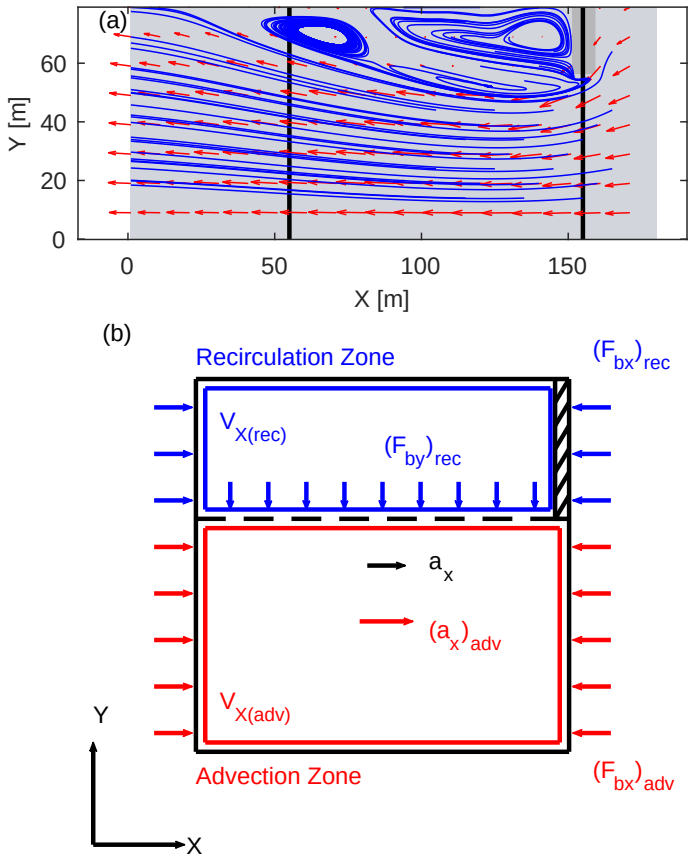

Figure 62: (a) An example of velocity field and streamlines affected by the macro-structures. The simulation was performed at $\delta x = 1$ m, but the results are displayed at a coarser grid resolution for clarity. Black lines represent a $\Delta x = 100$ m coarse grid. (b) Force balance for advection and diffusion zones in a coarse grid cell (similar to the center cell with sidewall obstacle in (a)) with two different estimates of fluid deceleration, a_x, and $(a_x)_{adv}$. Note that the dimensions and positions of the two zones are sketched for illustration purposes only. In a real channel, these depend on the geometry of the macro-structure as well as the flow field. The reaction forces are not labeled.

Method: Effective volume and effective area

To model effects of topographic dispersion (and counteract topographic dissipation), we argue the net force in the x direction at a coarse-grid cell face is applied over an effective volume $V_{X(\text{eff})}$ that is less than the full volume around the face, V_X. A similar argument applies for V_Y. The effective volume only includes regions where strong momentum fluxes are present, neglecting regions like recirculation zones where velocities are small. In the present study, we adopt the simplification made in Fig. 62, where a coarse cell is split into distinct advection and recirculation zones. The effective volume equals the volume of the advection zone, $V_{X(\text{adv})}$. In x direction, the effective volume is calculated as:

$$V_{X(\text{eff})} = \begin{cases} A_{X(\text{eff})}\Delta x, & \text{if } A_{X(\text{eff})} < A_X \\ V_X, & \text{otherwise} \end{cases} \tag{80}$$

where, $A_{X(\text{eff})}$ is the effective area that represents reduction in the cross-sectional area caused by partial-blocking. According to Bruwier et al. (2017), the effective area equals the minimum cross-sectional area across the grid cell, $A_{X(\text{min})}$. In the present study, we propose $A_{X(\text{eff})} \geq A_{X(\text{min})}$ with the equality holds only when certain conditions are met (see §E.2.3 for detailed formulation). The effective volume is different from the original face volume V_X only when $A_{X(\text{eff})} < A_X$; i.e., this approach assumes significant recirculation zones are generated only with severe contractions of the channel's cross-sectional area (as the case shown in Fig. 62). The similar equation for $V_{Y(\text{eff})}$ is readily deduced from the above.

The use of Eq. (80) simulates topographic dispersion caused by increased transverse velocity gradients at channel contractions. However, poorly-represented transverse velocity gradients also exists near the channel boundary walls, even without substantial channel contractions. Simulations performed at coarse resolution inevitably smooth this velocity gradient, leading to further topographic dissipation. A possible consequence of neglecting this near-wall velocity gradient is that topographic dissipation might not be completely suppressed with Eq. (80) alone. To test this concept, we also evaluate an alternative formula for calculating face volumes based on minimum areas as:

$$V_{X(\text{min})} = \begin{cases} A_{X(\text{min})}\Delta x, & \text{if } A_{X(\text{min})}\Delta x > \alpha V_X \text{ or } A_{X(\text{eff})} < A_X \\ \alpha V_X, & \text{otherwise} \end{cases} \tag{81}$$

where α is a model parameter. The idea for this formulation arises from the observation that topographic dissipation can be mathematically countered by reducing the volumes in momentum Eq. (78). Instead of using a smaller volume only at channel contractions – as implied by Eq. (80), the (staggered) face volumes for all cells are replaced by the minimum volumes, $V_{X(\text{min})}$, calculated from Eq. (81), which should provide higher velocities and weaker dissipation than Eq. (80). The $0 \leq \alpha \leq 1$ parameter in this approach sets a lower limit of $V_{X(\text{min})}$, which is necessary to avoid instabilities as $V \to 0$. The present study uses $\alpha = 0.7$, which is obtained from a sensitivity study (results not shown). It should be noted that Eq. (81) is certainly not an ultimate solution to topographic dissipation. The use of minimum volume and α are only considered a primitive attempt that shows the possibility of suppressing dissipation by reducing volume, but the exact amount of reduction remains further investigation (also discussed in §E.4.2).

E.2.3 Effects of grid alignment

Background

Subgrid models are often sensitive to mesh design. If a macro-structure intersects with a cell face (or edge), its partial-blocking effect can be directly simulated using areal porosity (Sanders et al., 2008). Specifically, the grid face area (or areal porosity) is reduced to model decrease in conveyance across the face. However, if the mesh is shifted such that the entire macro-structure is located in the cell interior then a face-based partial-blocking algorithm cannot capture the conveyance effects (Guinot et al., 2017). Grid alignment sensitivity means that a small shift of the mesh position over the high-resolution topography can cause a large change in the areal porosity (A_X, A_Y) and hence a change in the simulation results. We have found this to be the case with the baseline SB model of Z. Li and Hodges (2019a) applied to simulations in the Nueces River Delta (Texas, USA). Note that the drag coefficient cannot be used to compensate for misrepresentation of the cross-sectional flow area when the mesh is shifted. That is, the face flow area appears in both continuity (Eq. 74) and the barotropic term of the momentum equation (Eq. 75), whereas the drag term appears only in the momentum equation (Eq. 75). Even if we were able to reproduce the same model outcomes as those with unshifted mesh by adjusting drag coefficient, it would certainly be through completely different mechanisms, i.e., getting the "right" answer for wrong reasons – which has limited physical significance (Lane, 2005). Thus, shifting a mesh to move a macro-structure from the face to the interior requires some modification of (e.g.) A_X and/or V_X to compensate if we seek results that are (relatively) insensitive to the mesh alignment.

To address issues of grid alignment, Bruwier et al. (2017) suggested using the minimum areas ($A_{X(\text{min})}$ and $A_{Y(\text{min})}$ in x and y directions respectively) across a coarse cell to represent face areas (or areal porosities). With their approach, reduction of face area and the associated change in the reaction force are always captured regardless of the location of macro-structures. Unfortunately, their method did not completely remove mesh-dependency in twisted channels where grid lines are not aligned with channel directions. This effect is illustrated in Fig. 63, where $r = 16$ mesh is overlapped with $\delta x = 1$ m channel bathymetry. The white double arrow shows a cross section A_C where x-flux passes through. Note that the cross-section does not equal the channel width because mesh and channel boundaries are not aligned. The red arrows represent the minimum face areas $A_{X(\text{min})}$ within three coarse cells (named *G1*-*G3*) as suggested by Bruwier et al. (2017). It can be seen that for cell *G1* where an interior macro-structure exists, the minimum area $A_{X(\text{min})}$ represents a true contraction of channel's cross-sectional area. For *G2* and *G3*, however, using minimum areas leads to a decrease of channel's cross-sectional area, i.e., $(A_{X(\text{min})})_{G2} + (A_{X(\text{min})})_{G3} < A_C$. Thus, use of the minimum areas can cause false contractions and give biased estimates of the actual flow areas for narrow channels, which leads to an underestimation of conveyance.

Furthermore, grid alignment along an angled channel boundary – as commonly seen for natural river channels – often generates coarse-grid cells that contain only a few wet subgrid elements. Bruwier et al. (2017) showed that such “barely-wet" cells can be merged into their neighbor grids to reduce model error, but simply merging volumes and areas (or storage and areal porosity) neglects the spatial arrangements of macro-structures. If grid lines are not aligned with flow direction, numerical diffusion is also increased, which further reduces channel conveyance (Hasan, van Maren, & Cheong, 2012; Holleman, Fringer, & Stacey, 2013; Z. Li & Hodges, 2019b; Westerink et al., 2008).

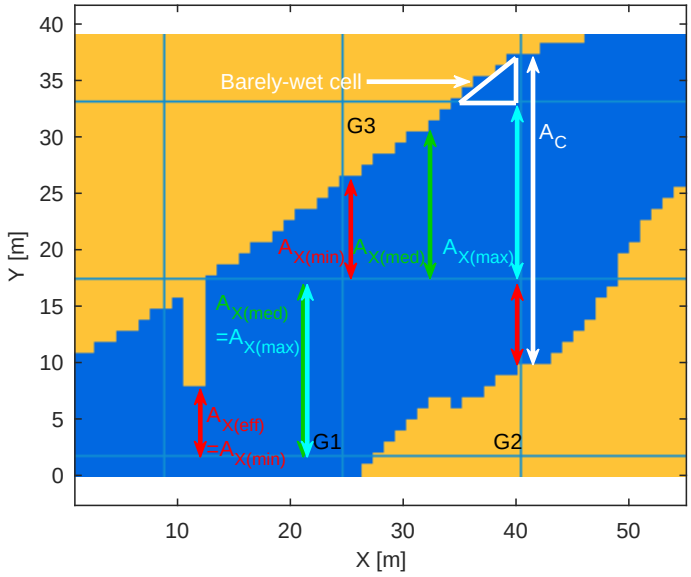

Figure 63: An illustration of channel's representative cross-sectional area for x-flux, A_C (white double arrow), grid-based minimum areas $A_{X(\text{min})}$ (red arrows), maximum area $A_{X(\text{max})}$ (cyan arrow), median area $A_{X(\text{med})}$ (green arrow) and a barely wet grid cell (white triangle). Blue represents river channel and brown represents land. The mesh shown is created with $r = 16$. Note that by using Eq. (82), the effective area is less than the original face area only in cell *G1*, which also leads to a corresponding decrease in effective volume.

Method: Correction on effective area

To handle the issue with grid alignment, we extend the minimum area idea of Bruwier et al. (2017) by replacing face areas A_X, A_Y in Eq. (74) and (75) with a more general concept of effective areas $A_{X(\text{eff})}$, $A_{Y(\text{eff})}$. The effective areas equal the minimum areas only if they are much smaller than typical cross-sectional areas at the coarse grid scale, (e.g., where an interior severe contraction of cross-section is detected). Otherwise the effective areas $A_{X(\text{eff})}$ and $A_{Y(\text{eff})}$ equal the areas A_X, A_Y provided by upscaling at cell faces, as in Z. Li and Hodges (2019a). Formally, the effective area is computed for A_X as:

$$A_{X(\text{eff})} = \begin{cases} A_{X(\text{min})}, & \text{if } \left(A_{X(\text{med})} - A_{X(\text{min})}\right) > \gamma \left(A_{X(\text{max})} - A_{X(\text{med})}\right) \\ A_X, & \text{otherwise} \end{cases} \tag{82}$$

with a similar equation for A_Y. In the above, γ is a model coefficient and the $A_{X(\text{med})}$, $A_{X(\text{max})}$, $A_{X(\text{min})}$ are median, maximum and minimum cross-sectional areas in the staggered coarse-grid cell surrounding the face. These terms are defined for a cell with a grid-coarsening ratio r (i.e., containing r subgrid cells in x direction), which has a set of r different cross-sectional areas $\{A_{X1}, A_{X2}, \ldots A_{Xr}\}$ in the x direction. Formally, the coarse-grid cell statistics are:

$$\begin{aligned} A_{X(\text{med})} &= \text{median}_{i=1}^{r}(A_{Xi}) \\ A_{X(\text{max})} &= \max_{i=1}^{r}(A_{Xi}) \\ A_{X(\text{min})} &= \min_{i=1}^{r}(A_{Xi}) \end{aligned} \tag{83}$$

The median, minimum and maximum areas are shown in Fig. 63 for the example cells *G1* and *G3*. The coefficient $\gamma > 0$ in Eq. (82) determines when $A_{X(\text{min})}$ can be identified as a true channel contraction.

The present study uses $\gamma = 2$, which identifies a contraction when the difference between median to minimum areas is twice the difference between maximum to median areas. In effect, this occurs when there is a subgrid cross-sectional area that is substantially smaller than would be expected if the areas A_{Xi} were uniformly distributed about the median. Coarse-grid cells *G1* and *G3* in Fig. 63 can be used as illustrative examples. Cell *G3* contains a section of (almost) straight channel boundary, but since the channel direction and grid lines are not aligned, the interior face areas A_{Xi} show (nearly) linear variation along the x axis. Applying Eq. (82) with $\gamma = 2$ yields similar magnitudes for $A_{X(\text{med})} - A_{X(\text{min})}$ and $A_{X(\text{max})} - A_{X(\text{med})}$ and results $A_{X(\text{eff})} = A_X$. This result indicates there is no severe contraction to generate partial blocking effects. For cell *G1*, the A_{Xi} values are the same for most cross sections because channel bank only takes a small region in the upper left corner. However, the existence of a sidewall obstacle leads to a small value for the minimum area, which provides $A_{X(\text{med})} - A_{X(\text{min})} \gg 2\left(A_{X(\text{max})} - A_{X(\text{med})}\right) = 0$. That is, the contraction area is substantially different than expected given the range of the cross-sectional areas on the high side of the median. The effective area in this case is set to the minimum area at the contraction location. The use of Eq. (82) successfully separates a true channel contraction caused by interior macro-structures (*G1*) from a false contraction caused by misalignment between channel and grid lines (*G3*). In §E.4, the selection of $\gamma = 2$ and other possible statistical approaches to identifying contractions are discussed.

Method: Mesh-shifting

For coarse-grid cells containing only a few wet subgrid cells (referred as "barely-wet" or *bw* coarse-grid cells, shown as the white triangle in Fig. 63), a smaller time step is required to maintain stability if the numerical algorithm is strictly CFL limited (Bruwier et al., 2017). To completely eliminate *bw* cells and their time-step constraint, Bruwier et al. (2017) developed a cell-merging technique that merges the *bw* cells with their neighbor coarse-grid cells. A disadvantage of this approach is that it destroys information on the spatial arrangements of the interior macro-structures. Fortunately, *FrehdC* is generally stable for localized velocities exceeding the CFL condition as long as the high velocity cells do not dominate a large contiguous area of the computational domain (Z. Li & Hodges, 2019b). Thus, for *FrehdC* an optimum mesh shift can be developed by minimizing the number of, rather than eliminating the area of, the *bw* cells.

The coarse-grid *bw* cells are a result of the relationship between the coarse-grid mesh and the underlying fine-grid topography, which has a number of possible permutations. As illustrated in Fig. 64, shifting the relationship between the coarse-grid mesh and the underlying fine-grid topography can result in different sets of *bw* cells. The coarse grid necessarily has some (0,0) origin whose position on the fine-grid is an arbitrary choice – i.e., *any* fine-grid cell could be chosen as the coarse-grid origin. It follows that a coarse-grid mesh with a coarsening ratio of $r = \Delta x/\delta x = \Delta y/\delta y$ has r unique positions along each of the x and y axes, providing r^2 unique coarse-fine mesh relationships. It is useful to define (p, q) as unique global indexes for the fine grid topography with $p \in \{1...N_{fx}\}$ and $q \in \{1...N_{fy}\}$ where N_{fx} and N_{fy} are the number of fine-grid cells along the x and y axes. Let (p_0, q_0) be an arbitrary baseline origin of the coarse-grid mesh in the fine-grid topography. The possible permutations of the coarse-grid mesh can be denoted as $M_{\zeta,\psi}$, where $\zeta, \psi = \{0, 1, ...r - 1\}$ are shifts of the coarse-grid origin to $(p_0 - \zeta, q_0 - \psi)$.

There are a number of possible ways to define what constitutes a *bw* cell and to quantify the cumulative effects of *bw* cells. For the present purposes, a general definition of a *bw* cell is a coarse-grid cell where the wetted surface area is a small fraction of the coarse-grid cell area, i.e., $A_Z < \beta\Delta x\Delta y$, where $0 < \beta < 1$ is a cut-off fraction. The appropriate value of β depends on the numerical model behavior when $A_Z \ll \Delta x\Delta y$, with $\beta = 0.2$ proving adequate for the tests herein. For *FrehdC*, the optimum coarse-fine mesh relationship is the $M_{\zeta,\psi}$ with the smallest number of *bw* coarse-grid cells.

It can be seen from Fig. 64b that as ζ and ψ change, new *bw* cells are created while existing ones are removed. The mesh-shifting optimization guarantees that the total number of *bw* cells is minimized. The potential issues of creating new *bw* cells are discussed below in §E.4.3. It should be noted that mesh-shifting and the concept of effective area/volume are two methods targeting two different problems incurred during grid-coarsening. Mesh-shifting handles the issue of *bw* cells, which is purely due to misalignment between grid lines and channel boundaries. The effective area/volume are used to simulate effects of interior macro-structures. Although grid alignment issue exists in determining effective area as well (§E.2.3), it only affects detailed calculation procedures, not the overall strategy of parametrizing macro-structures. It will be shown in §E.3 that both mesh-shifting

and effective area/volume are necessary in reducing model error and alleviating sensitivity of model performance to mesh design.

Figure 65 provides a flowchart illustrating the relationships between algorithms for mesh shifting, effective area, effective volume, the baseline SB approach, and the traditional roughness representation of microstructure. Mesh-shifting is performed prior to grid-coarsening as a preprocessing step that optimizes the high-resolution topography. The upscaling (grid-coarsening) process provides different sets of subgrid variables for the different methods. Within the scope of the present study, the face volumes V_X, V_Y in Eq. (74)-(77) are replaced by either $V_{X\,(\mathrm{eff})}$, $V_{Y\,(\mathrm{eff})}$ or $V_{X\,(\mathrm{min})}$, $V_{Y\,(\mathrm{min})}$ as two different approaches to model the effects of macro-structures and constrain topographic dissipation. The face areas A_X, A_Y are replaced with $A_{X\,(\mathrm{eff})}$ and $A_{Y\,(\mathrm{eff})}$. The volume modifications do not affect mass conservation as volumes do not appear in continuity (Eq. 74). The area modifications may affect the result of the continuity equation, but they do not change the inherent mass conservation in the method as the volume increment $\Delta\eta A_Z$ remains exactly balanced by the net fluxes through the faces. The test scenarios described in §E.3 are designed to examine model sensitivity to mesh-shifting, effective areas, and effective volumes as compared to the baseline SB case.

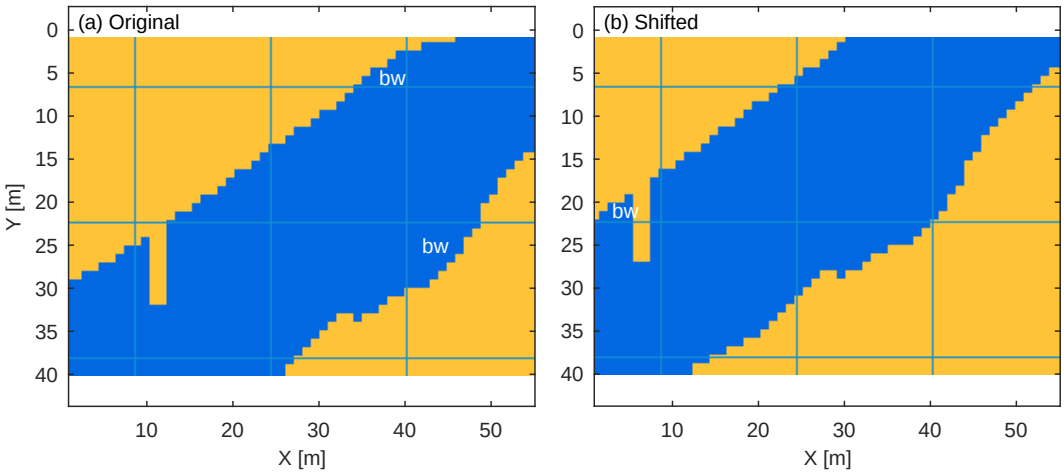

Figure 64: (a) The background bathymetry used in Fig. 63 with $r = 16$ mesh, which is used as $M_{0,0}$ position. Two *bw* cells are marked. (b) Bathymetry of the same region shifted with $\zeta = 5, \psi = 5$ ($M_{5,5}$). The two original *bw* cells are eliminated but a new one is created.

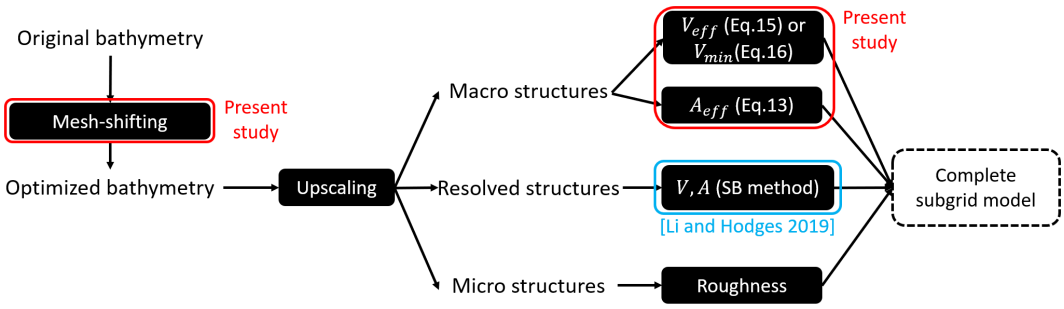

Figure 65: Flowchart illustrating the relations between different components of a complete subgrid method.

E.3 Test cases and results

E.3.1 Straight channel with sidewall obstacle

The above modifications to the governing equations and mesh design are tested on two domains. The first domain is shown in Fig. 66, where two 100×100 m square "lakes" are connected with a straight channel of 20 m width. The bottom elevations of the channel and lakes are uniform at 0 m. An object (e.g., bridge pier) with length D is placed on the sidewall of the channel as a subgrid macro-structure. Constant water levels of 0.3 m and 0.35 m are forced at $x = 0$ m and $x = 600$ m respectively. At steady-state, the solution has an overall surface gradient of 8.33×10^{-5}. A fine-grid simulation ($r = 1$) is executed with 0.25 m grid spacing, which is used as the "true solution". The subgrid simulations use coarse-grid spacing of $\Delta x = 20$ m ($r = 80$). The mesh is intentionally designed such that exactly one coarse-grid cell is placed across the channel width and the bridge pier does not intersect with grid faces.

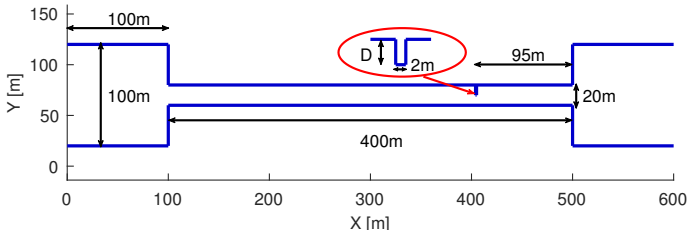

Figure 66: Top view of the outline of the straight channel computation domain. In the red ellipse is detailed view of regions near the bridge pier.

The following (Table 8) includes tests of five model scenarios executed in this study. The scenarios are created by selecting different treatments on macro-structures. The notation SB represents the baseline subgrid method described in Z. Li and Hodges (2019a). The new effective subgrid area approach (Eq. 82) is designated SB-A. The new effective volume approach (Eq. 80) is named SB-V. Tests implementing both new effective area and volume algorithms are designated SB-VA. Tests with effective area and volume algorithms for additional near-wall dissipation (Eq. 81) are SB-V_αA. For comparison with prior work, the roughness upscaling method of Volp et al. (2013) is applied with the baseline subgrid model and designated as SB_{Volp}.

Table 8: List of different test scenarios.

Test scenario	Reduce area	Reduce volume	Roughness upscaling
SB	No	No	No
SB-A	Yes (Eq. 82)	No	No
SB-V	No	Yes (Eq. 80)	No
SB-VA	Yes (Eq. 82)	Yes (Eq. 80)	No
SB-V_αA	Yes (Eq. 82)	Yes (Eq. 81)	No
SB_{Volp}	No	No	Yes (Volp et al., 2013)

The steady-state flow rate errors (computed as the difference of in-channel flow rate between test simulation at Δx and reference fine-grid simulation at δx, that is, $Q_{r=80} - Q_{r=1}$) are shown in Fig. 67. Taking flow towards $-x$ direction to be positive, it can be seen that for $D \in \{4, 6, 8, 10, 12, 14\}$ m, the SB-VA scenario minimizes flow rate error. By ignoring the macro-structure and its blocking effects, the SB simulation tends to overestimate flow rate, whereas taking minimal cross-sectional area alone (SB-A) underestimates flow rate because of topographic dissipation. As D increases, the flow rate errors tend to increase for all scenarios, indicating that not all processes caused by the macro-structure are captured by A_{eff} and V_{eff}. Such processes might include mass/momentum exchange between advection and recirculation zones (Fig. 62b) as well as upscaling of bottom roughness (discussed in §E.4, below). Clearly, SB-VA is an improvement over the SB scenario that uses the subgrid method described in Z. Li and Hodges (2019a). Results for the SB-V case (not shown) simply provide an amplification of the overestimation of the SB method.

Figure 68 shows the steady-state surface elevation profiles in the straight channel. Results for the subgrid scenarios are downscaled following Sanders and Schubert (2019). A severe decline of surface

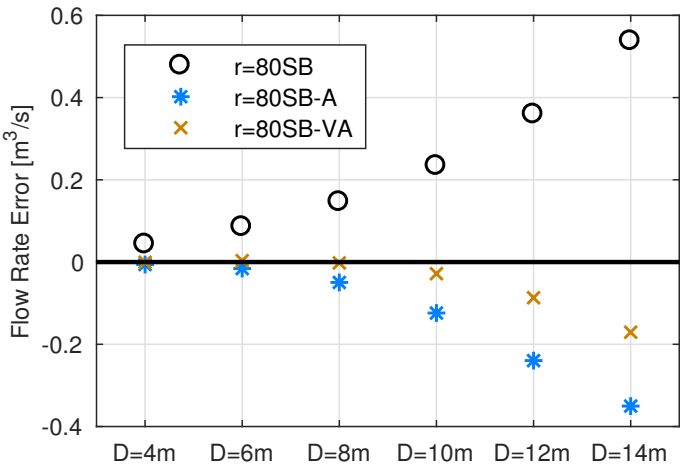

Figure 67: Steady-state flow rate error in the straight-channel domain (Fig. 66) for various D and subgrid scenarios tested. Positive error indicates overestimation of flow rate. Negative error means underestimation.

elevation across the bridge pier can be found for the fine-grid simulations, which is caused by the blocking effects from the interior macro-structure. The SB scenarios predict constant surface slope along the entire channel because the macro-structure is completely neglected. Both the SB-A and SB-VA scenarios show a change in surface gradient across the bridge pier. For $D = 6$ m, the difference between these two scenarios is minor. However, for $D = 12$ m the SB-A scenario overestimates the drop of free surface. Although slight overestimation is also found for SB-VA, it provides the best approximation of surface elevation to the fine-grid solution among the three tested scenarios.

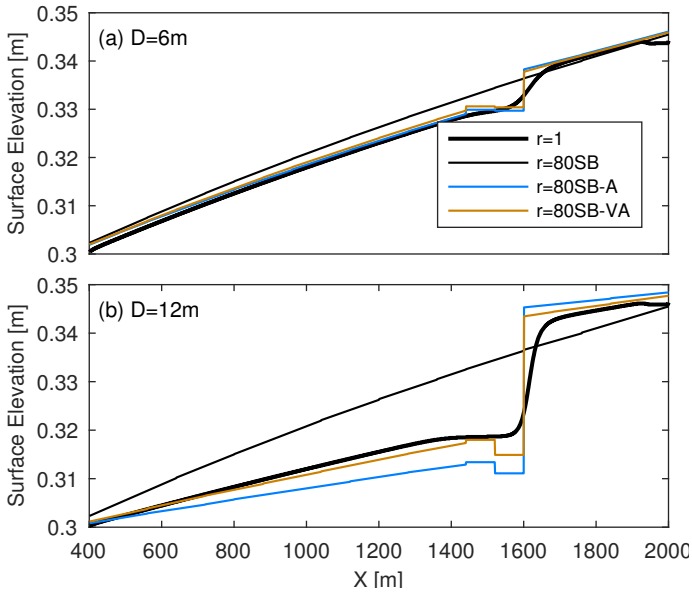

Figure 68: Profiles of steady-state surface elevations in longitudinal direction of the straight channel for $D = 6$ m and $D = 12$ m.

E.3.2 Twisted channel in the Nueces Delta

The second domain (Fig. 69a) is a semi-enclosed tidal-driven marshland. It consists of a "bay" on the east side, a twisted main channel and several well- or poorly-connected shallow lagoons. The boundary shapes of these features are modified from the 1×1 m lidar data of the Nueces Delta, which is a shallow coastal wetland located near the City of Corpus Christi (Texas, USA). The entire Nueces Delta has been modeled in Z. Li and Hodges (2019a, 2019b). For computational efficiency, the present domain only covers a 480×2000 m section. A grid-coarsening ratio $r = 16$ is used for the Nueces Delta test case. Mesh shifting is applied to minimize the number of *bw* cells, with results as shown in Fig. 70. The mesh with the minimum number of *bw* cells is shown in Figure 69a as the "No Pier" (NP) case. To test the effect of mesh shifting, a "No Pier Shifted" (NPS) case is designed with the coarse-grid mesh corresponding to the maximum number of *bw* cells. To evaluate the new macro-structure algorithm, three sidewall piers are added to a stretch of the channel (Fig. 69b), creating the "With Piers" (WP) case with exactly the same mesh arrangement as the NP case. To eliminate confounding effects of micro-structure and retain our focus on the macro-structure, the bottom elevations from the real submerged topography are replaced with a uniform value of 0 m throughout the domain for the NP, NPS, and WP cases. To provide insight into the interaction of micro-structure and macro-structure the original submerged topography is maintained in a "With Pier Bathymetry" (WPB) case. A view of the WPB bathymetry in the stretch of channel with the bridge piers is shown in Fig. 69c. The differences among the four test bathymetries are summarized in Table 9. Sinusoidal tide (with range of 0.2 m and period of 24 h) is added along the east boundary for these cases.

Table 9: List of differences among tested bathymetries.

Bathymetry	Sidewall macro-structures	Number of *bw* cells	Channel bottom
NP	No	Min.	Flat
NPS	No	Max.	Flat
WP	Yes	Min.	Flat
WPB	Yes	Min.	Uneven

For the Nueces Delta test scenarios, the relative flow rate errors across X1 (Fig. 69a) over one tidal period is shown in Fig. 71. One of the challenges of interpreting error behavior is that the two effects of poorly-modeled macro-structure – neglect of partial blocking and topographic dissipation have opposite effects; i.e., the former leads to overestimation of conveyance and the latter an underestimation. Thus, serendipitous cancellation of error can occur, which might result small mean or median error. To avoid such situations, we consider the interquartile range (IQR) to be a more important indicator of model performance than the mean or median error because it reflects the variation of error over the entire simulation period, which increases the chance of capturing model deviations from the reference simulation.

For the NP domain with the optimum mesh shift to minimize barely wet cells and without bridge piers (Fig. 71a), no severe channel contraction is detected in the main channel with $\gamma = 2$ (although several contractions are found in the lagoon regions close to the left boundary). The SB-A algorithm has slight higher error than the baseline SB method. Applying effective volume (SB-V) reduces flow rate error compared to SB and SB-A algorithms, whereas the SB-VA scenario produces slightly higher error than SB-V. It should be noted that using effective volume alone (SB-V) does not have much physical significance because Eq. 80 is derived for the cases where topographic dissipation is always associated with change in cross-sectional area, but SB-V shows superior performance to SB-VA in terms of flow rate error, which indicates the existence of additional dissipation processes that are not captured by Eq. (80). This statement is verified by results with SB-V_αA, where flow rate error further decreases with the use of reduced volumes for all coarse cells (Eq. 81). The additional dissipation is likely caused by smoothing the transverse velocity gradient near the channel boundary. The effective volume approach of SB-V_αA is also superior to the Volp et al. (2013) model, SB_{Volp}.

The contrast between results with the NP topography (optimized mesh shift) and the NPS topography (poorly-optimized mesh shift) in Figs. 71(a) and (b) is striking. Poor optimization of the mesh (maximizing the barely-wet cells) causes dramatically increased error and IQR across all the methods. A possible reason is increased numerical dissipation when flow enters and exits these additional *bw* cells, which cannot be compensated by any of the subgrid algorithms. These results illustrate the optimization of the mesh is critical to effectively applying subgrid algorithms. It should be noted that

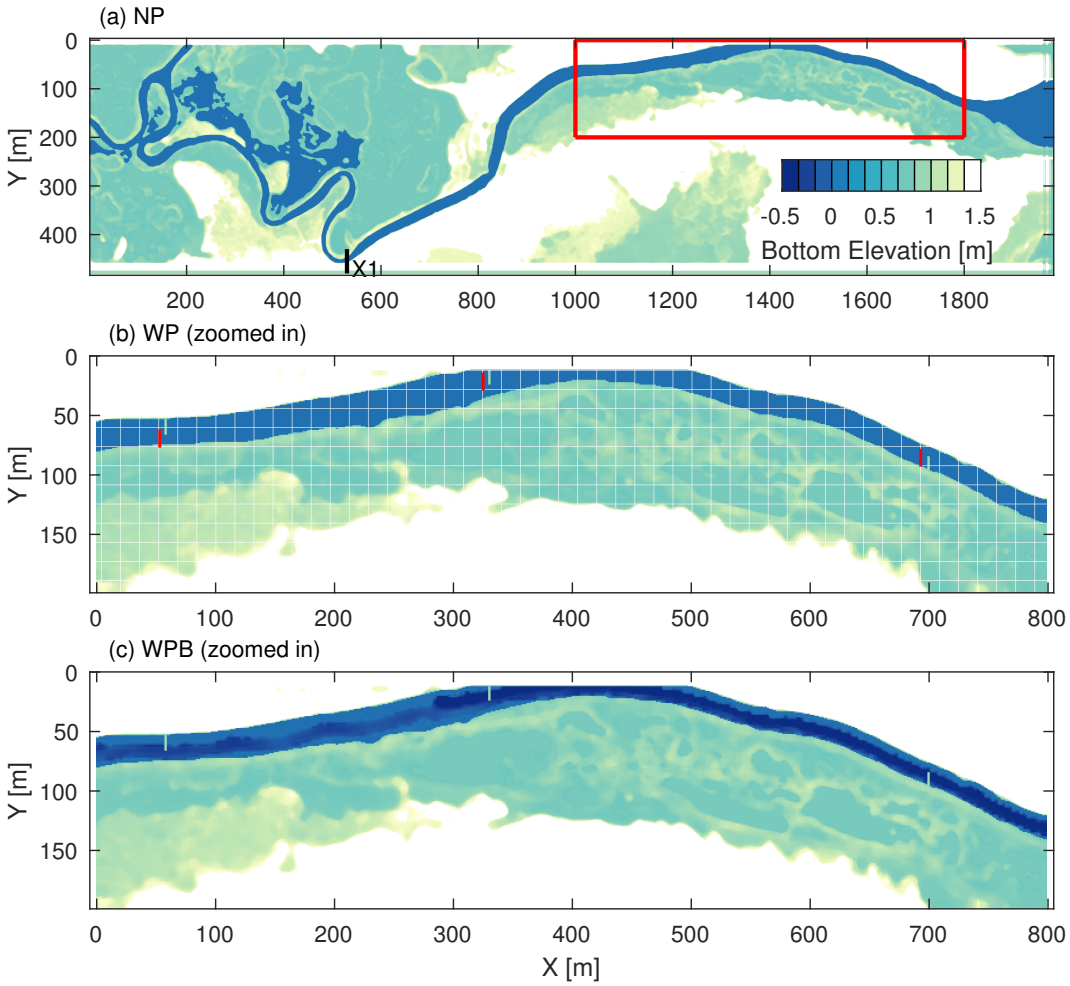

Figure 69: (a) Bathymetry of the full domain of the Nueces Delta test caseFFigures NP at 1×1 m resolution. In-channel flow rate is calculated at cross-section *X1*. (b) Details of bridge piers in channel WP within red box of frame (a). The white mesh represents $r = 16$ coarse grid cells. Red lines are cell faces whose effective area $A_{\text{eff}} < A$. (c) Details of channel WPB with non-uniform submerged bathymetry (coarse mesh not shown for clarity).

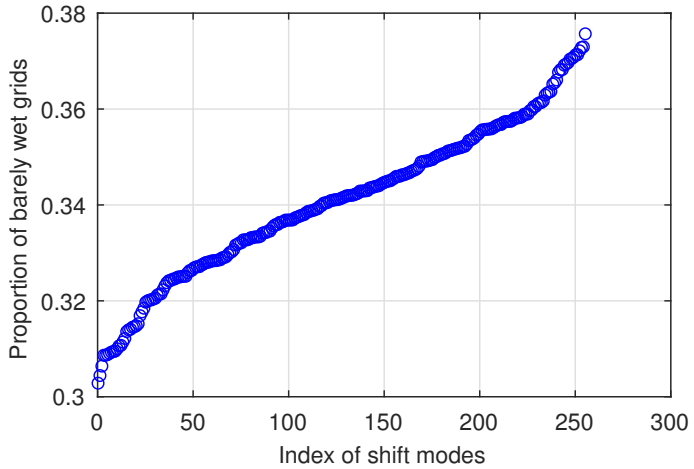

Figure 70: Proportion of barely-wet (*bw*) cells in all wet cells for the 256 possible shift modes ($r = 16$) for the NP bathymetry. Results displayed in ascending order.

despite this sensitivity to the mesh placement, the subgrid method (even with NPS bathymetry) still has its advantage over existing grid-coarsening methods without subgrid parametrization (e.g. Hodges, 2015) that cannot maintain surface connectivity of the main channel at $r = 16$ and completely prevent tidal intrusion into the lagoons (results not shown).

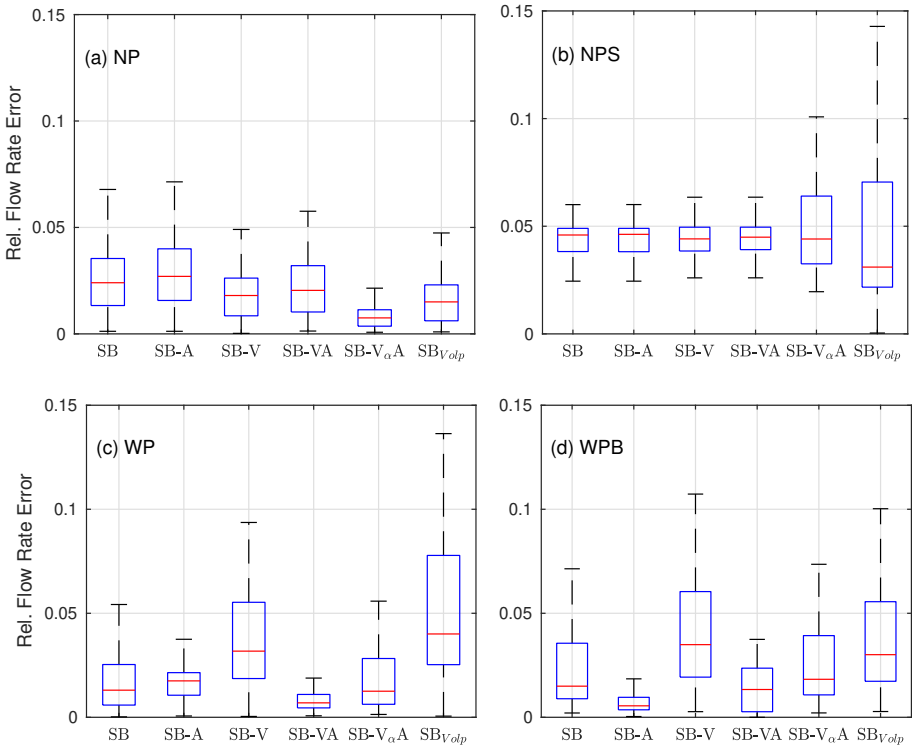

Figure 71: Relative flow rate error ($|Q_{r=16} - Q_{r=1}|/|Q_{r=1}|$) at cross-section X1 (Fig. 69) over one tidal period for the Nueces Delta test scenarios. The red mark represents the median over one tidal period and the blue box is the interquartile range.

Relative error results for the NP topography seem to imply the SB-V approach is superior to SB-A and the latter algorithm is unnecessary. However, addition of the bridge piers in the WP case, Fig. 71(c), indicates the effects are reversed when the geometry includes significant partial-blocking macro-structure. With the bridge piers included, the SB-VA has the minimum error. The IQR results for the flow error of the SB, SB-A, and SB-V$_\alpha$A algorithms are similar, whereas the SB-V has the highest error. That is, when partial-blocking behavior exists, treatments of both flow areas and volumes at channel contractions are important. Flow features are dominated by processes associated with partial-blocking macro-structures, making other dissipation mechanisms of secondary importance. It is useful to consider the temporal evolution of the root-mean square error (RMSE) of the surface elevation for the SB and SB-VA models, as shown in Fig. 72. It can be seen that for both NP and WP bathymetries the SB-VA (and SB-V$_\alpha$A) produces smaller RMSE$_\eta$ errors than the baseline SB method. Note that the RMSEs show periodic variations due to the semi-enclosed nature of the model domain. That is, an initial overestimation of flow rate leads to rapid increase of surface elevation, which then reduces the surface gradients between the open boundary and the interior lagoons, hence reducing flow rates. This behavior restrains further tidal intrusion and slows down the rising of free surface, as is evidenced by the sudden reduction in the rate that error is increasing for the WP SB scenario around 7 h into the simulation towards the end of the rising tide. Furthermore, when the tide falls, since the surface elevation is overestimated, it generates larger surface gradient that drains the lagoons quickly. As a result, the RMSE drops to almost zero at the end of the tidal cycle. This periodic behavior is thus not a result of applying the proposed subgrid method, but the differences between SB and SB-VA errors are certainly caused by the subgrid treatments to the macro-structures.

Non-uniform bottom topography is added to the 1×1 m for the control simulation in case WPB, providing the relative flow rate error behavior shown in Fig. 71(d). Here we see the SB-A algorithms

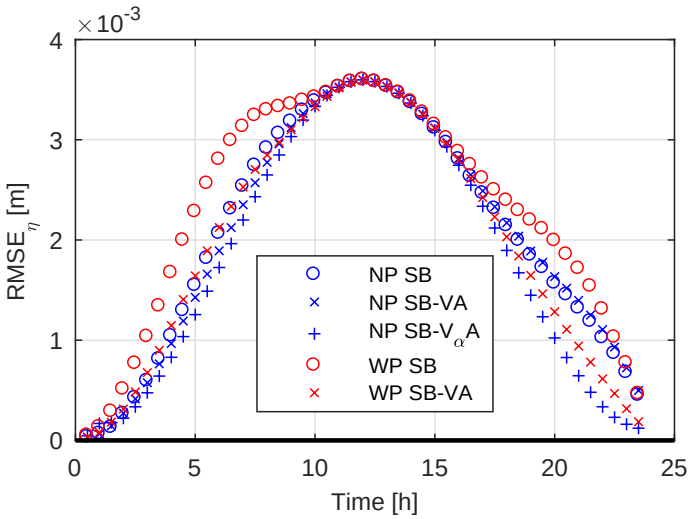

Figure 72: Temporal variation of surface error for selected NP and WP scenarios.

perform best, SB-VA the second best, the SB and SB-V$_\alpha$A being similar and the SB-V and SB$_{\text{Volp}}$ being somewhat worse. The superiority of SB-A over SB-VA indicates variation of bottom elevation induces higher flow resistance that is not represented by A_{eff} and V_{eff}. These results have implications for the importance of upscaling bottom drag, which is beyond the scope of the present study.

A comparison of the spatial distribution of water surface elevations for the WP scenarios provides further insight into the performance of the subgrid algorithms. Here we focus on the simulation during the rising tide ($T = 8$ h), as shown in Fig. 73. The flow rate IQR statistics in Fig. 71 indicate that the SB and SB-A are relatively similar in performance, but here it can be seen that the SB method results in higher in-channel water surface elevations from 600 to 1400 m compared to the $r = 1$ control, the SB-A and the SB-VA. These results indicate that SB allow increased conveyance in the channel compared to the SB-A and SB-VA. Overestimation of conveyance (and surface elevation) is also observed in SB-V. The flooding of the off-channel lagoons (left side of domain) provides another interesting point of comparison. The SB, and SB-V methods have higher water surface elevations than the $r = 1$ control in the off-channel lagoons, indicating there is too much connectivity. The SB-A method has too much blockage in the connections to the lagoons. Overall, the SB-VA method has the best combination of representing connectivity within the lagoon without overestimating conveyance in the channel.

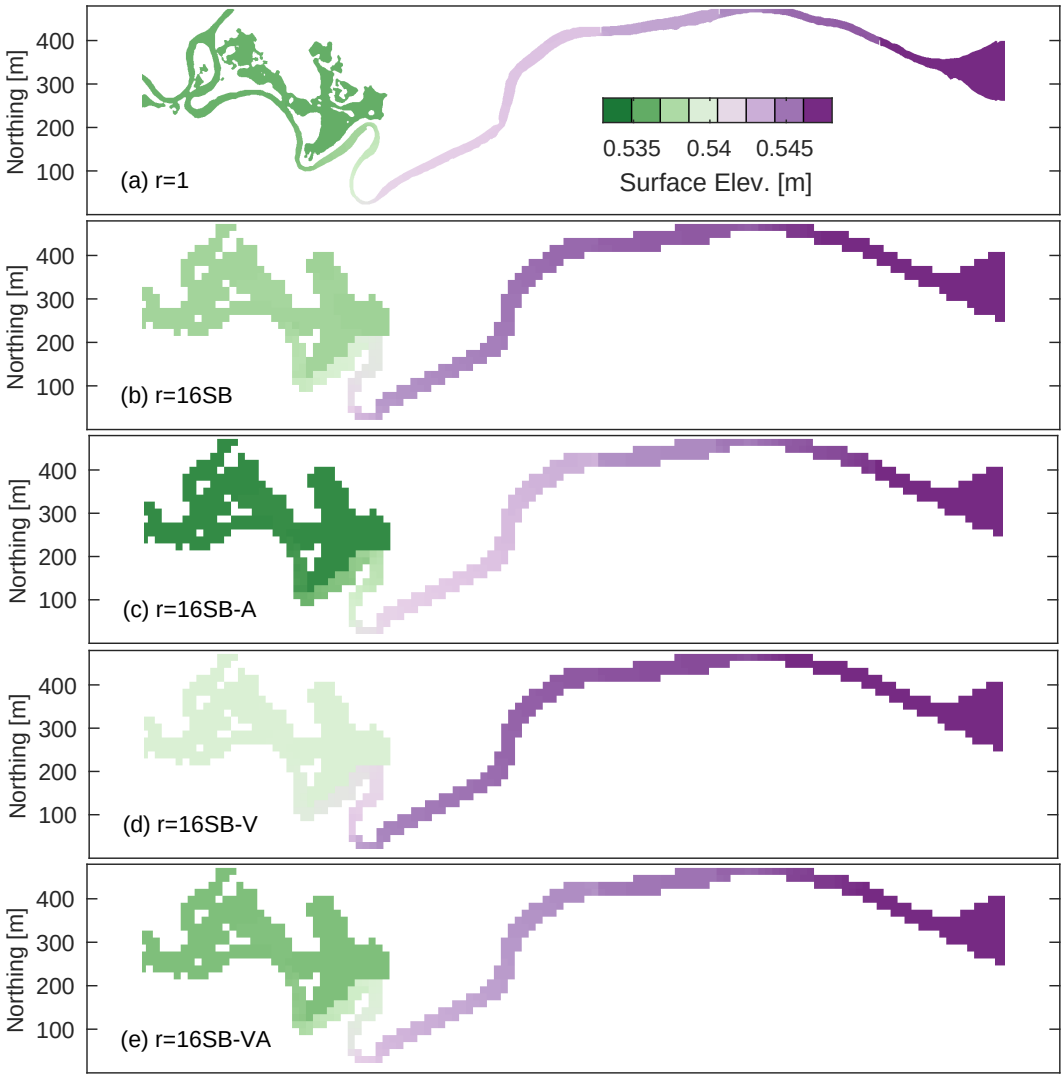

Figure 73: Surface elevation at $T = 8$ h (corresponds to rising tide) for WP scenarios. Tidal boundary condition enforced on right side of domain.

E.4 Discussion

The results above show that subgrid models characterized by both effective areas and effective volumes can improve the modeling of flow effects caused by macro-structures in 2D tidal marsh models. In general, the effective area approach reduces the modeled flow cross-section due to macro-structures that are interior to a coarse-grid cell (whose neglect otherwise leads to overestimation of conveyance). Unfortunately the effective area approach, by itself, leads to an overestimation of topographic dissipation – i.e., the tendency of tortuous flow paths to dilute the effects of pressure gradients driving the flow. The effective volume approach acknowledges that flow volumes "hiding out" behind obstructions are not affected by driving pressure gradients, and hence applying a smaller effective volume counters the tendency of the effective area approach to overestimate topographic dissipation. The effective area method used herein is an extension of Bruwier et al. (2017) by incorporating a conditional criterion (Eq. 82) that identifies and removes "false" channel contraction caused by misalignment between channel and grids. Room for further improving this approach is discussed in §E.4.1. Limitations and assumptions for the new effective volume method are discussed in detail in §E.4.2. A challenging problem is that macro-structure effects are inherently sensitive to the coarse-grid mesh placement, which is shown to significantly alter the effectiveness of the subgrid models. The sensitivity of model results to mesh-shifting and its implications are discussed in §E.4.3. Finally, the model tests herein were focused on side-wall macro-structure that caused flow blockages, as characterized by bridge piers in Figs. 66 and 69. For simplicity, these test cases used uniform bottom bathymetry with a uniform bottom roughness across all coarse and fine-grid cells. The interaction of the subgrid models with the more general macro-structure of non-uniform (but non-blocking) bathymetry and upscaling of micro-structure remains to be explored.

E.4.1 On the effective area

Clearly, the idealized effective area strictly applies only to Eq. (82) for a single interior sidewall obstacles that laterally contract the cross-sectional area. Macro-structures in real marshes have more complex geometries and form a variety of different blocking patterns and flow paths in the cell interior. To handle this increased complexity, other statistical properties might also be used to distinguish true and false channel contractions – which implies broad avenues for future research. Although the concept of simulating partial blocking as a reduction of cell face area is arguably valid for more complex geometry, developing well-grounded mathematical expressions of $A_{X\,(\mathrm{eff})}$ and $A_{Y\,(\mathrm{eff})}$ for such cases is beyond the scope of the present research. Similarly, herein we have not tested model sensitivity to the choice of parameter γ in Eq. (82): we consider this parameter to be merely an interim step showing the approach of Bruwier et al. (2017) – that used minimum areas – can be improved by a more flexible formulation. That is, this research demonstrates that modifications of face areas to represent subgrid features can be extended beyond the minimum area approach, but determining the optimum approach will require more detailed study and we doubt that the γ discriminator of Eq. (82) will prove sufficiently robust for a wide variety of geometries.

E.4.2 On the effective volume

The proposed model for effective volume introduces two substantial idealizations. First, the advection and recirculation zones are assumed completely separated (Fig. 62b). Second, topographic dissipation caused by near-wall velocity gradient is not parametrized. The separation of the advection and recirculation zones in V_{eff} implies that the mixing layer between the two zones and the associated turbulent mixing processes are neglected (Han et al., 2017). Furthermore, for simplicity the size of V_{eff} in any cell is a constant that is independent of the local velocity, which clearly is not a direct representation of the complex flow physics around an object. For tidal-driven flow that reverses regularly, the locations of the recirculation zones also depend on flow direction. It remains to be seen whether adding further complexities associated with the local flow field (direction and velocity) can improve a subgrid model.

Figure 71a implies that additional dissipation processes exist in narrow twisted channels, which are likely caused by smoothing of velocity gradients near the channel boundaries. From Fig. 71c, as expected, this near-wall dissipation cannot be adequately modeled using an effective volume concept similar to the one for recirculation zones, e.g., Eq. (81), because such dissipation is generated through different mechanisms, i.e., *not* through a sudden contraction and the associated recirculation region. The dissipation near channel boundaries will be related to the interaction of the micro-structure, the

sidewall boundary layer, and macro-structure geometry, which will require future studies at finer than the $\delta x = 1$ m resolution used herein as the "true solution" for evaluating model performance.

Similarly, including sidewall effects requires considering 3D flow effects (Jeon, Lee, & Kang, 2018; Monsalve, Yager, & Schmeeckle, 2017), which cannot be handled with the present model. To fully resolve the near-wall velocity gradient and quantify all complex mechanisms occurring there, experimental data (e.g. Velickovic, Zech, & Soares-Frazao, 2017) or full 3D non-hydrostatic simulation results (e.g. Munoz & Constantinescu, 2018) are likely required. Thus we consider the approach using the α parameter in Eq. (81) to be simply a demonstration that some further geometric dependency of the effective volume might be desirable, but optimization of the proposed α in the present model structure is unlikely to provide further insight.

The difficulty in characterizing the size of effective volume implies a key theoretical challenge, which is to quantify how the geometry of an arbitrary macro-structure affects flow. Both the mixing layer and boundary layer are affected by the geometry of the macro-structures (Babarutsi, Ganoulis, & Chu, 1989; X. Li & Djilali, 1995). However, for shallow coastal marshes with wetting/drying, macro-structures can vary over large spatial and temporal scales. Even if the detailed physical processes near channel boundaries can be resolved at sufficiently fine resolution, a robust quantification of macro-structures is still required for upscaling. The present study simplifies macro-structures to pier-like sidewall obstacles, whose primary effect is a contraction of channel's cross-sectional area. This research illustrates the need for a general mathematical formulation for upscaling geometry effects on flow and turbulence from measurable topography (macro-scale structures) to practical coarse-grid model scales.

E.4.3 Sensitivity to mesh design

The results comparing the optimum mesh (NP) and the unoptimized mesh (NPS) illustrate the sensitivity of model results to mesh placement (Fig. 71a and b). A similar observation is found in Bruwier et al. (2017). In the present work, a major cause for the increase of flow rate error with the NPS bathymetry is that the barely-wet (*bw*) cells for the unoptimized mesh are typically near the channel boundaries. Where the boundary is at an angle to the grid mesh an inflow in the x direction into a *bw* cell must be shifted to an outflow in the y direction (and vice versa), which enhances local topographic dissipation and reduces channel conveyance (Z. Li & Hodges, 2019b).

The NPS mesh also has increased error where upscaling blocks some *bw* areas in channel networks. This occurs because complex channel networks may have multiple disconnected water regions within a single coarse-grid cell. In the the baseline upscaling approach (Z. Li & Hodges, 2019a) the disconnected sub-regions with smaller wet areas in a single cell are represented as dry land. This simplification is a necessary limitation for an upscaling method that maintains the blockages to surface connectivity associated with subgrid features, but inevitably leads to local underestimation of cell storage for some *bw* cells. As a result, minimization of *bw* cells for the NP model also minimizes loss of volume in upscaling, which reduces the discrepancy with the fine-grid results. For example, the NP and NPS bathymetries at $r = 16$ show reductions of 0.03% and 2.18% volume, repectively (compared to $r = 1$ bathymetry) for a simple uniform surface elevation of 0.4 m.

We recommend minimizing the number of *bw* cells as a simple pre-processing step for *any* subgrid algorithm. However, it should be noted that our mesh-shifting guarantees global minimization of *bw* cells for a selected inundation level, but not necessarily local optimization across all possible levels. A coarse-grid cell that would be classified as *bw* at a particular water surface elevation might be entirely inundated at higher elevation; thus, there remains an open question as to how to optimize a coarse-grid mesh over a range of inundation levels, an effort that might require an adaptive mesh-optimization routine.

E.5 Conclusions

Porosity-based subgrid models show great potential for efficient simulations of hydrodynamics and salinity transport at shallow coastal marshes. But such models often neglect effects of subgrid-scale interior macro-structures, which makes their performance sensitive to mesh design. The present study focuses on detecting and parametrizing subgrid-scale sidewall macro-structures in narrow twisted channels, reproducing their effects using coarse-grid hydrodynamic models and reducing model sensitivity to mesh design. Three novel strategies are developed: (1) a mesh-shifting procedure that

optimizes mesh design by minimizing the number of partially-wet coarse-grid cells, i.e., coarse cells with only a few wet subgrid elements, (2) use of the effective grid-face areas $A_{X\,(\text{eff})}$ and $A_{Y\,(\text{eff})}$ to simulate partial-blocking effects of the macro-structures, and (3) use of the effective volumes $V_{X\,(\text{eff})}$ and $V_{Y\,(\text{eff})}$ to reduce topographic dissipation, which is caused by smoothing of transverse velocity gradient at coarse scale. These strategies are implemented into the existing subgrid model in the *FrehdC* code (Z. Li & Hodges, 2019a) and are tested on both synthetic and real bathymetries. Model evaluation is performed by comparing coarse-grid to fine-grid simulation results.

In the synthetic test case, a combined use of A_{eff} and V_{eff} minimizes error in flow rate and surface elevation for all tested dimensions of the macro-structure. In the realistic Nueces Delta computation domain, mesh-shifting is demonstrated as necessary to reducing model error. In conjunction with the mesh-shifting method, the combined A_{eff} and V_{eff} subgrid models provide the best approximation of the fine-scale surface elevations and flow rates. When severe contractions are absent, model performance is affected by additional dissipation processes that are not included in V_{eff}. The main advantage of the proposed treatments is the direct connection to idealized physical processes and the channel geometry, which makes it possible to develop analytical expressions for effects of macro-structures. We believe these advances are applicable over a broad range of shallow flows and can be used to limit the extensive efforts that are otherwise required when the drag coefficient is taken as a local calibration coefficient. Future studies are still required to parametrize processes not included in the present model, such as dissipation near channel boundaries and the effects of non-uniform submerged channel bathymetry. This research shows there is an urgent need for a mathematical framework to characterize and quantify the geometry of a variety of macro-structure scales, orientations, and topologies based on measurable data and their statistics.

References

Aizinger, V., Proft, J., Dawson, C., Pothina, D., & Negusse, S. (2013). A three-dimensional discontinuous Galerkin model applied to the baroclinic simulation of Corpus Christi Bay. *Ocean Dynamics*, *63*, 89–113. doi: /10.1007/s10236-012-0579-8

Alexander, H. D., & Dunton, K. H. (2002). Freshwater inundation effects on emergent vegetation of a hypersaline salt marsh. *Estuaries*, *25*(6B), 1426-1435.

Alvarez, M. P., Carol, E., & Dapena, C. (2015). The role of evapotranspiration in the groundwater hydrochemistry of an arid coastal wetland (Peninsula Valdes, Argentina). *Science of the Total Environment*, *506-507*, 299-307.

Arega, F., & Sanders, B. F. (2004). Dispersion model for tidal wetlands. *Journal of Hydraulic Engineering*, *130(8)*, 739–754. doi: 10.1061/(ASCE)0733-9429(2004)130:8(739)

Arthur, D., & Vassilvitskii, S. (2007). K-means++: The advantage of careful seeding. In *SODA 07: Proceedings of the Eighteenth Annual ACM-SIAM Symposium on Discrete Algorithms* (pp. 1027–1035).

Azinfar, H., & Kells, J. A. (2009). Flow resistance due to a single spur dike in an open channel. *Journal of Hydraulic Research*, *47*, 755–763. doi: 10.3826/jhr.2009.3327

Babarutsi, S., Ganoulis, J., & Chu, V. (1989). Experimental investigation of shallow recirculating flows. *Journal of Hydraulic Engineering*, *115*(7), 906–924.

Bates, P. D. (2000). Development and testing of a subgrid-scale model for moving-boundary hydrodynamic problems in shallow water. *Hydrological Processes*, *14*, 2073–2088. doi: 10.1002/1099-1085(20000815/30)14:11/12<2073::AID-HYP55>3.0.CO;2-X

Bates, P. D., Marks, K. J., & Horritt, M. S. (2003). Optimal use of high-resolution topographic data in flood inundation models. *Hydrological Processes*, *17*(3), 537–557. doi: 10.1002/hyp.1113

Begnudelli, L., Valiani, A., & Sanders, B. F. (2010). A balanced treatment of secondary currents, turbulence and dispersion in a depth-integrated hydrodynamic and bed deformation model for channel bends. *Advances in Water Resources*, *33*, 17–33. doi: 10.1016/j.advwatres.2009.10.004

Bricker, J. D., Inagaki, S., & Monismith, S. G. (2005). Bed drag coefficient variability under wind waves in a tidal estuary. *Journal of Hydraulic Engineering*, *131*(6), 497-508.

Bruwier, M., Archambeau, P., Erpicum, S., Pirotton, M., & Dewals, B. (2017). Shallow-water models with anisotropic porosity and merging for flood modelling on Cartesian grids. *Journal of Hydrology*, *554*, 693–709. doi: 10.1016/j.jhydrol.2017.09.051

Burchard, H., Deleersnijder, E., & Meister, A. (2003). A high-order conservative Patankar-type discretisation for stiff systems of production-destruction equations. *Applied Numerical Mathematics*, *47*, 1–30. doi: 10.1016/S0168-9274(03)00101-6

Candy, A. S. (2017). An implicit wetting and drying approach for non-hydrostatic baroclinic flows in high aspect ratio domains. *Advances in Water Resources*, *102*, 188–205. doi: 10.1016/j.advwatres.2017.02.004

Casas, A., Lane, S. N., Yu, D., & Benito, G. (2010). A method for parameterising roughness and topographic sub-grid scale effects in hydraulic modelling from LiDAR data. *Hydrololgy and Earth Systems Science*, *14*, 1567–1579. doi: 10.5194/hess-14-1567-2010

Casulli, V. (1990). Semi-implicit finite-difference methods for the 2-dimensional shallow-water equations. *Journal of Computational Physics*, *86*(1), 56-74.

Casulli, V. (1999). A semi-implicit finite difference method for non-hydrostatic, free-surface flows. *International Journal for Numerical Methods in Fluids*, *30*, 425-440.

Casulli, V. (2009). A high-resolution wetting and drying algorithm for free-surface hydrodynamics. *International Journal for Numerical Methods in Fluids*, *60*, 391–408. doi: 10.1002/fld.1896

Casulli, V., & Cattani, E. (1994). Stability, accuracy and efficiency of a semi-implicit method for three-dimensional shallow water flow. *Computer & Mathematics with Applications*, *27*(4), 99–112.

Casulli, V., & Cheng, R. T. (1992). Semi-implicit finite difference methods for three-dimensional shallow water flow. *International Journal for Numerical Methods in Fluids*, *15*, 629–648.

Cea, L., & French, J. R. (2012). Bathymetric error estimation for the calibration and validation of estuarine hydrodynamic models. *Estuarine, Coastal & Shelf Science*, *100*, 124-132.

Cea, L., French, J. R., & Vazquez-Cendon, M. E. (2006). Numerical modeling of tidal flows in complex estuaries including turbulence: An unstructured finite volume solver and experimental validation. *International Journal for Numerical Methods in Engineering*, *67*, 1909-1932.

Cea, L., Legout, C., Darboux, F., Esteves, M., & Nord, G. (2014). Experimental validation of a 2D

overland flow model using high resolution water depth and velocity data. *Journal of Hydrology*, *513*, 142–153. doi: 10.1016/j.jhydrol.2014.03.052

Chao, X., Jia, Y., Shields, F. D., Wang, S. S. Y., & Cooper, C. M. (2008). Three-dimensional numerical modeling of cohesive sediment transport and wind wave impact in a shallow oxbow lake. *Advances in Water Resources*, *31*, 1004-1014.

Chen, A. S., Evans, B., Djordjevic, D., & Savic, D. A. (2012). Multi-layered coarse grid modelling in 2D urban flood simulations. *Journal of Hydrology*, *470–471*, 1–11. doi: 10.1016/j.jhydrol .2012.06.022

Cheng, N. S. (2015). Resistance Coefficients for Artificial and Natural Coarse-Bed Channels: Alternative Approach for Large-Scale Roughness. *Journal of Hydraulic Engineering*, *141(2)*, 04014072. doi: 10.1061/(ASCE)HY.1943-7900.0000966

Cheng, R. T., Casulli, V., & Gartner, J. (1993). Tidal, residual, intertidal mudflat (TRIM) model and its applications to San Francisco Bay, California. *Estuarine, Coastal and Shelf Science*, *36*, 235-280.

Chou, Y., Holleman, R. C., Fringer, O. B., Stacey, M. T., Monismith, S. G., & Koseff, J. R. (2015). Three-dimensional wave-coupled hydrodynamics modeling in South San Francisco Bay. *Computers & Geosciences*, *85*, 10-21.

Chua, V. P., & Fringer, O. B. (2011). Sensitivity analysis of three-dimensional salinity simulations in North San Francisco Bay using the unstructured-grid SUNTANS model. *Ocean Modelling*, *39*, 332-350.

D'Alpaos, L., & Defina, A. (2007). Mathematical modeling of tidal hydrodynamics in shallow lagoons: A review of open issues and applications to the Venice Lagoon. *Computers & Geosciences*, *33*, 476–496. doi: 10.1016/j.cageo.2006.07.009

Defina, A. (2000). Two-dimensional shallow flow equations for partially dry areas. *Water Resources Research*, *36*(11), 3251–3264. doi: 10.1029/2000WR900167

Defina, A., D'Alpaos, L., & Matticchio, B. (1994). A new set of equations for very shallow water and partially dry areas suitable to 2D numerical models. *Proceedings of the Specialty Conference on Modelling of Flood Propagation Over Initially Dry Areas*, 72–81.

Del Rosario, E. A., & Montagna, P. A. (2018). Effects of the Rincon Bayou Pipeline on salinity in the upper Nueces Delta. *Texas Water Journal*, *9*(1), 30-49.

de Rooij, R. (2017). New insights into the differences between the dual node approach and the common node approach for coupling surface-subsurface flow. *Hydrol. Earth Syst. Sci.*, *21*, 5709–5724. doi: 10.5194/hess-21-5709-2017

Duan, Y., Liu, Z., Chen, Y., & Zhu, D. (2017). Improved 2D shallow water model able to capture the effects of complex bathymetric features through their subgrid modeling. *Hydraulic Engineering*, *143*(2), 04016081. doi: 10.1061/(ASCE)HY.1943-7900.0001246

Dunton, K. H., Ward, G. H., Montagna, P. A., Whitledge, T. E., Alexander-Mahala, H. D., Nelson, R. D., ... Stockwell, D. A. (2000). *Concluding report: Rincon Bayou Demonstration Project* (Tech. Rep. No. Volume II: Findings). United States Department of the Interior, Bureau of Reclamation, Oklahoma-Texas Area Office, Austin, Texas.

Fringer, O. B., Gerritsen, M., & Street, R. L. (2006). An unstructured-grid, finite-volume, nonhydrostatic, parallel coastal ocean simulator. *Ocean Modelling*, *14*, 139–173.

Gross, E. S., Bonaventura, L., & Rosatti, G. (2002). Consistency with continuity in conservative advection schemes for free-surface Mmodels. *International Journal for Numerical Methods in Fluids*, *38*(4), 307-327.

Gross, E. S., Koseff, J. R., & Monismith, S. G. (1999). Evaluation of advective schemes for estuarine salinity simulations. *Journal of Hydraulic Engineering*, *125*(1), 32-46.

Guinot, V. (2012). Multiple porosity shallow water models for macroscopic modelling of urban floods. *Advances in Water Resources*, *37*, 40–72. doi: /10.1016/j.advwatres.2011.11.002

Guinot, V. (2017a). Consistency and bicharacteristic analysis of integral porosity shallow water models. Explaining model oversensitivity to mesh design. *Advances in Water Resources*, *107*, 43–55. doi: /10.1016/j.advwatres.2017.06.008

Guinot, V. (2017b). A critical assessment of flux and source term closures in shallow water models with porosity for urban flood simulations. *Advances in Water Resources*, *109*, 133–157. doi: /10.1016/j.advwatres.2017.09.002

Guinot, V., Delenne, C., Rousseau, A., & Boutron, O. (2018). Flux closures and source term models for shallow water models with depth-dependent integral porosity. *Advances in Water Resources*, *122*, 1–26. doi: /10.1016/j.advwatres.2018.09.014

Guinot, V., Sanders, B. F., & Schubert, J. E. (2017). Dual integral porosity shallow water model for

urban flood modelling. *Advances in Water Resources*, *103*, 16–31. doi: /10.1016/j.advwatres .2017.02.009

Hajduk, H., Hodges, B. R., Aizinger, V., & Reuter, B. (2018). Locally Filtered Transport for computational efficiency in multi-component advection-reaction models. *Environmental Modelling & Software*, *102*, 185-198. doi: 10.1016/j.envsoft.2018.01.003

Han, L., Mignot, E., & Riviere, N. (2017). Shallow mixing layer downstream from a sudden expansion. *Journal of Hydraulic Engineering*, *143(5)*, 04016105. doi: 10.1061/(ASCE)HY .1943-7900.0001274

Hasan, G. M. J., van Maren, D. S., & Cheong, H. F. (2012). Improving hydrodynamic modeling of an estuary in a mixed tidal regime by grid refining and aligning. *Ocean Dynamics*, *62*, 395–409. doi: 10.1007/s10236-011-0506-4

Herbert, E. R., Boon, P., Burgin, A. J., Neubauer, S. C., Franklin, R. B., Ardon, M., ... Gell, P. (2015). A global perspective on wetland salinization: ecological consequences of a growing threat to freshwater wetlands. *Ecosphere*, *6*(10), 206. doi: 10.1890/ES14-00534.1

Hill, E. M., Tunnell, J. W., & Nicolau, B. A. (2015). Spatial and temporal effects of the Rincon Bayou Pipeline on hypersaline conditions in the Lower Nueces Delta, Texas, USA. *Texas Water Journal*, *6*(1), 11-32.

Hodges, B. R. (2004, Aug). Accuracy order of Crank-Nicolson discretization for hydrostatic free-surface flow. *Journal of Engineering Mechanics-ASCE*, *130*(8), 904–910. doi: 10.1016/ (ASCE)0733-9399(2004)130:8(904)

Hodges, B. R. (2014). A new approach to the local time stepping problem for scalar transport. *Ocean Modelling*, *77*, 1–19. doi: 10.1016/j.ocemod.2014.02.007

Hodges, B. R. (2015). Representing hydrodynamically important blocking features in coastal or riverine lidar topography. *Natural Hazards & Earth System Sciences*, *56*, 1011–1023.

Hodges, B. R., Imberger, J., Saggio, A., & Winters, K. (2000). Modeling basin-scale internal waves in a stratified lake. *Limnology and Oceanography*, *47*(7), 1603–1620.

Hodges, B. R., & Liu, F. (2014). Rivers and electric networks: crossing disciplines in modeling and simulation. *Foundations and Trends in Electronic Design Automation*, *8*(1), 1-116.

Hodges, B. R., & Rueda, F. J. (2008). Semi-implicit two-level predictor-corrector methods for non-linearly coupled, hydrostatic, barotropic/baroclinic flows. *International Journal of Computational Fluid Dynamics*, *22*(9), 593–607.

Holleman, R., Fringer, O., & Stacey, M. (2013). Numerical diffusion for flow-aligned unstructured grids with application to estuarine modeling. *International Journal for Numerical Methods in Fluids*. doi: 10.1002/fld.3774

Horritt, M. S., & Bates, P. D. (2001). Effects of spatial resolution on a raster based model fo flood flow. *Journal of Hydrology*, *253*, 239–249.

Horritt, M. S., Bates, P. D., & Mattinson, M. J. (2006). Effects of mesh resolution and topographic representation in 2D finite volume models of shallow water fluvial flow. *Journal of Hydrology*, *329*, 306–314. doi: 10.1016/j.jhydrol.2006.02.016

Hughes, J., Langevin, C., & Banta, E. (2017). Book 6: Modeling Techniques. In *Documentation for the MODFLOW 6 framework: U.S. Geological Survey Techniques and Methods* (chap. 57, Section A). U.S. Geological Survey. doi: 10.3133/tm6A57

Inoue, M., Park, D., Justic, D., & Wiseman Jr., W. J. (2008). A high-resolution integrated hydrology-hydrodynamic model of the Barataria Basin system. *Environmental Modelling & Software*, *23*, 1122-1132.

Ip, J. T. C., Lynch, D. R., & Friedrichs, C. T. (1998). Simulation of estuarine flooding and dewatering with application to Great Bay, New Hampshire. *Estuarine, Coastal & Shelf Science*, *47*, 119-141.

Jan, A., Coon, E. T., Graham, J. D., & Painter, S. L. (2018). A subgrid approach for modeling microtopography effects on overland flow. *Water Resources Research*, *54*, 6153–6167. doi: /10.1029/2017WR021898

Jeon, J., Lee, J. Y., & Kang, S. (2018). Experimental investigation of three-dimensional flow structure and turbulent flow mechanisms around a nonsubmerged spur dike with a low length-to-depth ratio. *Water Resources Research*, *54*, 3530–3556. doi: 10.1029/2017WR021582

Katul, G., Wiberg, P., Albertson, J., & Hornberger, G. (2002). A mixing layer theory for flow resistance in shallow streams. *Water Resources Research*, *38*(11), 1250. doi: 10.1029/ 2001WR000817

Kim, B., Sanders, B. F., Famiglietti, J. S., & Guinot, V. (2015). Urban flood modeling with porous shallow-water equations: A case study of model errors in the presence of anisotropic porosity.

Journal of Hydrology, *523*, 680–692. doi: 10.1016/j.jhydrol.2015.01.059

Kollet, S. J., & Maxwell, R. M. (2006). Integrated surface-groundwater flow modeling: A free-surface overland flow boundary condition in a parallel groundwater flow model. *Advances in Water Resources*, *29*, 945–958. doi: 10.1016/j.advwatres.2005.08.006

Lane, S. N. (2005). Roughness - time for a re-evaluation? *Earth Surface Processes and Landforms*, *30*, 251–251. doi: 10.1002/esp.1208

Launder, B. E., & Spalding, D. B. (1974). The numerical computation of turbulent flow computer methods. *Computer Methods in Applied Mechanics and Engineering*. doi: 10.1016/0045-7825(74)90029-2

Li, X., & Djilali, N. (1995). On the scaling of separation bubbles. *JSME International Journal Series B: Fluids and Thermal Engineering*, *38(4)*, 541-548.

Li, Z. (2019). *Representing effects of subgrid-scale topography on coarse-grid hydrodynamic models for shallow coastal marshes* (Unpublished doctoral dissertation). University of Texas at Austin.

Li, Z., & Hodges, B. R. (2019a). Modeling subgrid-scale topographic effects on shallow marsh hydrodynamics and salinity transport. *Advances in Water Resources*, *129*, 1-15. doi: 10.1016/j.advwatres.2019.05.004

Li, Z., & Hodges, B. R. (2019b). Model instability and channel connectivity for 2D coastal marsh simulations. *Environmental Fluid Mechanics*, *19*, 1309-1338. doi: /10.1007/s10652-018-9623-7

Li, Z., & Hodges, B. R. (2020). On modeling subgrid-scale macro-structures in narrow twisted channels. *Advances in Water Resources*, *135*, 103465. doi: 10.1016/j.advwatres.2019.103465

Li, Z., Passalacqua, P., & Hodges, B. R. (2017). *Hydrodynamic model development for the Trinity River Delta* (Tech. Rep.). Center for Water and the Environment, University of Texas at Austin. (Submitted to the Texas Water Development Board under contract 1600011928)

Lloyd, L., Tunnell, J. W., & Everett, A. (2013). *Using lidar elevation data to develop a topobathymetric digital elevation model for sub-grid inundation modeling at Langley Research Center* (Tech. Rep. Nos. CBBEP-85, project 1311). Coastal Bend Bays & Estuaries Program.

Loftis, J. D., Wang, H. V., DeYoung, R. J., & Ball, W. B. (2016). Nueces Delta salinity effects from pumping freshwater into the Rincon Bayou: 2009 to 2013. *Journal of Coastal Research*, *76*, 134–148. doi: 10.2112/SI76-012

Martins, R., Leandro, J., & Djordjevic, S. (2018). Wetting and drying numerical treatments for the Roe Riemann scheme. *Journal of Hydraulic Research*, *52*(2), 256–267. doi: 10.1080/00221686.2017.1289256

Matte, P., Secretan, Y., & Morin, J. (2017). Hydrodynamic modeling of the St. Lawrence fluvial estuary I: Model setup, calibration, and validation. *Journal of Waterway, Port, Coastal, Ocean Engineering*, *143(5)*, 04017010. doi: 10.1061/(ASCE)WW.1943-5460.0000397

Mazzolari, A., Trigo-Teixeira, A., & Araujo, M. A. V. C. (2015). Evaluation of different meshing criteria for areas exposed to flooding. *Computers and Fluids*, *121*, 81–91. doi: /10.1016/j.compfluid.2015.08.011

McMahon, T. A., Peel, M. C., Lowe, L., Srikanthan, R., & McVicar, T. R. (2013). Estimating actual, potential, reference crop and pan evaporation using standard meteorological data: a pragmatic synthesis. *Hydrol. Earth Syst. Sci.*, *17*, 1331-1363.

Medeiros, S. C., & Hagen, S. C. (2013). Review of wetting and drying algorithms for numerical tidal flow models. *International Journal for Numerical Methods in Fluids*, *71*, 473-487.

Monsalve, A., Yager, E. M., & Schmeeckle, M. W. (2017). Effects of bed forms and large protruding grains on near-bed flow hydraulics in low relative submergence conditions. *Journal of Geophysical Research: Earth Surface*, *122*, 1845–1866. doi: 10.1002/2016JF004152

Munoz, D. H., & Constantinescu, G. (2018). A fully 3-D numerical model to predict flood wave propagation and assess efficiency of flood protection measures. *Advances in Water Resources*, *122*, 148–165. doi: 10.1016/j.advwatres.2018.10.014

Murillo, J., Garcia-Navarro, P., & Burguete, J. (2009). Conservative numerical simulation of multi-component transport in two-dimensional unsteady shallow water flow. *Journal of Computational Physics*, *228*, 5539–5573. doi: 10.1016/j.jcp.2009.04.039

Neal, J., Schumann, G., & Bates, P. (2012). A subgrid channel model for simulating river hydraulics and floodplain inundation over large and data sparse areas. *Water Resources Research*, *48*(W11506). doi: /10.1029/2012WR012514

Niu, J., Shen, C., Li, S. G., & Phanikumar, M. S. (2014). Quantifying storage changes in regional Great Lakes watersheds using a coupled subsurface-land surface process model and GRACE, MODIS products. *Water Resoures Research*, *50*, 7359–7377. doi: 10.1002/2014WR015589

NRA. (2019). *Nueces River Authority, Rincon Bayou Pipeline Events.* Retrieved from `https://www.nueces-ra.org/CP/CITY/rincon/index.php` ((last accessed Jan. 11th, 2019),)

Ozgen, I., Liang, D., & Hinkelmann, R. (2016). Shallow water equations with depth-dependent anisotropic porosity for subgrid-scale topography. *Applied Mathematical Modelling*, *40*, 7447–7473. doi: 10.1016/j.apm.2015.12.012

Ozgen, I., Teuber, K., Simons, F., Liang, D., & Hinkelmann, R. (2015). Upscaling the shallow water model with a novel roughness formulation. *Environmental Earth Sciences*, *74*, 7371–7386. doi: /10.1007/s12665-015-4726-7

Ozgen, I., Zhao, J. H., Liang, D. F., & Hinkelmann, R. (2016). Urban flood modeling using shallow water equations with depth-dependent anisotropic porosity. *Journal of Hydrology*, *541*, 1165–1184. doi: /10.1016/j.jhydrol.2016.08.025

Patankar, S. V. (1980). *Numerical heat transfer and fluid flow*. McGraw-Hill.

Penman, H. L. (1948). Natural evaporation from open water, bare soil and grass. *Proceedings of the Royal Society of London A*, *193*, 120-145.

Platzek, F. W., Stelling, G. S., Jankowski, J. A., Patzwahl, R., & Pietrzak, J. D. (2016). An efficient semi-implicit subgrid method for free-surface flows on hierarchical grids. *International Journal for Numerical Methods in Fluids*, *80*, 715–741. doi: /10.1002/fld.4172

Powell, D. M. (2014). Flow resistance in gravel-bed rivers: Progress in research. *Earth-Science Reviews*, *136*, 301–338. doi: 10.1016/j.earscirev.2014.06.001

Ralston, D. K., Geyer, W. R., & Lerczak, J. A. (2010). Structure, variability, and salt flux in a strongly forced salt wedge estuary. *Journal of Geophysical Research*, *115*, C060055. doi: 10.1029/2009JC005806

Rayson, M. D., Gross, E. S., & Fringer, O. B. (2015). Modeling the tidal and sub-tidal hydrodynamics in a shallow, micro-tidal estuary. *Ocean Modelling*, *89*, 29-44.

Rueda, F. J., Sanmiguel-Rojas, E., & Hodges, B. R. (2007). Baroclinic stability for a family of two-level, semi-implicit numerical methods for the 3D shallow water equations. *International Journal of Numerical Methods in Fluids*, *54*(3), 237–268.

Ryan, A. J., & Hodges, B. R. (2011). *Modeling Hydrodynamic Fluxes in the Nueces River Delta* (Tech. Rep.). Center for Research in Water Resources, University of Texas at Austin. (CRWR Online Report 11-07, 92 pages, October 2011)

Sanders, B. F., & Schubert, J. E. (2019). PRIMo: Parallel raster inundation model. *Advances in Water Resources*, *126*, 79–95. doi: 10.1016/j.advwatres.2019.02.007

Sanders, B. F., Schubert, J. E., & Gallegos, H. A. (2008). Integral formulation of shallow-water equations with anisotropic porosity for urban flood modeling. *Journal of Hydrology*, *362*, 19–38. doi: 10.1016/j.jhydrol.2008.08.009

Schoenbaechler, C. A., Negusse, S., & Guthrie, C. G. (2014). *Nueces Delta Data Collection for Calibration and Validation of the Nueces Delta Hydrodynamic Model* (Tech. Rep.). Texas Water Development Board. (Final Report to the U.S. Army Corps of Engineers, Fort Worth District. January 21, 2014)

Sehili, A., Lang, G., & Lippert, C. (2014). High-resolution subgrid models: background, grid generation, and implementation. *Ocean Dynamics*, *64*, 519–535. doi: 10.1007/s10236-014-0693-x

Shin, G. (2016). *A subgrid approach for unresolved topography in shallow water hydrodynamic modeling* (Unpublished doctoral dissertation). University of Texas at Austin.

Silva, C. P., Marti, C. L., & Imberger, J. (2014). Horizontal transport, mixing and retention in a large, shallow estuary: Rio de la Plata. *Environmental Fluid Mechanics*, *14*, 1173-1197.

Skalicky, T. (2019). LASPack Reference Manual [Computer software manual]. Retrieved from `http://www.mgnet.org/mgnet/Codes/laspack/html/laspack.html` ((last accessed Dec. 10th, 2018),)

Snedden, G. A., Cretini, K., & Patton, B. (2015). Inundation and salinity impacts to above- and belowground productivity in *Spartina patens* and *Spartina alterniflora* in the Mississippi River deltaic plain: Implications for using river diversions as restoration tools. *Ecological Engineering*, *81*, 133–139. doi: 10.1016/j.ecoleng.2015.04.035

Spitz, Y. H., & Klinck, J. M. (1998). Estimate of bottom and surface stress during a spring-neap tide cycle by dynamical assimilation of tide gauge observations in the Chesapeake Bay. *Journal of Geophysical Research*, *103*(C6), 12761-12782.

Stachelek, J., & Dunton, K. H. (2013). Freshwater inflow requirements for the Nueces Delta, Texas: *Spartina alterniflora* as an indicator of ecosystem condition. *Texas Water Journal*, *4*(2), 62–73.

Stelling, G. S. (2012). Quadtree flood simulations with sub-grid digital elevation models. *Proceedings*

of the Institution of Civil Engineers-Water Management, *165(10)*, 567–580. doi: 10.1680/wama.12.00018

Sullivan, J. C., Torres, R., Garrett, A., Blanton, J., Alexander, C., Robinson, M., ... Hayes, D. (2015). Complexity in salt marsh circulation for a semi-enclosed basin. *Journal of Geophysical Research: Earth Surface*, *120*, 1973–1989. doi: 10.1002/2014JF003365

TCOON. (2019). *Texas Coastal Ocean Observation Network.* Retrieved from `http://cbi.tamucc.edu/TCOON/` ((last accessed Jan. 11th, 2019),)

Teng, J., Jakeman, A. J., Vaze, J., Croke, B. F. W., Dutta, D., & Kim, S. (2017). Flood inundation modelling: A review of methods, recent advances and uncertainty analysis. *Environmental Modelling & Software*, *90*, 201–216. doi: 10.1016/j.envsoft.2017.01.006

Torres, R., & Styles, R. (2007). Effects of topographic structure on salt marsh currents. *Journal of Geophysical Research*, *112*(F02023).

Tracy, H. (1957). *Discharge characteristics of broad-crested weir* (Tech. Rep.). Geological Survey Circular 397.

Tunnell, J., & Lloyd, L. (2011). *Effects of Rincon Bayou Pipeline Inflows on Salinity Structure Within the Nueces Delta, Texas*. CBBEP Publication 76., Project Number 1106.

Velickovic, M., Zech, Y., & Soares-Frazao, S. (2017). Steady-flow experiments in urban areas and anisotropic porosity model. *Journal of Hydraulic Research*, *55:1*, 85–100. doi: 10.1080/00221686.2016.1238013

Viero, D. P., & Valipour, M. (2017). Modeling anisotropy in free-surface overland and shallow inundation flows. *Advances in Water Resources*, *104*, 1–14. doi: /10.1016/j.advwatres.2017.03.007

Volp, N. D., van Prooijen, B. C., & Stelling, G. S. (2013). A finite volume approach for shallow water flow accounting for high-resolution bathymetry and roughness data. *Water Resources Research*, *49*, 4126–4135. doi: 10:1002/wrcr.20324

Wadzuk, B. M., & Hodges, B. R. (2009). Hydrostatic versus nonhydrostatic Euler-Equation modeling of nonlinear internal waves. *ASCE Journal of Engineering Mechanics*, *135*(4), 1069–1080.

Wang, B., Fringer, O. B., Giddings, S. N., & Fong, D. A. (2009). High-resolution simulations of a macrotidal estuary using SUNTANS. *Ocean Modelling*, *28*, 167-192.

Ward, G. H. (1997). *Processes and Trends of Circulation Within the Corpus Christi Bay National Estuary Program Study Area* (Tech. Rep. No. CBBEP-21). Corpus Christi, Texas, USA: Coastal Bend Bays and Estuaries Program. Retrieved from `http://cbbep.org/publications/CCBNEP21.pdf`

Watson, E. B., Szura, K., Wigand, C., Raposa, K. B., Blount, K., & Cencer, M. (2016). Sea level rise, drought and the decline of *Spartina patens* in New England marshes. *Biological Conservation*, *196*, 173–181. doi: 10.1016/j.biocon.2016.02.011

Westerink, J. J., Luettich, R. A., Feyen, J. C., Atkinson, J. H., Dawson, C., Roberts, H. J., ... Pourtaheri, H. (2008). A basin- to channel-scale unstructured grid hurricane storm surge model applied to Southern Louisiana. *Monthly Weather Review*, *136*, 833–864. doi: 10.1175/2007MWR1946.1

Wu, G., Shi, F., Kirby, J. T., Mieras, R., Liang, B., Li, H., & Shi, J. (2016). A pre-storage, subgrid model for simulating flooding and draining processes in salt marshes. *Coastal Engineering*, *108*, 65–78. doi: 10.1016/j.coastaleng.2015.11.008

Wunderlich, W. O. (1972). *Heat and Mass Transfer Between a Water Surface and the Atmosphere* (Tennessee Valley Authority Report No. 0-6803). Norris Tennessee.: Water Resources Research Laboratory.

Yang, J., Zhang, H., Yu, X., Graf, T., & Michael, H. (2018). Impact of hydrogeological factors on groundwater salinization due to ocean-surge inundation. *Advances in Water Resources*, *111*, 423–434. doi: 10.1016/j.advwatres.2017.11.017

Yu, D., & Lane, S. (2006b). Urban fluvial flood modelling using a two-dimensional diffusion-wave treatment, part 2: development of a sub-grid-scale treatment. *Hydrological Processes*, *20*, 1567–1583. doi: 10.1002/hyp.5936

Yu, D., & Lane, S. N. (2006a). Urban fluvial flood modelling using a two-dimensional diffusion-wave treatment, part 1: mesh resolution effects. *Hydrological Processes*, *20*, 1541–1565. doi: 10.1002/hyp.5935

Yu, D., & Lane, S. N. (2011). Interactions between subgrid-scale resolution, feature representation and grid-scale resolution in flood inundation modelling. *Hydrological Processes*, *25*, 36–53. doi: 10.1002/hyp.7813

Yuan, D., Lin, B., & Falconer, R. A. (2007). A modelling study of residence time in a macro-tidal

estuary. *Estuarine, Coastal & Shelf Science*, *71*, 401-411.

Zacharias, I., & Gianni, A. (2008). Hydrodynamic and dispersion modeling as a tool for restoration of coastal ecosystems. Application to a re-flooded lagoon. *Environmental Modelling & Software*, *23*, 751-767.

Zhang, C., Li, L., & Lockington, D. (2014). Numerical study of evaporation-induced salt accumulation and precipitation in bare saline soils: Mechanism and feedback. *Water Resources Research*, *50*, 8084-8106.

Zheng, L., Chen, C., & Liu, H. (2003). A modeling study of the Satilla River Estuary, Georgia. I: Flooding-drying process and water exchange over the salt marsh-estuary-shelf complex. *Estuaries*, *26*, 651-669.